Supplementary Information for

Fetal monitoring using a wearable ultrasound patch for risky pregnancies

Geonho Park[1,9], Yizhou Bian[1,9], Hao Huang[1,9], Sai Zhou[2,9], Siyu Qin[3], Muyang Lin[1], Xinyi Yang[2], Aaron Lee[4], Anand Ramkumar[5], Mariana Tome[5], Jayne Lander[5], Xiangjun Chen[2], Shenghan Wang[1], Pranavi Bheemreddy[3], Liam Stanton[1], Mabel Shehada[4], Ruotao Wang[1], Alexa Roa[4], Chengchangfeng Lu[3], Wentong Yue[1], Ray S. Wu[1], Xiaoxiang Gao[1], Hongjie Hu[1], Amer Yaghi[1], Mark Liu[6], Lawrence Impey[5], Sally L. Collins[5], Aris T Papageorghiou[5], Louise C. Laurent[7], Antoniya Georgieva[5#], Sheng Xu[1,2,3,4,8#]

[1]Aiiso Yufeng Li Family Department of Chemical and Nano Engineering, University of California San Diego, La Jolla, CA 92093, USA.
[2]Materials Science and Engineering Program, University of California San Diego, La Jolla, CA 92093, USA.
[3]Department of Electrical and Computer Engineering, University of California San Diego, La Jolla, CA 92093, USA.
[4]Shu Chien–Gene Lay Department of Bioengineering, University of California San Diego, La Jolla, CA 92093, USA.
[5]Nuffield Department of Women's and Reproductive Health, University of Oxford, Oxford OX3 9DU, UK.
[6]Qualcomm Institute Makerspace, University of California San Diego, La Jolla, CA 92093, USA.
[7]Department of Obstetrics, Gynecology, and Reproductive Sciences, University of California San Diego, La Jolla, CA 92093, USA.
[8]Department of Radiology, University of California San Diego, La Jolla, CA 92093, USA.
[9]These authors contributed equally to this work: Geonho Park, Yizhou Bian, Hao Huang, Sai Zhou.
[#]e-mail: shengxu@ucsd.edu, antoniya.georgieva@wrh.ox.ac.uk

Table of Contents

Supplementary Discussion 1: Continuous prenatal monitoring

The primary goal of antepartum fetal surveillance (also referred to as prenatal monitoring) is to prevent irreversible fetal injury or stillbirth[1]. Current methods, including cardiotocography[2], fetal movement[3], and ultrasound-based assessments[4], are performed intermittently and seek to detect subacute uteroplacental insufficiency[1,5]. These methods focus on monitoring the gradual changes in fetal health, allowing healthcare providers to intervene before any permanent damage occurs. However, the intermittent nature of these assessments means that they may miss sudden, acute events that can lead to fetal compromise.

Many stillbirths are suspected to result from acute events, such as umbilical cord accidents, placental abruption, and premature rupture of the membrane[5]. These acute events cannot be predicted by the current intermittent approaches. Umbilical cord accidents, including cord compression, nuchal cord (where the cord is wrapped around the baby's neck), and prolapsed cord (where the cord slips into the birth canal ahead of the baby), can lead to a rapid decrease in the fetal oxygen supply[6]. Placental abruption is a serious pregnancy complication in which the placenta partially or completely detaches from the inner wall of the uterus[7]. This detachment can disrupt the supply of oxygen and nutrients to the fetus and cause severe internal bleeding in the uterus[7]. Premature rupture of the membrane (also known as amniotic sac) can lead to infections and preterm labor, posing high risks to both the mother and fetus[8].

Continuous prenatal monitoring can detect both subacute and acute fetal compromise. It has the potential to identify signs of sudden fetal distress as they occur, allowing for timely interventions that could prevent stillbirth and other severe outcomes.

Supplementary Discussion 2: Wearable fetal monitors

Numerous wearable devices have emerged to extract fetal signals in combination with other maternal sensors (Supplementary Fig. 1)[9-11]. Fetal monitoring technologies vary considerably in terms of sensing modality, number and configuration of sensors, spatial resolution, and clinical application. These wearable devices can continuously detect fetal heart rate, electrocardiogram, oximetry, and movements. Here, we provide a summary of state-of-the-art technologies, highlighting general limitations. Additional technical details for these technologies can be found in the cited references.

First, wearable fetal heart rate monitors, such as HeraBEAT (HeraMED)[12] and Moyo fetal heart rate monitor (Moyo)[13], have been introduced to address the limitations of handheld devices, such as Sonoline B (Sonoline)[14], SD1 (Edan)[15], and Newman (Babybeat)[16] that only offer intermittent measurements. These devices utilize ultrasound and operate in continuous wave Doppler mode, leveraging two ultrasound transducers for transceiving[9]. Although Doppler signals are intended to originate from the movements of fetal heart valves, any movements are translated into signals[9]. The absence of spatial resolution of the continuous wave Doppler mode is a crucial limitation because it results in the mixing of different signals. Additionally, during advanced gestation, the increased frequency of uterine contractions can influence fetal heart rate[17]. Consequently, the measured fetal heart rate may not be accurate, and therefore, monitoring fetal heart rate alone does not adequately reflect the physiological changes within the uterus.

To better understand how uterine contractions influence fetal heart rate, wearable cardiotocography can simultaneously monitor these two signals. Traditional wearable cardiotocography, such as Corometrics 250cx (GE Healthcare)[18], Avalon FM50 (Philips)[19], and Sense4baby (Advanced Maternity Innovations)[20], relies on continuous wave Doppler for fetal heart rate and a tocodynamometer for uterine contractions (Supplementary Fig. 1). Due to their large form factor, these devices necessitate belts for optimal sensor placement and wired connections to external hardware for power and signal transfer. Such fixations impose constraints on the maternal abdomen, making them less feasible for prolonged use. Additionally, the mechanical mismatch between the bulky devices and the maternal skin is prone to signal loss and motion artifacts.

Minimally invasive methods, such as fetal scalp electrodes and intrauterine pressure catheters, provide more direct measurements of fetal heart rate and uterine contractions, enhancing signal integrity under critical conditions[17]. Accurate monitoring becomes essential in high-risk pregnancies to enable prompt interventions because fetal and maternal movements can disrupt cardiotocography signals[21]. Additionally, amniotic sac rupture may reduce fluid levels, hindering ultrasound transmission[17]. Scalp electrode provides direct fetal heart rate tracings by inserting spiral wires into the fetal head. Intrauterine pressure catheters quantify the pressure intensity of the uterine contraction, while tocodynamometers only monitor the contraction frequency and duration[22]. However, the use of scalp electrodes and intrauterine catheters is restricted to labor monitoring[17]. In addition, scalp electrodes may lead to complications such as scalp trauma[17], while intrauterine pressure catheters may cause infections and uterine rupture[22].

More recently developed devices have focused on miniaturized and flexible wearable cardiotocography, such as ANNE (Sibel Health)[23] and Farus wearable ultrasound and tocodynamometer (Farus)[24], which minimize the mechanical mismatch between the device and the maternal skin (Supplementary Fig. 1). These devices integrate power, signal processors, and wireless connections into the device casing, eliminating the need for securing belts. This advancement largely improves portability and user-friendliness in wearable cardiotocography.

Second, wearable electrocardiogram devices employ biopotential electrodes, such as AN24 (Monica Healthcare, now Novii by GE Healthcare)[25,26], Avalon beltless fetal monitoring solution (Philips)[27], Invu (Nuvo)[28], Meridian M110 (MindChild Medical)[29], Bloomlife electrophysiological monitor (Bloomlife)[30], Nemo fetal monitoring system (Nemo Healthcare)[31], and Femom lite (Biorithm)[32]. Maternal electrocardiograms (~200 μV) often interfere with weak fetal electrocardiograms (~3 μV)[25]. Additionally, movement and positional changes of the fetus cause fluctuations in electrical impedance, further compromising signal integrity[25]. To overcome the low signal amplitude of fetal electrocardiograms, various systems utilize an array of electrodes on the maternal abdomen with advanced signal decomposition algorithms to isolate the subtle fetal from the maternal electrocardiograms. The AN24 uses a five-electrode configuration: one as a common ground and the remaining four placed in upper, lower, right lateral, and left lateral positions, achieving 85% reliability in estimating fetal heart rate (Supplementary Fig. 1)[26]. The Meridian M110 (MindChild Medical) uses 32 electrodes distributed across the maternal abdomen and has demonstrated 89.9% reliability[33]. While the increased electrode density enhances spatial resolution to handle fetal movement and signal interference, the modest improvement in reliability suggests that increasing the electrode count adds complexity to circuitry and signal processing but offers diminishing marginal benefits.

Third, wearable fetal oximetry devices, such as Lumerah (Raydiant Oximetry)[34] and Storx intrapartum fetal monitoring (Storx Technologies)[35], have been proposed to measure fetal blood oxygen levels. However, light penetration through the various tissue layers poses immense challenges, especially with signal interference from maternal signals and motion artifacts[36]. For example, while the initial placement of a wearable oximetry device can be optimized, fetal movements may cause signal loss. Consequently, reliably measuring blood oxygen levels in human fetuses has not yet been demonstrated.

Finally, wearable fetal movement devices are based on accelerometers (Supplementary Fig. 1)[37-42]. Accelerometers can capture various signals, including both fetal and maternal movements, which are often irregular[38]. Additionally, when the position of the fetus changes, the signal amplitude of different fetal movements also changes[42]. Therefore, it is challenging to distinguish which signals are fetal movements. To improve signal quality, the integration of acoustic sensors with accelerometers has been explored[41,42]. These devices are currently in the proof-of-concept phase, with belts and sleeves employed to secure the accelerometers, signal processing units, and batteries.

Supplementary Discussion 3: Implications and limitations of cardiotocography

Cardiotocography measures fetal heart rate and uterine contractions[9]. Changes in baseline, variability, and transient accelerations and decelerations of the fetal heart rate are due to the fetal central nervous system's responses to various environmental changes[17].

Fetal heart rate and heart rate variability serve as important indicators of fetal well-being[9,17,43]. These parameters reflect the physiological responses of the fetus under varying conditions, particularly the oxygenation state. Thus, monitoring these parameters has been widely used for identifying conditions arising from deprived oxygen levels, such as impending asphyxia during labor[44].

Typically, the fetal heart rate lies within the range of 120–160 beats per minute (bpm), with the baseline declining with advanced gestation[9]. Deviations from this range include bradycardia, defined as a baseline below 120 bpm, and tachycardia, characterized as a baseline exceeding 160 bpm[43]. Variability is categorized as absent, minimal (1 to 5 bpm), moderate (5 to 25 bpm), or marked (>25 bpm)[43]. Moderate and marked variabilities are often regarded as normal physiological responses as the sympathetic and parasympathetic nervous systems adjust the fetal heart rate based on dynamic in-utero conditions[43]. Absent or minimal variabilities may indicate hypoxia but are not always reliable as they may also be associated with other factors such as fetal sleep cycle[9], and thus need further evaluation[43].

Acceleration (transient increase in the fetal heart rate) suggests optimal fetal well-being[17]. Such elevation is often associated with fetal movements or external stimuli. Importantly, regular occurrences of accelerations are a reassuring sign, indicating that the fetus is well-oxygenated and the nervous system is responsive to its movements and external stimuli[17].

Uterine contractions are used in monitoring the onset of active labor as the uterus and cervix prepare for labor[22]. The tocodynamometer measures the frequency and duration of uterine contractions by placing a pressure transducer on the maternal abdomen to sense and record changes in tension as the uterus contracts[22].

The uterus, composed of smooth muscles, is capable of progressive stretching[17]. In the antepartum period, two primary types of contractions are observed[17]. First, sporadic and weak contractions of short duration occur in a localized area in the uterus. These contractions often occur in early stages of pregnancy[17]. Second, Braxton Hicks contractions, which are more intense, may take place irregularly, approximately once per hour at around 30-week of gestation, increasing up to every 5 to 10 min at term[17]. More frequent and regular contractions signal the onset of labor, leading to cervical dilation[17]. During labor, uterine contraction monitoring is used to detect labor abnormalities. For example, hypocontractile or hypercontractile uterine activity can lead to prolonged labor or uterine tachysystole, respectively, posing risks to fetal health[17].

By using cardiotocography during labor, the timing between fetal heart rate and uterine contraction has been associated with fetal health[17]. The fetal heart rate response to uterine contractions can indicate how well the fetus is coping with external stress[17]. Specifically, these patterns are categorized into three distinct types (i.e., early, late, and variable decelerations), each defined based on the temporal relationship between fetal heart rate and uterine contractions[43].

Early deceleration is characterized by a concurrent decline in fetal heart rate with the onset of uterine contraction[43]. This phenomenon is a result of pressure exerted on the fetal head during contraction, which in turn alters cerebral blood flow[17]. Then, the central nervous system is stimulated, prompting a deceleration in fetal heart rate. As the contraction amplifies, the fetal heart rate continues to decelerate. Finally, as contraction subsides, the fetal heart rate returns to the baseline. Early deceleration demonstrates the adaptive capabilities of the fetal central nervous system and is not indicative of fetal distress[43].

Late deceleration is characterized by a subsequent decline in fetal heart rate following the onset of uterine contraction[43]. Specifically, the nadir of the fetal heart rate is observed post-peak contraction. This deceleration process is commonly attributed to transient fetal hypoxia due to placental insufficiency[17]. In scenarios where placental function is sub-optimal, diminished blood flow during contractions may result in reduced oxygenation from the placenta to the fetus[17]. In response to the low oxygenation state, the fetal central nervous system decelerates the heart rate. As contraction ends, the fetal heart rate begins to recover and reverts to its baseline heart rate.

Variable deceleration is characterized by the unpredictable onset of fetal heart rate relative to the timing of uterine contractions[43]. These decelerations exhibit an abrupt onset and decline without a consistent relationship to the contraction phase. The predominant factor for variable decelerations is umbilical cord compression, leading to a transient decrease in blood flow between the fetus and the placenta[17]. This hemodynamic alteration elicits a temporary deceleration in fetal heart rate. As the umbilical cord blood flow returns to normal, the fetal heart rate returns back to the baseline.

While cardiotocography is useful, monitoring merely the fetal heart rate and uterine contraction comes with inherent challenges and has led to misdiagnosis[9,45]. Consequently, cardiotocography cannot serve as a stand-alone diagnostic tool and requires additional sensors for a more comprehensive and accurate assessment of fetal well-being.

First, cardiotocography interprets fetal well-being based on the central nervous system's response to alterations in blood flow[9,17]. Thus, the reliability of these measurements is constrained by the complexity of the underlying biological processes. This means that these measurements indirectly reflect fetal well-being, serving more as a potential consequence rather than a direct cause of the fetal health.

Second, alterations in fetal heart rate are one of the many central nervous responses. Others include systemic vasoconstriction and vasodilation of the intricate cardiovascular system[46]. In severe cases, the brain–sparing effect may be activated, resulting in the dilation of cerebral vessels to enhance brain perfusion, while vessels in other areas are constricted[46].

Third, the intrinsic variability in fetal heart rate presents challenges in deciphering the significance of specific patterns[9]. Determining the threshold for clinical intervention requires distinguishing between transient benign changes and those that are indicative of sustained fetal compromise. For instance, growth-restricted fetuses can sometimes exhibit a normal fetal heart rate range[17] and variability[2], while fetuses with bradycardia can be found to be well-oxygenated post-delivery[45]. Such data can precipitate unnecessary interventions, including Cesarean sections or operative vaginal deliveries, thereby exposing both the mother and the fetus to additional risks, including potential postnatal complications[9].

Consequently, cardiotocography has a false-positive rate of up to ~50% (ref. [9]), leading to unnecessary interventions and preterm birth[2,47]. While cardiotocography is a valuable source of information, findings must be integrated within a broader clinical context, limiting the effectiveness of cardiotocography as a stand-alone diagnostic approach.

Supplementary Discussion 4: Blood flow monitoring with ultrasonography

Ultrasonography is an invaluable tool in contemporary obstetrics due to its safety and diagnostic effectiveness[48-51]. Unlike fetal heart rate monitoring, which measures the response of the fetal central nervous system to alterations in blood flow (Supplementary Discussion 3), spectral Doppler ultrasound provides a direct quantitative measurement of the fetal and placental blood flow[1,52].

First, prenatal diagnostic options are notably limited compared to those available postnatally. Postnatal diagnostics utilize direct observations (such as skin paleness, scarring, and coughing), pain symptoms, and various measurements (such as blood pressure, body temperature, and oxygen saturation). In comparison, prenatal assessments are based on maternal perceptions and ultrasound-based measurements[3,53]. Additionally, while postnatal diagnoses often use blood pressure measurements as a standard indicator of cardiovascular well-being, prenatal monitoring heavily relies on ultrasound-based blood flow assessments[48].

Second, blood flow is generally stable in healthy fetuses[54]. The intrinsic variability in fetal heart rate caused immense challenges for accurate diagnosis with cardiotocography (Supplementary Discussion 3). Parameters such as umbilical artery blood flow exhibit minimal variations even during maternal physical exercise[55]. The relative stability of blood flow suggests that alterations are indicative of hypoxia or other vulnerable states in the fetus[55].

Third, fetal hypoxia is a primary cause of adverse prenatal and perinatal outcomes, including intrauterine growth restrictions[49,50], stillbirths[56], and hypoxic-ischemic encephalopathy[57], which may result in cerebral palsy[58] and permanent disability[52]. Spectral Doppler is an essential tool to diagnose hypoxic fetuses and aids in distinguishing pathological from healthy conditions[59-62]. For example, fetal biometry, while instrumental in detecting small for gestational age fetuses, does not unequivocally differentiate intrauterine growth restriction from small yet healthy fetuses[61]. Umbilical artery Doppler signals effectively differentiate the two cases. Intrauterine growth restriction is often associated with abnormal blood flow patterns (such as absent or reversed end diastolic flow), while small but healthy fetuses are characterized by normal blood flow patterns (forward end diastolic flow)[49,50].

Fourth, third-trimester pregnancy is often the most vulnerable when the fetal demand for oxygen and nutrients reaches its peak and there is a higher tendency for cord accidents (Supplementary Discussion 1)[63]. With prolonged distress, fetal asphyxia is the final common pathway leading to stillbirth[64]. Thus, blood flow assessment can guide the timing of delivery complicated by fetal hypoxia[49,51]. Profound compromise in blood flow may necessitate earlier delivery to prevent irreversible organ damage or stillbirth. During such critical states, the brain-sparing effect, a cerebral autoregulation mechanism to continuously supply sufficient oxygen to the brain, may be activated by the vasodilation of cerebral vessels and vasoconstriction of other vessels[46,65]. The surveillance of fetal blood flow allows for the optimization of the timing of delivery, balancing the risks of prematurity against the risks of hypoxia[49].

Despite the importance of continuous blood flow monitoring, current clinical protocols only provide intermittent ultrasound-based measurements in high-risk pregnancies[49,50]. This intermittent approach may overlook emergent complications or severe fetal distress, potentially increasing the risk of stillbirth. Continuous blood flow monitoring via spectral Doppler can provide real-time information about fetal well-being, enable clinicians to make informed decisions, and eventually reduce the likelihood of complications associated with undiagnosed fetal distress[48,50,52].

Supplementary Discussion 5: Clinically relevant vessels for monitoring

In fetal ultrasonography, three indices derived from spectral Doppler waveforms are used to assess fetal well-being based on reported reference ranges[66,67].

The systolic-to-diastolic ratio ($S/D\ ratio$) is defined as:

$$S/D\ ratio = \frac{PSV}{EDV} \tag{1}$$

where PSV is the peak systolic velocity and EDV is the end diastolic velocity.

The pulsatility index (PI) is defined as:

$$PI = \frac{PSV - EDV}{MFV} \tag{2}$$

where MFV is the mean flow velocity.

The resistance index (RI) is defined as:

$$RI = \frac{PSV - EDV}{PSV} \tag{3}$$

Routine hospital examinations of spectral Doppler indices are conducted in three major vessels: umbilical artery, umbilical vein, and middle cerebral artery[60].

The umbilical cord is a helical free-floating tube composed of two arteries and one vein. The umbilical arteries transport deoxygenated blood from the fetus to the placenta[50]. The spectral Doppler signal exhibits low resistance and continuous forward flow throughout systole and diastole in a healthy fetus[50]. Additionally, resistance decreases (i.e., increasing end diastolic velocity) from the fetal insertion point to the placental insertion point along the length of the umbilical cord, because the branching of the umbilical artery at the placental end results in a larger cumulative cross-sectional area and greater compliance of the vessels[49,50]. In healthy pregnancy, the $S/D\ ratio$, PI, and RI decrease with gestational progression[50]. As a reference, the median $S/D\ ratio$ diminishes from 3.23 at 24-week to 2.68 at 32-week and 2.19 at 40-week gestation; the median PI diminishes from 1.10 at 24-week to 0.96 at 32-week and 0.79 at 40-week gestation; and the median RI diminishes from 0.69 at 24-week to 0.63 at 32-week and 0.55 at 40-week gestation[68]. However, a substantial increase in these Doppler indices or the critical finding of absent or reversed end diastolic flow can signify fetal growth restriction[49,50].

The umbilical vein delivers oxygenated blood from the placenta to the fetus, typically showing continuous and non-pulsatile flow[50]. Fetal breathing is commonly observed in the umbilical venous flow in the third trimester due to changes in intrathoracic pressure[50]. On the other hand, pulsatile umbilical vein waveforms, which reflect the pulsatility of the fetal heart rate, can indicate a detrimental defect in fetal circulation, especially in the fetal heart and placental function[49,50]. A compromised fetal heart can cause back pressure through the fetal right ventricle, right atrium, ductus venosus, and into the umbilical vein[50]. Placental insufficiency can also alter the normal pressure gradient in the umbilical vein[50].

The middle cerebral artery is a major branch of the circle of Willis, carrying oxygenated blood for the fetal cerebral circulation[49]. Similar to the umbilical artery waveform, the middle cerebral artery spectral Doppler shows pulsatile forward flow throughout the cardiac cycle under normal conditions[50]. Two abnormalities can be monitored. First, the brain-sparing reflex is a physiological response to compensate for hypoxic or nutrient-deficient conditions[49]. Blood flow redistributes to prioritize the brain for survival and development[49]. This is characterized by increased end diastolic velocity in the spectral Doppler of the middle cerebral artery, which is reflected by a low PI[49]. Clinically, the cerebroplacental ratio (CPR), defined as the PI ratio of the middle cerebral artery to the umbilical artery, serves as an index to gauge the adequacy of fetal brain perfusion relative to placental blood flow[50]. The median CPR is 1.37 at 20-week, 2.34 at 30-week, and 1.80 at 40-week gestation[46]. Second, fetal anemia is characterized by decreased circulating red blood cells in the fetus[51]. An increased PSV in the middle cerebral artery, exceeding 1.5 times the median at a particular gestational age, is indicative of fetal anemia[51]. The median PSV is 25.5 cm/s at 20-week, 40.5 cm/s at 30-week, and 64.4 cm/s at 40-week gestation[69].

Supplementary Discussion 6: Novelty of the UPatch

The UPatch enables continuous fetal blood flow monitoring, which is essential for high-risk pregnancies.

First, a key limitation of current ultrasound-based fetal blood flow assessments is the need for a trained sonographer to manually place the sample gate, making continuous monitoring impractical[70]. The autonomous vessel tracking algorithm demonstrated in this work eliminates this limitation, enabling continuous measurements even during fetal movement. This advancement is particularly valuable in low-resource settings, where access to skilled sonographers is often limited or unavailable[71].

Second, fetal vessels are small and located at relatively large depths, making signal attenuation a critical challenge. The UPatch addresses this limitation through three hardware developments: super multipass dicing, an acoustic lens, and a soft Faraday cage. These developments enable reliable signal acquisition while maintaining a compact, wearable form factor.

Supplementary Discussion 7: Transducer dicing

Transducer dicing is a critical fabrication step in ultrasound array design. There are two primary dicing methods that are utilized: laser-based and blade-based dicing.

For transducer dicing using a laser, a key challenge is the thickness of the entire material stack. The UPatch is composed of PZT-5H 1–3 composite and conductive epoxy backing layer (Von Roll 3022 E–Solder, EIS) with a total thickness of ~1 mm. First, while laser dicing can effectively cut through PZT, it is limited to thin material stacks (e.g., 0.262 mm[72], 0.08 mm[73], and 0.045 mm[74]). As a result, laser dicing is feasible for selectively dicing the PZT layer only or for high-frequency applications where the entire material stack is very thin. However, it is impractical for achieving precise dicing of the 1 mm-thick material stack used in this study. Second, a key limitation of laser dicing is the heat generated during processing[73], which evaporates Pb to reduce its concentration and possibly induces a metastable pyrochlore phase, leading to a complete loss of piezoelectric properties[75]. Annealing and repolarization are required to restore piezoelectric properties, introducing additional processing steps.

Dicing ultrasound transducers typically utilizes blades with diamond grits embedded in electroplated nickel binders[76]. As the blade rotates, the diamond grits abrade the transducers. The sharp edges of the diamond grits mechanically chip away microscopic fragments of the transducers[76]. However, dicing thick material stacks with conventional mechanical dicing techniques remains challenging. To address this, additional preparation steps are often required to separately process the PZT and backing layer[77,78]. A common approach involves interposers, which are 3D-printed with the target pitch[79]. The backing layer is molded within the interposers, which separate individual channels. The PZT is then placed on top of the backing-interposer structure with careful alignment. Finally, the PZT is diced with the desired pitch. This method requires each material stack layer to be separately prepared, aligned, and assembled, introducing multiple fabrication steps that increase complexity, processing time, and the likelihood of errors.

Optimal dicing outcomes depend on two dicing blade parameters. First, the size of the grits, composed of synthetic diamonds, influences the chipping mechanism during dicing[76]. Larger grit particles are more robustly anchored within the nickel binders, offering slower degradation rates. In contrast, smaller grit sizes are more advantageous for decreasing the amount of force on the transducer. This translates to finer dicing because it minimizes surface chipping and diminishes blade vibrations, resulting in a more precise cut. Second, the blade thickness determines the transducer kerf[76]. While a smaller thickness is preferable for achieving higher precision in transducer dicing, it increases the potential for blade vibration, which in extreme cases may lead to blade failure.

While utilizing smaller grit size and blade thickness is more advantageous for finer dicing, it introduces processing complexities. The conventional dicing strategy utilizes a full depth cut, wherein the entire transducer thickness (e.g., 1 mm in this study) is diced with a single pass

(Supplementary Fig. 2)[80]. This strategy often induces substantial blade vibration due to the long contact edge between the blade and the transducer, which means that a large force is exerted on the blade, causing it to vibrate and potentially leading to blade breakage[76]. To minimize such vibration, a feed speed of 0.1 mm/s was typically utilized, extending the entire cutting process to ~15 h. Despite the low feed speed, this technique frequently caused thin blades to break. Thus, a larger blade thickness was required.

To address these challenges, in this study, we employed a super multipass dicing strategy, which dices each transducer element in incremental steps of 50 μm depth over a series of 20 rounds to achieve the full 1 mm depth (Supplementary Fig. 2). By reducing the depth of cut in each pass, this approach decreases the contact edge between the dicing blade and the transducer[76]. A shorter contact edge means that less force is exerted on the blade, which in turn reduces blade vibration and minimizes the risk of chipping the transducer (Supplementary Fig. 2). Therefore, the super multipass technique enables the use of thinner blades with smaller grit sizes, which generate transducers with narrower kerf without blade breakage. With such optimized processing, the transducer dicing can be performed at 10 mm/s, decreasing the total processing time to ~3 h (Supplementary Fig. 2).

The conventional method produced a 0.12 mm kerf, while the super multipass strategy produced transducers with a 0.05 mm kerf (Supplementary Figs 3 and 4). This preserved more active piezoelectric elements, improving the signal-to-noise ratio by 7.2 dB (Fig. 1b). Additionally, because the transducers were still fully diced, the crosstalk between individual channels was similar to that of the transducers diced with the conventional method (Supplementary Figs 3 and 4). The super multipass dicing method provides a one-step solution using a standard dicing machine, eliminating the need for complex, multi-step fabrication while maintaining high dicing precision.

Supplementary Discussion 8: Acoustic lens

Ultrasound wave propagation is characterized by attenuation-induced energy loss (such as absorption, scattering, and reflection), resulting in a decreased signal-to-noise ratio as imaging depth increases[81].

The UPatch has an elevational length of 12 mm, providing a natural elevational focal depth of ~14 cm (Supplementary Fig. 7). Reducing the elevational length can reduce the natural focal depth, but this strategy compromises the acoustic energy output[81]. To ensure sufficient acoustic energy output while achieving optimal focal depth, we designed and fabricated an acoustic lens.

The acoustic lens focuses the ultrasound beam in the elevational dimension and concentrates energy into the lateral-axial imaging plane, thereby enhancing the signal-to-noise ratio[81]. A two-dimensional image in the lateral-axial plane assumes reconstruction from a thin slice but is actually from a thick slab due to the elevational beamwidth[81]. A large elevational beamwidth captures signals from both tissues and red blood cells for Doppler calculation, which compromises the signal-to-noise ratio[81,82]. The acoustic lens reduces signals from regions outside the area of interest and enhances the signal-to-noise ratio[83]. Therefore, in this study, we used an acoustic lens to focus the beam in the elevational direction, which reduces signals from regions outside the area of interest and enhances the signal-to-noise ratio[83].

The lens design is based on Snell's law:

$$\frac{\sin\theta_1}{\sin\theta_2} = \frac{v_2}{v_1} \tag{4}$$

where θ_1 is the incidence angle, θ_2 is the refraction angle, v_1 is the ultrasound wave velocity in the incident medium, and v_2 is the velocity in the refracted medium (Supplementary Fig. 5)[84].

Given a known speed of sound in the loading medium (such as biological tissues to be imaged), the acoustic lens modulates the ultrasound beam's shape depending on its speed of sound. Speed of sound is determined by the lens material. Rubbers are widely used due to their low acoustic impedance and simple fabrication process. The acoustic impedance of rubbers closely aligns with that of biological tissues (~1.68 MRayl), facilitating efficient ultrasound transmission into the tissue[85]. Additionally, rubber's low adhesion to metals enables facile molding from precisely machined metal molds[86]. Despite the relatively high acoustic attenuation of rubbers, the energy loss is minimal in imaging applications due to the small thickness of the lens.

The side of the lens tightly bonded to the transducer is flat, leading to an incidence angle of 90°, thereby eliminating refraction at the transducer/lens interface. The other side, which contacts the loading medium, is the interface where the refraction occurs. Given rubbers' lower speed of sound than water, simulations indicate that a convex lens with a constant radius effectively focuses the acoustic beam. The lens radius can be calculated as:

$$R_{lens} = F * |n - 1| \tag{5}$$

where F is the focal depth and R_{lens} is the lens radius. n is given by:

$$n = \frac{C_{medium}}{C_{lens}} \tag{6}$$

where C_{medium} is the speed of sound in the loading medium, and C_{lens} is the speed of sound in the lens[87].

We measured the acoustic properties of two silicone rubbers typically used in wearable ultrasound, Ecoflex and polydimethylsiloxane, using transmitters with broad bandwidths: P4-1 (ATL) for 1–4 MHz and L11-5 (Philips) for 5–10 MHz. The speeds of sound were 1007 m/s and 957 m/s, respectively (Supplementary Fig. 5). Despite Ecoflex exhibiting a slightly higher speed of sound, indicating a smaller lens radius and thicker lens, the difference between the two rubbers is negligible. Ecoflex has a lower attenuation coefficient than polydimethylsiloxane in the 1–10 MHz frequency range (Supplementary Fig. 5)[88-91]. Thus, we chose Ecoflex as the lens material. With a depth of interest of ~10 cm and an average speed of sound in tissue of 1540 m/s, we derived the lens radius to be 53 mm based on equations (5) and (6).

A three-dimensional model and its corresponding mold were designed in SolidWorks according to the transducer's dimensions (Supplementary Fig. 6). The designed mold was precisely machined using computer numerical control machining. Then, the lens was fabricated by casting and curing Ecoflex within the mold (Supplementary Fig. 6). The lens was then bonded to the transducer using Ecoflex to minimize the interfacial acoustic impedance mismatch.

We scanned the elevational-axial acoustic field to evaluate the lens' elevational beam focusing performance. Using the acoustic lens, the focal depth of the UPatch moved from 14 cm to 10 cm, which balanced the elevational resolution throughout the entire 20 cm depth of a typical womb

(Fig. 1c and Supplementary Fig. 7). Additionally, the elevational beamwidth decreased from 6.0 mm to 4.5 mm at the focal point, improving the signal-to-noise ratio (Supplementary Fig. 7). While the acoustic lens enhances the signal amplitude at the focal region, it can also introduce minor attenuation due to the added lens material, which elongates the acoustic path and causes additional acoustic interfaces with impedance mismatch. These competing effects can offset each other. As a result, despite the more confined beam profile, the peak amplitude remains comparable at the focal point with and without the acoustic lens due to the attenuation introduced by the lens (Supplementary Fig. 7).

Beam steering controls lateral positioning in the XZ plane, while the acoustic lens enhances elevational beam focusing in the YZ plane to improve signal quality. The acoustic lens focusing remains beneficial even when the beam is steered off-axis in the XZ plane. When steered from -7.5° to 7.5°, the angle range of the duplex imaging algorithm used in this work, the elevational beamwidth is consistent at ~4.5 mm and ~6.0 mm for with and without the acoustic lens, respectively (Supplementary Fig. 8). The improved beam confinement leads to higher contrast and better vessel visualization, ensuring more reliable blood flow measurements.

Supplementary Discussion 9: Soft Faraday cage

The UPatch is vulnerable to electromagnetic interference due to its operational frequency within the radiofrequency spectrum. These interferences primarily originate from two sources: external electronic devices and contact with the human body.

External electronic devices (e.g., smartphones, Wi-Fi routers, and medical equipment) emit electromagnetic signals to the surrounding environment, coupling to the UPatch[92]. The in-band electromagnetic noise at 2.5 MHz is unlikely to couple into the UPatch through the air due to its long wavelength (120 m). However, these electronic devices also emit electromagnetic signals at frequencies different from ultrasound signals, which can still contribute to in-band interference through several mechanisms. First, external electromagnetic signals can couple with the UPatch due to its physical dimensions being comparable to the wavelength. For example, Wi-Fi signals operate at 2.4 GHz, which corresponds to a wavelength of ~12.5 cm. This wavelength is comparable to the size and geometry of the UPatch, allowing electromagnetic interference to occur. Second, intermodulation of various external electromagnetic signals can cause down conversion to in-band interference[93]. Multiple electromagnetic signals can undergo nonlinear mixing within the backend system, generating new frequency components through intermodulation[93]. These newly generated signals can span a broad range of frequencies, including those overlapping with ultrasound signals, potentially degrading signal quality and affecting system performance. Third, ground loops can allow external electromagnetic signals to couple into the system, generating low-frequency interference[94]. In a single-ended configuration, ground loops can behave like coils, introducing parasitic inductance that enables inductive coupling with external electromagnetic fields, further exacerbating interference[95].

Direct contact with the human body transmits noise to the UPatch due to its biopotentials and antenna effects. Biopotentials (such as electrocardiogram and electromyogram) generated from the human body can also be modulated by external electromagnetic signals, resulting in noises near the ultrasound frequency band[96,97]. The antenna effects are a phenomenon where the human body inadvertently acts as an antenna that couples electromagnetic waves in the air[98].

Ultrasound signals collected from deep tissues are intrinsically weak[81]; thus, these electromagnetic interferences can degrade signal and image quality. Consequently, devising effective screening strategies is imperative for the UPatch to image the fetus and acquire high-fidelity spectral Doppler signals from fetal vessels.

Various methods can reduce electromagnetic noise. First, analog and digital filters (such as low-pass, high-pass, and band-pass filters) are commonly used to attenuate noise outside the frequency band of interest[99]. The backend system (Vantage 256, Verasonics) incorporates these filters, effectively eliminating outside-band noise (such as biopotentials) which are typically below 10 kHz[100]. However, due to the wideband nature of electromagnetic noise in the air, filters alone are insufficient for lowering the noise floor of in-band signals. Second, specialized circuits can reduce thermal noise (caused by irregular movement of electrons inside electronic components due to ambient temperature) coupled to ultrasound signals during the filtering, amplification, and digitization processes[99]. However, this method increases the footprint, making the UPatch less wearable. Third, ground shielding the entire surroundings of the UPatch can reduce the noise floor by directly blocking the noise.

Electromagnetic interference is ubiquitous and omnidirectional, and the most effective shielding approach is a Faraday cage to prevent unwanted coupling from various sources[99]. These three-dimensional shields redistribute the charges across the cage surface, thereby neutralizing both static and dynamic electrical fields[99]. Metals are often used to construct the cage due to their high conductivity for the charges to move freely and quickly for effective redistribution[99]. A key design guideline to develop a soft Faraday cage is based on fundamental wave propagation theory. The effectiveness of a Faraday cage in blocking electromagnetic signals depends on the spacing between stretchable traces, which is governed by:

$$L < \frac{c}{10f\sqrt{\epsilon_r}} \tag{7}$$

where L is the spacing between adjacent net traces, c is the speed of light, f is the maximum frequency of the blocked signals, and ϵ_r is the relative permittivity[101].

We designed a soft Faraday cage to shield the UPatch from electromagnetic noise. The previous design incorporated two isolated copper electrode layers[102], which provided two-dimensional shielding but could not block electromagnetic interference from entering through the edges of the two electrodes[103]. In contrast, the UPatch was designed with a soft Faraday cage that was made of laser-ablated polyimide/copper laminates and vertical interconnect accesses. The soft Faraday cage connects the edges of the two electrodes using stitching vertical interconnect accesses. The transducers were placed between the mesh ground electrode and electromagnetic shielding electrode (Supplementary Fig. 9). Most of the body noise coupled to the UPatch will be shunted to the mesh ground electrode close to the skin. Various electromagnetic frequency signals can undergo intermodulation, generating spurious low-frequency signals that may overlap with the ultrasound frequency band, leading to interference[94]. The added electromagnetic shielding layer to the top of the signal electrodes can potentially shield noise from the air. The closely patterned electrical connections prevent electromagnetic interference from entering the UPatch from the edges, providing three-dimensional shielding in all directions (Supplementary Fig. 10). The maximum spacing between adjacent net traces was 0.9 mm, which can effectively block electromagnetic waves up to 20 GHz, covering all frequency bands used in common electronic devices[99].

We analyzed the power spectral density, which quantitatively measures the effectiveness of the soft Faraday cage[104]. In radiofrequency electronics (such as cellular transceivers, Bluetooth, and Wi-Fi), dBm/Hz is the standard unit in power spectral density plot because the signal power in these systems is typically in the milliwatt range[105]. However, from a general signal processing perspective, dB/Hz is a more appropriate unit for describing spectral density in relative terms[106]. The baseline noise level was also referenced to 1 W, ensuring consistency in the relative power representation.

We evaluated baseline noise levels of the backend system, UPatch without the soft Faraday cage, and UPatch with the soft Faraday cage. The baseline noise levels of the backend system were measured in two conditions: input termination at 50 Ω and open circuit. The input termination at 50 Ω matches the system's impedance and minimizes electromagnetic interference, while the open circuit captures the system's overall susceptibility to environmental noise. The baseline noise levels under 50 Ω input termination and open circuit were negligibly similar (Fig. 1d). This observation indicates that the noise is primarily contributed by the system itself rather than by external sources. Therefore, the measured baseline noise level can be considered a reliable representation of the system's intrinsic noise, regardless of the termination condition[107]. The noise level of the UPatch with the soft Faraday cage closely mirrored the baseline noise level of the backend system, which is mainly composed of thermal noise (Fig. 1d). In the absence of the soft Faraday cage, the noise floor increased by 11.7 dB/Hz at 2.5 MHz, the center frequency of the UPatch.

We also performed measurements under both phantom and in vivo conditions (Supplementary Figs 11–13). Noise levels were characterized using the probability density function, which captures the distribution of instantaneous signal amplitudes over time[108]. Broader distributions indicate greater variability due to environmental or physiological noise, making it suitable for statistically quantifying noise[108]. Phantom measurements revealed the UPatch's susceptibility to ambient electromagnetic noise, while in vivo measurements demonstrated additional susceptibility to physiological noise. The soft Faraday cage effectively attenuated environmental interference from nearby electronic devices (Supplementary Fig. 11) and reduced noise contributions from both environmental and physiological sources, resulting in improved signal fidelity (Supplementary Fig. 12). As a result, duplex imaging with the soft Faraday cage showed enhanced image quality and reduced noise in both phantom and in vivo settings (Supplementary Fig. 13).

The soft Faraday cage provided shielding against electromagnetic noise while conforming to the skin. Thus, this shielding strategy can be effectively adapted to enhance electromagnetic compatibility and reduce noise in soft electronics.

Supplementary Discussion 10: Umbilical cord phantom

Commercially available fetal phantoms primarily support structural B-mode imaging[109]. To the best of our knowledge, no commercially available phantoms accurately replicate the complex flow dynamics and anatomical variability of the umbilical cord and fetus.

To further validate the UPatch's ability to detect the umbilical cord in varying orientations, we developed an umbilical cord phantom that replicated the anatomical complexity of the intertwined arteries and veins in the cord. The phantom design incorporated two helically wrapped arteries (diameter ~3 mm) around a vein (diameter ~6 mm) to simulate the intertwined vascular geometry observed in vivo (Supplementary Fig. 18)[110]. We used deionized water as the surrounding medium, reflecting the high water content (~98%) of amniotic fluid to replicate the in vivo acoustic environment (Supplementary Fig. 18)[111].

Commercially available silicone tubing (Metaland) does not accurately mimic the acoustic impedance of soft tissue (~1.65 MRayl)[81]. Its substantially lower impedance (~1.07 MRayl) results in pronounced mismatch at fluid–structure interfaces, producing strong reflection during insonation across multiple vascular boundaries of the umbilical cord (Supplementary Fig. 18)[112]. To address this limitation, we selected Elastic 50A resin (Formlabs), which has acoustic impedance (~1.66 MRayl) that closely aligns with the acoustic impedance of soft tissue (Supplementary Fig. 18)[113,114]. Using the Elastic 50A resin, high-resolution stereolithographic printing enabled precise and repeatable fabrication of the complex intertwined geometry of the umbilical cord (Supplementary Fig. 19).

We conducted duplex imaging of the umbilical cord phantom across a range of vessel orientations to mimic real-world dynamics caused by fetal and maternal movements (Supplementary Fig. 20). These experiments demonstrated that the UPatch could reliably acquire the umbilical vessel flow signals despite dynamic anatomical orientation changes in the in-utero environment.

Supplementary Discussion 11: Acoustic exposure safety parameters

The UPatch was activated at 30 V with a pulse repetition frequency (PRF) of 3000 Hz, which were the highest values used in this study.

Using power P from a radiation force balance or a hydrophone (Supplementary Figs 24 and 25), spatial average temporal average intensity (I_{SATA}) can be calculated by:

$$I_{SATA} = \frac{P}{A} \tag{8}$$

where A is the area of the aperture (306.6 mm^2 in this study)[115]. This equation is valid for operation with an unfocused wave, making it applicable to brightness and color-flow modes in this study[115].

After waveform deconvolution using the data from calibrating the hydrophone sensitivity (Supplementary Fig. 24), the hydrophone measurements calculated the derated pressure as:

$$p_{\alpha}(z) = p(z)10^{\left(-\frac{\alpha z f_{awf}}{20dB}\right)} \tag{9}$$

where α is the attenuation coefficient (conservatively assumed to be 0.3 dB·cm^{-1}·MHz^{-1})[115], z is the distance from the UPatch along the beam axis to the plane containing the point of interest, and f_{awf} is the acoustic working frequency. Then, the derated pulse pressure squared integral can be calculated as:

$$ppsi_{\alpha}(z) = \int p_{\alpha}^{2}(z,t)dt \tag{10}$$

where measurements are based on the maximum value of $ppsi_{\alpha}(z)$ between the break-point depth z_{bp} and focal depth[116]. And z_{bp} is defined as:

$$z_{bp} = 1.5 \times D_{eq} \tag{11}$$

where D_{eq} is the equivalent aperture diameter and is defined as:

$$D_{eq} = \sqrt{\frac{4}{\pi}A} \tag{12}$$

Thus, z_{bp} is estimated to be 29.64 mm.

The derated pulse intensity integral is calculated by:

$$pii_{\alpha}(z) = \frac{1}{\rho c} ppsi_{\alpha}(z) \tag{13}$$

where ρ is the density of water (997 kg·m^{-3}) and c is the speed of sound in water (1480 m·s^{-1})[81]. Therefore, the derated spatial peak pulse average intensity is defined as:

$$I_{SPPA,\alpha}(z) = \frac{1}{t_d(z)} pii_{\alpha}(z) \tag{14}$$

where $t_d(z)$ is the pulse duration, which is 1.25 multiplied by the interval between the time when the time integral of the square of the instantaneous acoustic pressure reaches 10% and 90% of its final value[117,118].

The derated spatial peak temporal average intensity can be calculated as:

$$I_{SPTA,\alpha}(z) = PRF\ pii_{\alpha}(z) \tag{15}$$

The mechanical index (MI) describes the relative probability of eliciting micromechanical bio-effects, such as those associated with cavitation-induced damage[115,119], and is defined as:

$$MI = \frac{p_{r,\alpha}(z_{MI})}{\sqrt{f_{awf}}} \tag{16}$$

where $p_{r,\alpha}$ represents the derated peak rarefactional pressure in MPa, measured along the beam axis at depth z_{MI} where $ppsi_{\alpha}(z)$ is maximum, and f_{awf} is in MHz.

The thermal index (TI) is an index of the estimated temperature rise in tissues and is defined as:

$$TI = \frac{Acoustic\ power\ output}{Acoustic\ power\ ouput\ needed\ to\ produce\ 1\ ^{\circ}\mathrm{C}\ rise} \tag{17}$$

TI estimates temperature rise, postulating that the attenuation within tissue is homogeneous with an attenuation coefficient of 0.3 dB·cm^{-1}MHz^{-1}, which is lower than the attenuation coefficient of most soft tissues[120]. Depending on the tissues in the scanning plane, TI is divided into three types: soft tissue TI (TIS), bone TI (TIB), and cranium TI (TIC)[116,120].

First, the TIS is the maximum of the calculated values from equations (18) and (19):

$$TIS_{as,ns} = \frac{P_{1\times 1} \cdot f_{awf}}{210\ mW\ MHz} \tag{18}$$

where $TIS_{as,ns}$ is the TIS at surface (non-scanning), $P_{1\times 1}$ is the bounded–square output power over a 1 cm^2 area.

$$TIS_{bs,ns} = \min\left[\frac{P_\alpha(z_{s,ns})\times f_{awf}}{210\,mWMHz}, \frac{I_{SPTA,\alpha}(z_{s,ns})\times f_{awf}}{210\,mWcm^{-2}MHz}\right] \tag{19}$$

where $TIS_{bs,ns}$ is the TIS below surface (non-scanning), $P_\alpha(z_{s,ns})$ is the derated output power at depth $z_{s,ns}$, and $I_{SPTA,\alpha}(z_{s,ns})$ is the derated spatial peak temporal average intensity at depth $z_{s,ns}$. The derated power can be calculated as:

$$P_\alpha(z_{s,ns}) = P(z_{s,ns})10^{\left(-\frac{\alpha z f_{awf}}{10\,dB}\right)} \tag{20}$$

where depth $z_{s,ns}$ is defined as:

$$z_{s,ns} = depth\ of\ max\{min[I_{spta,\alpha}(z) \times 1\ cm^2, P_\alpha(z)]\} \tag{21}$$

The TIB is calculated as:

$$TIB = \min\left[\frac{\sqrt{P_\alpha(z_{b,ns})\times I_{SPTA,\alpha}(z_{b,ns})}}{50\,mWcm^{-1}}, \frac{P_\alpha(z_{b,ns})}{4.4\,mW}\right] \tag{22}$$

where depth $z_{b,ns}$ is defined as:

$$z_{b,ns} = depth\ of\ max\{P_\alpha(z) \times I_{SPTA,\alpha}(z)\} \tag{23}$$

The TIC can be calculated by:

$$TIC = \frac{P/D_{eq}}{40\,mWcm^{-1}} \tag{24}$$

For duplex imaging, each TI based on B-mode and color Doppler modes was calculated separately and summed. The *TI* for Spectral Doppler mode was calculated for each focusing depth, and the highest value was reported.

Supplementary Discussion 12: Thermal safety of the UPatch

Safety guidelines for obstetric ultrasound are provided by the American Institute of Ultrasound in Medicine (AIUM)[121], British Medical Ultrasound Society (BMUS)[122], and Food and Drug Administration (FDA)[115]. The UPatch is an ultrasound device that may expose the mother and fetus to various safety hazards. Therefore, the device must be characterized accurately to meet the recommendations of the regulatory bodies.

The FDA has different recommendations for Track 1 and Track 3 devices (Track 2 is not available due to historical reasons)[115]. The UPatch was characterized to meet the recommendations for both Track 1 and Track 3 devices to ensure rigorous thermal safety evaluation.

The FDA Track 1 recommendations provide maximum values for the I_{SATA}, $I_{SPPA,\alpha}$, $I_{SPTA,\alpha}$, and MI for fetal applications. These recommended maximum values are $I_{SATA} < 20$ mW/cm^2, $I_{SPPA,\alpha} < 190$ W/cm^2, $I_{SPTA,\alpha} < 94$ mW/cm^2, and $MI < 1.9$ (ref. [115]). The I_{SATA} of the UPatch (0.72 mW/cm^2) is substantially lower than the recommended maximum value and the Corometrics

250CX Series (GE Healthcare)[18] fetal heart rate monitor, which is reported to be < 5 mW/cm^2 (Supplementary Fig. 25). For $I_{SPPA,\alpha}$, the measured values from the hydrophone were 4.51 W/cm^2 for duplex imaging and 16.42 W/cm^2 for spectral Doppler. Additionally, the $I_{SPTA,\alpha}$ values were 19.86 mW/cm^2 for duplex imaging and 58.5 mW/cm^2 for spectral Doppler. The MI was 0.20 for duplex imaging and 0.37 for spectral Doppler (Fig. 1f). The UPatch operates well below the FDA Track 1 recommended maximum values.

The FDA Track 3 recommendations require device manufacturers to display MI and TI values according to the Output Display Standard in IEC 60601-2-37 (ref. [115,123]). MI and TI values are displayed in real time to ensure that clinicians adhere to the "as low as reasonably achievable" principle, minimizing patient exposure to ultrasound energy – although evidence suggests these are rarely checked in practice[124]. While there is no specific recommendation from the FDA[115] for the maximum TI, an explanation is requested for TI over six. The AIUM[121] and BMUS[122] set recommendations for maximum dwell time based on TI values. According to these guidelines, the recommended dwell time for obstetric scanning is set as: no dwell time limit for $TI \leq 0.7$, maximum dwell time < 60 min for $0.7 < TI \leq 1.0$, maximum dwell time < 30 min for $1.0 < TI \leq 1.5$, maximum dwell time < 15 min for $1.5 < TI \leq 2.0$, maximum dwell time < 4 min for $2.0 < TI \leq 2.5$, maximum dwell time < 1 min for $2.5 < TI \leq 3.0$, and scanning with $TI > 3.0$ is not recommended for obstetric uses.

The maximum increase in the surface temperature of the UPatch in air was measured to be 0.53 °C (Supplementary Fig. 23). The device maintained a stable surface temperature well below safety thresholds, supporting its viability for extended clinical use. Using measurements from a radiation force balance or a hydrophone, we calculated the highest TI values for duplex imaging and spectral Doppler. For duplex imaging, the TIS was 0.02, TIB was 0.05, and TIC was 0.05 (Fig. 1f). For spectral Doppler, the TIS was 0.10, TIB was 0.38, and TIC was 0.17 (Fig. 1f). All of these values were < 0.7, suggesting no dwell time limit for the UPatch according to AIUM and BMUS recommendations[121,122]. For obstetric imaging, the TIS is most relevant thermal index up to 10 weeks from the last menstrual period or a crown-rump length of about 33–34 mm, and TIB is the most relevant thereafter[121].

In summary, the UPatch adheres to recommendations by the FDA Track 1 and Track 3 (ref. [115]), AIUM[121], and BMUS[122]. Additionally, we strictly followed the as low as reasonably achievable principle to minimize ultrasound wave exposure to the fetus and the mother[115].

Supplementary Discussion 13: Beamforming of the UPatch on the abdomen

Beamforming is traditionally performed using a fixed array configuration. Thus, the UPatch image reconstruction assumes that the 64 channels are on a static surface. However, the curvature of the pregnant woman's abdomen differs from person to person and varies at different locations of the abdomen, introducing phase aberration to the beamforming of the UPatch[125]. This curvature for the third trimester typically has a radius ranging from 14 cm to 18 cm[126,127].

To mitigate this problem, phase aberration was corrected for a curvature radius of 16 cm, accommodating the typical abdominal geometry (Supplementary Fig. 26). The aberration correction was applied in both transmission and reception, which adjusted the time delay profile of the ultrasound waves to ensure accurate image reconstruction. The delay-and-sum beamformer used the same curvature profile for consistent aberration correction during reception. With this phase aberration correction, the UPatch could provide high-quality images even with varying maternal abdominal curvatures (Supplementary Figs 28–30). Additionally, while the curved shape of the maternal abdomen focuses the ultrasound beam, we compensated for the bending radius by beamforming, so unwanted focusing was largely alleviated.

Supplementary Discussion 14: Vessel tracking algorithms

Traditional methods require clinicians to manually maneuver the handheld clinical ultrasound device and select the appropriate sample gate on the duplex image for spectral Doppler analysis of fetal vessels (Supplementary Fig. 33)[53]. This approach can only provide intermittent measurements and faces challenges during dynamic physiological changes (e.g., fetal and maternal movements, respiratory processes, and uterine contractions)[48,51]. These changes can alter the locations of fetal vessels and sample gates[128,129]. For example, the umbilical cord can rotate and orient in various directions[53]. Such movements can displace the sample gate initially placed on the umbilical artery to other tissues (Fig 3c). Thus, strategies are needed to adaptively adjust the sample gate to the moving vessel.

Efforts to address this challenge remain in early stages of development. One approach involved developing a vessel tracking algorithm that detects the vessel wall using A-mode[130]. However, this algorithm cannot differentiate between various vessel types (such as the umbilical arteries and vein) or vessel orientations (such as the transverse and longitudinal planes). In a separate study, computer vision was used to estimate the ultrasound Doppler angle for automatic angle correction. Yet this method still requires a clinician to initially identify the vessel of interest[131]. Furthermore, a machine learning model applied to M-mode images successfully detected the vessel diameter but was limited to the transverse view of the vessel[132].

Image segmentation offers a promising alternative for vessel detection because different vessel types and orientations provide distinct features. Thus, commercial devices have recently implemented image segmentation-based strategies. The Arietta 65 (Fujifilm) claims to automate sample gate selection for mitral valve in the apical four-chamber view[133] and received FDA clearance in November 2020 (ref. [134]), but the automated sample gate feature[133] was not included in its regulatory submission. The Acuson Origin (Siemens) received FDA clearance in October 2023 (ref. [135]). This artificial intelligence system places sample gates for 12 cardiac views, supporting up to 4 anatomical locations with a total of 42 sample gate placements[135,136]. The automated sample gate feature in Kosmos (cart-based ultrasound system; EchoNous) and Kosmos Mobile (wireless ultrasound system; EchoNous) was introduced in September 2024 (ref. [137-139]) but has not received FDA clearance[140]. An artificial intelligence system was proposed to provide sample gate selection for apical four-chamber view, specifically for the left ventricular outflow tract, mitral valve, pulmonary valve, and tricuspid valve[138].

These developments reflect exciting progress in echocardiography. However, there remains no commercially available solution for automated sample gate selection in fetal ultrasound. Unlike cardiac imaging, which benefits from anatomical landmarks that are changing periodically, fetal imaging must contend with continuously shifting anatomy due to fetal and maternal movements. The intertwined vascular geometry of the umbilical cord, comprising two arteries helically wrapped around a central vein, results in dynamic variation in depth, orientation, and position

(Supplementary Fig. 20). Additionally, these existing commercial probes must be held by humans or robotic arms, making them impractical for continuous monitoring.

The image segmentation in this study utilizes color Doppler signals in the duplex image. This method effectively differentiates the umbilical artery from the umbilical vein by identifying differences in the flow direction and pulsatility (Fig. 3a). It enables dynamic tracking and adaptive sample gate selection in response to changing vessel geometry and motion, representing a substantial advance over existing cardiac-focused approaches and addressing an unmet need in continuous fetal blood flow monitoring. Additionally, we optimized the computational load by reducing the number of frames analyzed by the tracking algorithm. The UPatch is self-adhering and integrates autonomous vessel tracking specifically designed for fetal ultrasound, enabling prolonged monitoring without the need for a sonographer or a robotic arm. This method facilitates autonomous monitoring during physiological changes, thereby enhancing the reliability and effectiveness for fetal monitoring.

Supplementary Discussion 15: Working principles of vessel tracking algorithm

The tracking algorithm leverages pulsatility characteristics encoded in the color Doppler signal to quantitatively differentiate the vessels.

Each pixel in the frame is assigned a color intensity value ranging from 1 to 128 (Supplementary Fig. 36). Values from 1 to 64 represent flow away from the UPatch using cool hues, where lower color intensity values correspond to cyan (higher velocity), and higher values correspond to dark blue (lower velocity). Values from 65 to 128 represent flow toward the UPatch using warm hues, where lower color intensity values correspond to dark red (lower velocity), and higher values correspond to yellow (higher velocity).

Based on this numerically assigned pixel color intensity, the inter-frame color difference compares the color intensity of each pixel among consecutive frames. A high inter-frame color difference reflects greater temporal variation in flow velocity, characteristic of arterial pulsatility. In contrast, low variation corresponds to steadier flow typically observed in veins.

Thus, the algorithm evaluated the inter-frame color difference to assess pulsatility to obtain pixels designated for the umbilical artery (Supplementary Fig. 36). We implemented a threshold of 4.875 in this case for the inter-frame color difference across each vessel region (Supplementary Fig. 36). Regions exceeding this threshold are classified as artery, while those below are identified as vein (Supplementary Fig. 36).

The color (cool or warm hues) of the vessel in the image does not affect classification because the algorithm measures the change in color intensity between consecutive frames, not the absolute value of the color. Thus, the tracking algorithm can identify arteries regardless of whether they appear as cool or warm hues because their pulsatility consistently results in greater inter-frame color differences compared to veins.

Binary segmentation maps were generated, followed by morphological opening and closing to remove granular noise and smooth region boundaries. Opening removes small, isolated artifacts, while closing fills gaps and connects nearby regions[141,142]. These two steps improve segmentation quality by preserving large, coherent vessel structure.

Among the identified regions, the one with the largest pixel area is designated as the primary region because larger regions offer more stable signals, are less affected by noise, and align with the selection process typically used by sonographers in clinical practice. Because $Area_1$ contained 2,078 pixels and $Area_2$ contained 7,129 pixels, $Area_2$ was selected as the primary region (Supplementary Fig. 37).

Finally, we computed the geometric centroid of the selected primary region to define the sample gate location. The centroid, calculated as the mean x and y coordinates of all pixels within the segmented region, had a coordinate ((554, 685) in this case), ensuring a spatially robust placement of the sample gate (Supplementary Fig. 38).

Supplementary Discussion 16: Umbilical vein tracking

Most clinical applications of fetal Doppler focus on the umbilical artery[48,51,67]. Therefore, this study optimized the tracking algorithm specifically for the detection of the umbilical artery (Fig. 3a).

Nevertheless, this tracking algorithm can also be adapted to detect the umbilical vein. The umbilical vein transports oxygenated blood from the placenta to the fetus, ensuring it receives essential oxygen and nutrients for its growth and development (Supplementary Discussion 5)[143]. Thus, monitoring the umbilical vein is likely to provide direct insights into fetal oxygenation.

While the umbilical arteries and vein are intertwined, their color Doppler signals are typically opposite due to their opposite flow directions (Supplementary Fig. 28). Thus, if the color Doppler signal of the arteries is red (indicating flow towards the UPatch), the signal of the vein will be blue (indicating flow away from the UPatch), or vice versa. Additionally, the umbilical vein is typically non-pulsatile because the placenta acts as a blood reservoir (Supplementary Discussion 5)[48]. Therefore, when the tracking algorithm calculates the variance in color Doppler pixel intensity over several consecutive frames, it can identify the umbilical vein as the non-pulsatile region (Fig. 3a). A similar segmentation method can then be applied to identify the primary region and its spatial centroid of the umbilical vein for sample gating (Fig. 3a). This adaptation allows the tracking algorithm to be utilized for continuous umbilical vein tracking and blood flow monitoring.

Supplementary Discussion 17: Response time during image segmentation

Due to limitations in the computational power of the backend system, the autonomous tracking algorithm cannot simultaneously perform duplex imaging, tracking, and spectral Doppler recording. Thus, the algorithm sequentially reconstructs a duplex image, tracks the umbilical artery to obtain a sample gate, and records spectral Doppler signals (Fig. 3a). In such cases, fetal movement may affect the performance of the image segmentation algorithm. Fast movements can particularly cause the initially registered sample gate to shift away from the target vessel before the next round of image segmentation begins.

To address this issue, we integrated a standard deviation threshold at the end of the image segmentation sequence. This ensures that when the algorithm detects fast cord movements, it does not provide a sample gate until the movement is slowed down. The algorithm computes the x and y coordinates of tracked points across consecutive frames. A threshold based on the standard deviation of these coordinate changes was applied to identify and exclude tracked points with abrupt displacements, which may occur during rapid fetal movements. This approach reduces the likelihood of erroneous sampling and ensures reliable tracking performance during continuous monitoring of dynamic conditions. Consequently, sample gates were applied only to vessels that have no or slow movements (Supplementary Video 1).

Despite this improvement, the method still has limitations. First, the autonomous tracking algorithm cannot detect movements after spectral Doppler signals have been acquired. Second, waiting until the vessel stops moving quickly to apply a sample gate leads to variability in the response time. Third, the algorithm cannot acquire spectral Doppler during vessel movement.

To mitigate these issues, three solutions are proposed. First, an additional algorithm can be developed to identify signal loss in the spectral Doppler based on its luminosity[132]. This would detect fast movements, enabling the algorithm to identify when the signal is lost and switch back to duplex imaging for further tracking. Currently, we minimized this issue by acquiring 3 s of spectral Doppler prior to switching back to duplex imaging (Fig. 3c and Supplementary Video 1). This approach ensures that spectral Doppler signals are acquired for a short duration, minimizing the impact of movement.

Second, image segmentation-based machine learning models can directly generate a sample gate from a single image[144]. The current tracking algorithm requires multiple frames to calculate the sample gate, resulting in variability in response time (Supplementary Video 1). To solve this problem, machine learning models, trained on annotated datasets, allow individual images to generate a sample gate. This approach minimizes variability in response time and tracks the target vessel during movement.

Third, integrating a more advanced graphics processing unit in the backend system can substantially enhance the beamforming framework[145]. Recent advances in graphics processing units enable a much larger number of parallel executing cores, facilitating faster computation and allowing simultaneous duplex imaging and spectral Doppler acquisition[146]. This approach allows spectral Doppler acquisition even during movement, thereby improving overall efficiency and response time.

Supplementary Discussion 18: Evaluation of the autonomous tracking algorithm

The vessel tracking algorithm is based on conventional image processing techniques, which do not require cross-validation. Machine learning or artificial intelligence-based models require a labeled training dataset to learn features and a separate testing dataset to evaluate performance. Our approach applies deterministic operations directly to the input data and does not involve model training. There is no differentiation between training and testing datasets. Therefore, cross-validation procedures, which are essential for evaluating generalizability in trained models, are not applicable in this context.

The autonomous tracking algorithm in this study was evaluated using three methods to test its accuracy and reliability across different scenarios. In fetal ultrasound, manual sample gating by experienced sonographers remains the clinical gold standard for assessing signal quality and tracking accuracy[147]. The evaluation method we employed aligns with established clinical standards and other studies in the literature[135,148]. Additionally, in contrast to these cited studies[135,148], which employed only a single validation method, our approach was comprehensively validated using three independent methods. In the FDA-cleared Acuson Origin (Siemens) system, the autonomous sample gate placement underwent validation using only 168 images as part of its FDA clearance process[135]. The validation accuracy evaluated by three sonographers was defined as "no adjustment or only minor adjustment needs to be made by the user"[135]. In the peer-reviewed study, accuracy of a deep learning-based sample gating was validated using a method similar to our first validation method[148]. To the best of our knowledge, these reported works were the only studies that demonstrate tracking algorithm validation for ultrasound imaging.

The first two methods were based on pre-collected images, allowing direct comparison against a sonographer with over 30 years of experience in fetal ultrasonography. In the first method, a double-blind setup was used where both the tracking algorithm and the sonographer selected optimal tracking points in the same images collected using the UPatch. The differences between these points were then measured in axial and lateral dimensions, providing a quantifiable metric of the algorithm's accuracy (Fig. 3e).

In the second method, the sonographer visually assessed the accuracy of the tracking algorithm. She categorized the tracked points into three levels: "Optimal" for points suitable for acquiring high-quality spectral Doppler signals, "Sub-optimal" for points that might yield low quality signals, and "Non-diagnostic" for points incapable of providing usable Doppler signals (Supplementary Fig. 39). However, these evaluations did not account for the actual spectral Doppler signals that could be acquired from the tracked points.

Thus, a third method was employed to quantify the differences between the systolic-to-diastolic ratios collected from the points of the autonomous tracking algorithm and those selected by a sonographer. This method incorporated the spectral Doppler signals obtained from the tracked points, providing a more practical assessment of the algorithm's performance.

This three-step evaluation process provided a robust framework for optimizing the tracking algorithm. By incorporating offline sonographer comparisons of the sample gates and practical online assessments of spectral Doppler accuracy, the study ensured the algorithm was finely tuned for clinical uses.

Supplementary Discussion 19: Ultrasound sample gate

Accurately delineating the sample gate within the duplex image is crucial[149]. Ideally, the sample gate should cover the entire vessel diameter to ensure accurate measurement of the complete hemodynamic profile[48]. However, clinicians commonly position a 2 mm sample gate at the vessel's center to record the spectral Doppler signals (Supplementary Fig. 33)[50]. There are two practical reasons.

First, the 2 mm size ensures that the vessel does not shift away from the sample gate during measurements[48]. The umbilical arteries are closely intertwined with the umbilical vein, necessitating a clear distinction between them. This sample gate size is typically smaller than most fetal vessels in the third trimester, allowing assessment of the target vessel even during small vessel movements[53].

Second, Doppler indices derived from the vessel's center are negligibly different from those derived from the entire vessel diameter. Blood flow within vessels typically exhibits a parabolic profile (laminar flow), with red blood cells traveling at varying velocities[81]. This velocity gradient is characterized by the highest velocities at the vessel's center and the lowest velocities near the vascular wall due to viscous drag[81]. Doppler indices, such as the systolic-to-diastolic ratio, pulsatility index, and resistance index, are derived from the peak systolic velocity, end diastolic velocity, and mean flow velocity extracted from the spectral waveform envelope[48,51]. The peak systolic velocity, end diastolic velocity, and mean flow velocity extracted from the spectral waveform envelope of the entire vessel diameter are negligibly different from those extracted from the spectral waveform envelope of the vessel center. Thus, these Doppler indices are not affected much when the sample gate is positioned at the vessel's center.

Because of such practical considerations, this study utilized the standard sample gate size of 2 mm.

Supplementary Discussion 20: Continuous monitoring of the umbilical artery

Doppler indices vary along the umbilical artery, with blood flow resistance highest at the fetal abdominal cord insertion, intermediate at the free-loop cord, and lowest at the placental cord insertion[49]. Thus, it is important to sample spectral Doppler consistently at the same site of the umbilical artery throughout the duration of continuous monitoring[60].

Continuous monitoring of the umbilical cord at the fetal abdominal insertion site presents practical difficulties, particularly in advanced gestation[49]. First, the fetus can move or rotate in the uterus, causing the umbilical cord at the fetal abdominal insertion site to move out of the sonographic window. Second, the site may be obscured by fetal lower limbs or oligohydramnios, a condition characterized by low amniotic fluid levels that limit the acoustic window[49].

Sampling a fixed position of the free-loop cord also has disadvantages. First, the umbilical cord can extend an average length of 64 cm, making it challenging to sample consistently at the same position during continuous monitoring[150]. The umbilical cord is constantly displaced as it floats inside the amniotic fluid under various environmental changes, including fetal movement, fetal breathing, maternal movement, maternal breathing, and uterine contractions[51].

The umbilical cord at the placental cord insertion is also moving, but the placenta is fixed on the maternal uterine wall[48,51]. Although the umbilical cord itself moves, its position at the placental cord insertion remains relatively identifiable by using the placenta as a stable anatomical reference (Supplementary Fig. 35)[50]. As a result, the UPatch was positioned to insonate the umbilical cord at the placental cord insertion. In our experiments, after identifying the optimal location and orientation using a clinical device, we laminated the UPatch. Throughout various maternal and fetal movements, this consistent anatomical reference enables reliable imaging at the placental cord insertion, ensuring continuous monitoring without relocating the UPatch.

We conducted a study in which the UPatch was tested across a range of common maternal postures: lying supine, lying on the right side, lying on the left side, and sitting upright (Supplementary Fig. 35). In all cases, the UPatch successfully acquired the umbilical cord Doppler signals. As a result, the UPatch did not require repositioning and could maintain continuous spectral Doppler sampling at the placental cord insertion throughout the monitoring period.

Supplementary Discussion 21: Ultrasound incident angle

Accurate measurements of blood flow velocities are influenced by the ultrasound incident angle, which is the angle between the ultrasound beam and the direction of blood flow[131]. To derive accurate velocity, measuring the ultrasound incident angle is essential. Conventionally, an angle correction cursor is aligned to the flow direction within the vessel visualized in the duplex image to calculate the incident angle[48,51]. However, this method may be inaccurate because the vessel may not lie in the incident plane[48].

To circumvent the need for angle measurements and eliminate its associated inaccuracies, Doppler indices, such as the systolic-to-diastolic ratio, pulsatility index, and resistance index, are widely employed[48]. These indices are angle-independent because they are normalized (Supplementary Discussion 5)[48]. This allows reliable assessment of vascular resistance and blood flow characteristics that are not subject to the variances of vessel orientations. Consequently, these angle-independent indices are preferred in clinical diagnosis[66,67].

Supplementary Discussion 22: Abnormality in a pre-eclamptic participant

We continuously monitored 52 participants across a range of gestational ages in third trimester and clinical conditions to evaluate the UPatch's ability to capture hemodynamic changes. One pre-eclamptic participant exhibited markedly abnormal patterns in her Doppler indices. To highlight the diagnostic value of continuous monitoring of blood flow, we present a comparative analysis between a healthy participant at 32 weeks 6 days and the pre-eclamptic one at 28 weeks 3 days gestational age.

The average fetal heart rate was 149.5 bpm for the healthy and 143.3 bpm for the pre-eclamptic participants (Fig. 4b). Both were within the normal range of 120–160 bpm (Supplementary Discussion 3)[17,43]. In addition, their fetal heart rate variabilities were 20.3 bpm and 21.5 bpm, respectively, characterized as moderate variability, indicating healthy fetuses (Supplementary Discussion 3)[17,43]. Thus, cardiotocography devices could not detect the compromised fetal health of the pre-eclamptic participant.

Notable differences were observed in the resistance index, pulsatility index, and systolic-to-diastolic ratio between the two participants. The healthy participant had an average resistance index of 0.62, pulsatility index of 1.04, and systolic-to-diastolic ratio of 2.61 (Fig. 4b and Supplementary Fig. 40). In contrast, the pre-eclamptic participant had an average resistance index of 0.85, pulsatility index of 2.04, and systolic-to-diastolic ratio of 5.11 (Fig. 4b and Supplementary Fig. 41).

For the healthy participant's gestational age, the 50th percentile values are 0.63 for resistance index, 0.96 for pulsatility index, and 2.68 for systolic-to-diastolic ratio[68]. For the pre-eclamptic participant's gestational age, the 50th percentile values are 0.66 for resistance index, 1.03 for pulsatility index, and 2.93 for systolic-to-diastolic ratio[68]. The healthy participant's values were near the 50th percentile, whereas the pre-eclamptic participant's values were markedly higher, indicating poor blood flow exchange between the fetus and placenta.

Following the detection of abnormal umbilical artery blood flow in the pre-eclamptic participant using the UPatch, the research activities were halted. The mother underwent intensive monitoring with clinically validated devices, and the baby was delivered 4 days later, at 203 days of gestation, via Cesarean section. The UPatch detected abnormalities that conventional cardiotocography failed to identify, leading to a timely intervention that saved the fetus. The newborn is thriving, demonstrating the real-world clinical value of this technology.

Supplementary Discussion 23: Clinical importance of continuous monitoring of blood flow

Continuous monitoring of blood flow using the UPatch enables clinically meaningful assessment of fetal well-being throughout pregnancy.

First, in current obstetric practice, cardiotocography is used to continuously monitor fetal heart rate, particularly for inpatients. When prolonged fetal heart rate decelerations or abnormal patterns are observed, Doppler ultrasound is typically employed by sonographers to assess umbilical blood flow[59]. This two-step process is time-consuming and labor-intensive, which may delay or miss the optimal timing to detect fetal complications, reflecting a technological gap. The UPatch addresses this gap by providing continuous monitoring of both fetal heart rate and umbilical blood flow in a single system without the need for a sonographer.

Second, the UPatch enables baseline measurement of umbilical blood flow and differentiate normal from abnormal physiological fluctuations. Normal fluctuations can temporarily alter spectral Doppler waveforms. When captured by intermittent scans, such altered values do not reflect true pathology and may raise false positive concerns or trigger unnecessary clinical interventions (Supplementary Figs 40–91)[151]. This limitation of intermittent scans reduces reliability in dynamic and complicated clinical settings, often requiring serial measurements over several days. The UPatch addresses this limitation by providing a continuous data stream of umbilical blood flow, allowing clinicians to distinguish sustained compromise from transient, self-resolving physiological fluctuations, which supports more reliable, real-time clinical decision-making.

Third, unlike fetal heart rate, which requires complex time-series analysis, Doppler indices offer clinically validated measurements of fetal hemodynamics[9,152]. Fetal heart rate interpretation relies on pattern recognition to assess baseline, variability, accelerations, and decelerations over a long period of time, because isolated values are insufficient to reveal fetal well-being[9]. However, these time-series features show poor correlation with gestational trends and perinatal risks[2,9,153]. In contrast, the three Doppler indices used in this study are well-established parameters heavily used in hospitals to assess placental and fetal vascular resistance[66-68,154,155]. Doppler indices have well-defined reference ranges, exhibit consistent gestational trends, and stratify risk groups with great sensitivity[59,67,68]. Continuous monitoring with the UPatch enables real-time acquisition of these indices without the need for time-series analysis (Fig. 4e–i and Supplementary Figs 96 and 97).

Fourth, the UPatch provides continuous, actionable information that supports more precise risk management of the trade-off between preterm delivery (delivery before 37 weeks) and stillbirth than cardiotocography[156]. Before 37 weeks, clinicians aim to avoid delivery unless fetal compromise is evident. In a pre-eclamptic patient (28 weeks 3 days gestational age) in this study, the UPatch identified umbilical flow abnormalities that were not evident on conventional cardiotocography, prompting an intervention that saved a baby (Fig. 4a–d).

Supplementary Discussion 24: Data processing

Data preprocessing and processing were performed locally on the backend system (Vantage 256, Verasonics), which is a research-grade ultrasound platform widely used for real-time data acquisition[157,158]. Data preprocessing is the initial step, including down-sampling and denoising, which are applied to the raw radiofrequency signals. Then, data processing, including beamforming to generate duplex images, autonomous tracking to identify the sample gate, and spectral Doppler estimation to extract velocity waveforms, is implemented for real-time data acquisition.

By directly transferring raw radiofrequency signals to the backend system, this protocol ensured minimal latency with negligible delay. Privacy was maintained because all participant data were transmitted by a flexible cable and remained within the local processing station, eliminating security concerns associated with wireless transmission or cloud-based storage. Additionally, the study was approved by the Institutional Review Board, ensuring compliance with privacy regulations. Computational requirements were sufficiently managed by the backend system, which was specifically designed to handle high-throughput ultrasound data processing[158].

To optimize storage, the system prioritizes clinically actionable data and discard unnecessary high-volume raw imaging. Specifically, instead of storing full duplex images and spectral Doppler waveforms, the system extracts and saves Doppler indices (such as resistance index, pulsatility index, and systolic-to-diastolic ratio) and fetal heart rate, which are one-dimensional and require minimal storage. This approach ensures storage efficiency while providing essential information for clinical decision-making.

Supplementary Discussion 25: Circuit integration

The current UPatch with a wired connection for power and data is optimal for hospital monitoring. However, wireless home monitoring presents distinct clinical advantages. First, it offers a comfortable environment that can yield more precise baseline measurements of fetal blood flow, which is critical for high-risk pregnancies (such as gestational diabetes and pre-eclampsia)[54]. Additionally, it can allow research into how maternal exercise influences fetal hemodynamics[55]. Second, continuous home monitoring generates more extensive data over time, allowing for trend analysis and research into the mechanisms of fetal complications and stillbirth[159]. Third, it supports regular assessments without the inconvenience and costs associated with hospital visits, crucial for those with limited access to healthcare facilities, especially in low/middle-income areas[11,160].

A recently introduced wearable ultrasound circuit has enabled wireless home monitoring[132]. This system can multiplex the signals from all 32 channels of transducer elements through a single transceiver. A Wi-Fi module transmits the received signals to a smartphone, monitoring tissue interfaces and providing critical insights during physical activities (such as biking and high-intensity training). However, its imaging capabilities are limited due to the circuit comprising only a single transceiver. First, while multiplexing can enable imaging, the transducer elements are activated sequentially. This means that there is a time delay between received signals, resulting in low image quality from moving tissue interfaces and red blood cells[161]. Second, for color Doppler imaging, the transceiver must activate the same transducer at a high pulse repetition frequency (~3000 Hz) to assess the mean phase differences among multiple pulse echos[81]. This setup, while feasible for a single transducer, results in a loss of spatial resolution and intrinsically low Doppler signal-to-noise ratio[82]. Due to these limitations, this circuit is inadequate for producing high-quality ultrasound images.

Multiple transceivers are needed to achieve high-quality imaging, but there are three major challenges[162]. First, the increased power consumption from additional transceivers will necessitate more efficient power management solutions to sustain battery life[163]. Second, heat generation poses a substantial challenge because additional circuit components will cause heat accumulation, requiring advanced thermal management strategies to ensure the device's safe use[162]. Third, multiple transceivers will complicate the firmware design, requiring more sophisticated signal processing algorithms[162]. Despite its challenges, the integration of multiple transceivers into wearable ultrasound circuits will enable high-quality imaging for wireless home monitoring.

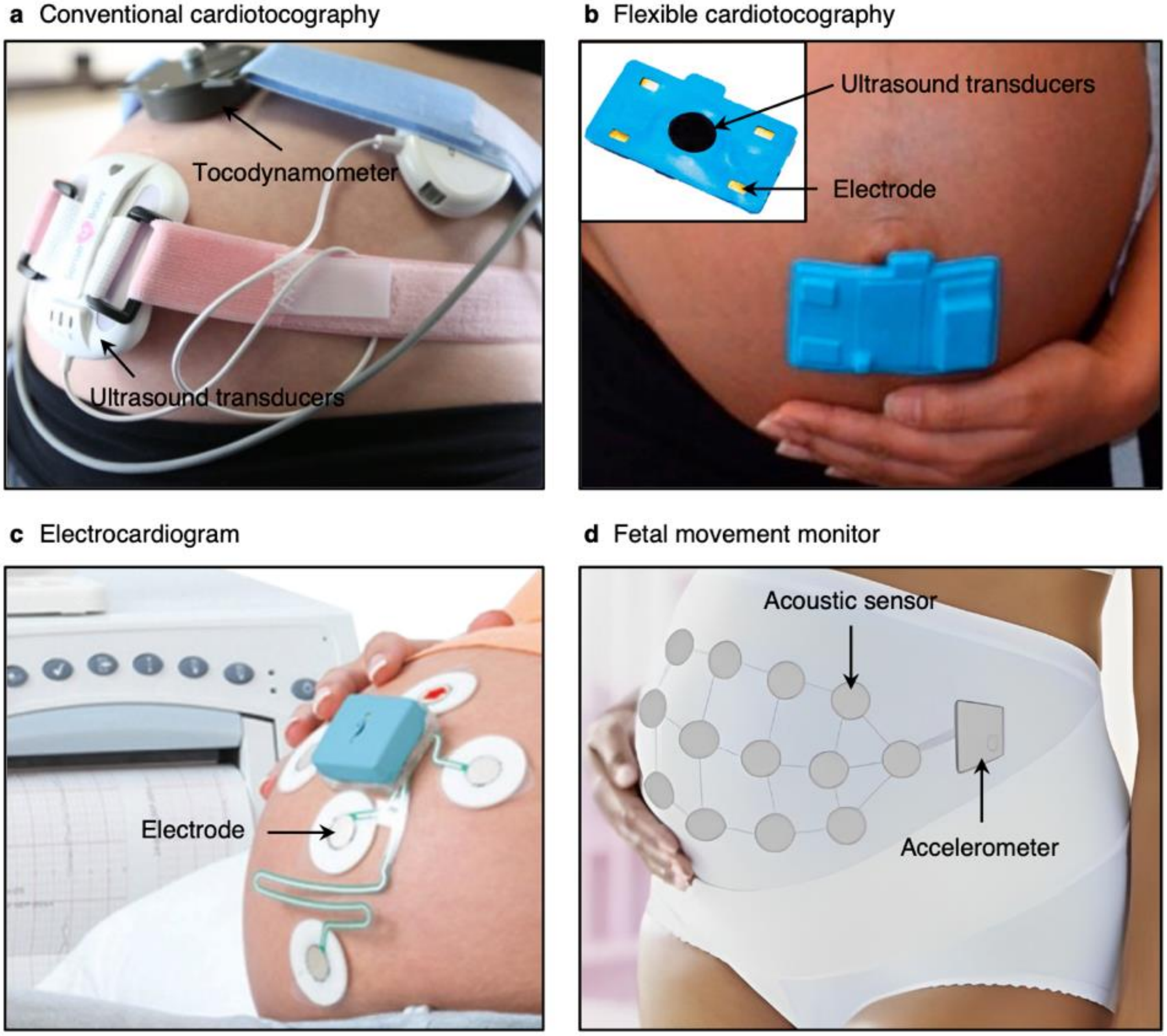

Supplementary Fig. 1 | Existing wearable fetal monitors. a, Conventional cardiotocography comprising ultrasound transducers for fetal heart rate monitoring and a tocodynamometer for uterine contraction monitoring developed by Sense4baby[20]. **b**, Flexible cardiotocography using two ultrasound transducers for fetal heart rate recording and four electrodes for maternal electrocardiogram and electrohysterogram to derive uterine contraction developed by Sibel Health[23]. **c**, Fetal electrocardiogram measured with five electrodes to derive fetal heart rate developed by Monica Healthcare (now GE Healthcare)[25]. This configuration claims to derive fetal heart rate regardless of fetal position in the maternal abdomen. **d**, Fetal movement sensor using an accelerometer and several acoustic sensors proposed by University College Dublin[42].

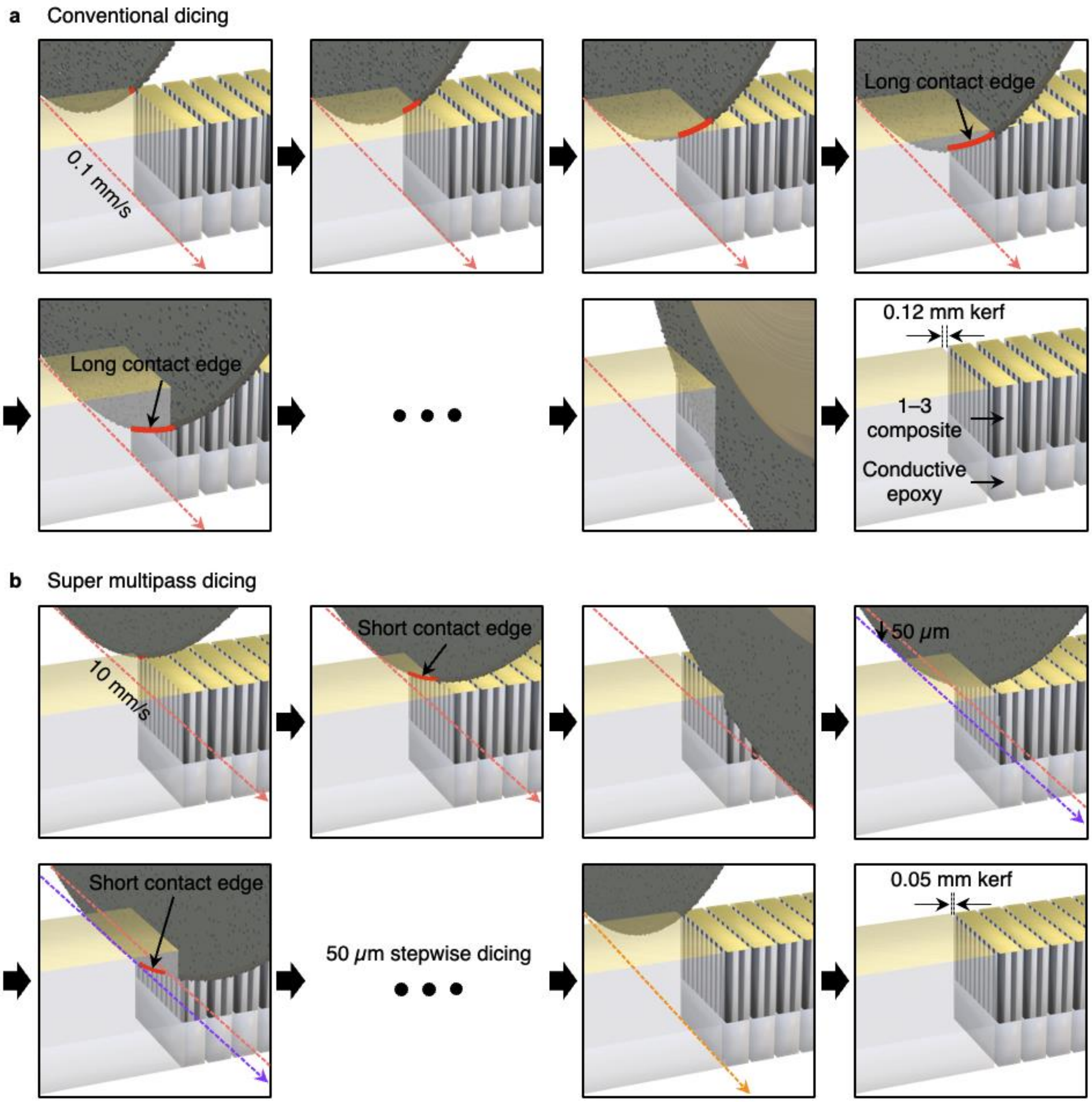

Supplementary Fig. 2 | Dicing strategies. a, Conventional dicing strategy. The blade is lowered to the entire transducer depth of 1 mm and diced at 0.1 mm/s feed speed. This method results in a long contact edge, producing a 0.12 mm kerf. The entire process takes ~15 h to dice a 64-channel array with a 0.4 mm pitch for a 25.55 mm by 12 mm transducer element. **b**, Super multipass dicing used in this study. A thinner dicing blade is used with 50 μm stepwise depth cuts. The blade is first lowered 50 μm from the top of the transducer and diced at 10 mm/s. Then, it is subsequently lowered to another 50 μm depth for dicing. This method results in a short contact edge. A total of 20 stepwise cuts are performed to achieve a 0.05 mm kerf for the same array size, which only takes ~3 h.

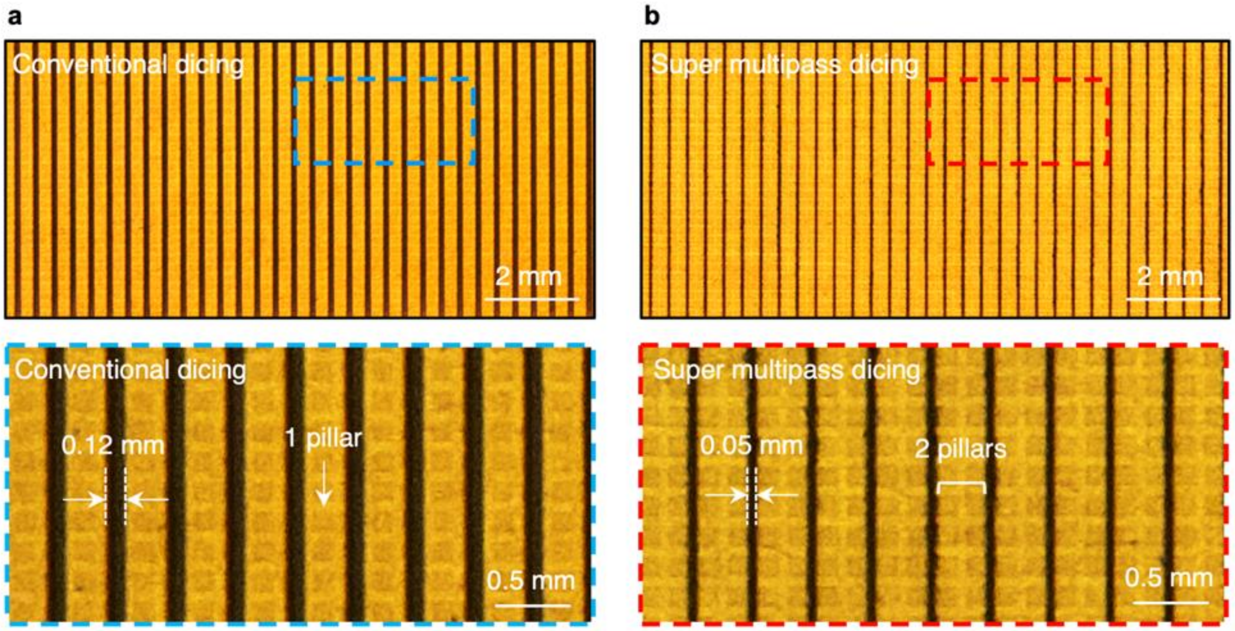

Supplementary Fig. 3 | 1–3 composite side of the transducers diced with different strategies. **a**, Optical images of transducers diced with the conventional strategy. The kerf is 0.12 mm and can only accommodate one piezoelectric pillar of the 1–3 composite. **b**, Optical images of transducers diced with the super multipass strategy. The kerf is 0.05 mm and can accommodate two piezoelectric pillars of the 1–3 composite.

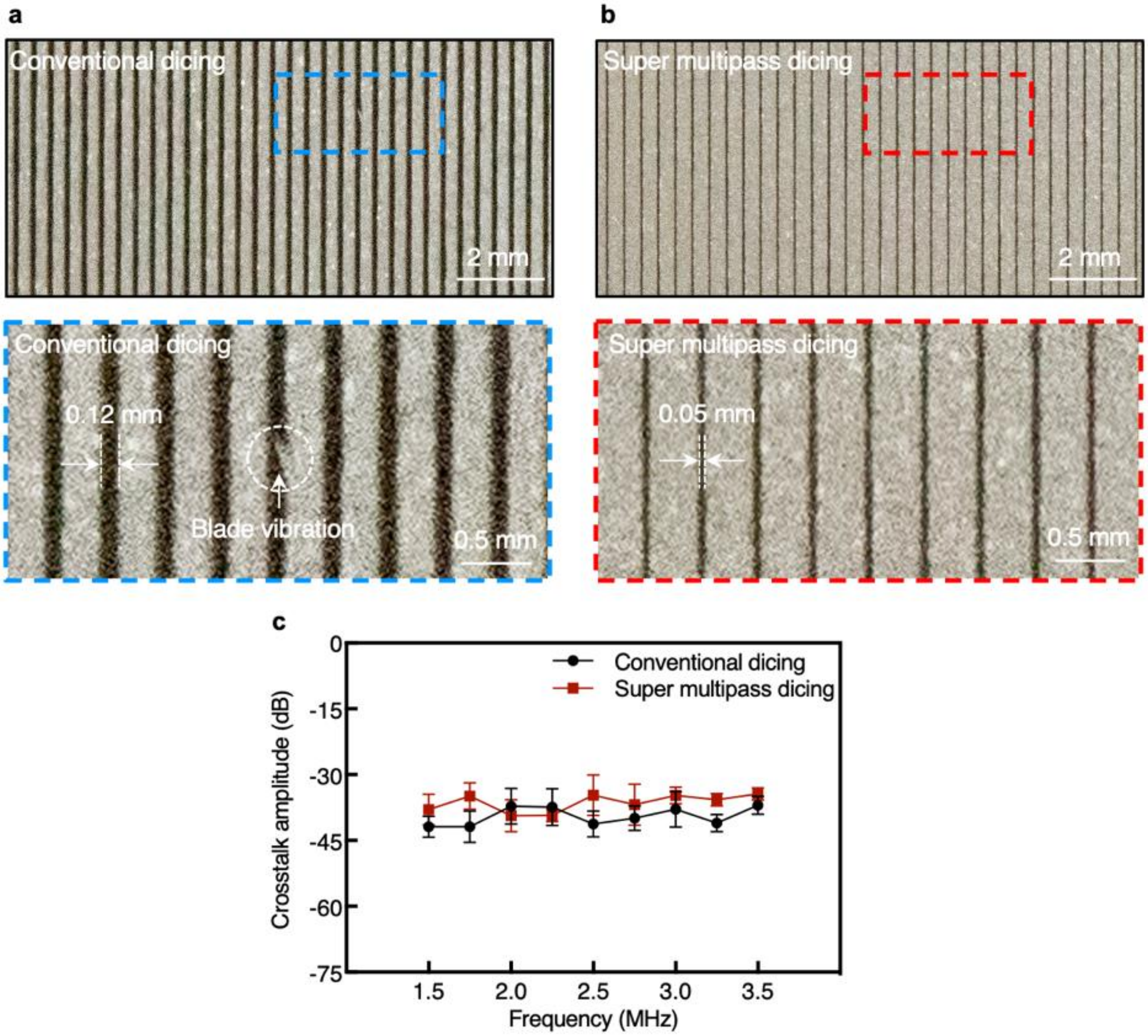

Supplementary Fig. 4 | Comparison of transducers diced with different strategies. a, Optical images of the backing layer side of the transducer diced with the conventional strategy. The kerf is 0.12 mm and blade vibration can cause defects in the transducers. **b**, Optical images of backing layer side of the transducer diced with the super multipass strategy. The kerf is 0.05 mm. **c**, Transducers diced with both strategies demonstrate similar crosstalk amplitude. Error bars in **c** show ±standard deviations (n = 4).

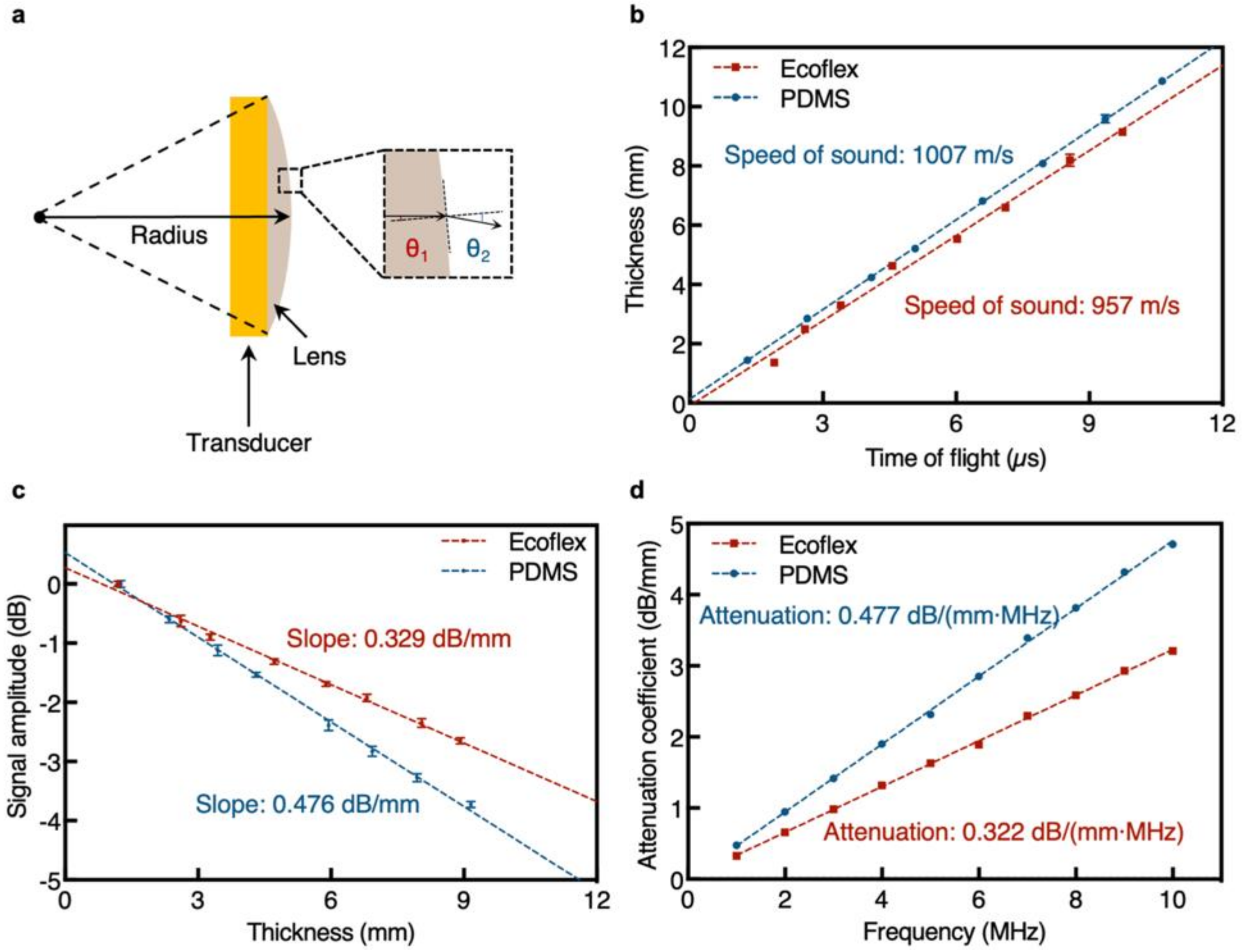

Supplementary Fig. 5 | Design of the acoustic lens. a, Schematics of the lens. The speed of sound of the lens material is used to determine the lens radius. θ_1 and θ_2 are the incidence angle and refraction angle, respectively. **b**, Speed of sound and **c**, acoustic attenuation coefficients at 1 MHz ultrasound frequency of soft acoustic lens materials. **d**, Acoustic attenuation coefficients at 1–10 MHz ultrasound frequencies of soft acoustic lens materials. Each data point in **d** is obtained from a linear fit in **c**. Ecoflex has a lower speed of sound and attenuation coefficient than those of polydimethylsiloxane (PDMS). Error bars in **b** and **c** show ±standard deviation (n = 4).

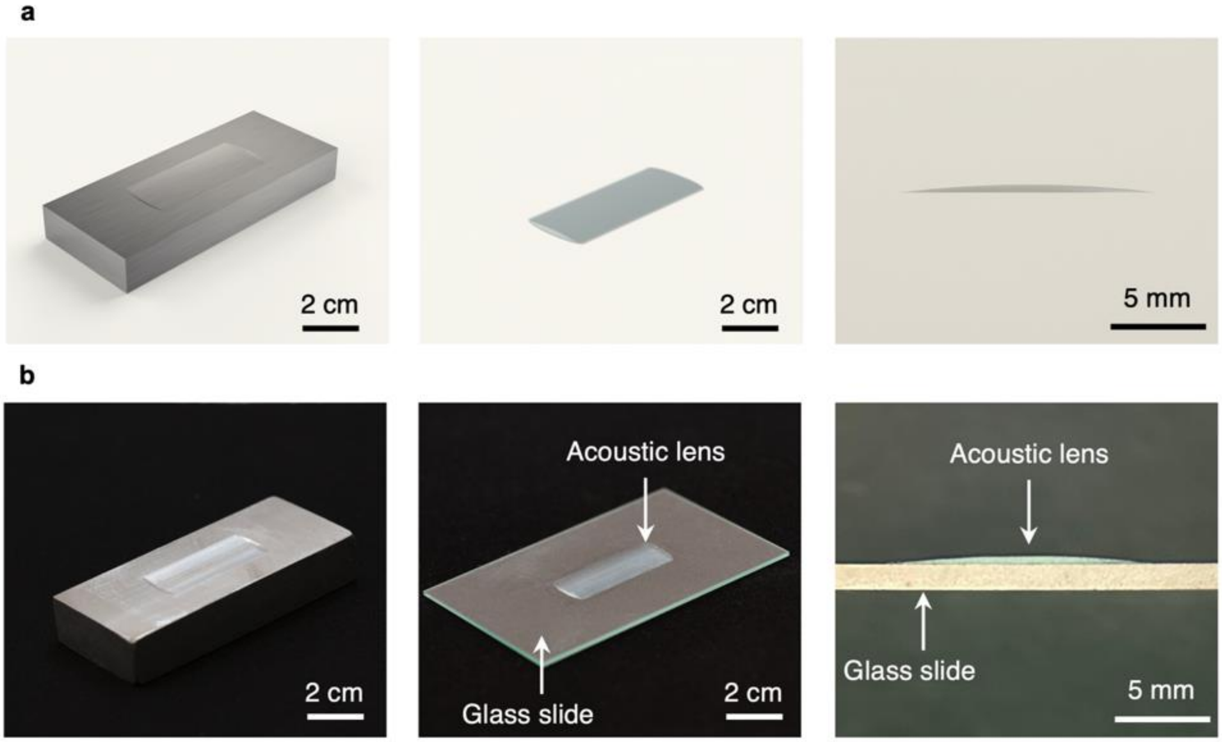

Supplementary Fig. 6 | Fabrication of the acoustic lens. a, Designs and **b**, optical images of the aluminum block mold (left), the molded lens (middle), and the cross section of the lens (right). The aluminum block mold was fabricated using computer numerical control machining. Ecoflex was molded and cured inside the mold to produce an acoustic lens.

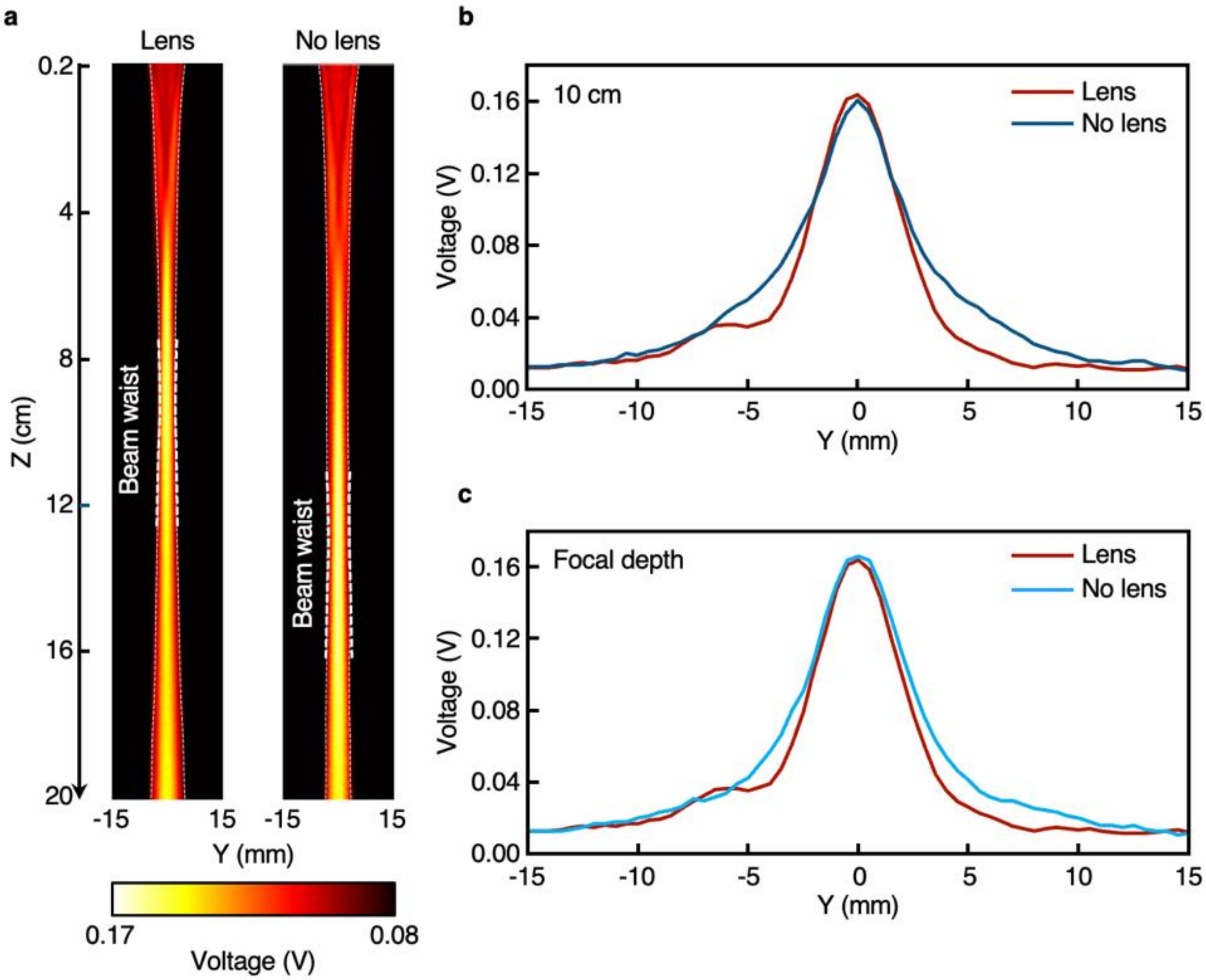

Supplementary Fig. 7 | Characterization of the acoustic lens. a, Hydrophone scanning of the acoustic fields of the UPatch with and without the lens in the YZ plane. The acoustic lens shifts the elevational focal region from ~14 cm to ~10 cm, the typical depth of interest for fetal monitoring. The images share the same color bar for hydrophone output voltage, which can be converted to acoustic pressure. Elevational beamwidth comparisons at **b**, 10 cm and **c**, focal depth with and without the acoustic lens. For **c**, the red line is the signal at 10 cm (lens) while the light blue line is the signal at 14 cm (no lens). In both **b** and **c**, the lens decreases the elevational beamwidth with negligible attenuation.

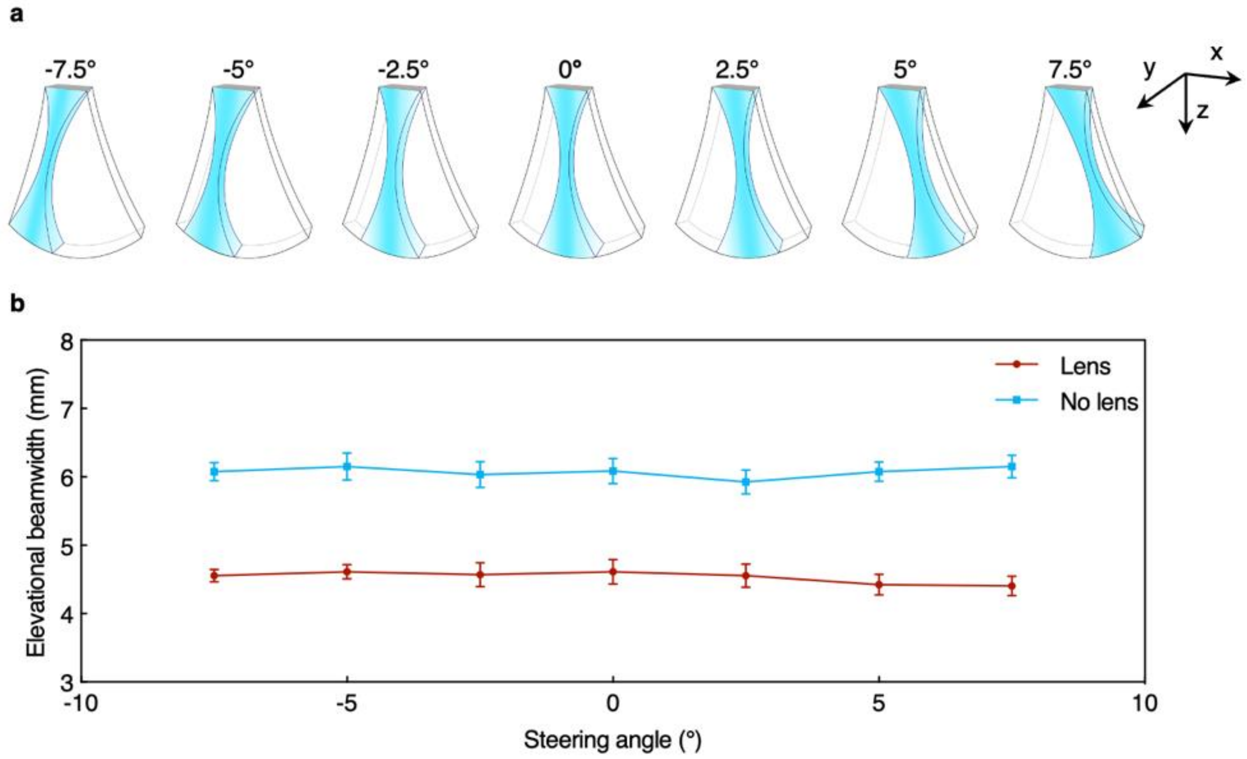

Supplementary Fig. 8 | Elevational beamwidth during beam steering. **a**, Schematics illustrating three-dimensional acoustic propagation during beam steering. Beam steering occurs in the XZ plane, while the acoustic lens focuses the beam in the YZ plane. **b**, Experimental data comparing the elevational beamwidth at different steering angles with and without the acoustic lens. In both cases, the elevational beamwidth remains consistent across the steering range. Error bars in **b** show ±standard deviation (n = 4).

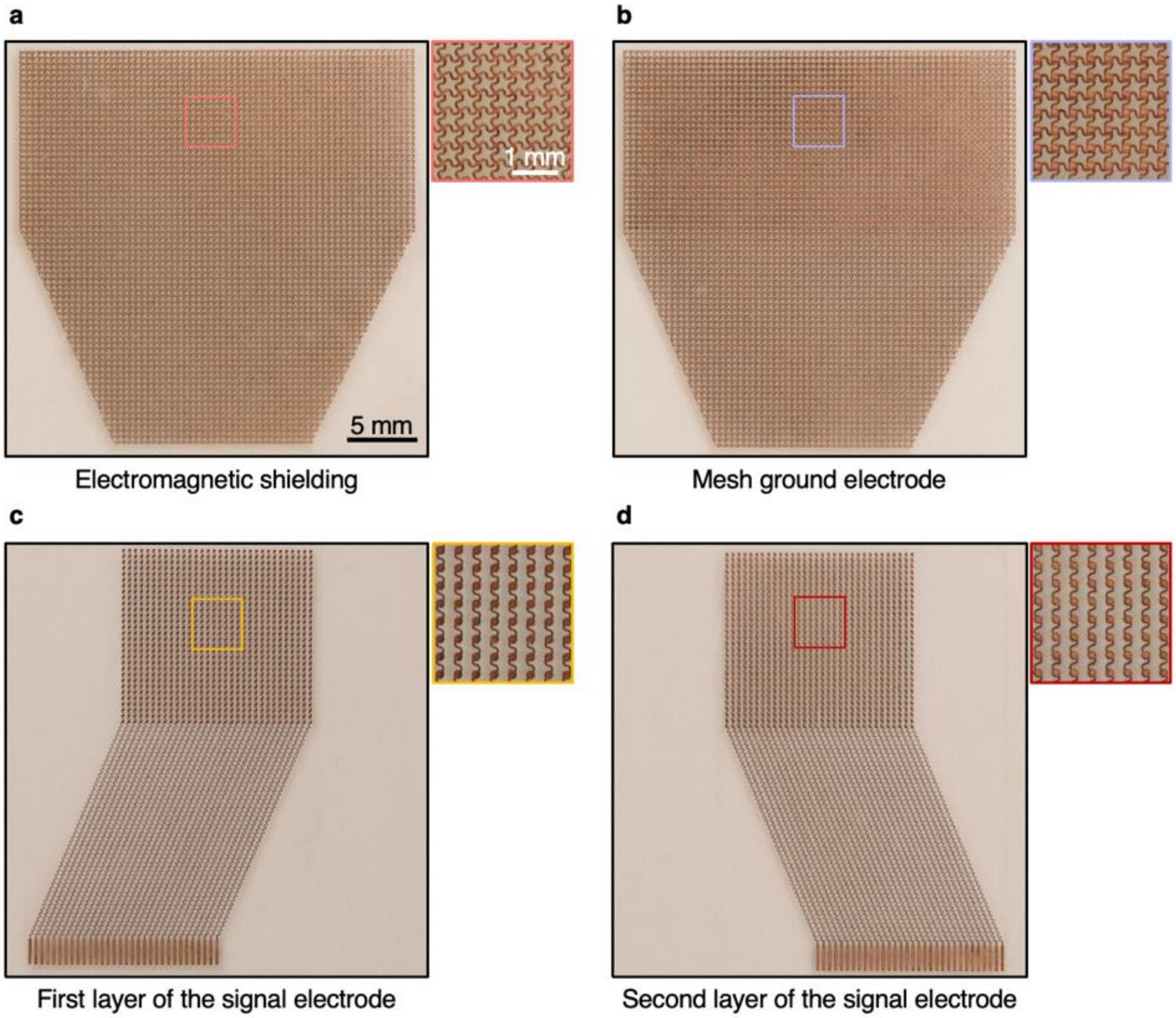

Supplementary Fig. 9 | Photographs of each layer of electrodes. **a**, Electromagnetic shielding layer. **b**, Mesh ground electrode layer. **c**, The first layer of the signal electrode. **d**, The second layer of the signal electrode. Insets are the serpentine design of each layer. The first and second layers of the signal electrodes activate 32 channels each. The electromagnetic shielding and mesh ground electrode layers minimize electromagnetic interference from the surrounding environment. The photographs and insets share the same scale bar, respectively.

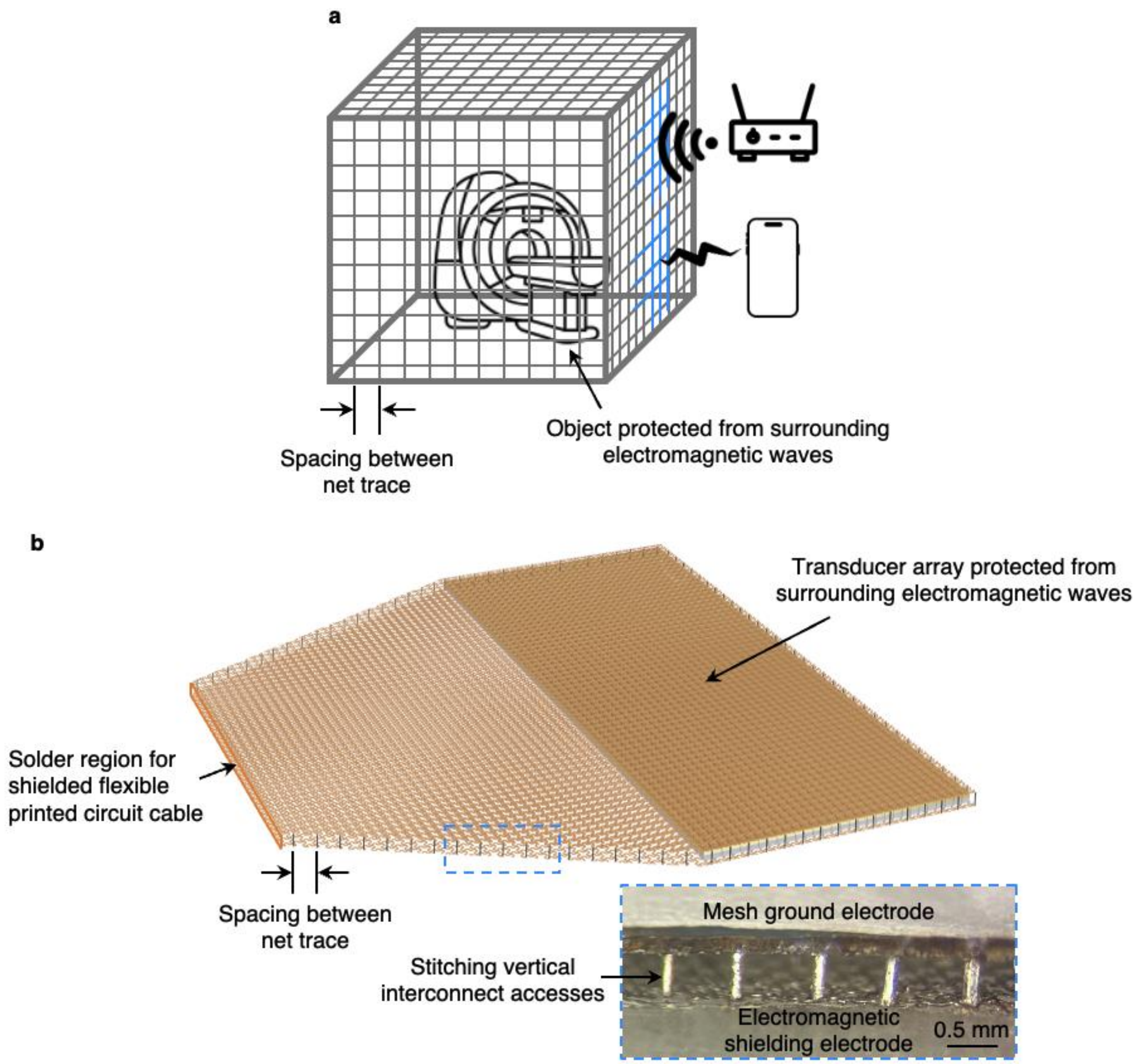

Supplementary Fig. 10 | Faraday cages. a, Schematics of a Faraday cage. The Faraday cage protects sensitive electronic equipment by absorbing electromagnetic waves from other electronic sources (e.g., Wi-Fi routers and smartphones). The spacing between the metal traces determines the frequency bands of the electromagnetic waves that can be blocked. **b**, Schematics of the soft Faraday cage. Inset is a zoomed-in photograph of the stitching vertical interconnect accesses. The electromagnetic shielding and mesh ground electrode layers are patterned with serpentine traces and encapsulated in a soft elastomer. The stitching vertical interconnect accesses enable a three-dimensional enclosure of the transducer, thereby providing effective isolation within the soft Faraday cage.

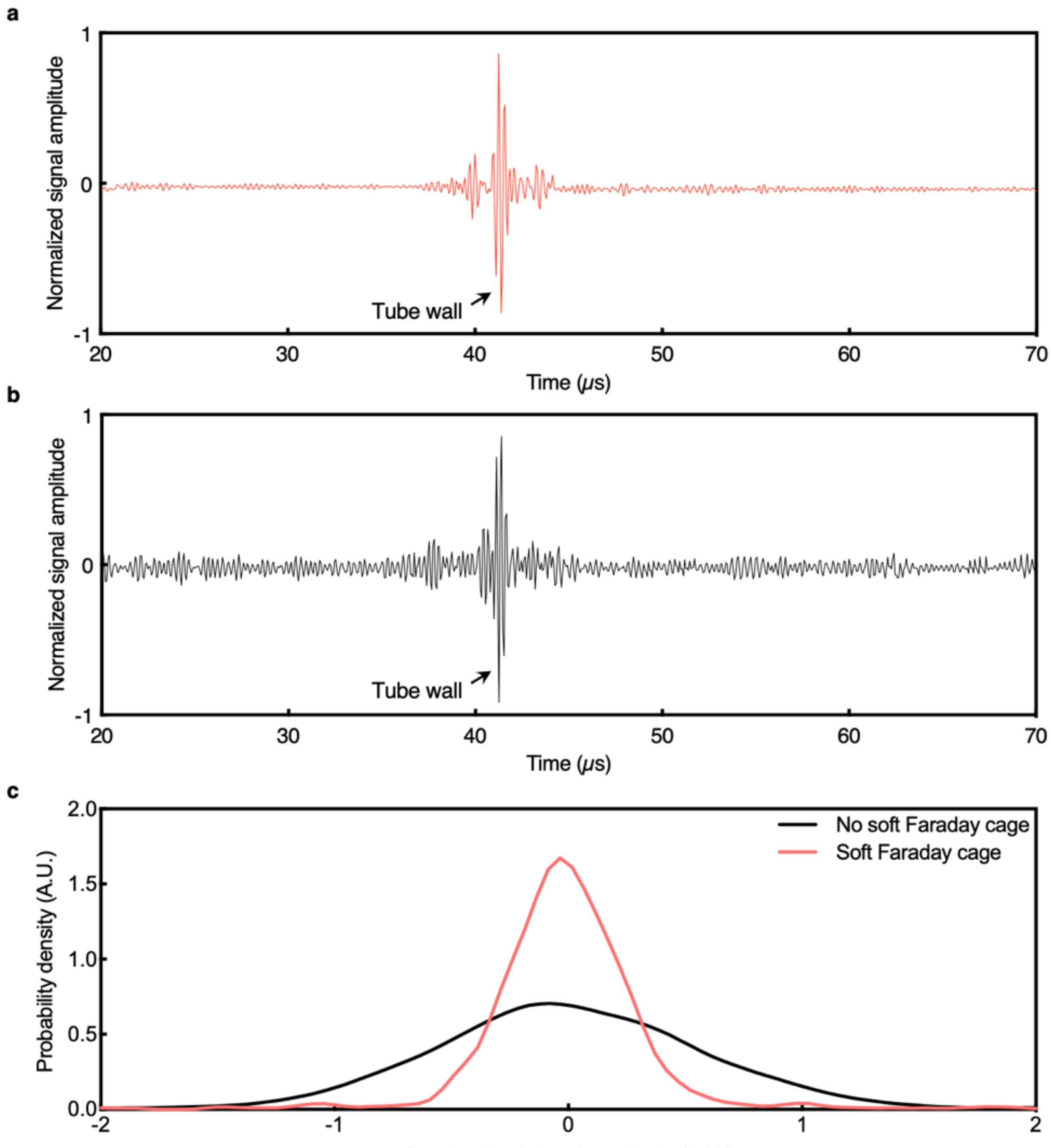

Supplementary Fig. 11 | Effects of the soft Faraday cage on phantom measurements. Radiofrequency signals **a**, with and **b**, without the soft Faraday cage. **c**, Probability density function comparison with and without the soft Faraday cage. The narrower distribution of measurements with the soft Faraday cage indicates reduced susceptibility to ambient electromagnetic noise.

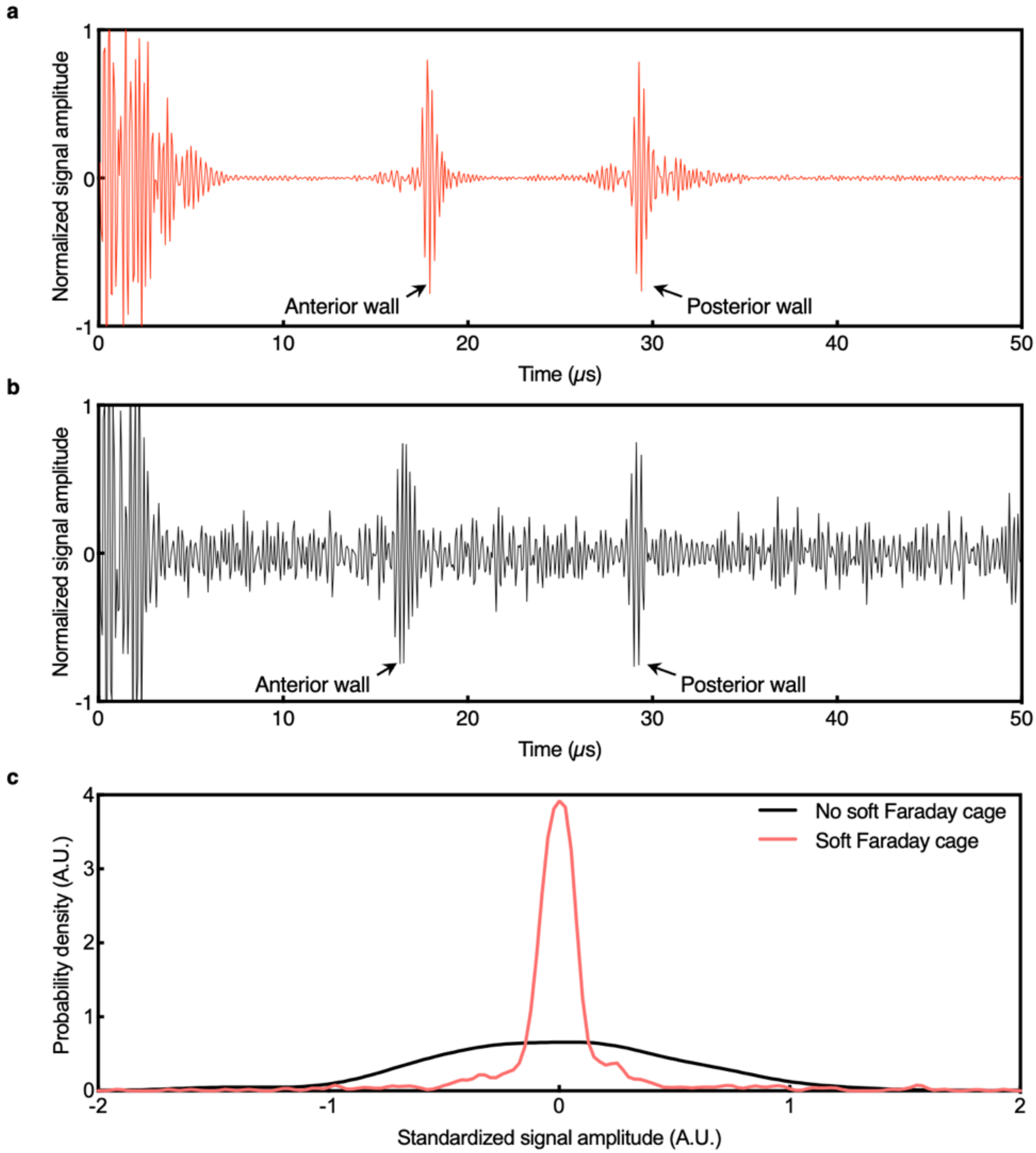

Supplementary Fig. 12 | Effects of the soft Faraday cage on adult carotid artery measurements. Radiofrequency signals **a**, with and **b**, without the soft Faraday cage. **c**, Probability density function comparison with and without the soft Faraday cage. The narrower distribution of measurements with the soft Faraday cage indicates reduced electromagnetic interference, potentially from both physiological and environmental sources, enhancing in vivo signal fidelity.

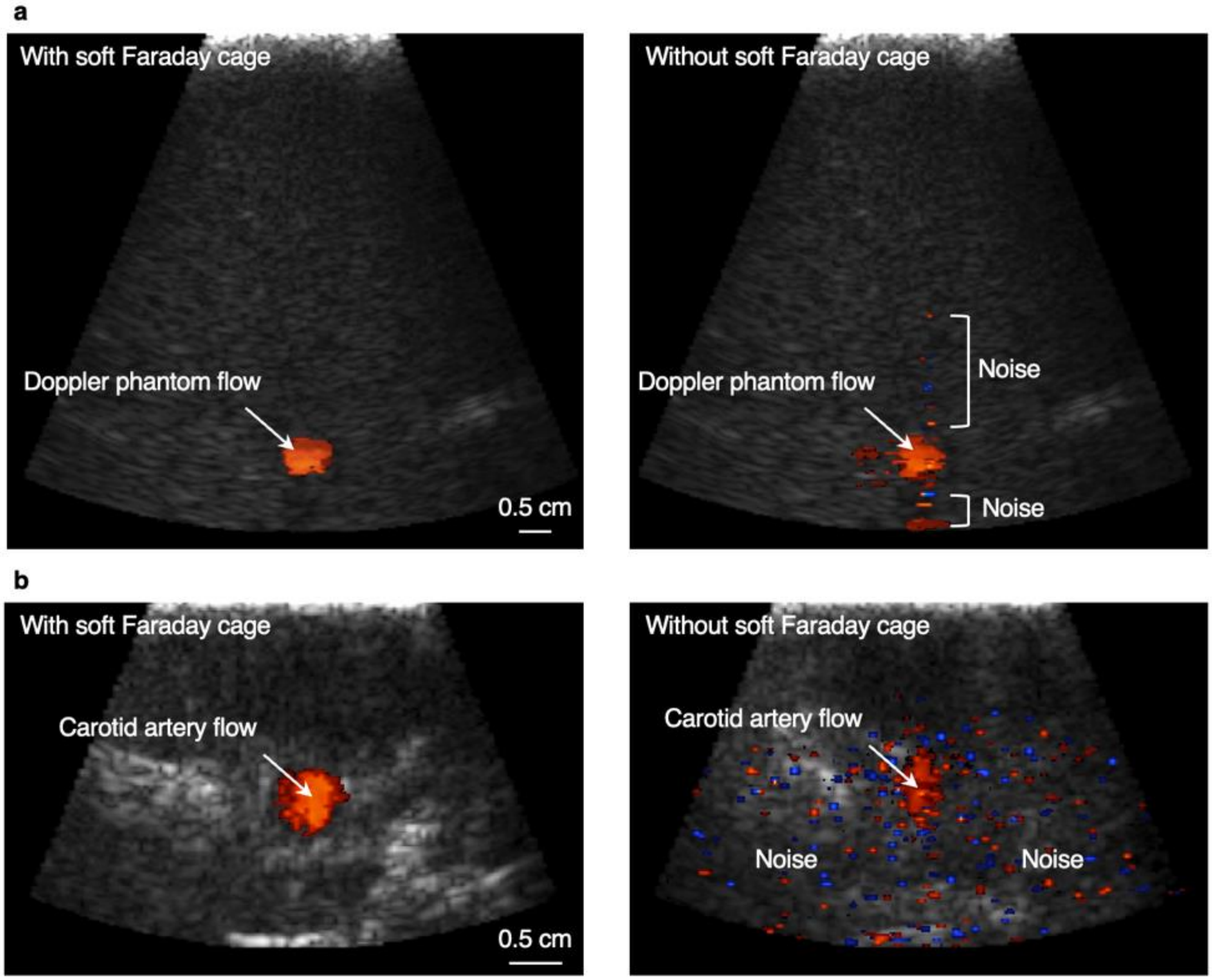

Supplementary Fig. 13 | Effects of the soft Faraday cage on noise levels in duplex imaging. a, Duplex images of a phantom with and without the soft Faraday cage. The images share the same scale bar. **b**, Duplex images of the carotid artery in a healthy adult with and without the soft Faraday cage. The images share the same scale bar. The use of the soft Faraday cage reduces noise and improves image quality.

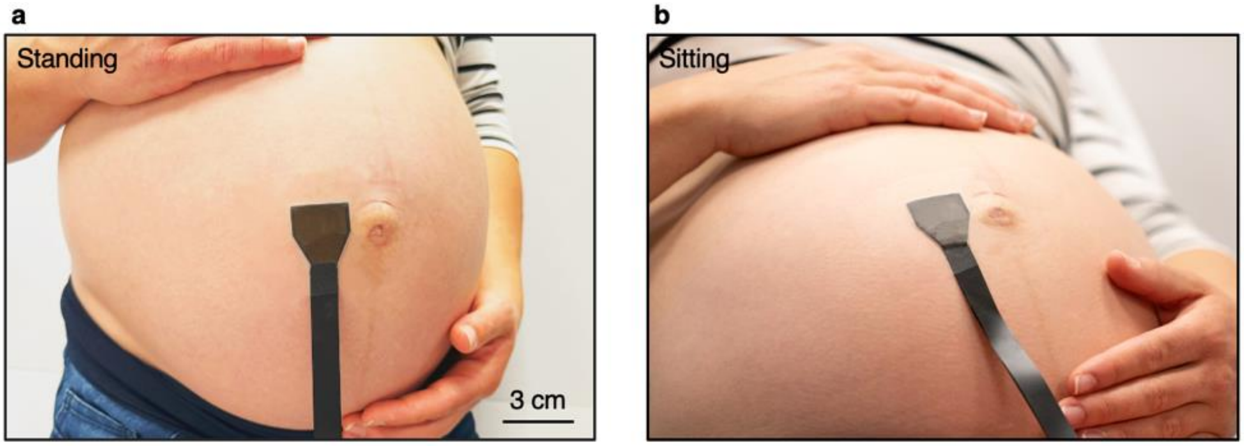

Supplementary Fig. 14 | Photographs of the UPatch on a pregnant woman. The UPatch is laminated on a pregnant participant in **a**, standing and **b**, sitting positions. The UPatch conforms closely to the contour of the abdominal surface, ensuring intimate contact for effective ultrasound transmission. The photographs share the same scale bar.

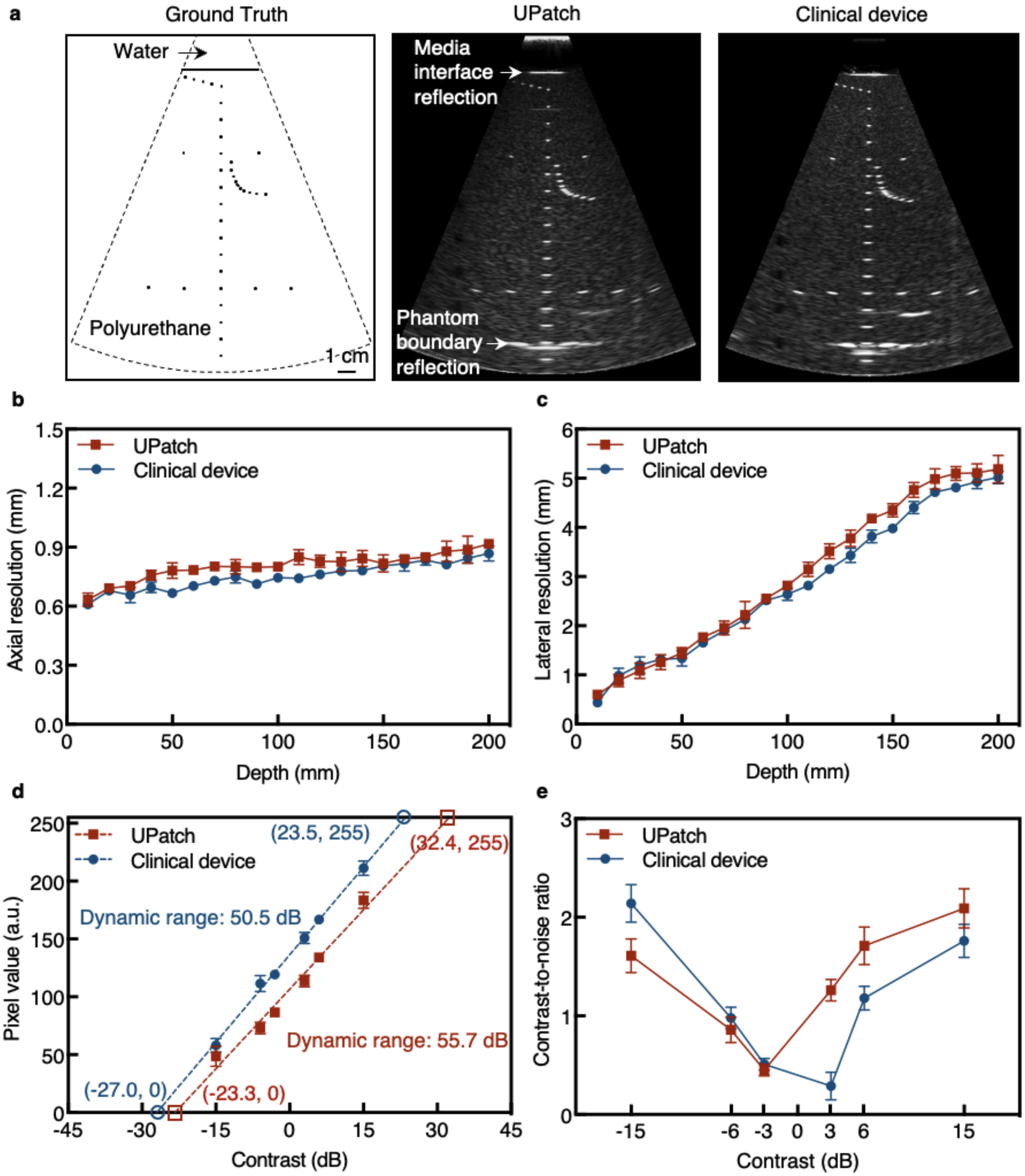

Supplementary Fig. 15 | Brightness mode characterizations. a, Schematics of the phantom (left), and brightness-mode images from the UPatch (middle) and a clinical device (P4–1, ATL) (right). The brightness-mode image quality is comparable between the UPatch and clinical device. The images share the same scale bar. **b**, Axial resolution from depths 10 mm to 200 mm. **c**, Lateral resolution from depths 10 mm to 200 mm. **d**, Dynamic range calculated based on six grayscale targets (-15 dB, -6 dB, -3 dB, +3 dB, +6 dB, and +15 dB). **e**, Contrast-to-noise ratio calculated based on the six grayscale targets. Error bars in **b-e** show ±standard deviation (n = 4).

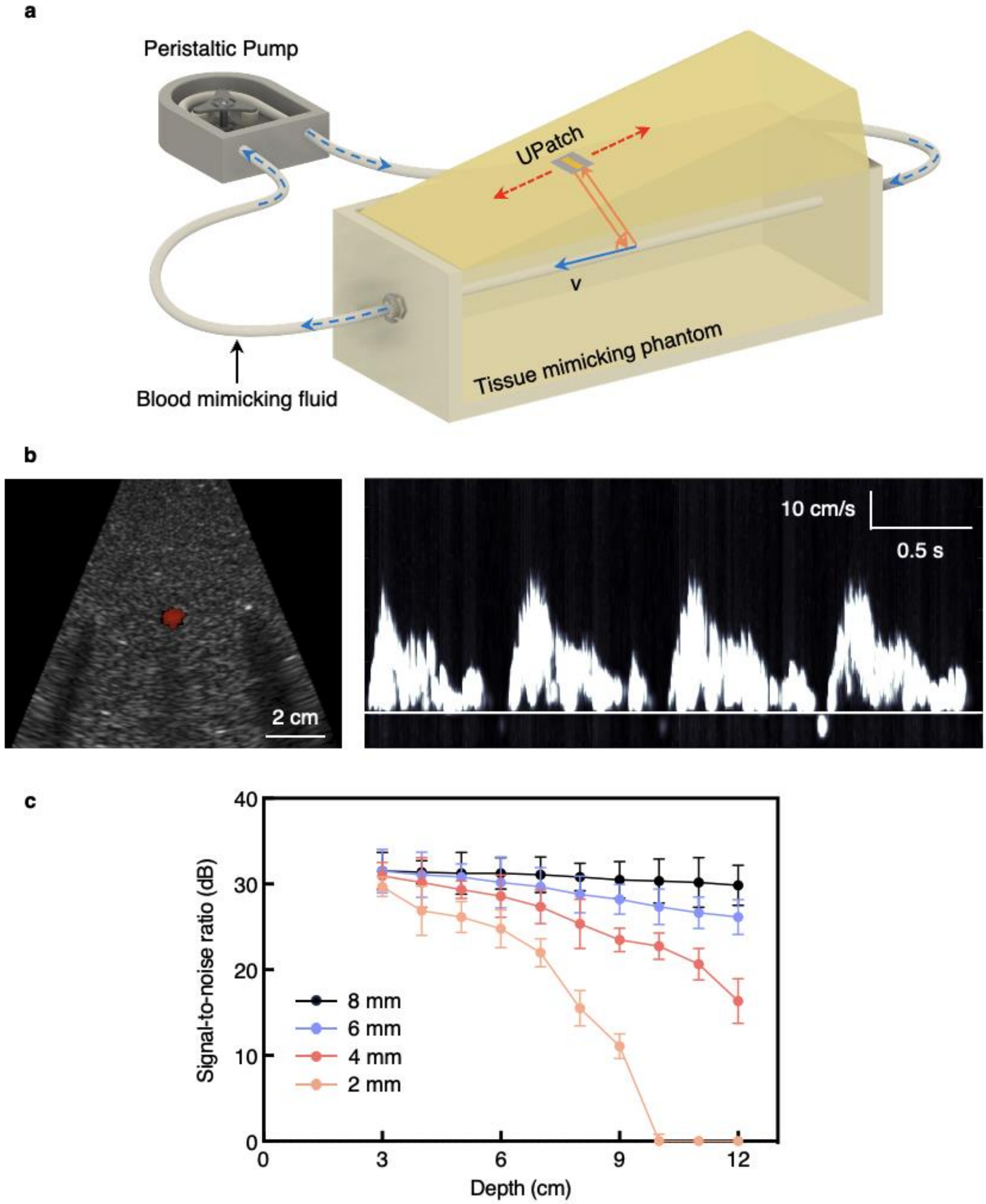

Supplementary Fig. 16 | Doppler characterizations. a, Schematic setup of a commercial Doppler phantom (CIRS ATS523A) for Doppler characterizations. Blood-mimicking fluid was pumped into the phantom with a known Doppler angle using a peristaltic pump. The depth from the UPatch to the phantom vessel ranges from 3 cm to 12 cm. **b**, Exemplary color-flow image (left) and spectral Doppler signal (right) acquired from the phantom using the UPatch. **c**, Signal-to-noise ratio of color Doppler signals of the UPatch at different phantom vessel depths. The UPatch can detect the smallest phantom vessel diameter of 2 mm at a depth of 10 cm. Error bars in **c** show ±standard deviation (n = 4).

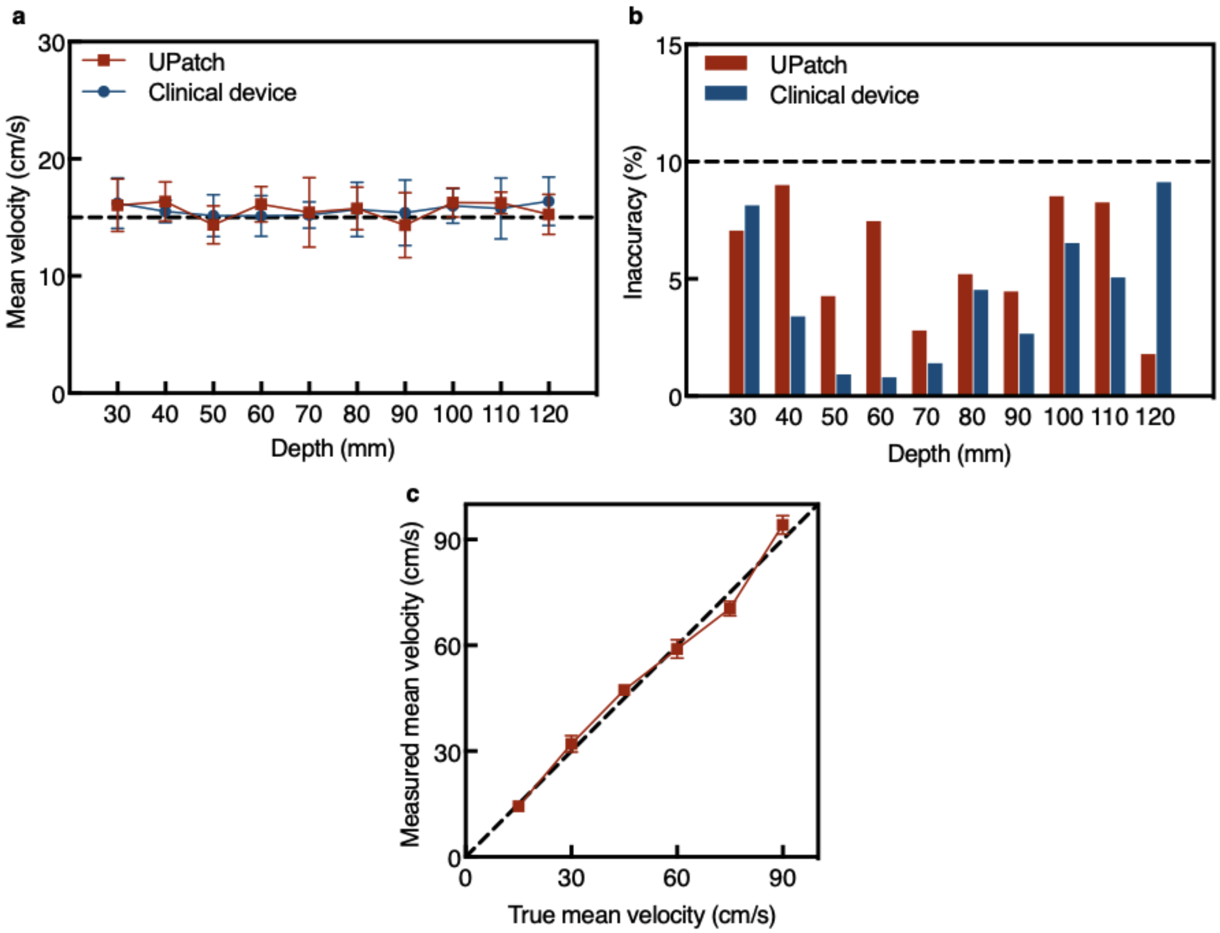

Supplementary Fig. 17 | Blood flow measurement accuracy. **a**, Mean blood flow velocity at each depth. The black dashed line shows the ground truth mean velocity of 15 cm/s set on the peristaltic pump. **b**, Inaccuracy of the mean blood flow velocity as a function of depth. The dashed line shows the inaccuracy threshold of 10% typically used in ultrasound quality assurance protocols[164]. The two devices demonstrate similar levels of inaccuracies. **c**, Measured mean velocities as a function of different ground truth mean velocities at a depth of 50 mm. The black dashed line represents the linearity between the measured and ground truth velocities. Error bars in **a** and **c** show ±standard deviation (n = 4).

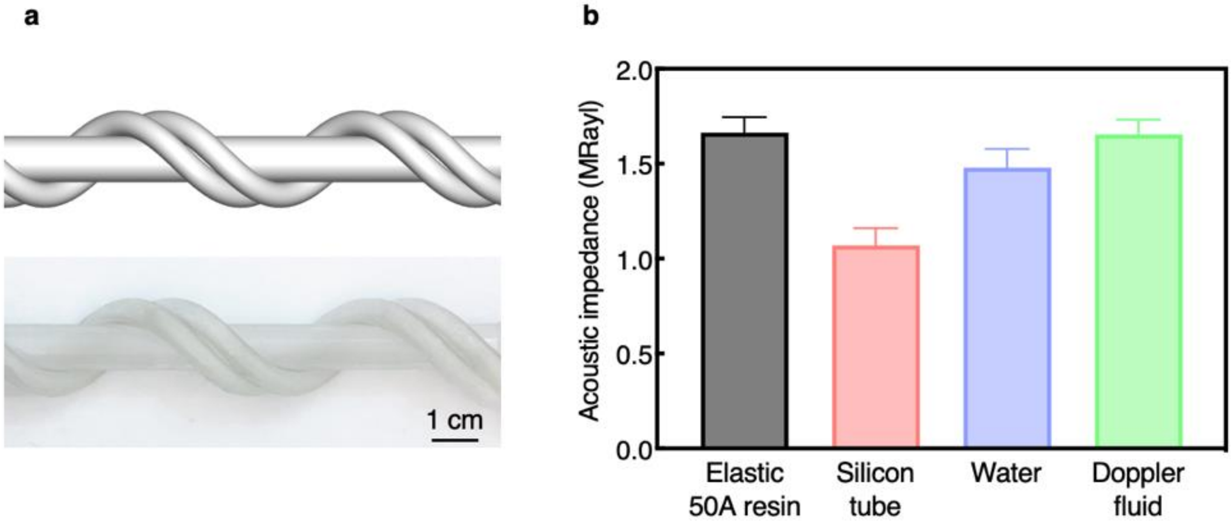

Supplementary Fig. 18 | Design of the umbilical cord phantom. a, Model (top) and image of the stereolithographically printed phantom (bottom) of the helical umbilical cord. The umbilical cord is composed of two arteries and one vein. **b**, Acoustic impedances of different materials. The Elastic 50A resin (Formlabs) exhibits small acoustic impedance mismatch with water and Doppler fluid[81,165], minimizing acoustic reflection at fluid–structure interfaces. In contrast, the greater mismatch of silicone tubing (Metaland) leads to substantial acoustic reflection, particularly when insonating through multiple interfaces of the umbilical cord.

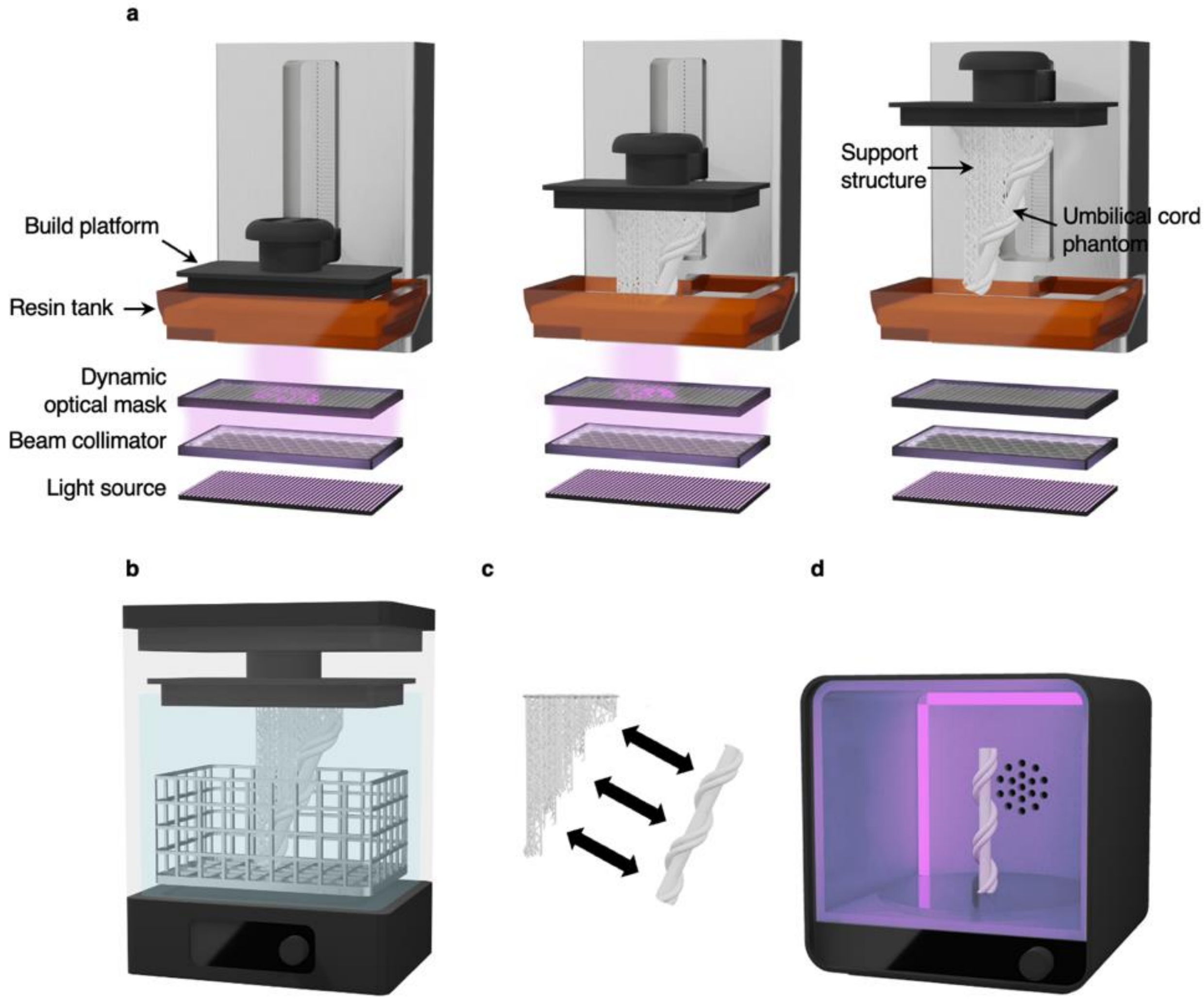

Supplementary Fig. 19 | Stereolithographic fabrication of the umbilical cord phantom. a, Schematic of the stereolithography process showing layer-by-layer photopolymerization of resin to fabricate an umbilical cord phantom. A vertically translating build platform enables sequential printing within a resin tank. A light source passes through the beam collimator to produce coherent illumination. A dynamic optical mask modulates the illumination to define each layer's geometry. A support structure is printed in parallel with the umbilical cord phantom to ensure geometric stability during stereolithography. **b**, Post-print washing process. The structure is immersed in solvent to remove uncured resin. **c**, Manual removal of support structures to isolate the umbilical cord phantom. **d**, Final polymerization step. An ultraviolet light fully cures the umbilical cord phantom to improve mechanical and chemical robustness.

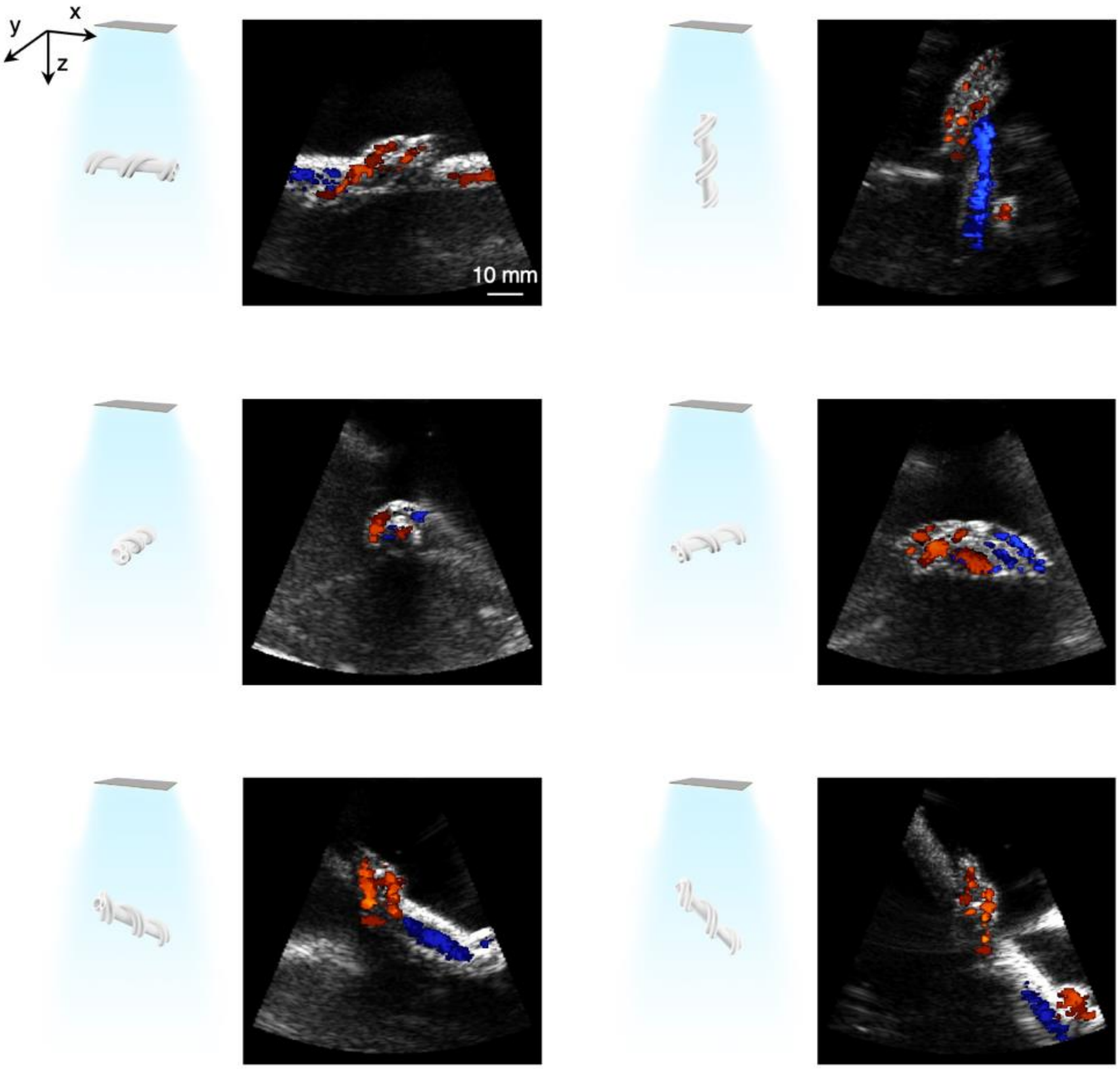

Supplementary Fig. 20 | UPatch imaging of the umbilical cord phantom across various anatomical orientations. The UPatch can image the umbilical cord phantom in diverse spatial configurations. This capability supports the device's application in dynamic in utero environments, accommodating variations in umbilical cord position due to fetal motion and anatomical variability.

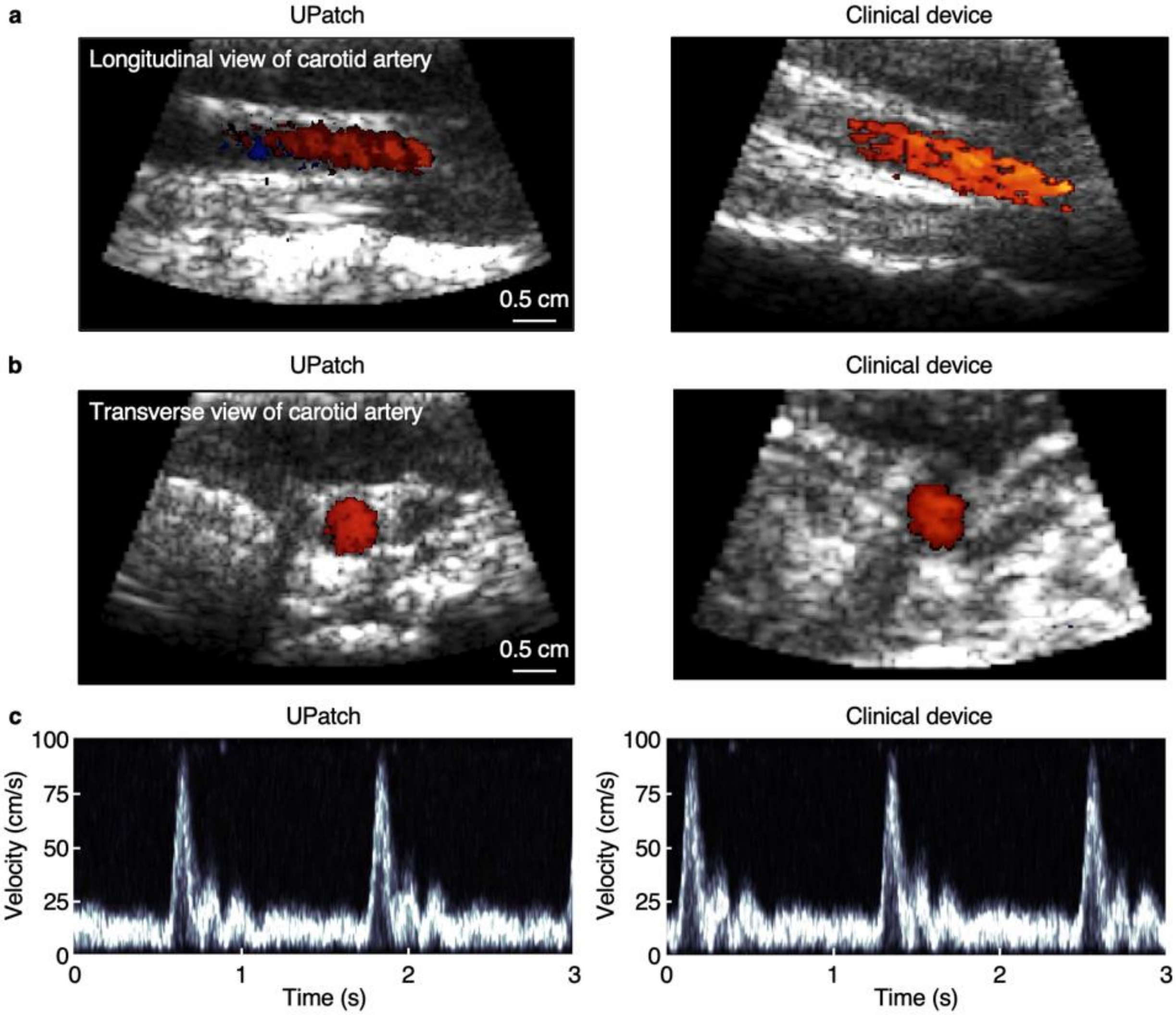

Supplementary Fig. 21 | Measurements on the carotid artery of a healthy adult. Duplex imaging of the carotid artery showing the **a**, longitudinal view and **b**, transverse view with the UPatch (left) and clinical device (right). Anatomy and blood flow of the carotid artery can be recognized from the brightness mode and color Doppler mode, respectively. The images share the same scale bar. **c**, Blood flow measurements of the carotid artery using the spectral Doppler mode. Blood flow spectra obtained from the UPatch (left) and clinical device (right) are comparable on the same participant.

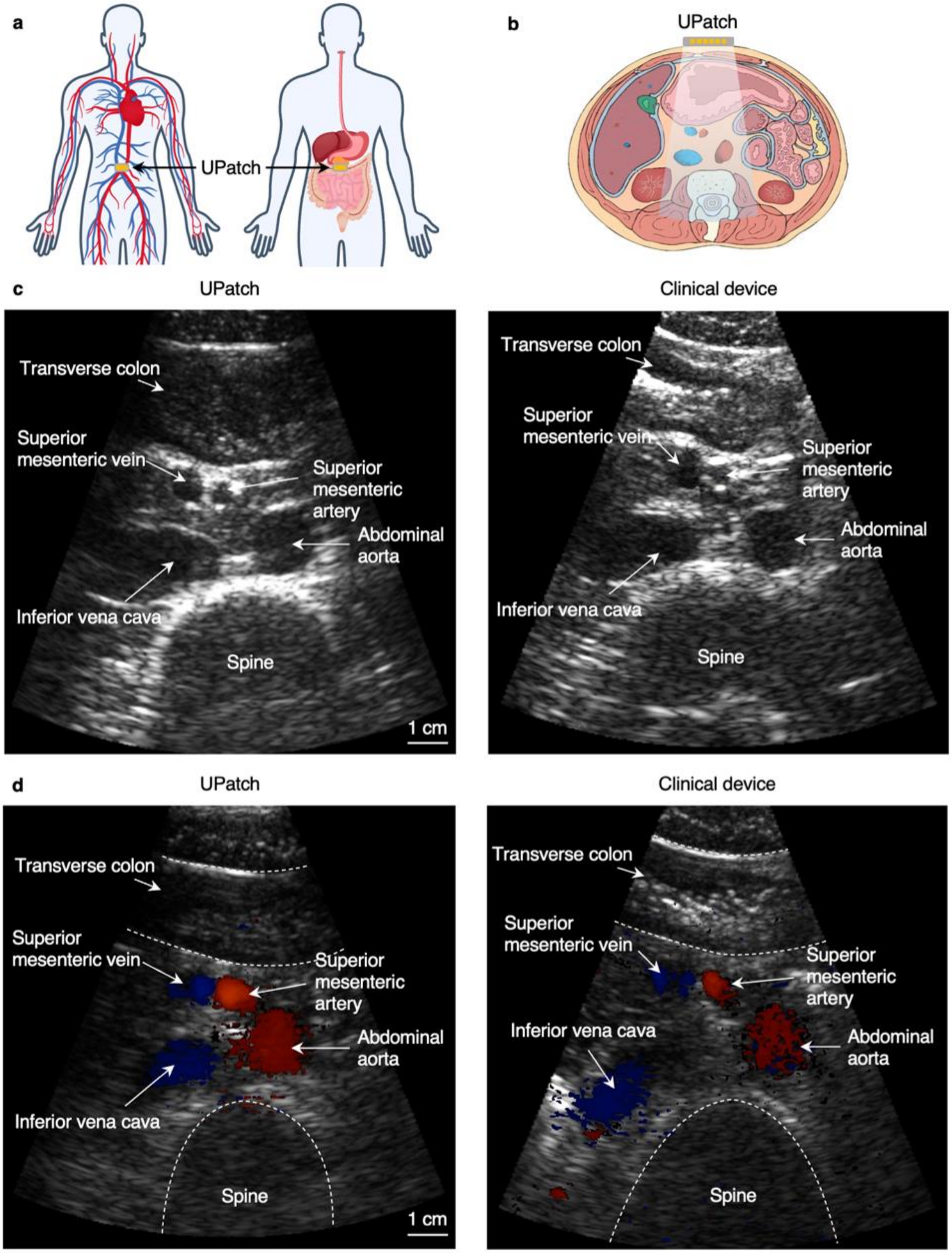

Supplementary Fig. 22 | Measurements on the abdominal cross-section of a healthy adult. a, Schematics showing the position of the UPatch imaging the cardiovascular system (left) and digestive system (right). **b**, Schematics illustrating the transverse anatomical view of the abdomen. Transverse view of the abdominal anatomy in **c**, brightness and **d**, duplex modes. Both the UPatch and clinical device can clearly recognize the structures of the transverse colon, superior mesenteric vein, superior mesenteric artery, inferior vena cava, abdominal aorta, and spine. The images share the same scale bar.

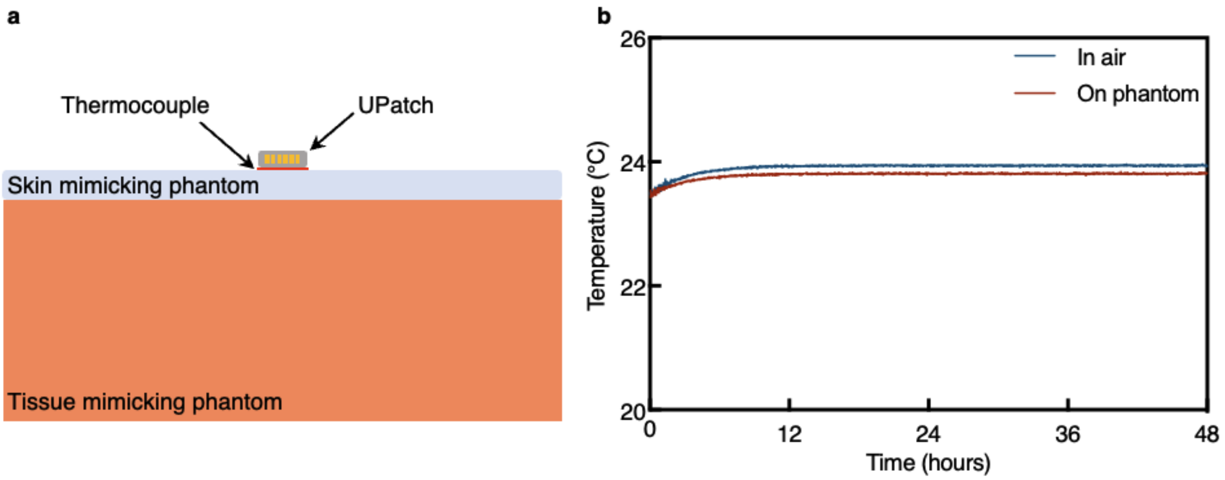

Supplementary Fig. 23 | Surface temperature characterizations. a, Schematic setup for the on phantom testing. The setup includes a skin and tissue mimic phantom (NPL, UK) with similar acoustic and thermal properties to those of human skin and tissues. The thermocouple was placed in between the UPatch and the skin mimic phantom during the measurement. **b**, Surface temperature measurements on phantom and in air. The in-air test was performed by placing the UPatch and thermocouple in still air[166]. The maximum temperature increase was ~ 0.53 °C, which was < 0.7 °C for continuous monitoring recommended by the AIUM[121] and BMUS[122].

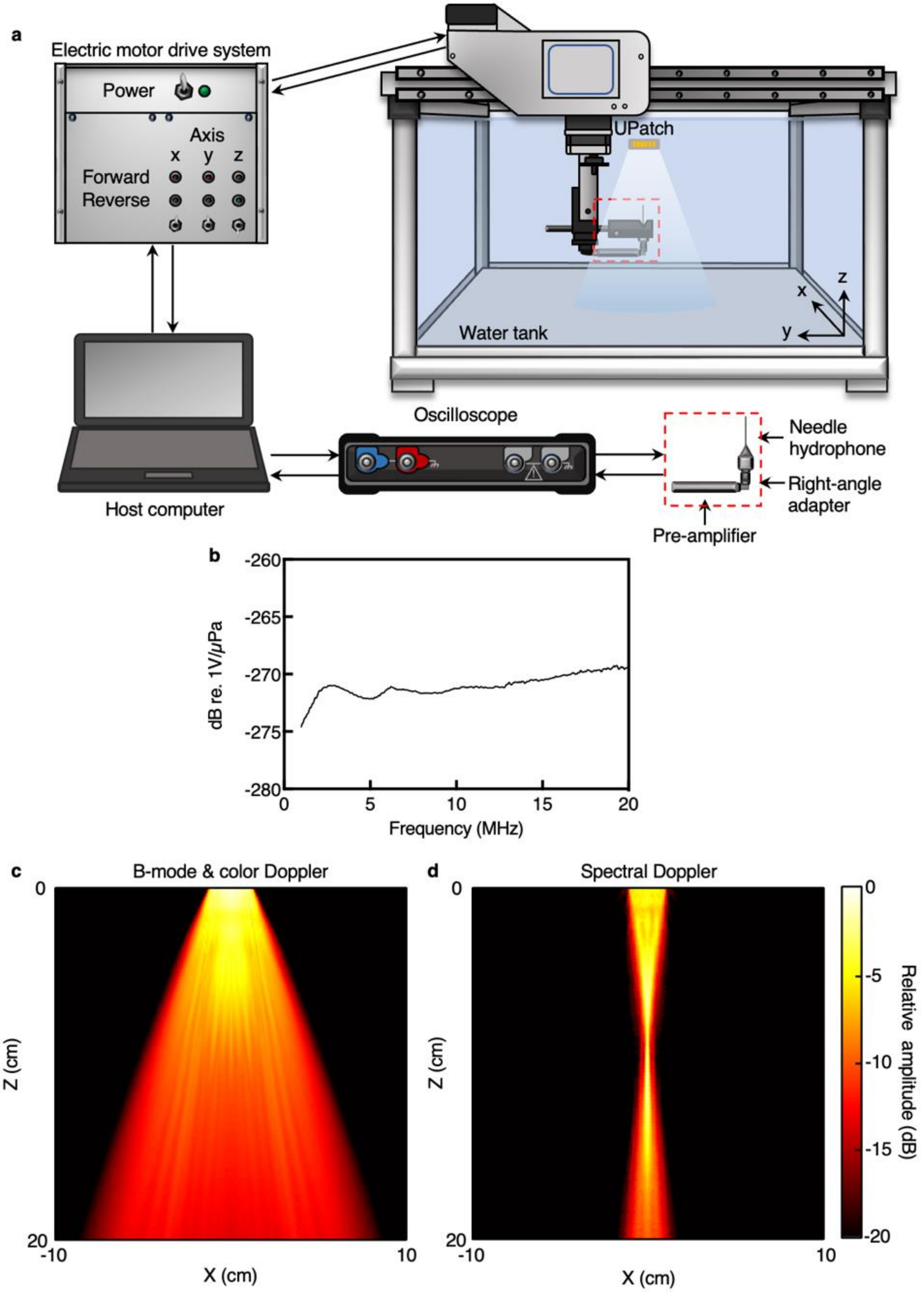
a
Electric motor drive system
Power
Axis
x y z
Forward
Reverse
UPatch
x
z
y
Water tank
Oscilloscope
Host computer
Needle hydrophone
Right-angle adapter
Pre-amplifier
b
dB re. 1V/μPa
-260
-265
-270
-275
-280
0
5
10
15
20
Frequency (MHz)
c
B-mode & color Doppler
Z (cm)
0
20
-10
10
X (cm)
d
Spectral Doppler
Z (cm)
0
20
-10
10
X (cm)
Relative amplitude (dB)
0
-5
-10
-15
-20

Supplementary Fig. 24 | Safety measurements with a hydrophone. a, Schematic setup with a hydrophone system. Ultrasound intensity from the UPatch can be measured in a water tank. **b**, Magnitude data from calibrating the hydrophone sensitivity for accurate calculation of its acoustic properties. Acoustic field scans of **c**, a diverging beam (for brightness and color-flow modes) and **d**, a focused beam (for the spectral Doppler mode) with the UPatch in the XZ plane. The images share the same color bar.

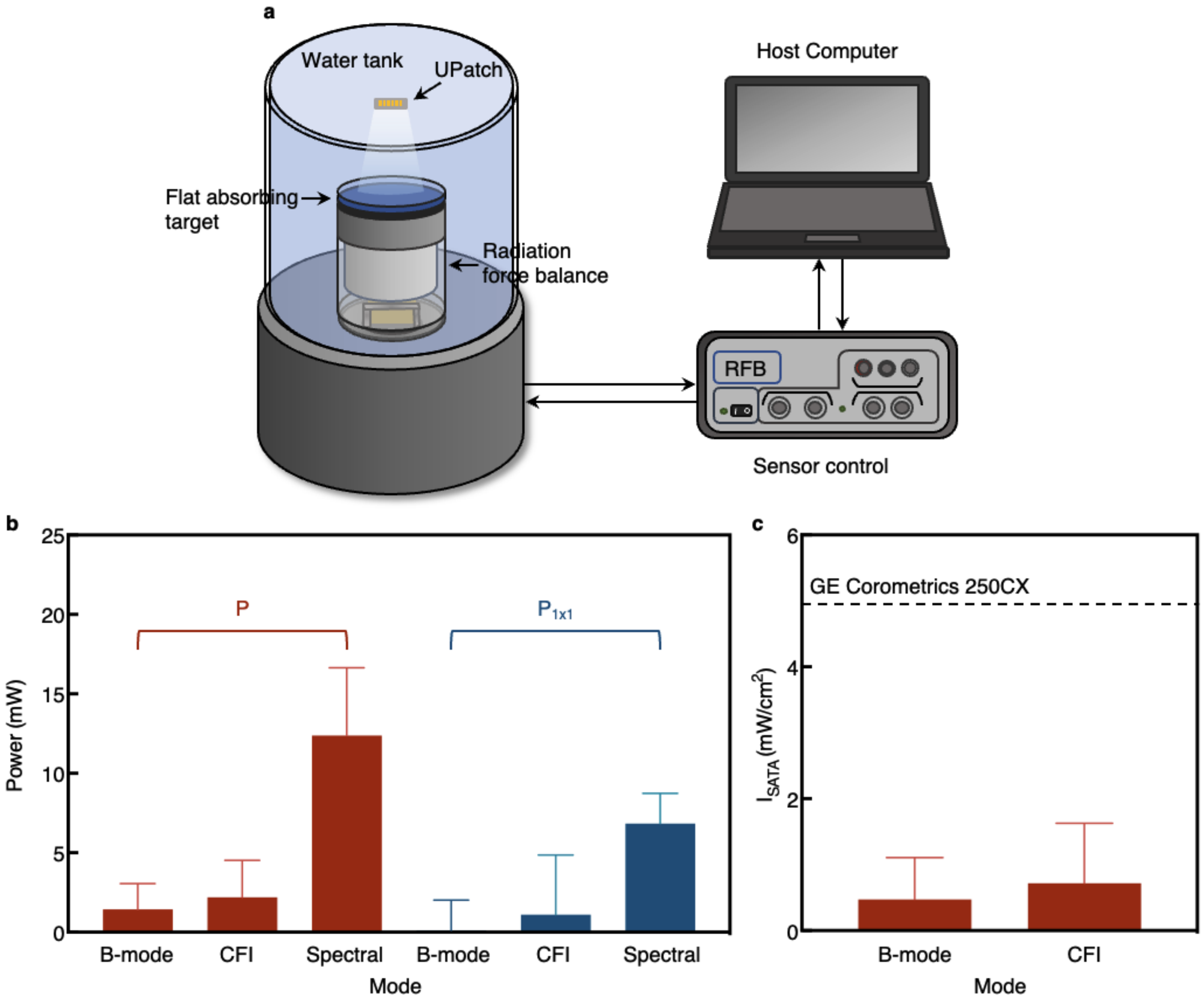

Supplementary Fig. 25 | Safety measurements with a radiation force balance. a, Schematic setup with a radiation force balance. The ultrasound beam from the UPatch is uniformly absorbed in the flat absorbing target and the radiation force balance can accurately measure the power of the transmitted beam. **b**, Power (P) and bounded-square output power over a one square centimeter area (P_{1x1}) were measured in brightness (B-mode), color-flow imaging (CFI), and spectral Doppler modes. **c**, Spatial average temporal average intensity (I_{SATA}) derived from power (Supplementary Discussion 11). The black dashed line represents I_{SATA} of GE Corometrics 250CX fetal heart rate monitors[18]. Error bars in **b** and **c** show ±standard deviation (n = 4).

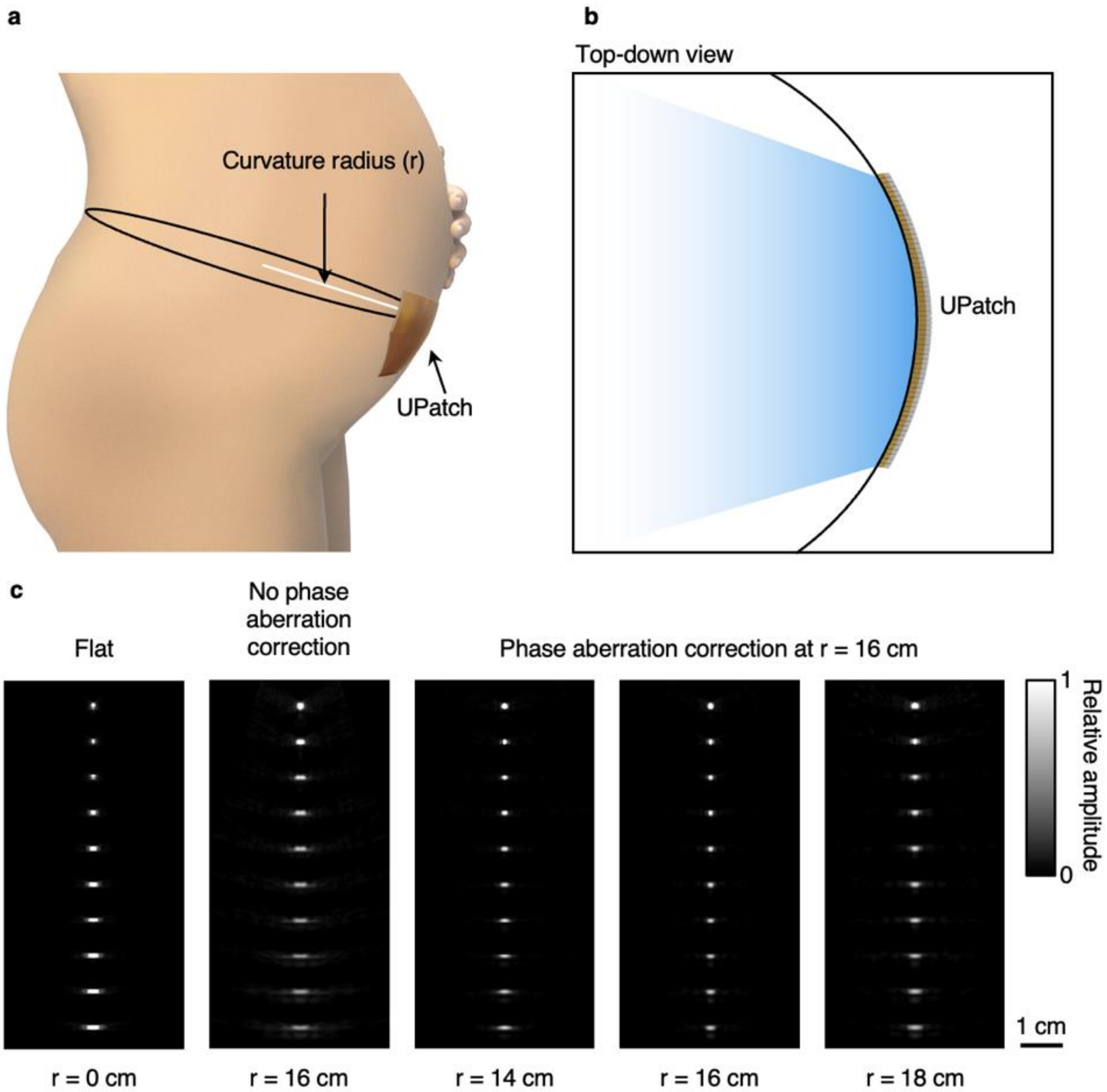

Supplementary Fig. 26 | Deformation of the UPatch. a, Schematics of the UPatch on the maternal abdomen. **b**, Top-down view of the UPatch on the maternal abdomen. **c**, Simulation results of the image quality. The maternal abdominal curvatures can induce phase aberration and affect the image quality of the UPatch. To address this, the phase aberration was corrected at a curvature radius of 16 cm, which encompasses the typical curvature radii from 14 cm to 18 cm in the third trimester[126,127]. The phase aberration correction improved the image quality within this curvature range. Simulations were performed with the Matlab Field II toolbox. The images share the same scale bar.

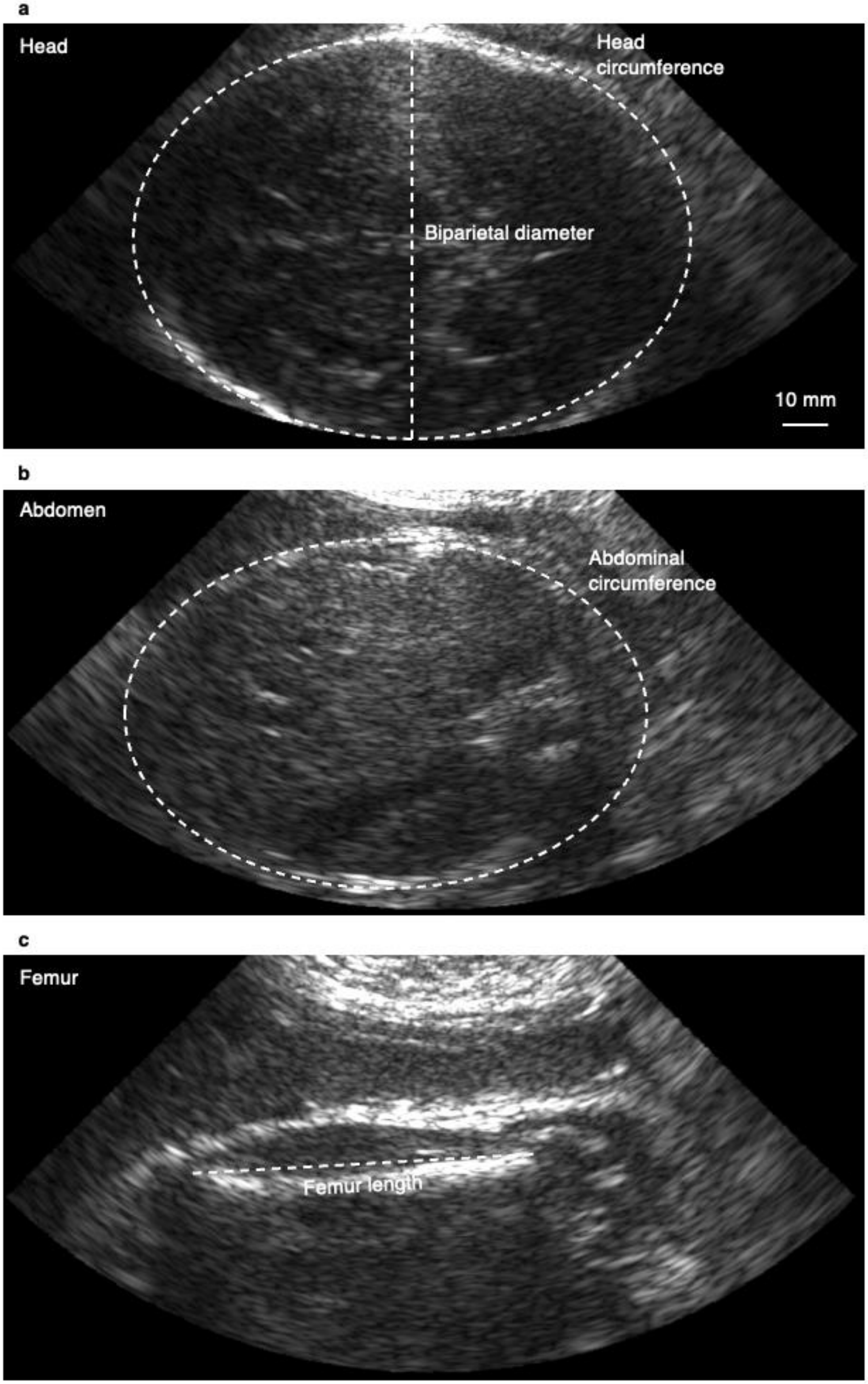
a
Head
Head circumference
Biparietal diameter
10 mm
b
Abdomen
Abdominal circumference
c
Femur
Femur length

Supplementary Fig. 27 | Fetal biometry. Brightness-mode images of a fetal **a**, head, **b**, abdomen, and **c**, femur. All images share the same scale bar. Biparietal diameter, head circumference, abdominal circumference, and femur length can be measured to calculate the estimated fetal weight using the Hadlock IV formula[167]. For this particular fetus, its weight is calculated to be 3.56 kg using the UPatch and 3.54 kg using the clinical device.

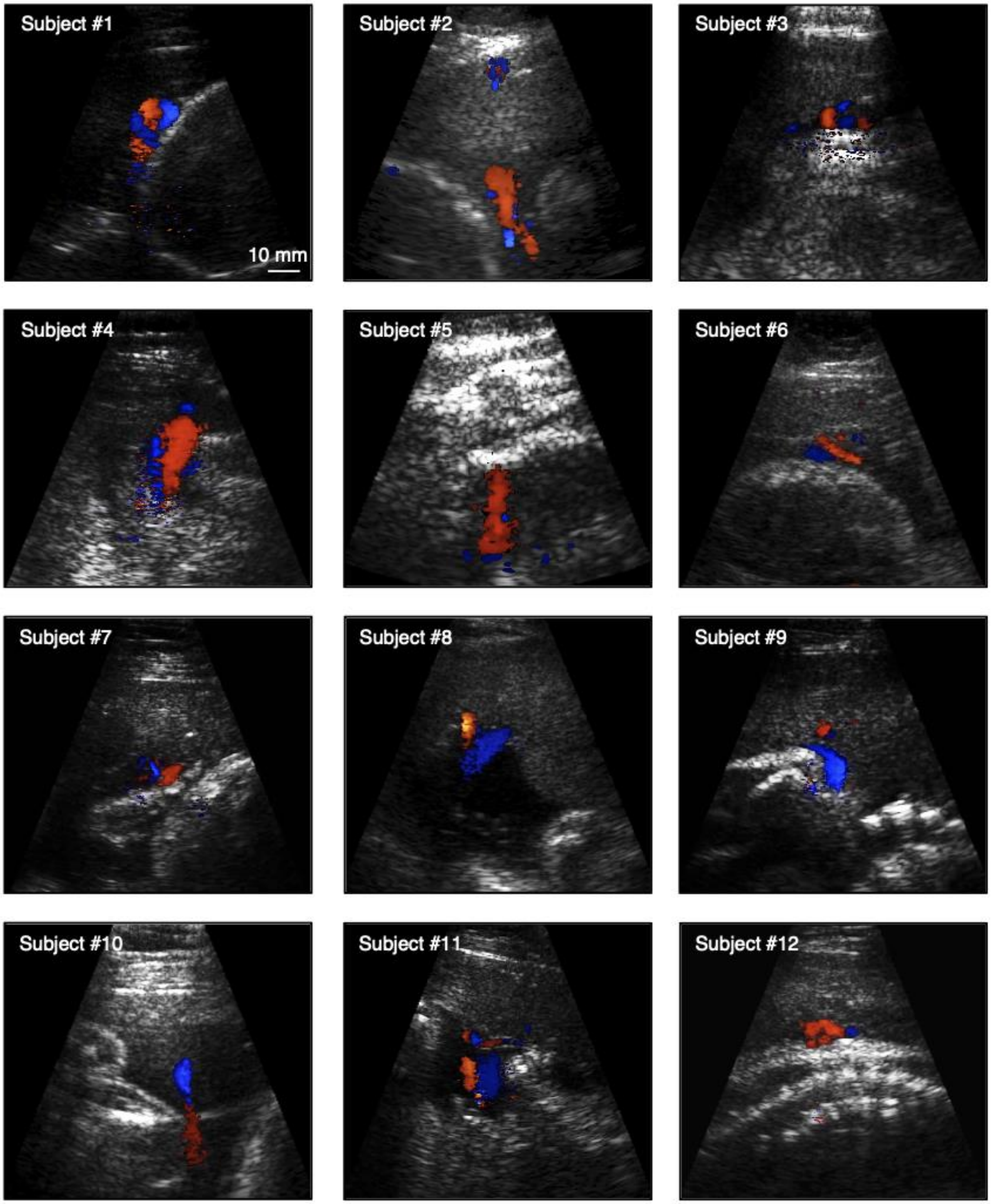

Supplementary Fig. 28 | Duplex images of the umbilical cord on the first 12 participants. The UPatch can visualize the umbilical cord, including both the umbilical artery and vein, in pregnant participants of a diverse demographic range. All images were acquired by a sonographer specializing in fetal ultrasonography. All images share the same scale bar.

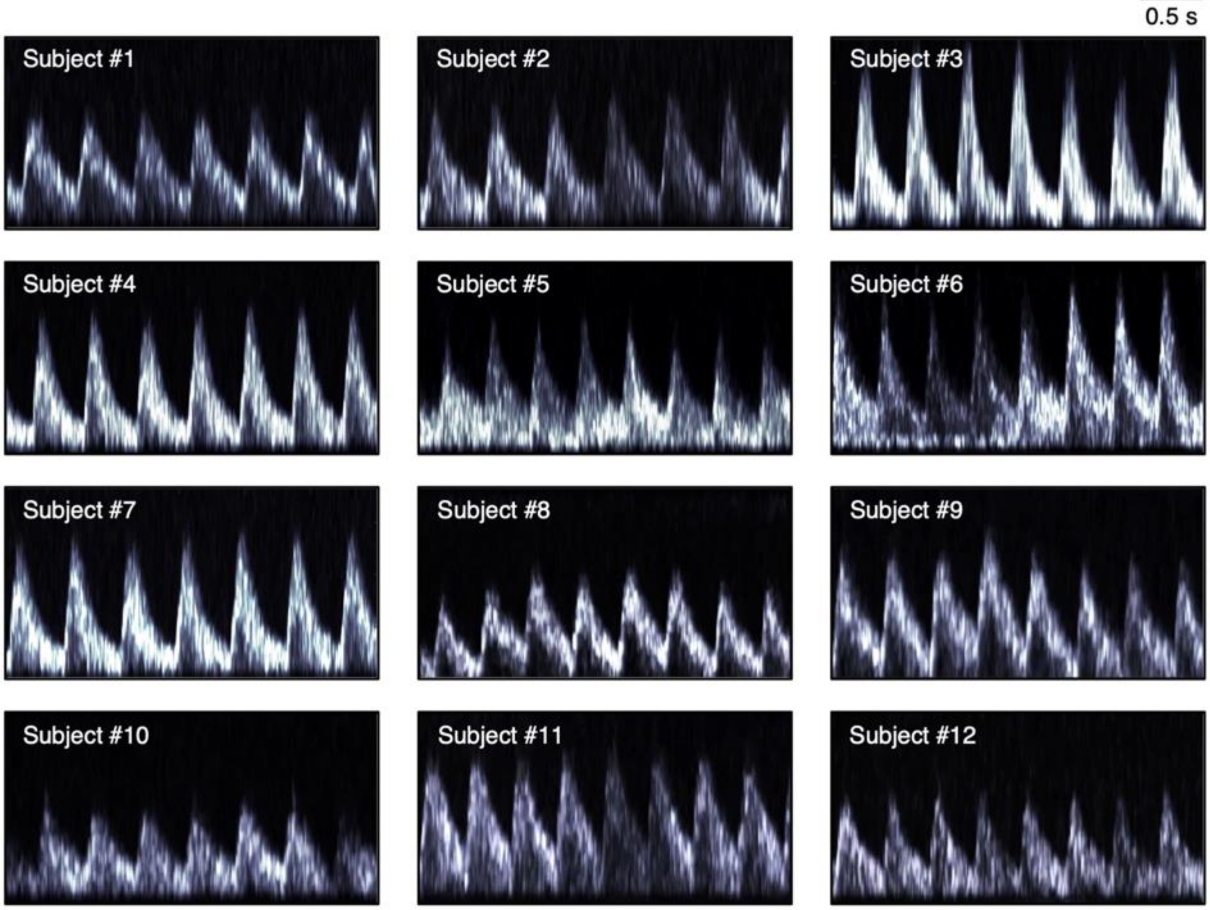

Supplementary Fig. 29 | Spectral Doppler of the umbilical artery on the first 12 participants. The UPatch can acquire spectral Doppler signals from the umbilical artery from pregnant participants of a diverse demographic range. All signals were acquired by a sonographer specializing in fetal ultrasonography. All images share the same scale bars.

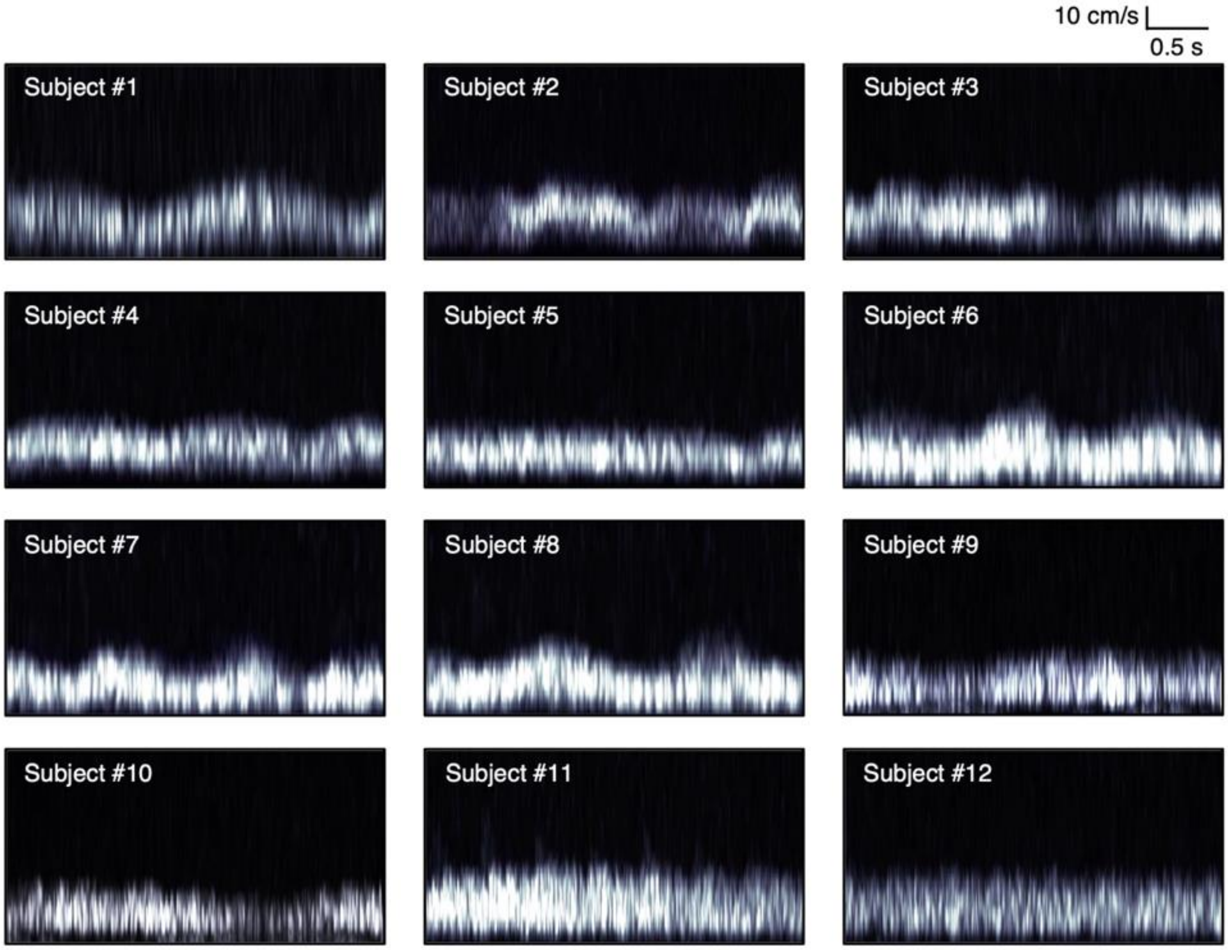

Supplementary Fig. 30 | Spectral Doppler of the umbilical vein on the first 12 participants. The UPatch can acquire spectral Doppler signals from the umbilical vein from pregnant participants of a diverse demographic range. All signals were acquired by a sonographer specializing in fetal ultrasonography. All images share the same scale bars.

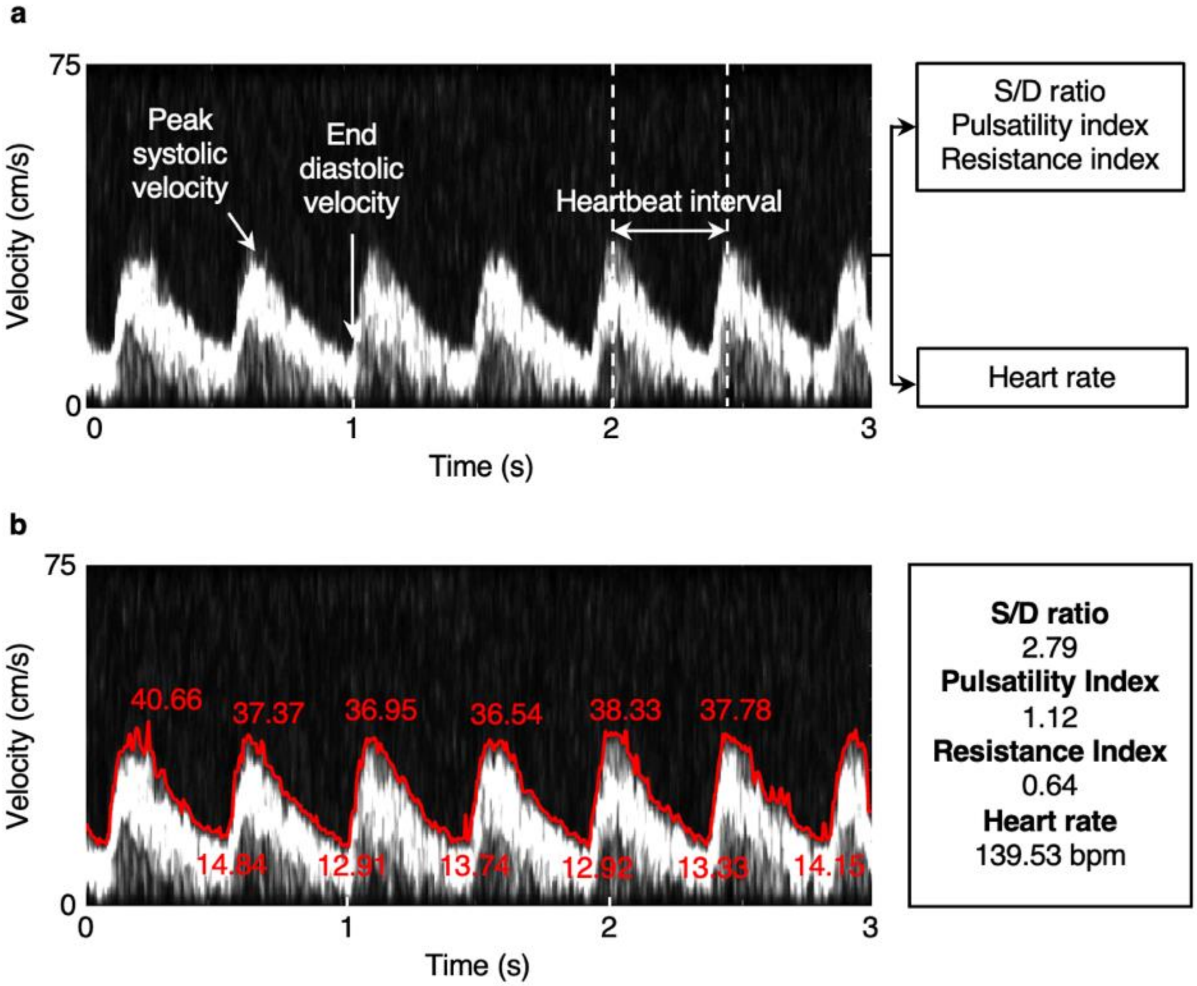

Supplementary Fig. 31 | Envelope extraction from spectral Doppler signals. a, Spectral Doppler signals from the fetal umbilical artery. Peak systolic velocity, end diastolic velocity, and heartbeat intervals can be manually identified and used to derive the systolic-to-diastolic (S/D) ratio, pulsatility index, resistance index, and heart rate. **b**, The envelope extraction algorithm we developed in this study allows automated derivation of these parameters[102].

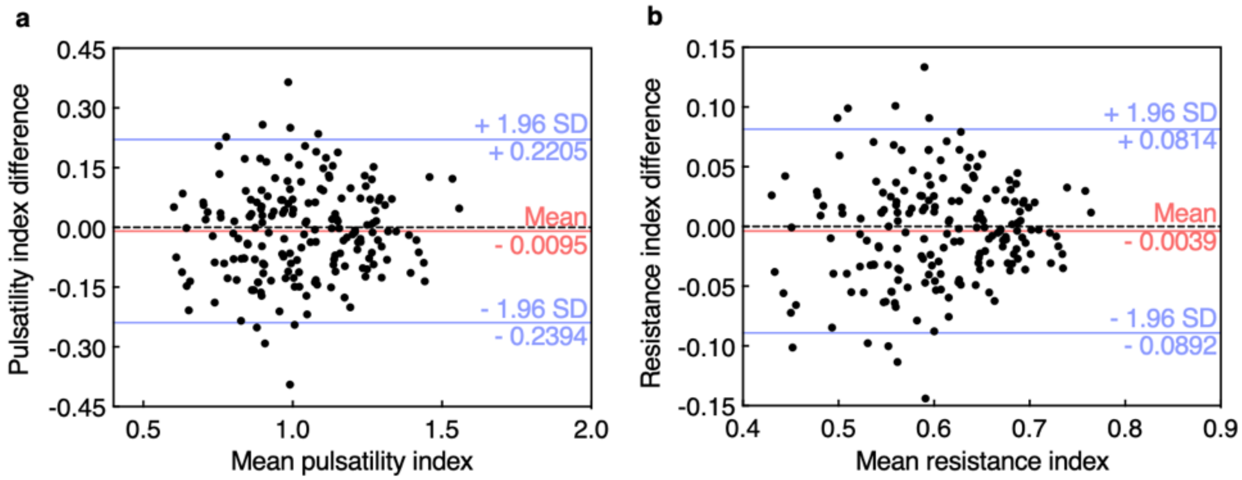

Supplementary Fig. 32 | Statistical analysis of the pulsatility index and the resistance index. Bland-Altman plots of **a**, the pulsatility index and **b**, the resistance index measured using the UPatch and a handheld clinical ultrasound device (Voluson E10, GE). Solid red lines are the mean differences between the two devices, solid blue lines are 95% limits of agreement (1.96 standard deviations above and below the mean differences), and black dashed lines are the zero difference between the two devices. Each plot has three measurement pairs by repeating three times with the same devices on the same participant for each of the 62 participants.

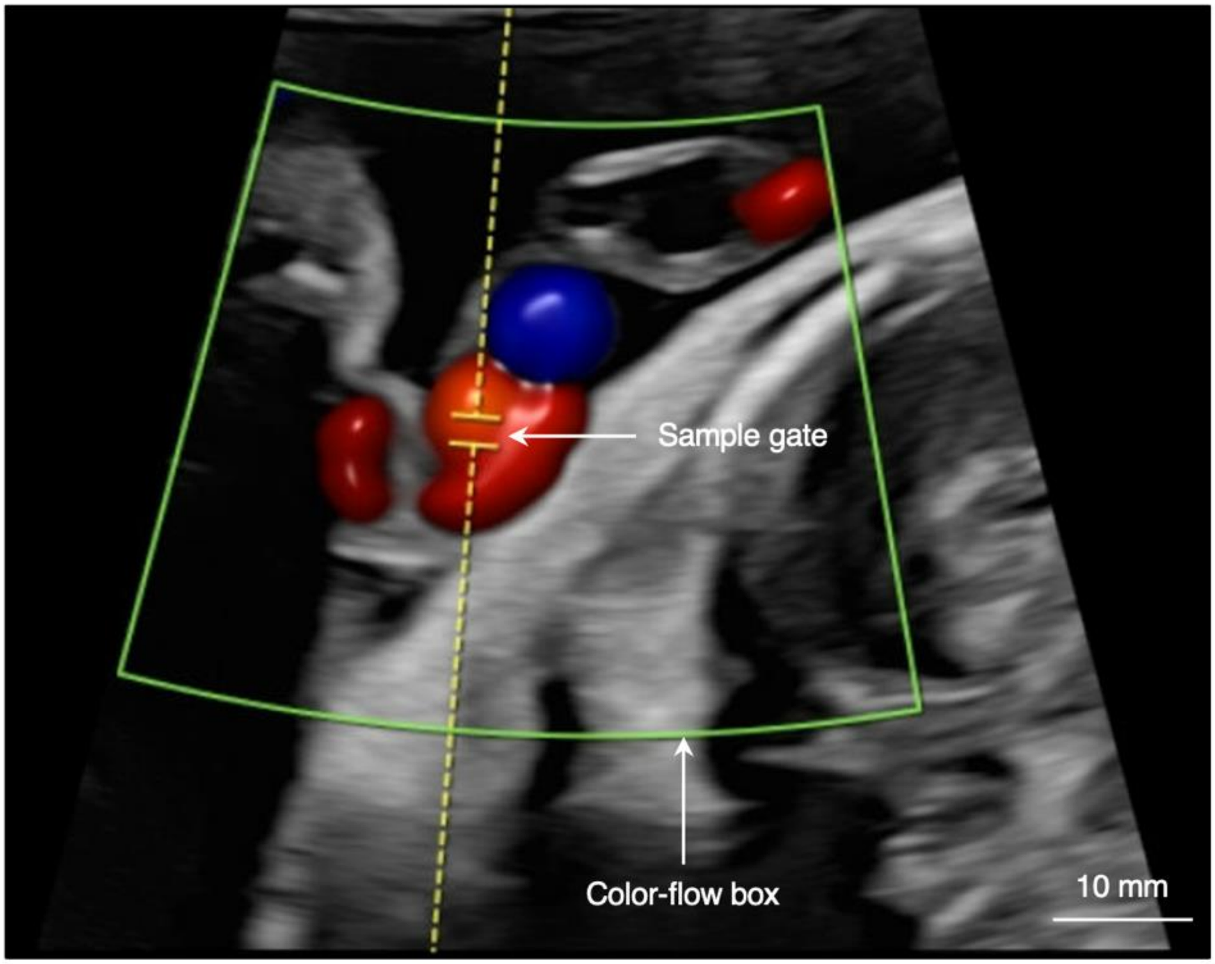

Supplementary Fig. 33 | Imaging with a handheld clinical ultrasound device. Duplex imaging of the umbilical cord with a handheld clinical ultrasound device (GE Voluson E10) requires maneuvering by a sonographer. First, a color-flow box (green) is manually moved to find the color-flow signals from the umbilical cord. Then, a sample gate (yellow) is chosen inside the color-flow box for spectral Doppler recording.

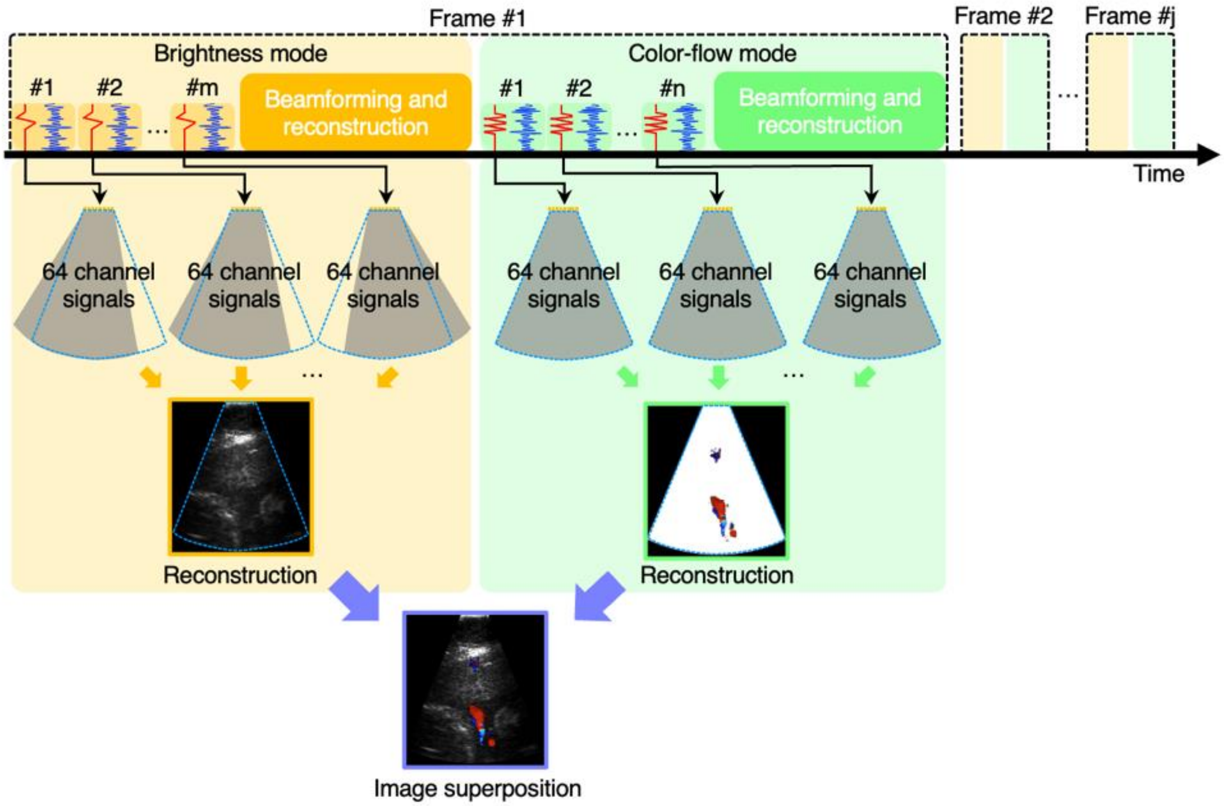

Supplementary Fig. 34 | Data acquisition processes of the UPatch. The UPatch requires a complex beamforming process to synthesize an image from 64 channels. Reconstructing a brightness-mode image requires compounding radiofrequency signals from multiple steered beams. Reconstructing a color-flow image requires estimating the mean frequency across multiple transmitted and received beams. These two images are overlaid to form a duplex image.

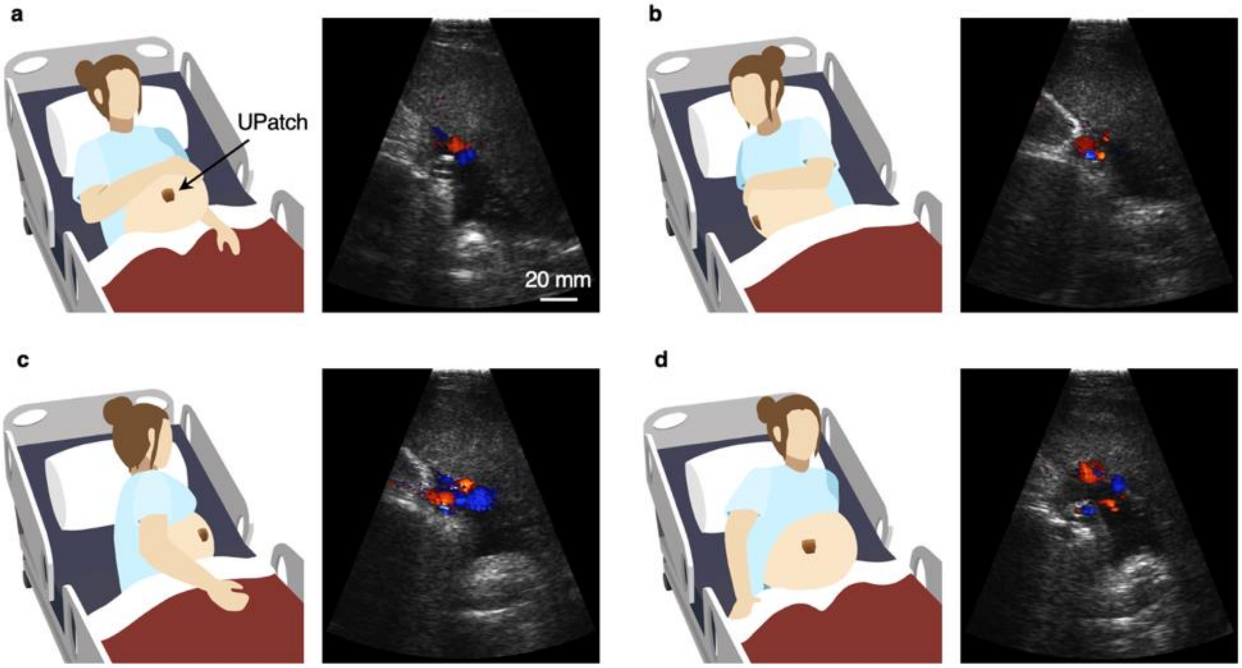

Supplementary Fig. 35 | Duplex imaging of the UPatch across various maternal positions. When positioned to insonate the umbilical cord at the placental cord insertion site, the UPatch maintains reliable signal acquisition during four common postures: **a**, lying supine, **b**, lying on the right side, **c**, lying on the left side, and **d**, sitting upright. The images share the same scale bar.

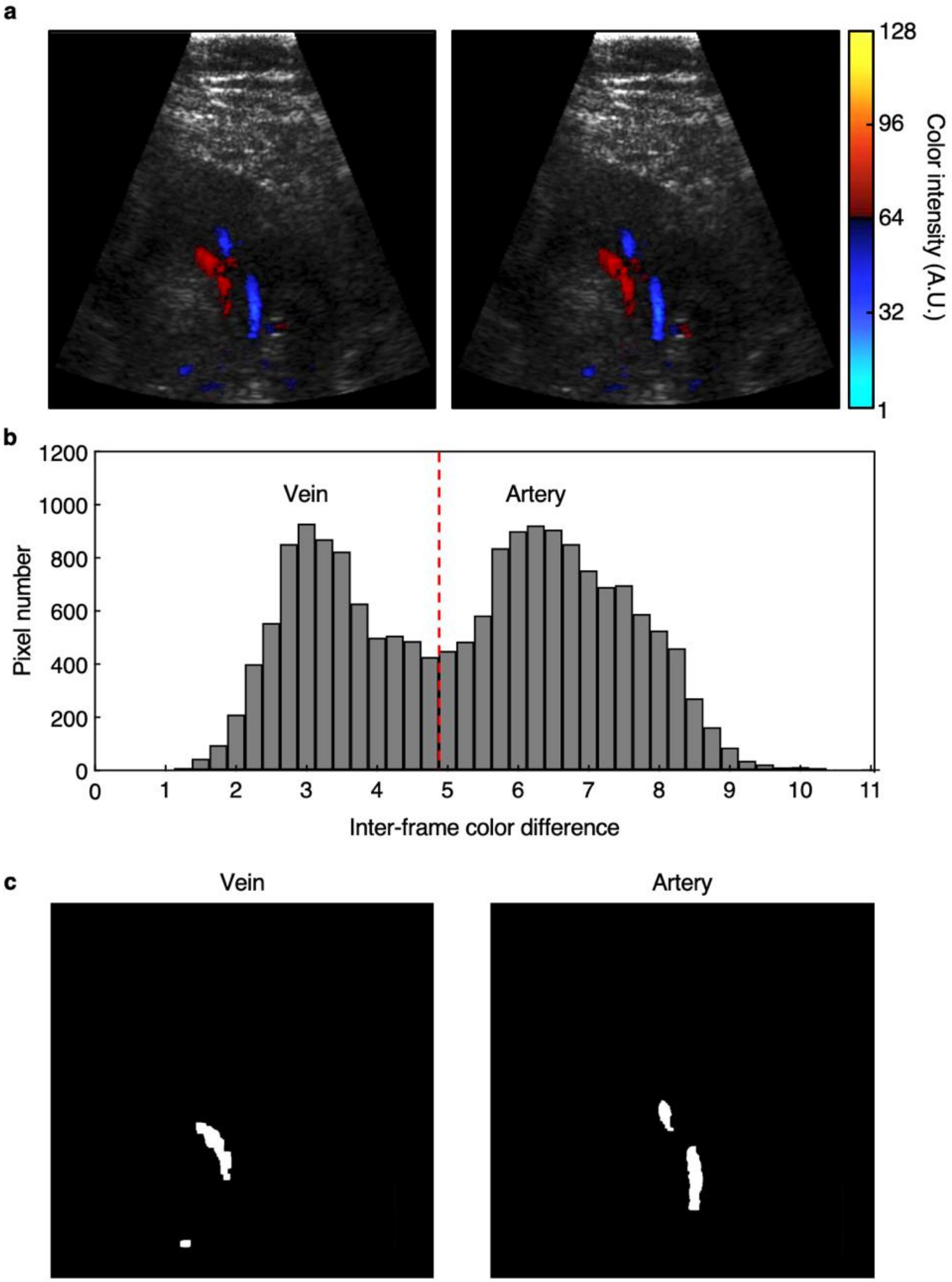
a
128
96
64
32
1
Color intensity (A.U.)
b
Vein
Artery
Pixel number
0
200
400
600
800
1000
1200
0
1
2
3
4
5
6
7
8
9
10
11
Inter-frame color difference
c
Vein
Artery

Supplementary Fig. 36 | Segmentation of the umbilical vessels. **a**, Two consecutive duplex imaging frames showing color Doppler signals in the umbilical vessel region. The images share the same color bar. **b**, Histogram of inter-frame color differences, which is the change in pixel color intensity values between consecutive frames, reflecting temporal fluctuations in blood flow velocity. Due to differences in pulsatility, the artery and vein exhibit distinct inter-frame color differences. The dashed line at 4.875 indicates the threshold value used to differentiate arterial and venous pixels in this study. **c**, Binary segmentation maps of the vein (left) and artery (right), generated by applying the threshold in **b**. The color (cool or warm hues) of the vessel in the image does not affect classification of artery or vein because the algorithm measures the change in color intensity between consecutive frames, not the absolute color.

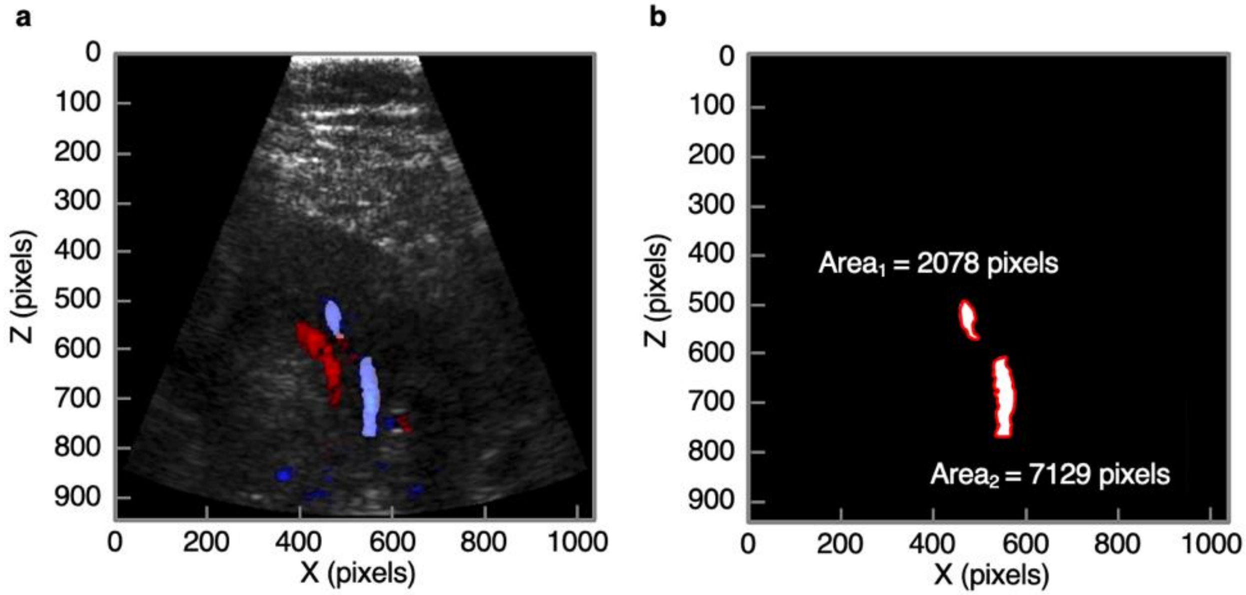

Supplementary Fig. 37 | Recognition of the primary region of the umbilical artery. a, Duplex image with assigned pixel coordinates in the XZ plane for vessel localization. **b**, Number of pixels for each segmented arterial region. The region with the largest area (Area$_2$ in this case) was designated as the primary region.

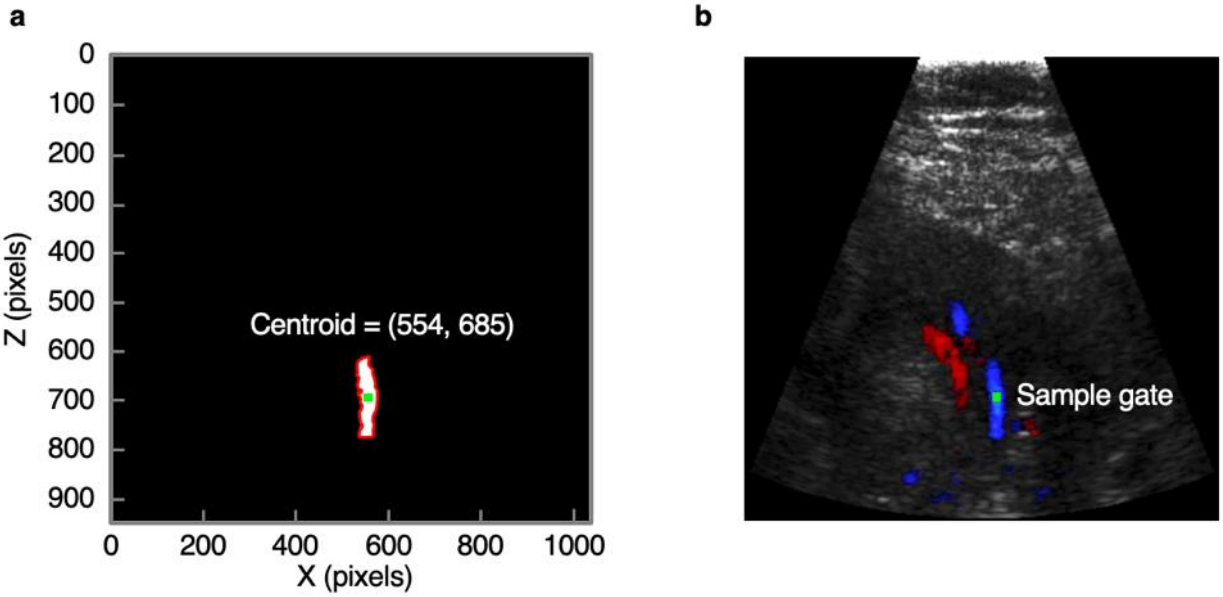

Supplementary Fig. 38 | Identification of the centroid for sample gate placement. a, Centroid calculation of the segmented primary arterial region. The centroid was computed using the geometric center of the pixel distribution. **b**, The sample gate was placed at the calculated centroid position within the duplex image. The color of the artery in the duplex image, whether toward (warm hue) or away from (cool hue) the UPatch, does not affect the centroid placement.

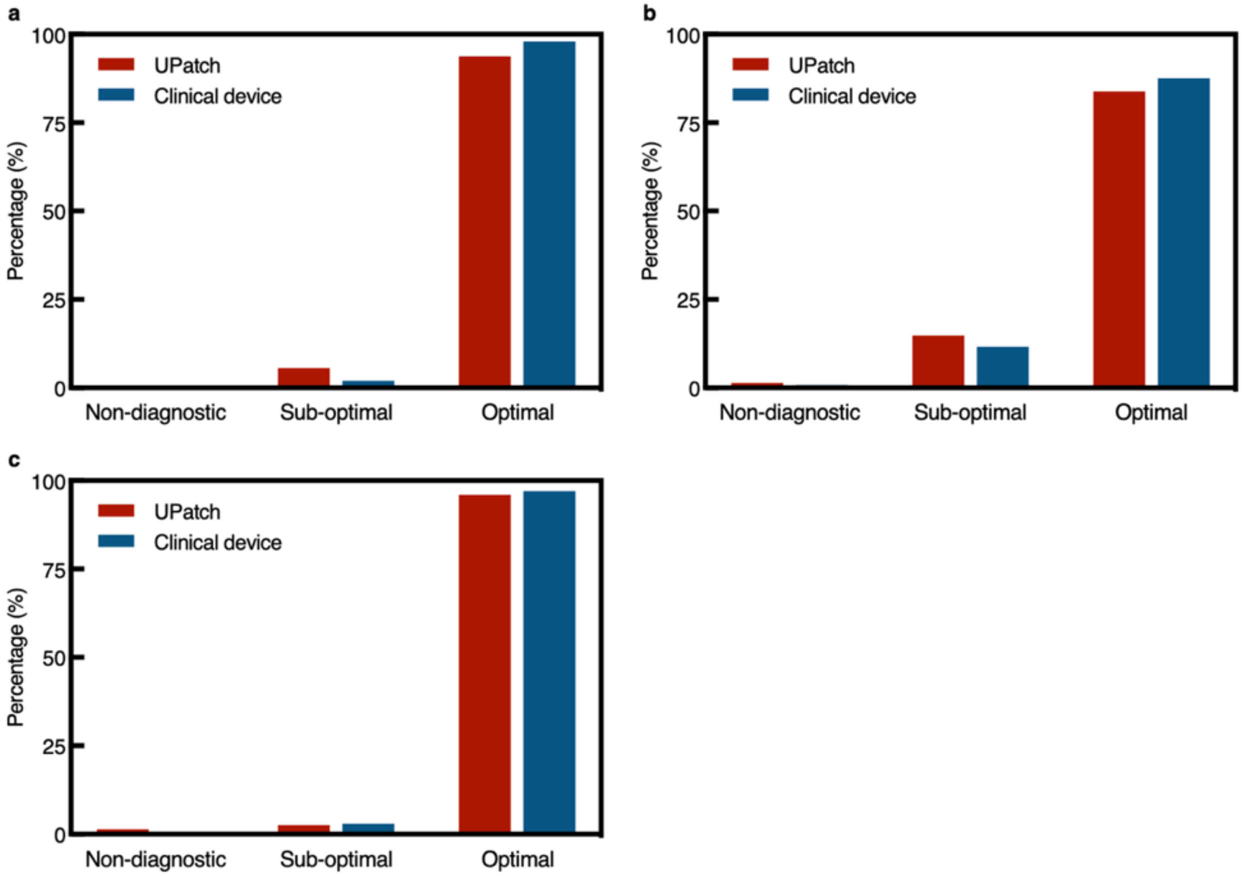

Supplementary Fig. 39 | Sonographer evaluation of the tracking algorithm. Validation by **a**, a sonographer with 30 years, **b**, a sonographer with 8 years, and **c**, a sonographer with 20 years of fetal ultrasonography experience. The tracking algorithm was used to register the sample gate of the umbilical artery in frames collected using a clinical device (Voluson E10, GE) and the UPatch. The sonographers evaluated as "Optimal" for sample gates that are suitable for acquiring spectral Doppler signals, "Sub-optimal" for sample gates that may yield spectral Doppler signals of low quality, and "Non-diagnostic" for sample gates that are incapable of providing any spectral Doppler signals. These results demonstrate that the tracking algorithm achieves comparable performance when applied to both the UPatch and the clinical device.

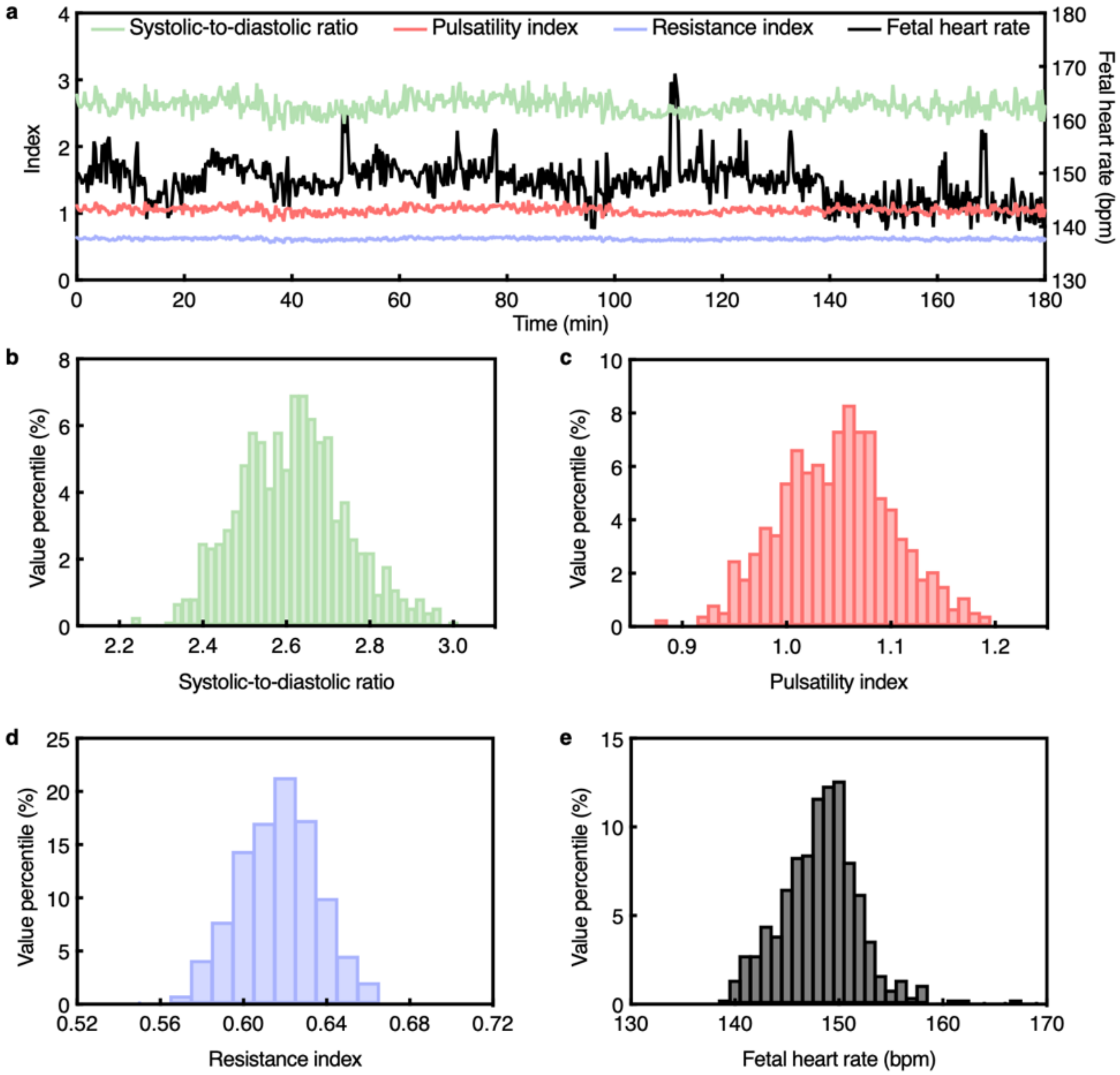

Supplementary Fig. 40 | Continuous fetal monitoring using the UPatch in Participant #1. a, Time series data from the 3-h continuous monitoring session. Systolic-to-diastolic ratio, pulsatility index, and resistance index are plotted on the left y-axis, and fetal heart rate is plotted on the right y-axis. Histograms of **b**, systolic-to-diastolic ratio, **c**, pulsatility index, **d**, resistance index, and **e**, fetal heart rate over the recording period.

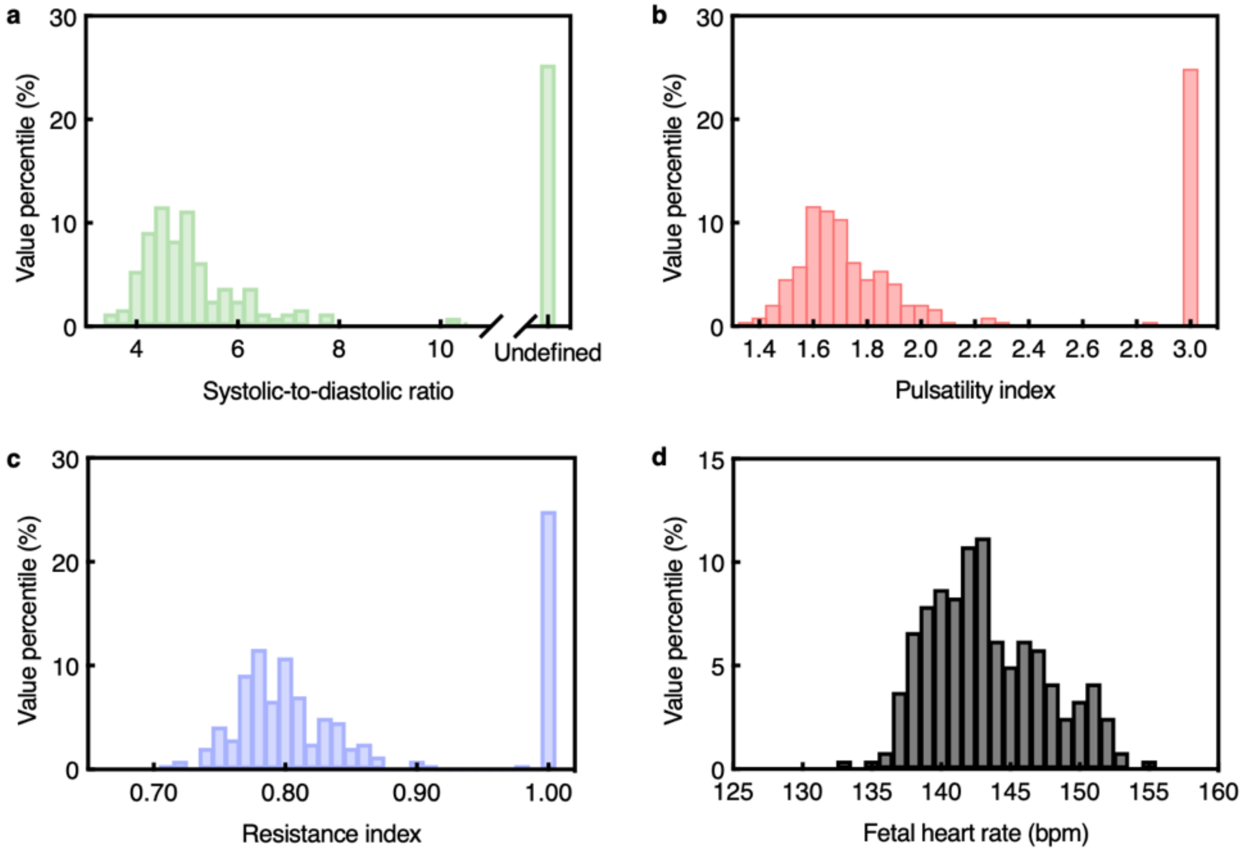

Supplementary Fig. 41 | Continuous fetal monitoring using the UPatch in Participant #2. Histograms of **a**, systolic-to-diastolic ratio, **b**, pulsatility index, **c**, resistance index, and **d**, fetal heart rate over the recording period. The time series data is in Fig. 4d in the main text. The systolic-to-diastolic ratio was not plotted in the time series due to the presence of undefined values.

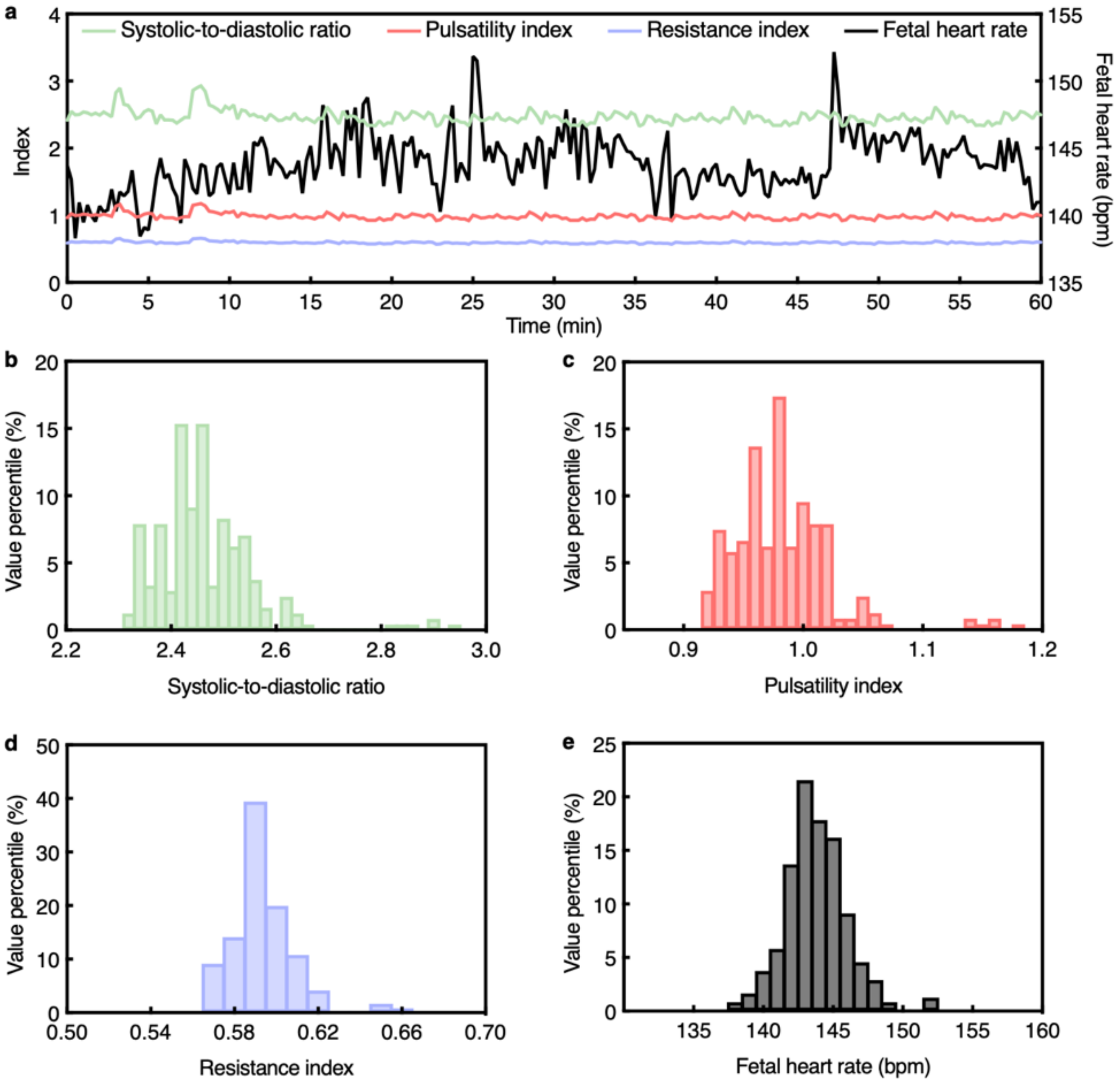

Supplementary Fig. 42 | Continuous fetal monitoring using the UPatch in Participant #3. a, Time series data from the 1-h continuous monitoring session. Systolic-to-diastolic ratio, pulsatility index, and resistance index are plotted on the left y-axis, and fetal heart rate is plotted on the right y-axis. Histograms of **b**, systolic-to-diastolic ratio, **c**, pulsatility index, **d**, resistance index, and **e**, fetal heart rate over the recording period.

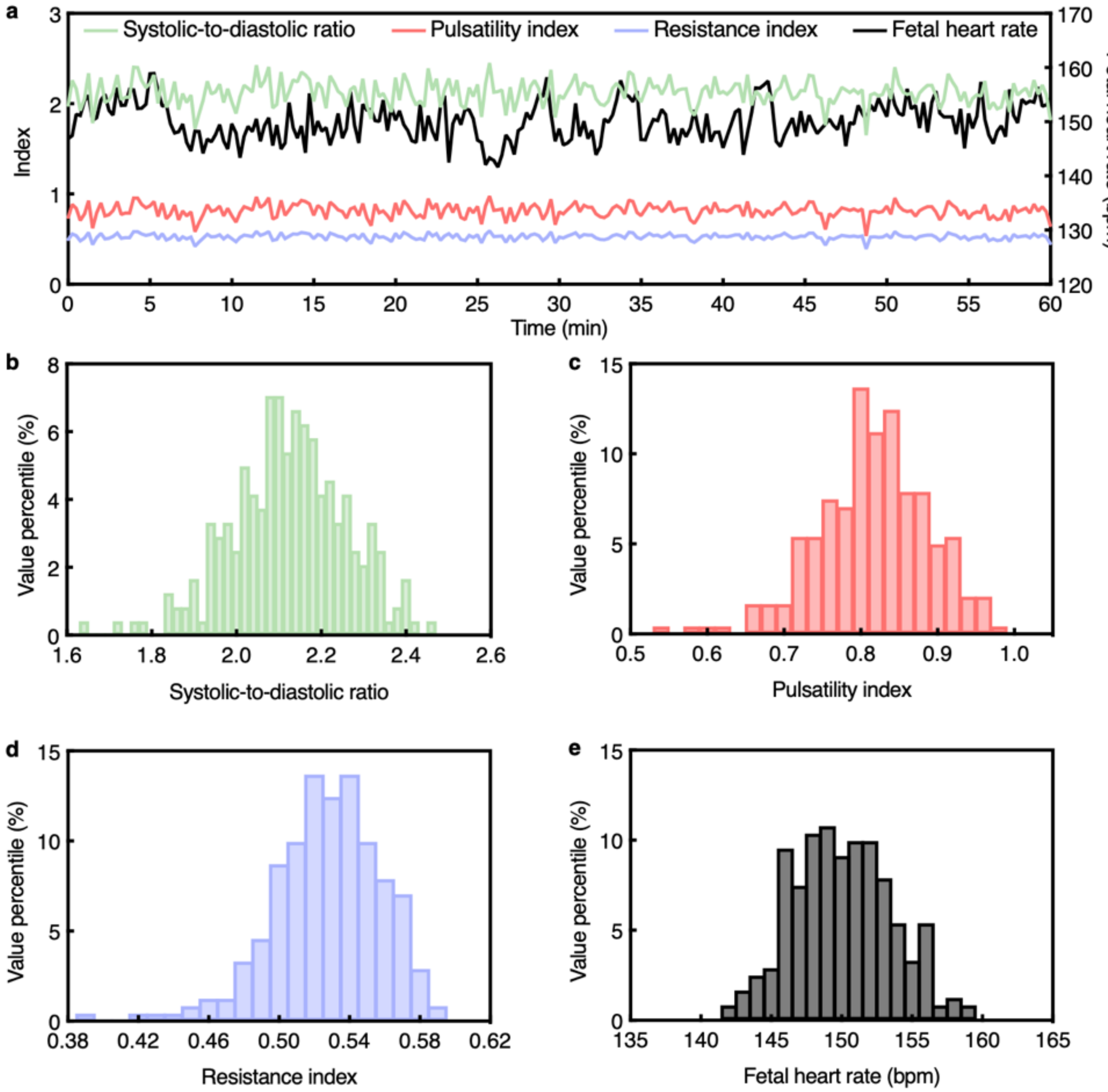

Supplementary Fig. 43 | Continuous fetal monitoring using the UPatch in Participant #4. a, Time series data from the 1-h continuous monitoring session. Systolic-to-diastolic ratio, pulsatility index, and resistance index are plotted on the left y-axis, and fetal heart rate is plotted on the right y-axis. Histograms of **b**, systolic-to-diastolic ratio, **c**, pulsatility index, **d**, resistance index, and **e**, fetal heart rate over the recording period.

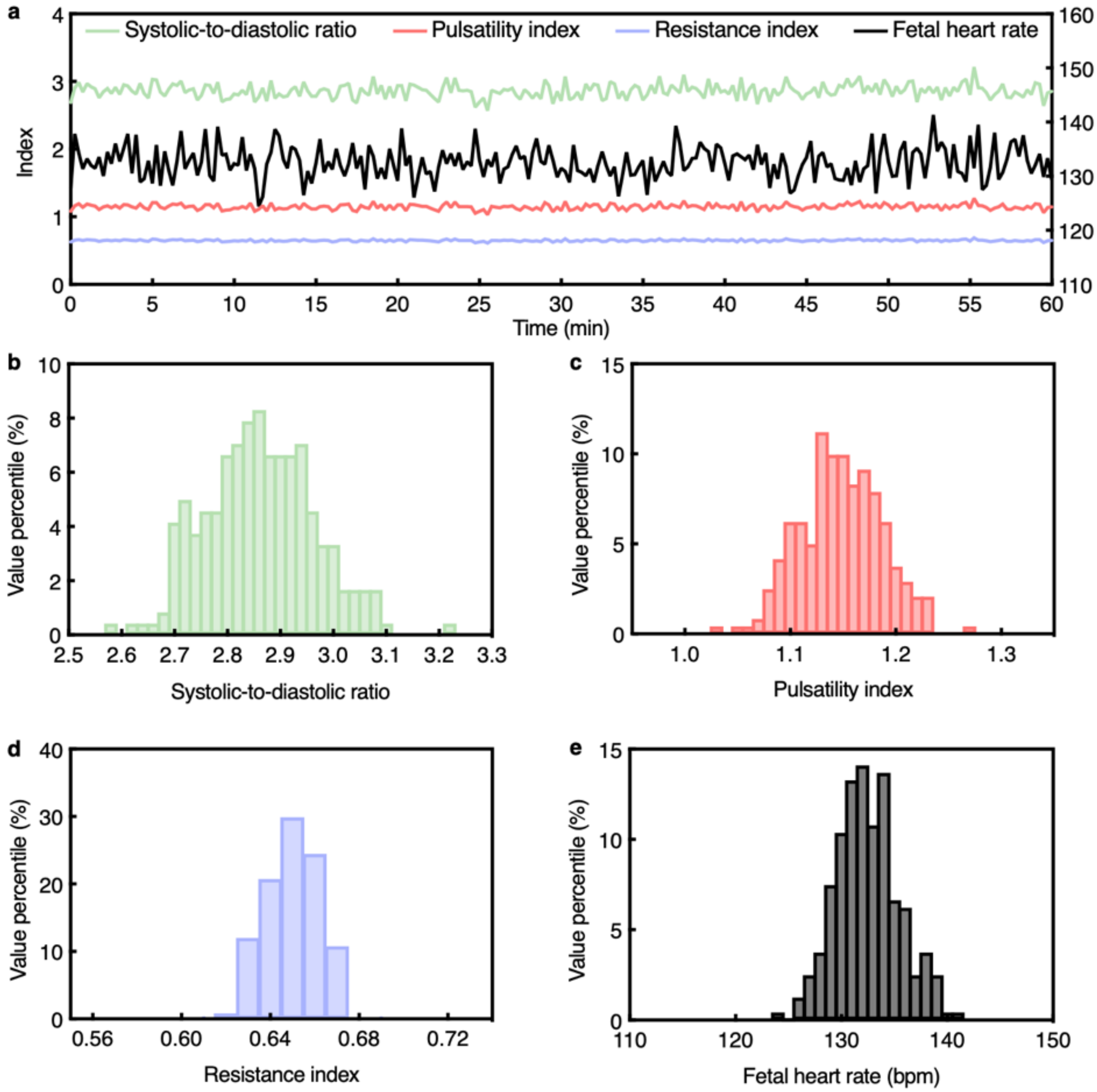

Supplementary Fig. 44 | Continuous fetal monitoring using the UPatch in Participant #5. a, Time series data from the 1-h continuous monitoring session. Systolic-to-diastolic ratio, pulsatility index, and resistance index are plotted on the left y-axis, and fetal heart rate is plotted on the right y-axis. Histograms of **b**, systolic-to-diastolic ratio, **c**, pulsatility index, **d**, resistance index, and **e**, fetal heart rate over the recording period.

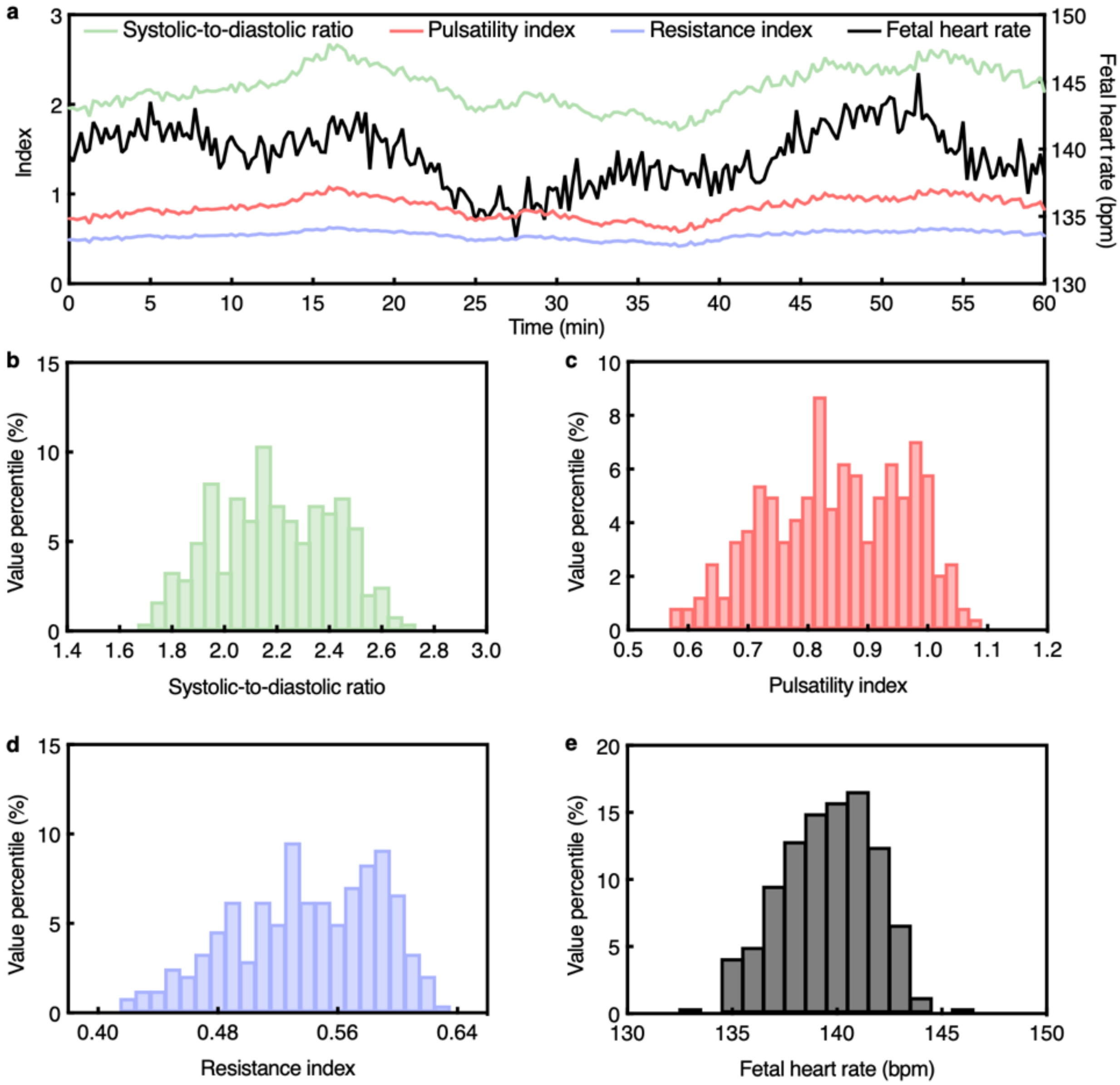

Supplementary Fig. 45 | Continuous fetal monitoring using the UPatch in Participant #6. a, Time series data from the 1-h continuous monitoring session. Systolic-to-diastolic ratio, pulsatility index, and resistance index are plotted on the left y-axis, and fetal heart rate is plotted on the right y-axis. Histograms of **b**, systolic-to-diastolic ratio, **c**, pulsatility index, **d**, resistance index, and **e**, fetal heart rate over the recording period.

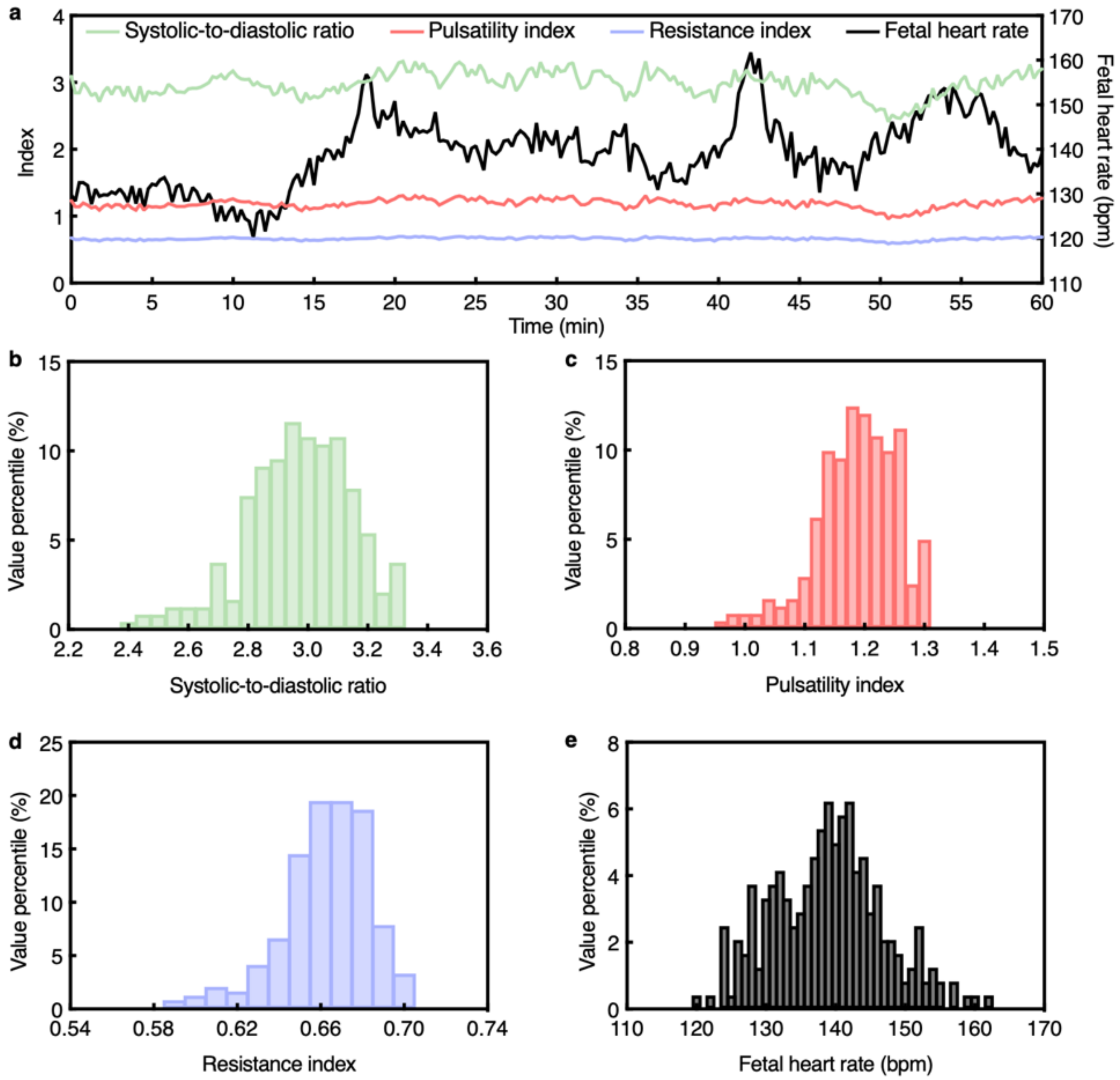

Supplementary Fig. 46 | Continuous fetal monitoring using the UPatch in Participant #7. a, Time series data from the 1-h continuous monitoring session. Systolic-to-diastolic ratio, pulsatility index, and resistance index are plotted on the left y-axis, and fetal heart rate is plotted on the right y-axis. Histograms of **b**, systolic-to-diastolic ratio, **c**, pulsatility index, **d**, resistance index, and **e**, fetal heart rate over the recording period.

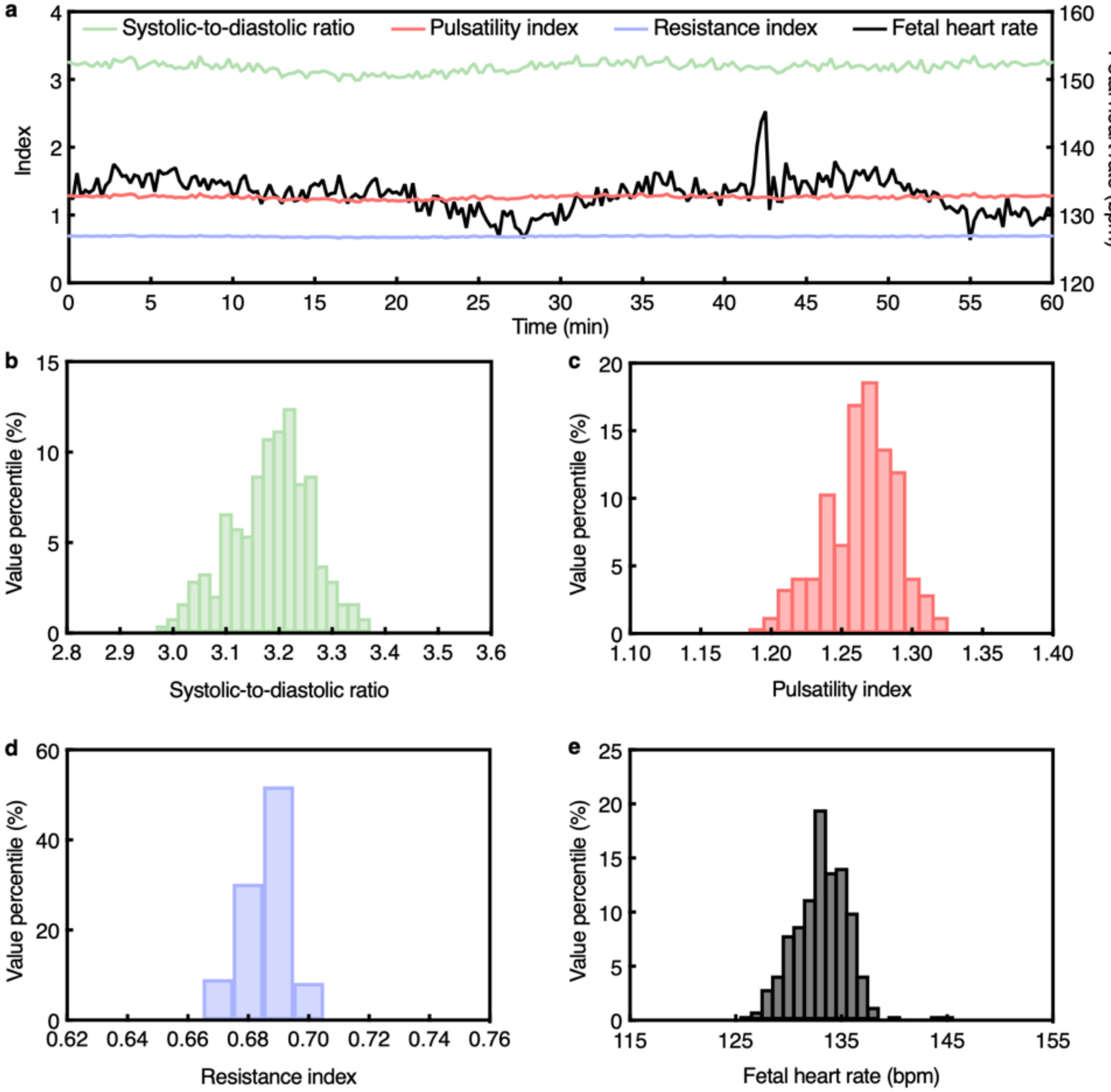

Supplementary Fig. 47 | Continuous fetal monitoring using the UPatch in Participant #8. a, Time series data from the 1-h continuous monitoring session. Systolic-to-diastolic ratio, pulsatility index, and resistance index are plotted on the left y-axis, and fetal heart rate is plotted on the right y-axis. Histograms of **b**, systolic-to-diastolic ratio, **c**, pulsatility index, **d**, resistance index, and **e**, fetal heart rate over the recording period.

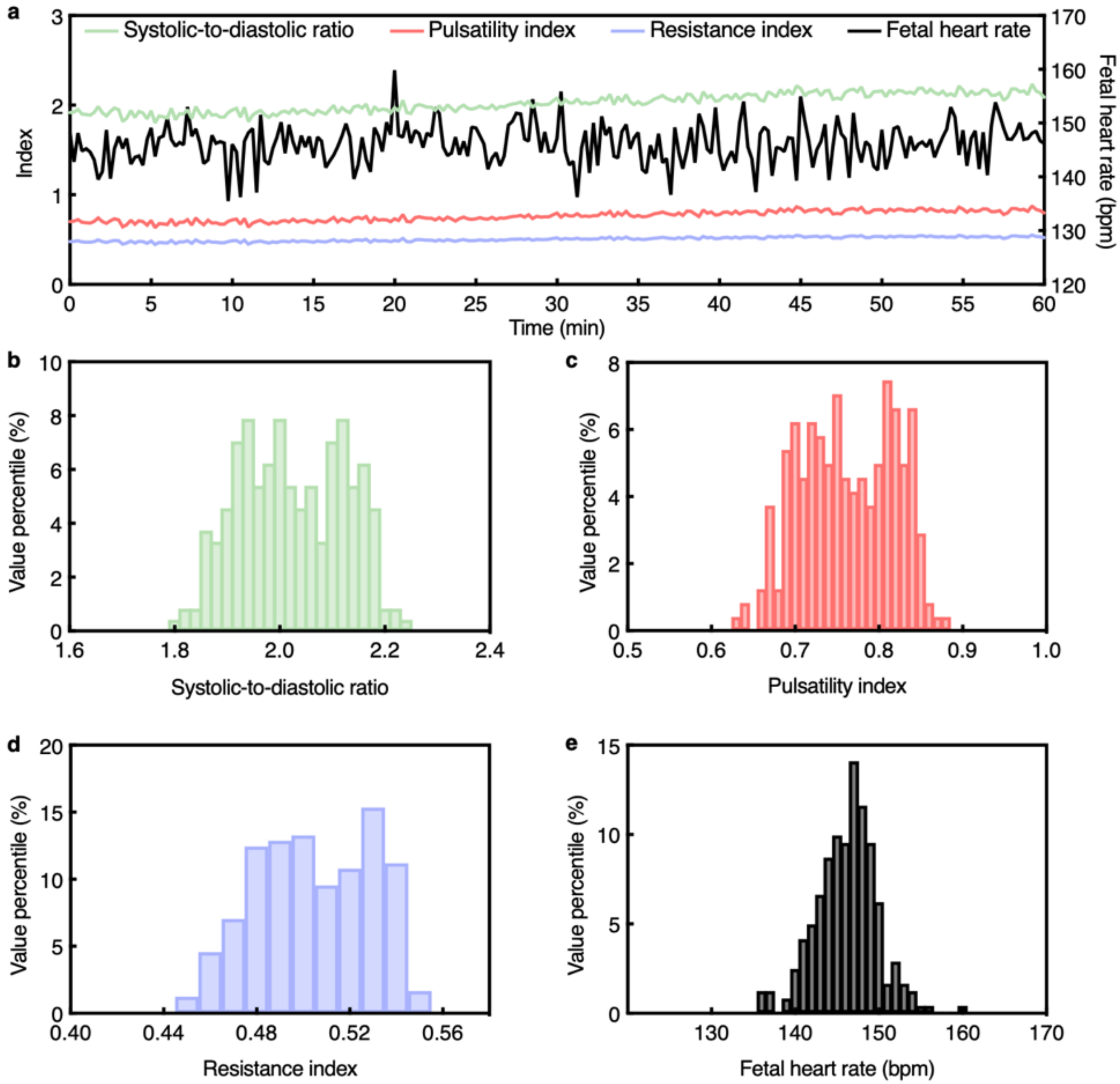

Supplementary Fig. 48 | Continuous fetal monitoring using the UPatch in Participant #9. a, Time series data from the 1-h continuous monitoring session. Systolic-to-diastolic ratio, pulsatility index, and resistance index are plotted on the left y-axis, and fetal heart rate is plotted on the right y-axis. Histograms of **b**, systolic-to-diastolic ratio, **c**, pulsatility index, **d**, resistance index, and **e**, fetal heart rate over the recording period.

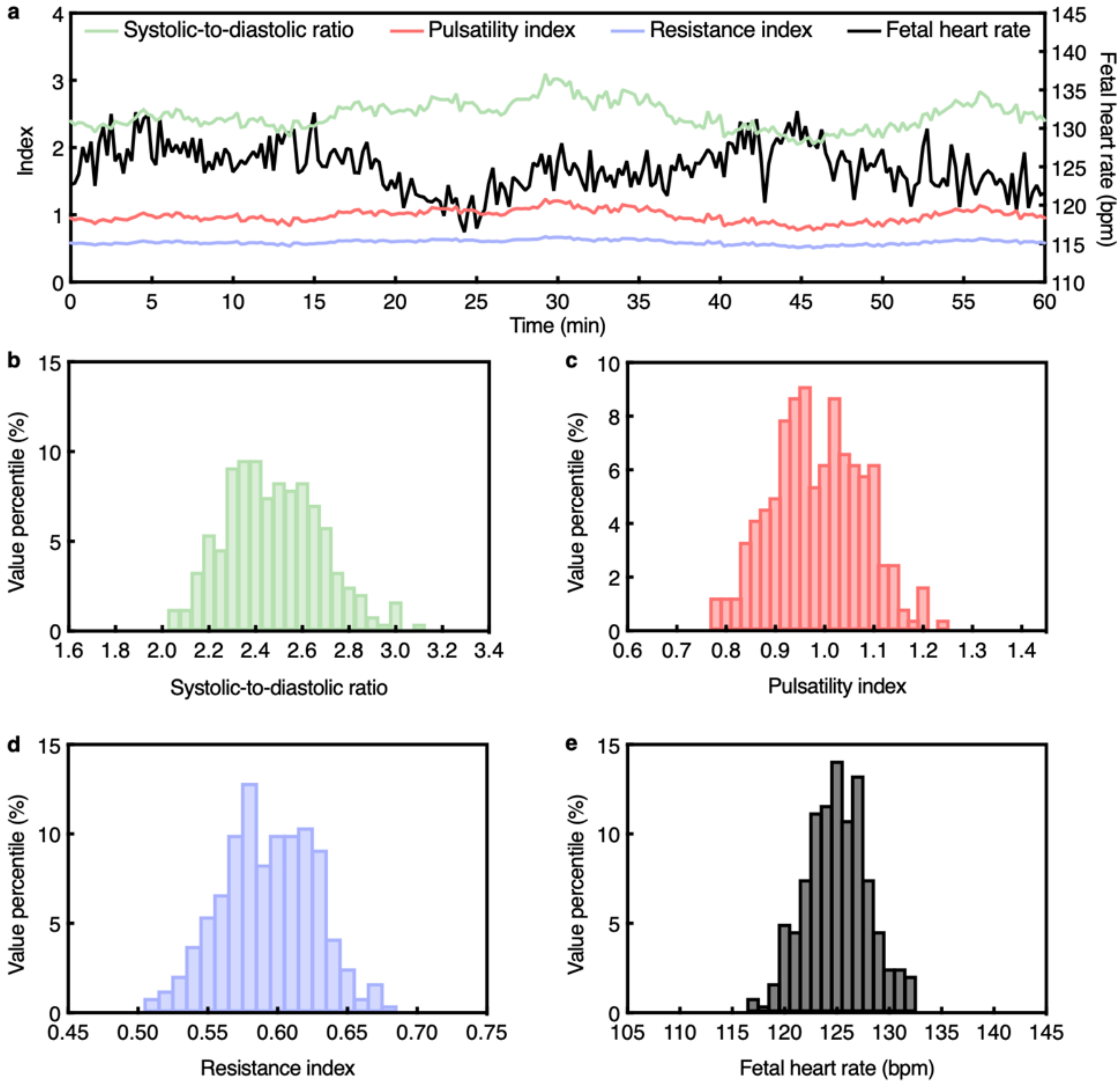

Supplementary Fig. 49 | Continuous fetal monitoring using the UPatch in Participant #10. a, Time series data from the 1-h continuous monitoring session. Systolic-to-diastolic ratio, pulsatility index, and resistance index are plotted on the left y-axis, and fetal heart rate is plotted on the right y-axis. Histograms of **b**, systolic-to-diastolic ratio, **c**, pulsatility index, **d**, resistance index, and **e**, fetal heart rate over the recording period.

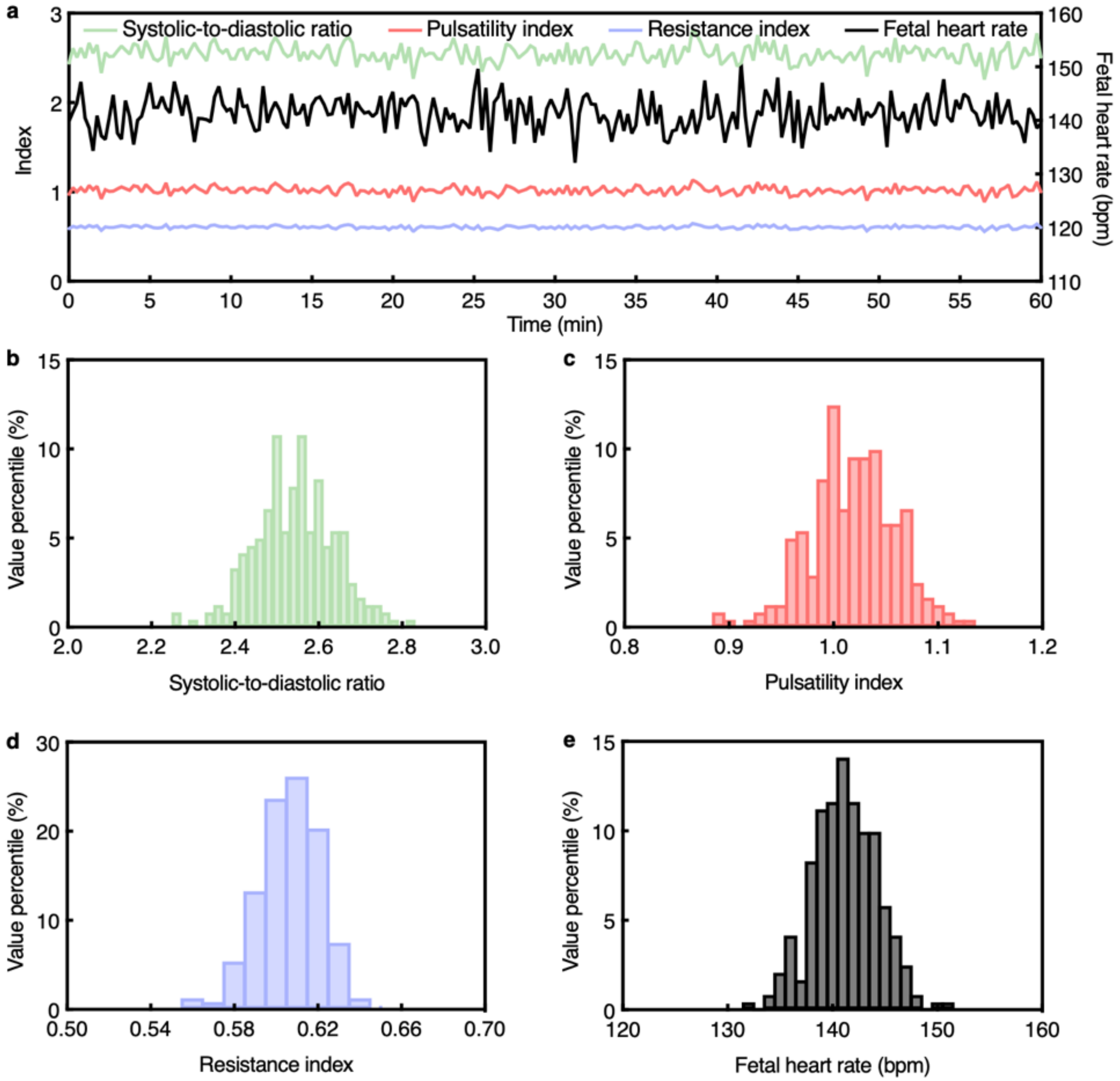

Supplementary Fig. 50 | Continuous fetal monitoring using the UPatch in Participant #11. a, Time series data from the 1-h continuous monitoring session. Systolic-to-diastolic ratio, pulsatility index, and resistance index are plotted on the left y-axis, and fetal heart rate is plotted on the right y-axis. Histograms of **b**, systolic-to-diastolic ratio, **c**, pulsatility index, **d**, resistance index, and **e**, fetal heart rate over the recording period.

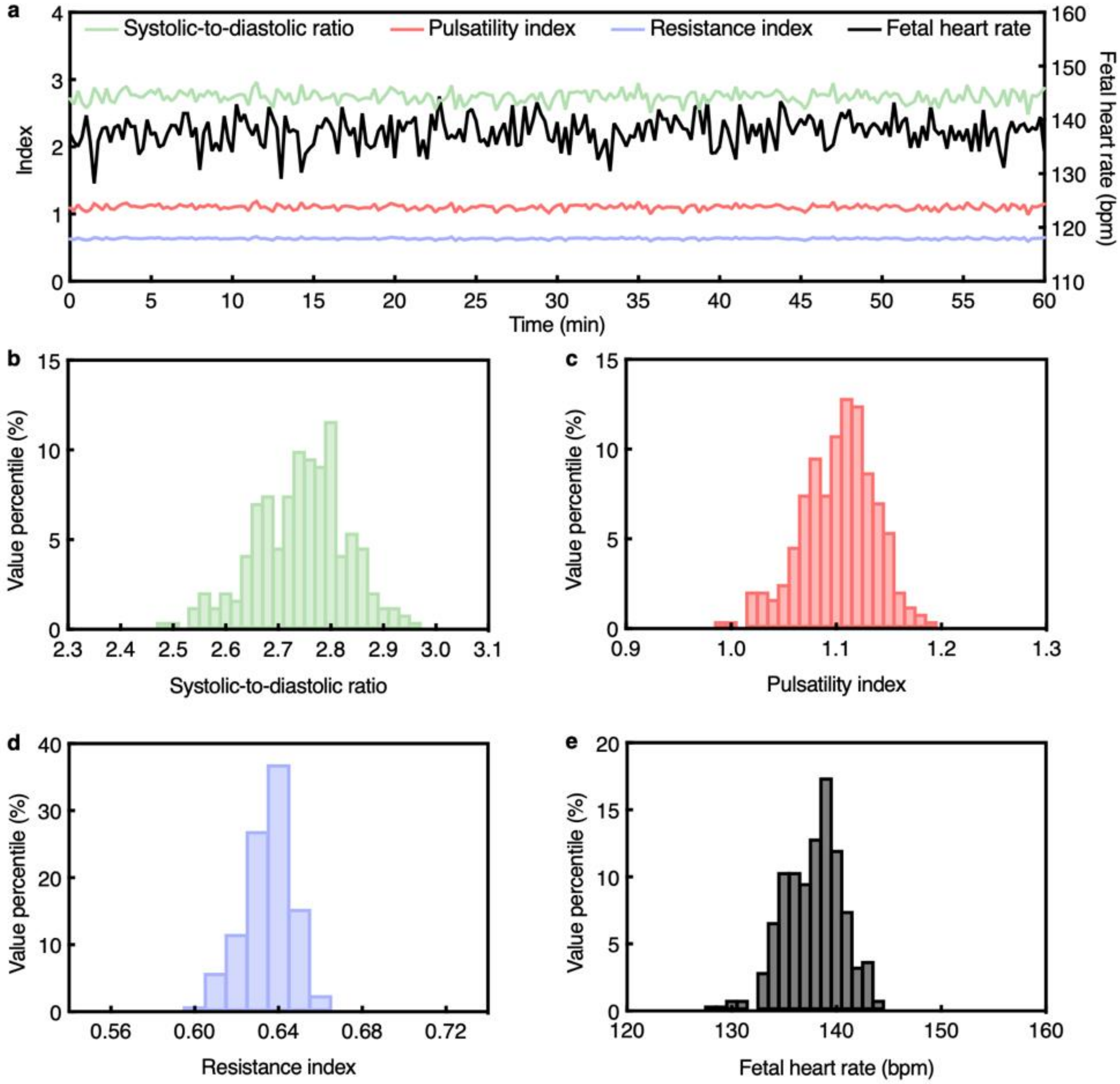

Supplementary Fig. 51 | Continuous fetal monitoring using the UPatch in Participant #12. a, Time series data from the 1-h continuous monitoring session. Systolic-to-diastolic ratio, pulsatility index, and resistance index are plotted on the left y-axis, and fetal heart rate is plotted on the right y-axis. Histograms of **b**, systolic-to-diastolic ratio, **c**, pulsatility index, **d**, resistance index, and **e**, fetal heart rate over the recording period.

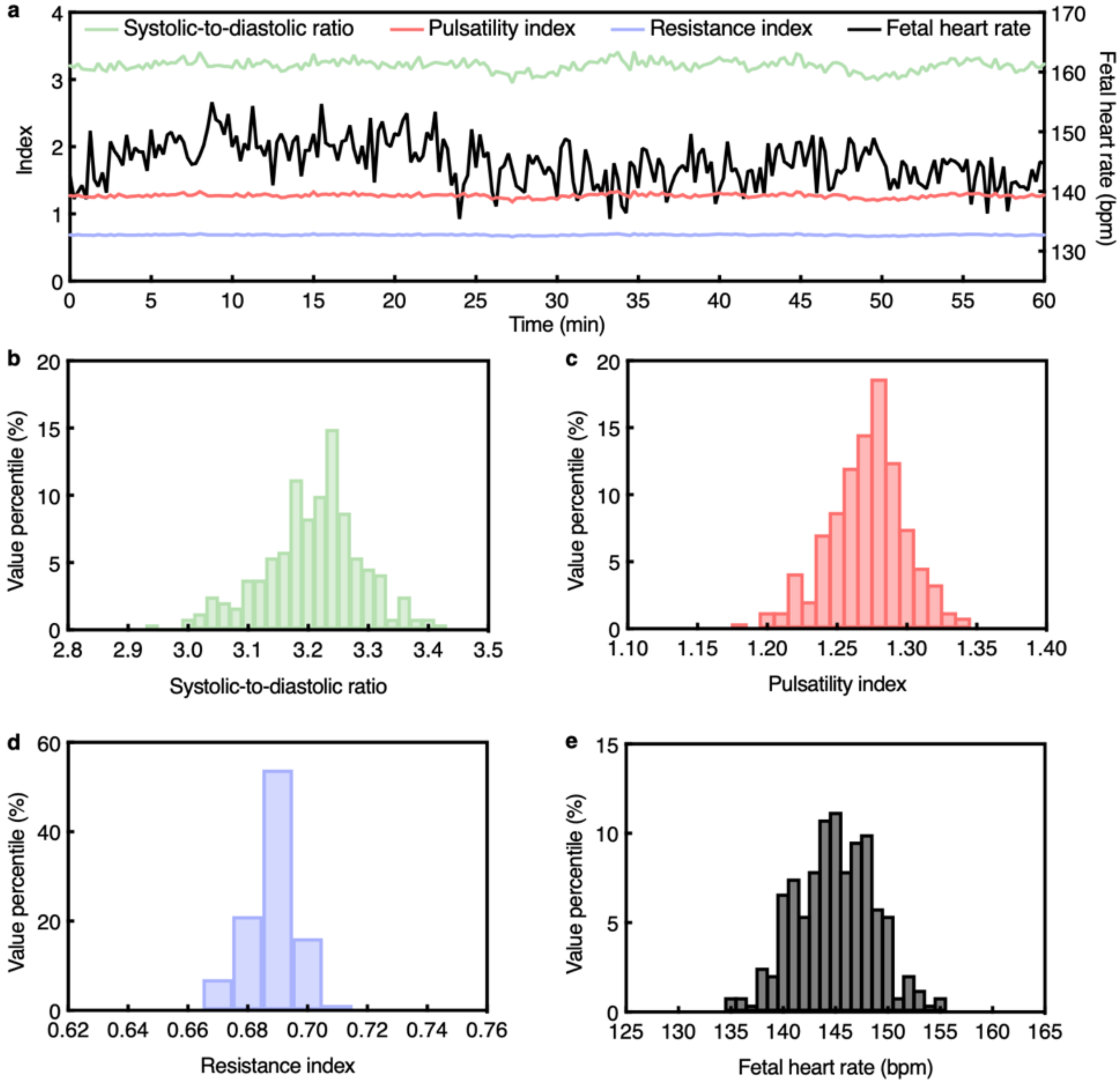

Supplementary Fig. 52 | Continuous fetal monitoring using the UPatch in Participant #13. a, Time series data from the 1-h continuous monitoring session. Systolic-to-diastolic ratio, pulsatility index, and resistance index are plotted on the left y-axis, and fetal heart rate is plotted on the right y-axis. Histograms of **b**, systolic-to-diastolic ratio, **c**, pulsatility index, **d**, resistance index, and **e**, fetal heart rate over the recording period.

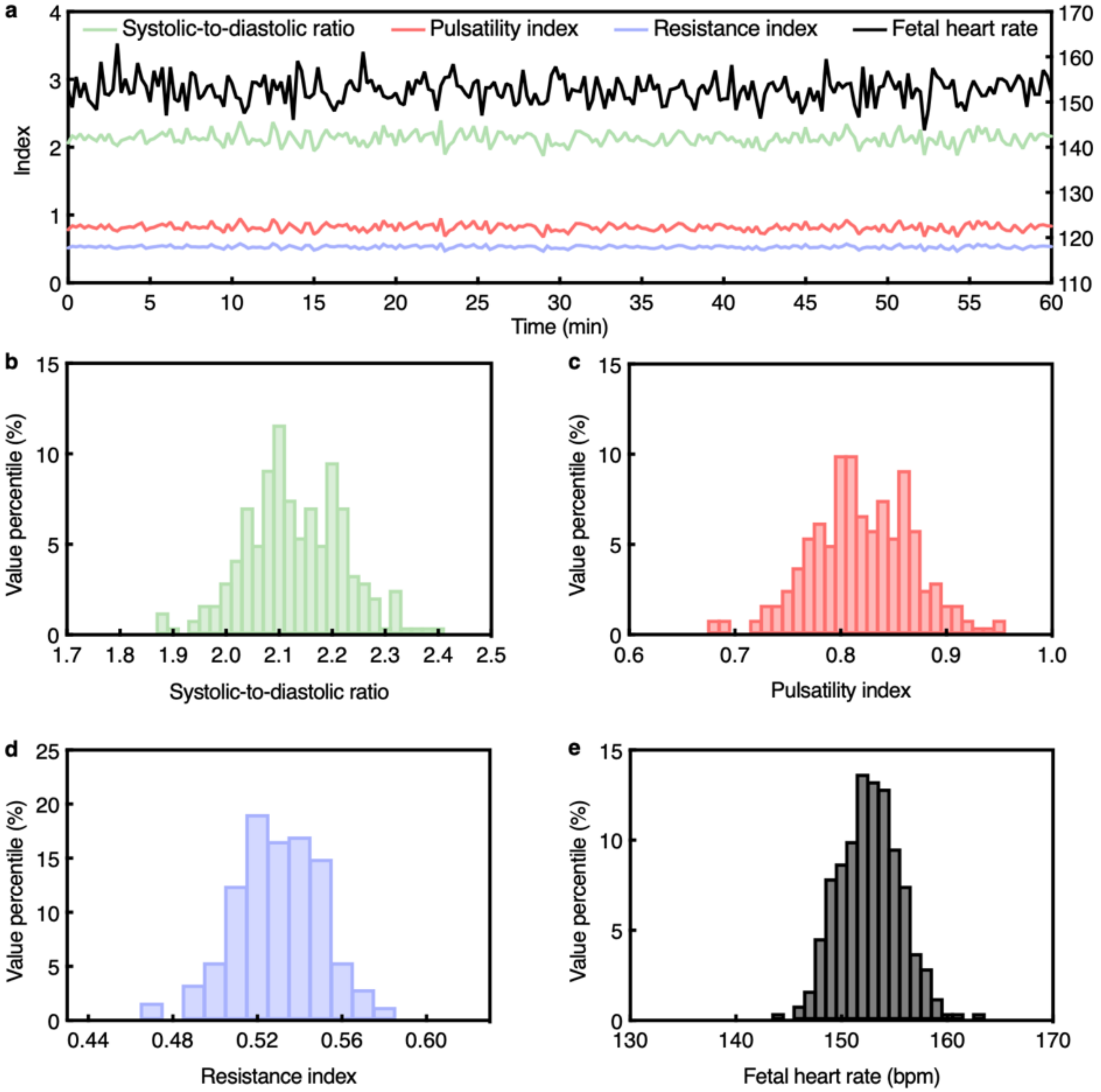

Supplementary Fig. 53 | Continuous fetal monitoring using the UPatch in Participant #14. a, Time series data from the 1-h continuous monitoring session. Systolic-to-diastolic ratio, pulsatility index, and resistance index are plotted on the left y-axis, and fetal heart rate is plotted on the right y-axis. Histograms of **b**, systolic-to-diastolic ratio, **c**, pulsatility index, **d**, resistance index, and **e**, fetal heart rate over the recording period.

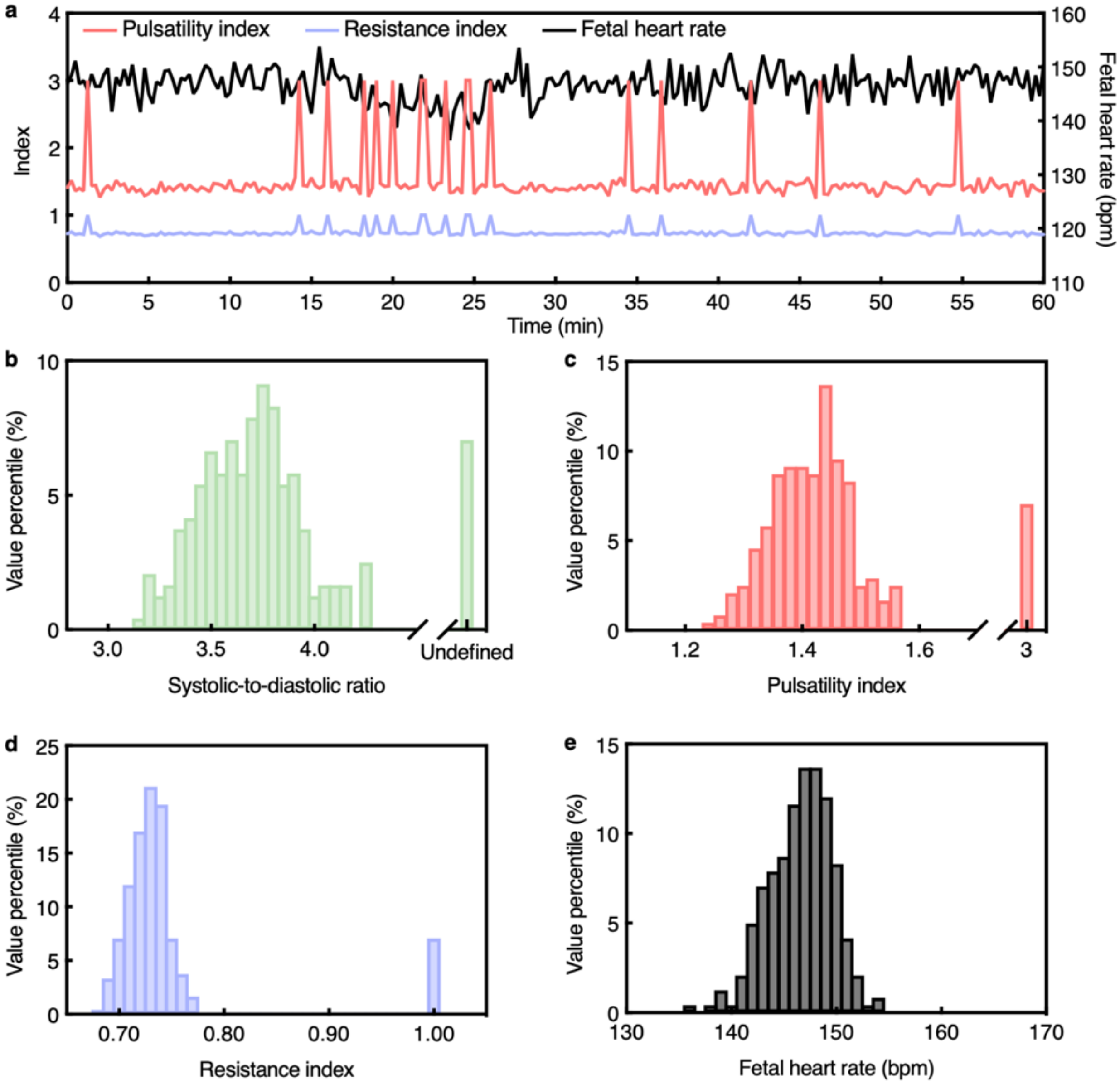

Supplementary Fig. 54 | Continuous fetal monitoring using the UPatch in Participant #15. a, Time series data from the 1-h continuous monitoring session. Pulsatility index and resistance index are plotted on the left y-axis, and fetal heart rate is plotted on the right y-axis. The systolic-to-diastolic ratio was not plotted in the time series due to the presence of undefined values. Histograms of **b**, systolic-to-diastolic ratio, **c**, pulsatility index, **d**, resistance index, and **e**, fetal heart rate over the recording period.

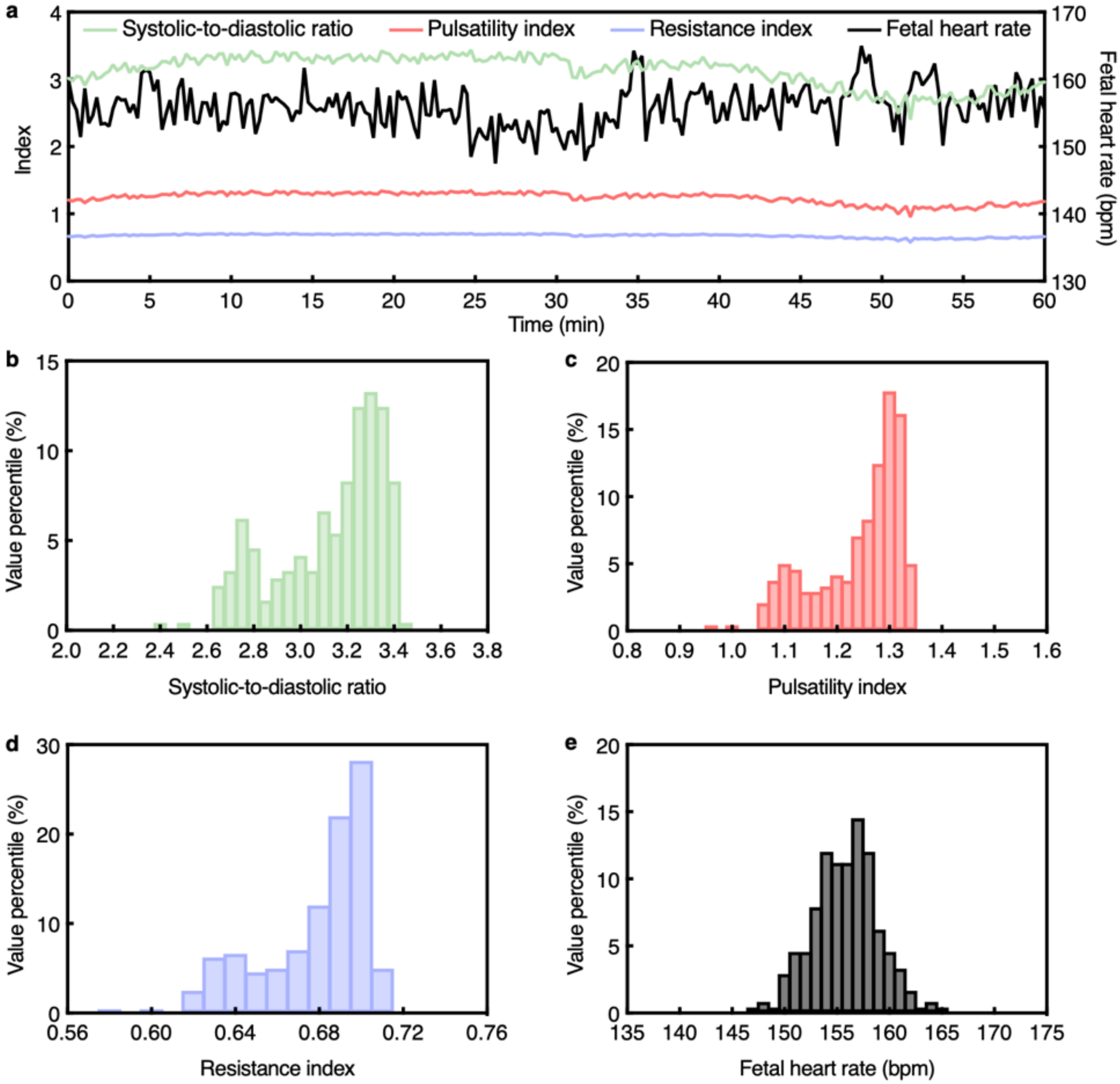

Supplementary Fig. 55 | Continuous fetal monitoring using the UPatch in Participant #16. a, Time series data from the 1-h continuous monitoring session. Systolic-to-diastolic ratio, pulsatility index, and resistance index are plotted on the left y-axis, and fetal heart rate is plotted on the right y-axis. Histograms of **b**, systolic-to-diastolic ratio, **c**, pulsatility index, **d**, resistance index, and **e**, fetal heart rate over the recording period.

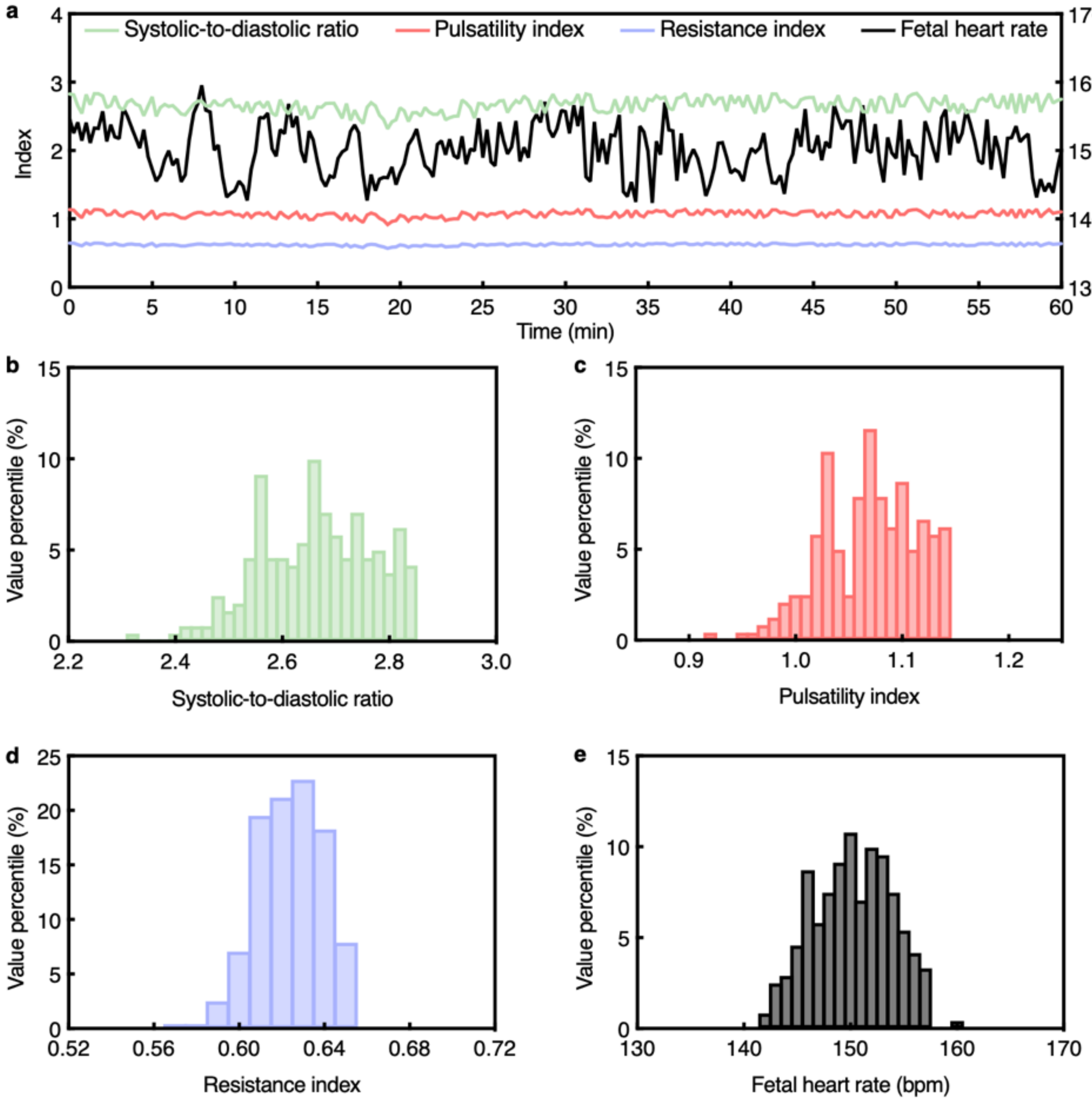

Supplementary Fig. 56 | Continuous fetal monitoring using the UPatch in Participant #17. a, Time series data from the 1-h continuous monitoring session. Systolic-to-diastolic ratio, pulsatility index, and resistance index are plotted on the left y-axis, and fetal heart rate is plotted on the right y-axis. Histograms of **b**, systolic-to-diastolic ratio, **c**, pulsatility index, **d**, resistance index, and **e**, fetal heart rate over the recording period.

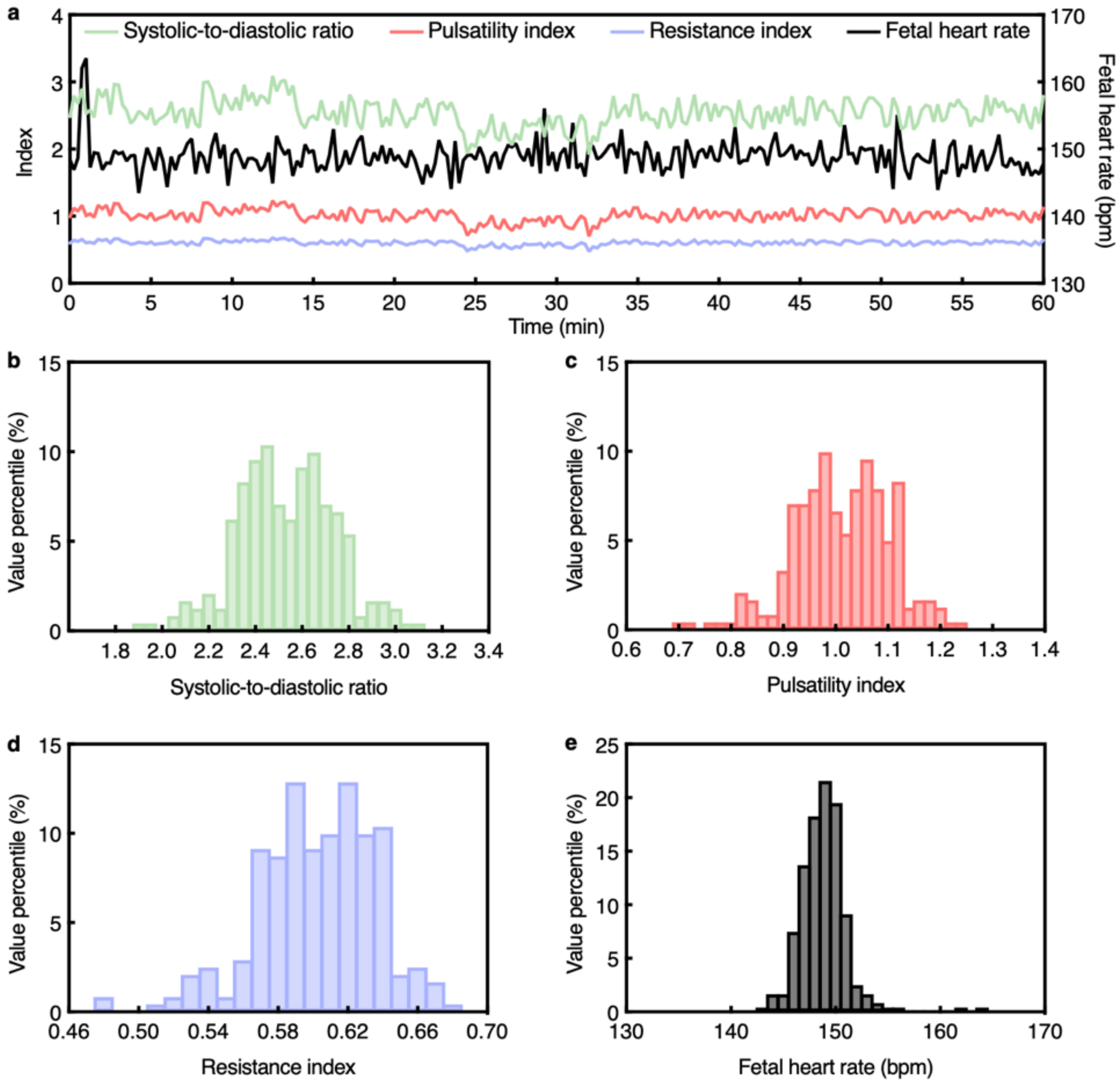

Supplementary Fig. 57 | Continuous fetal monitoring using the UPatch in Participant #18. a, Time series data from the 1-h continuous monitoring session. Systolic-to-diastolic ratio, pulsatility index, and resistance index are plotted on the left y-axis, and fetal heart rate is plotted on the right y-axis. Histograms of **b**, systolic-to-diastolic ratio, **c**, pulsatility index, **d**, resistance index, and **e**, fetal heart rate over the recording period.

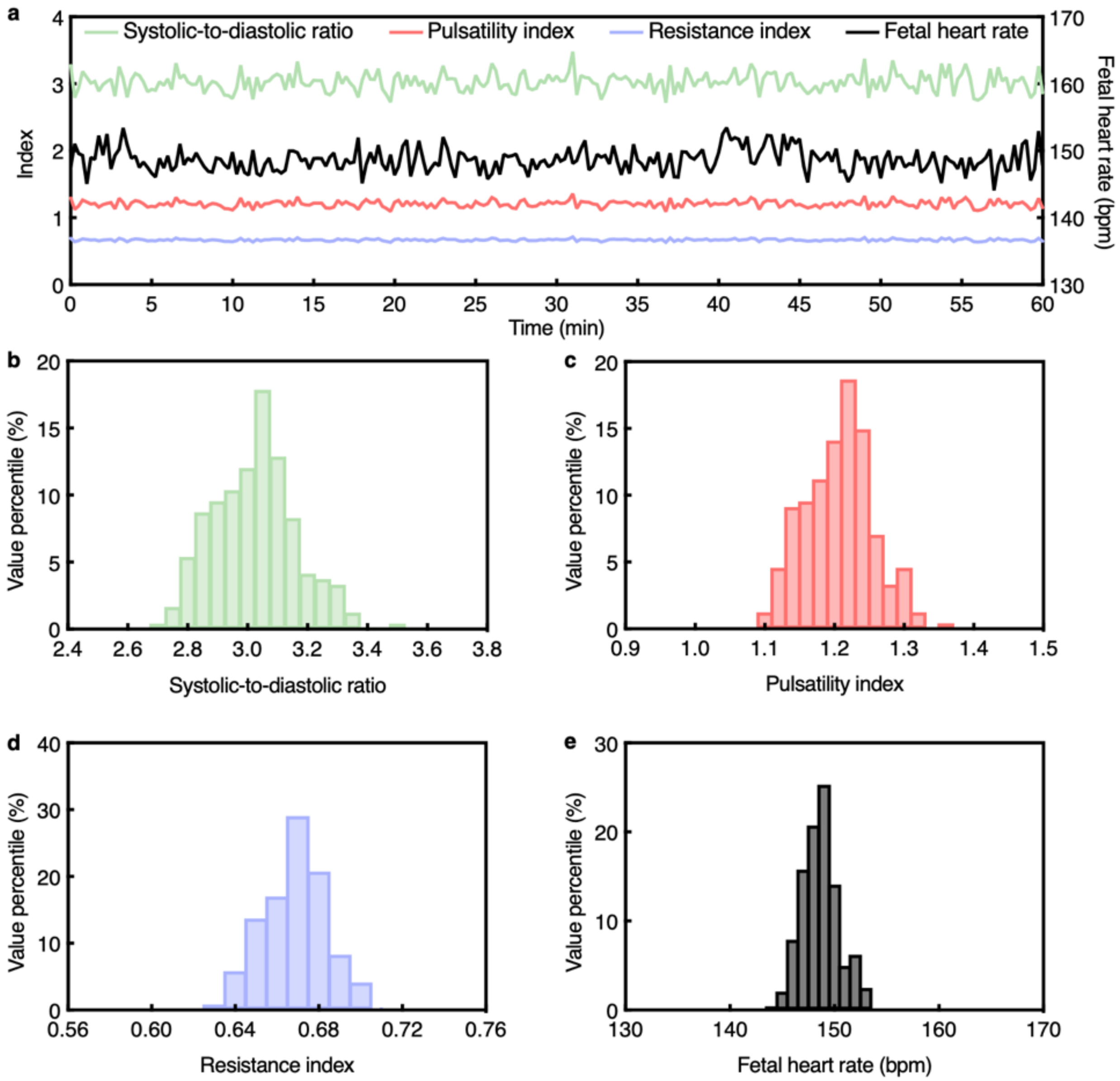

Supplementary Fig. 58 | Continuous fetal monitoring using the UPatch in Participant #19. a, Time series data from the 1-h continuous monitoring session. Systolic-to-diastolic ratio, pulsatility index, and resistance index are plotted on the left y-axis, and fetal heart rate is plotted on the right y-axis. Histograms of **b**, systolic-to-diastolic ratio, **c**, pulsatility index, **d**, resistance index, and **e**, fetal heart rate over the recording period.

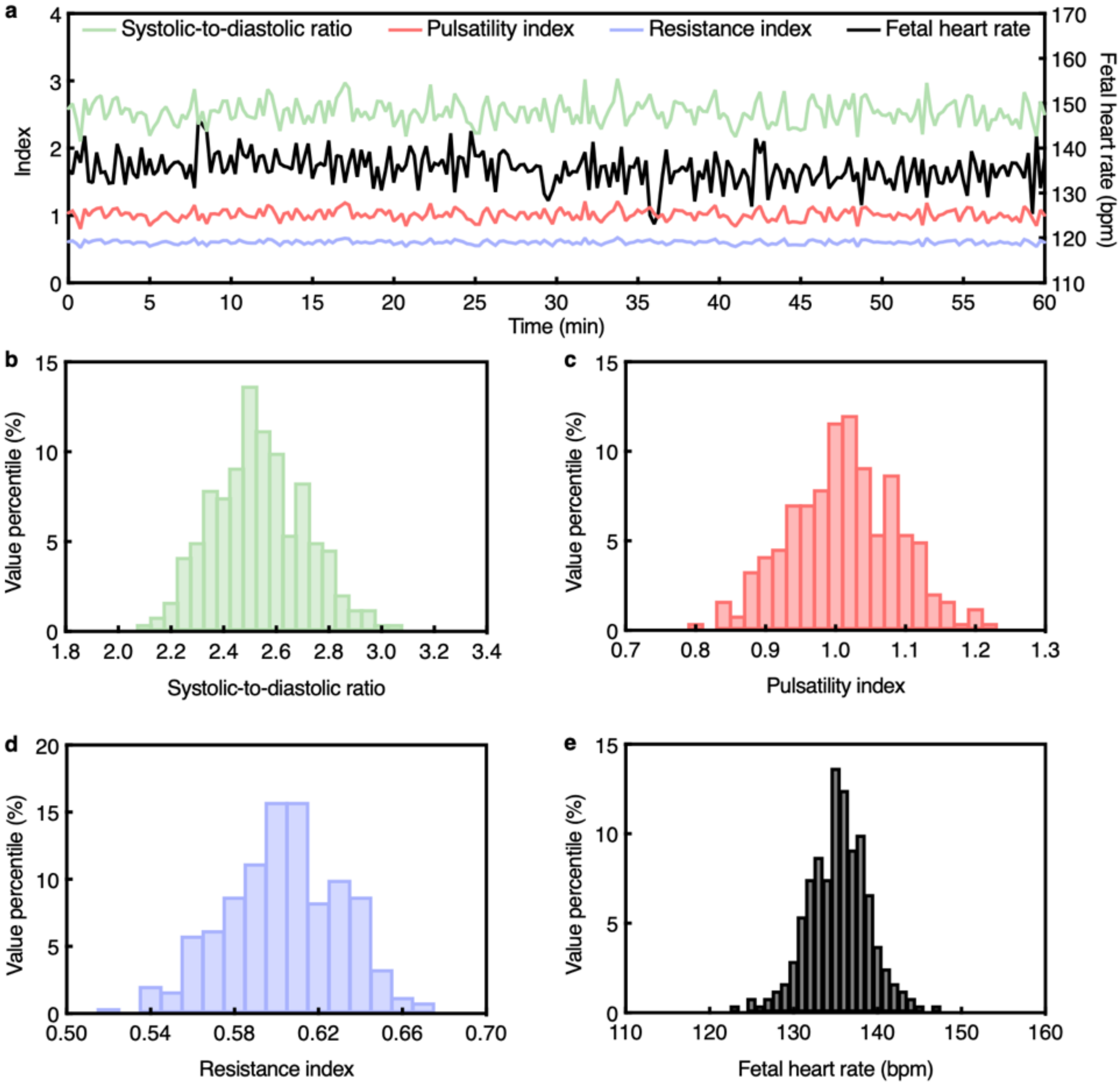

Supplementary Fig. 59 | Continuous fetal monitoring using the UPatch in Participant #20. a, Time series data from the 1-h continuous monitoring session. Systolic-to-diastolic ratio, pulsatility index, and resistance index are plotted on the left y-axis, and fetal heart rate is plotted on the right y-axis. Histograms of **b**, systolic-to-diastolic ratio, **c**, pulsatility index, **d**, resistance index, and **e**, fetal heart rate over the recording period.

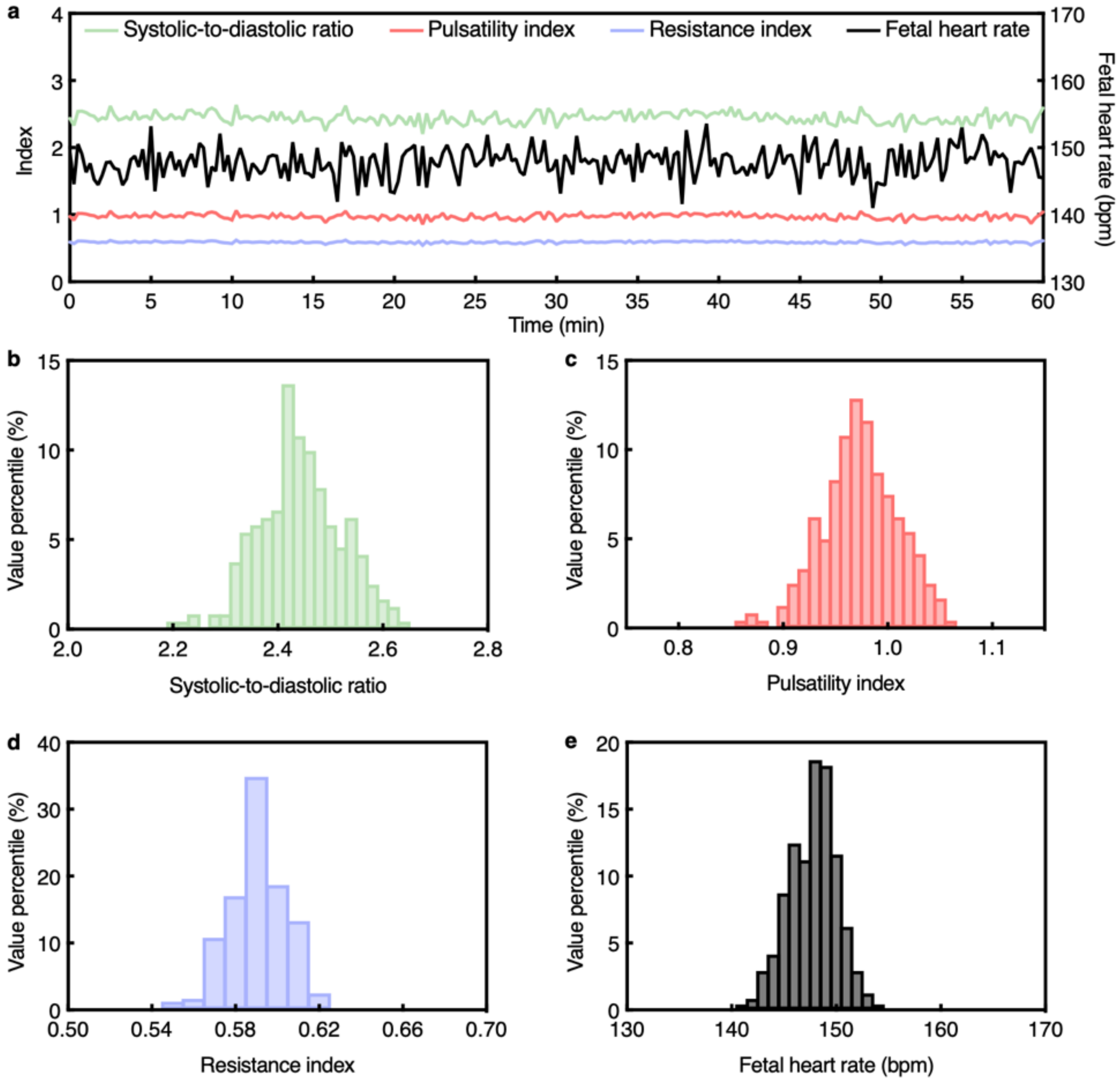

Supplementary Fig. 60 | Continuous fetal monitoring using the UPatch in Participant #21. a, Time series data from the 1-h continuous monitoring session. Systolic-to-diastolic ratio, pulsatility index, and resistance index are plotted on the left y-axis, and fetal heart rate is plotted on the right y-axis. Histograms of **b**, systolic-to-diastolic ratio, **c**, pulsatility index, **d**, resistance index, and **e**, fetal heart rate over the recording period.

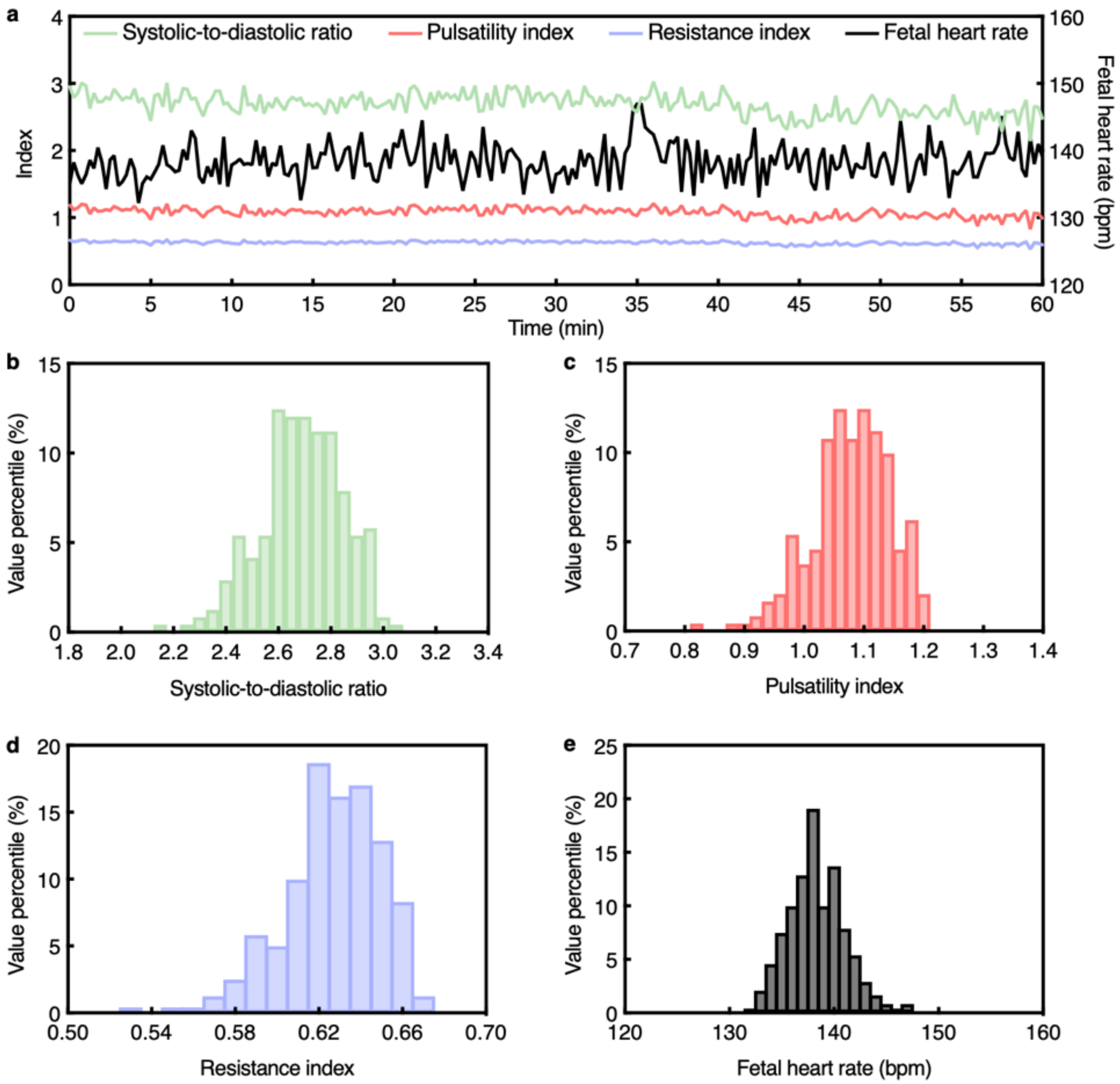

Supplementary Fig. 61 | Continuous fetal monitoring using the UPatch in Participant #22. a, Time series data from the 1-h continuous monitoring session. Systolic-to-diastolic ratio, pulsatility index, and resistance index are plotted on the left y-axis, and fetal heart rate is plotted on the right y-axis. Histograms of **b**, systolic-to-diastolic ratio, **c**, pulsatility index, **d**, resistance index, and **e**, fetal heart rate over the recording period.

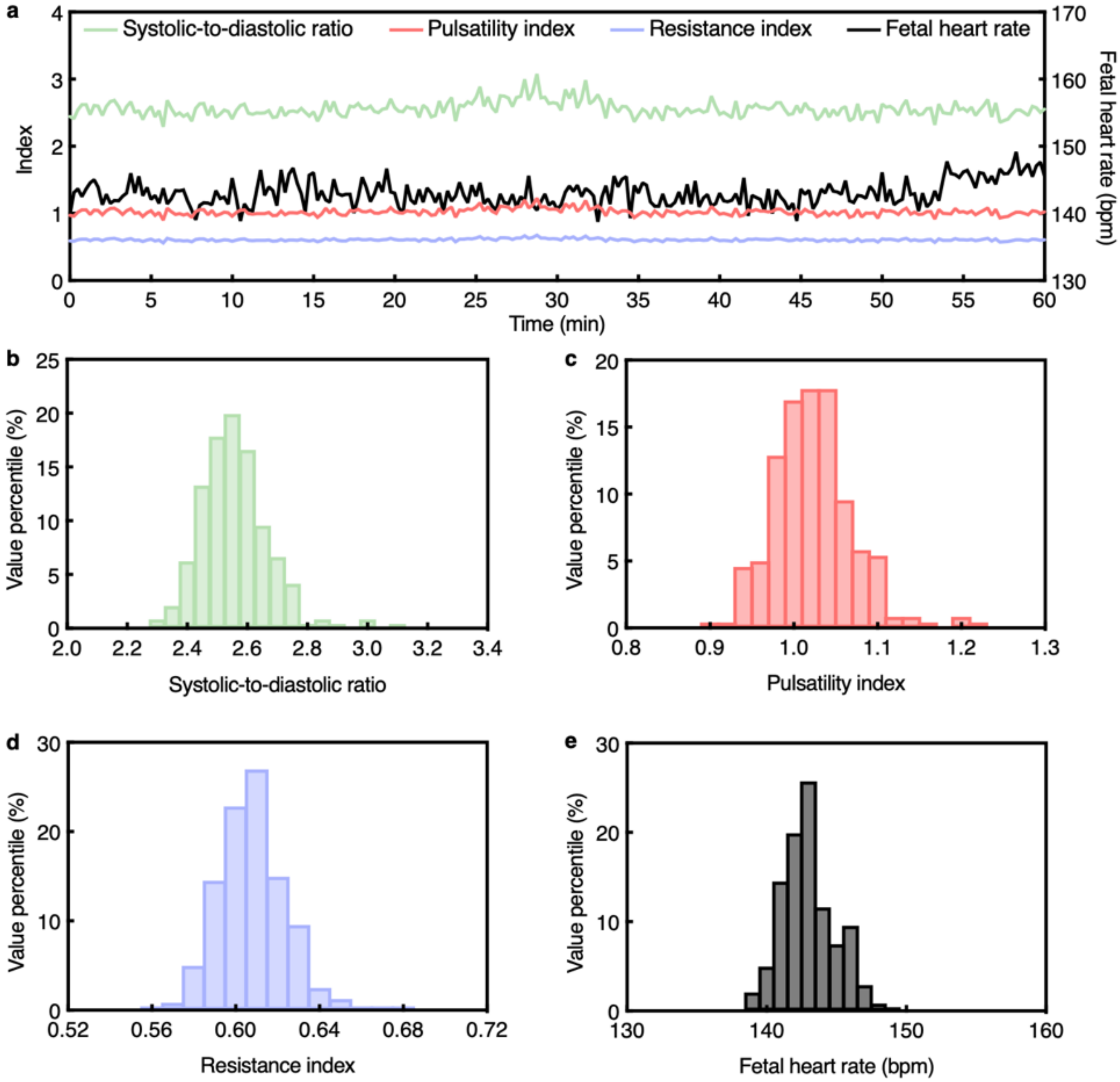

Supplementary Fig. 62 | Continuous fetal monitoring using the UPatch in Participant #23. a, Time series data from the 1-h continuous monitoring session. Systolic-to-diastolic ratio, pulsatility index, and resistance index are plotted on the left y-axis, and fetal heart rate is plotted on the right y-axis. Histograms of **b**, systolic-to-diastolic ratio, **c**, pulsatility index, **d**, resistance index, and **e**, fetal heart rate over the recording period.

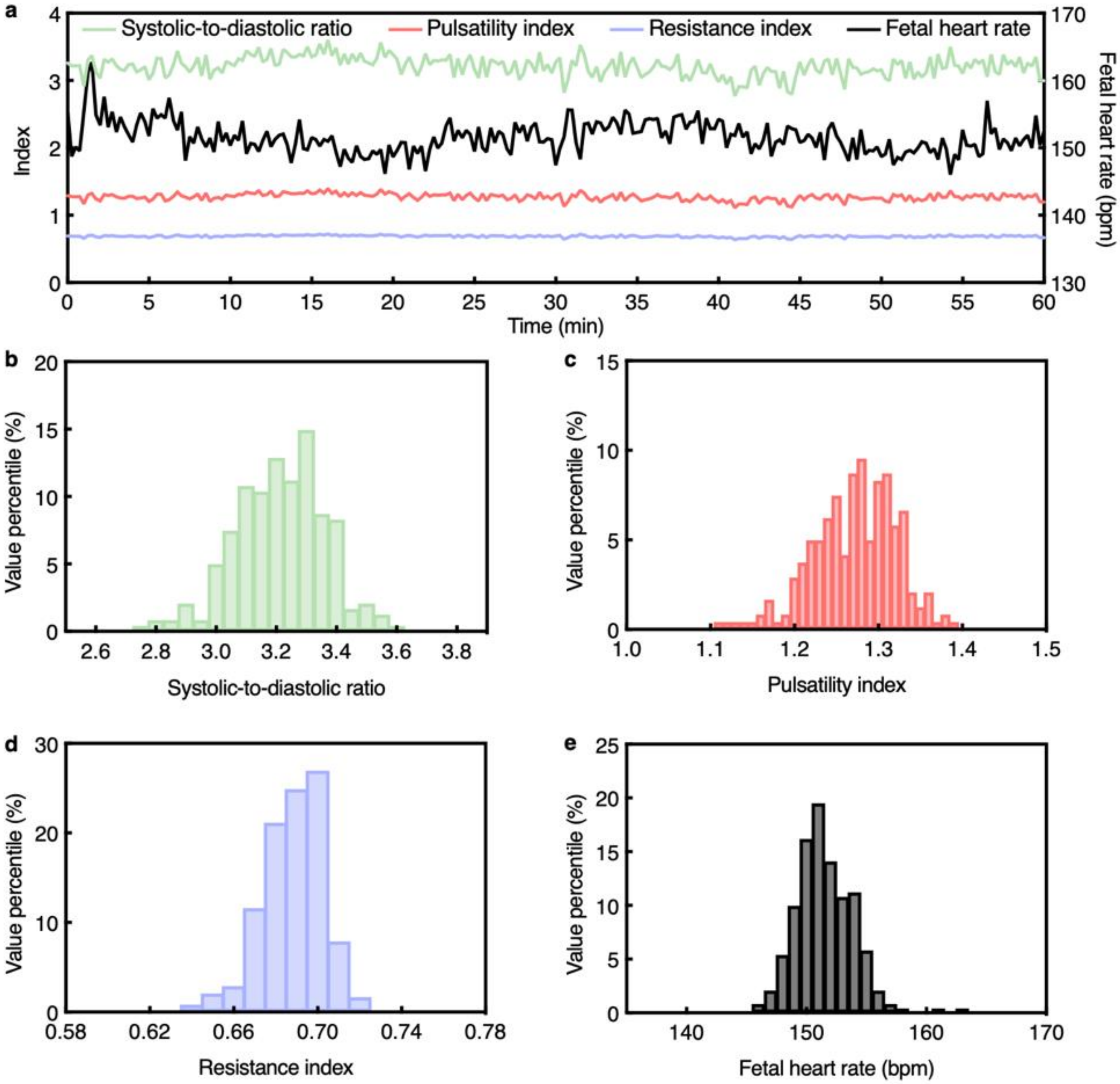

Supplementary Fig. 63 | Continuous fetal monitoring using the UPatch in Participant #24. a, Time series data from the 1-h continuous monitoring session. Systolic-to-diastolic ratio, pulsatility index, and resistance index are plotted on the left y-axis, and fetal heart rate is plotted on the right y-axis. Histograms of **b**, systolic-to-diastolic ratio, **c**, pulsatility index, **d**, resistance index, and **e**, fetal heart rate over the recording period.

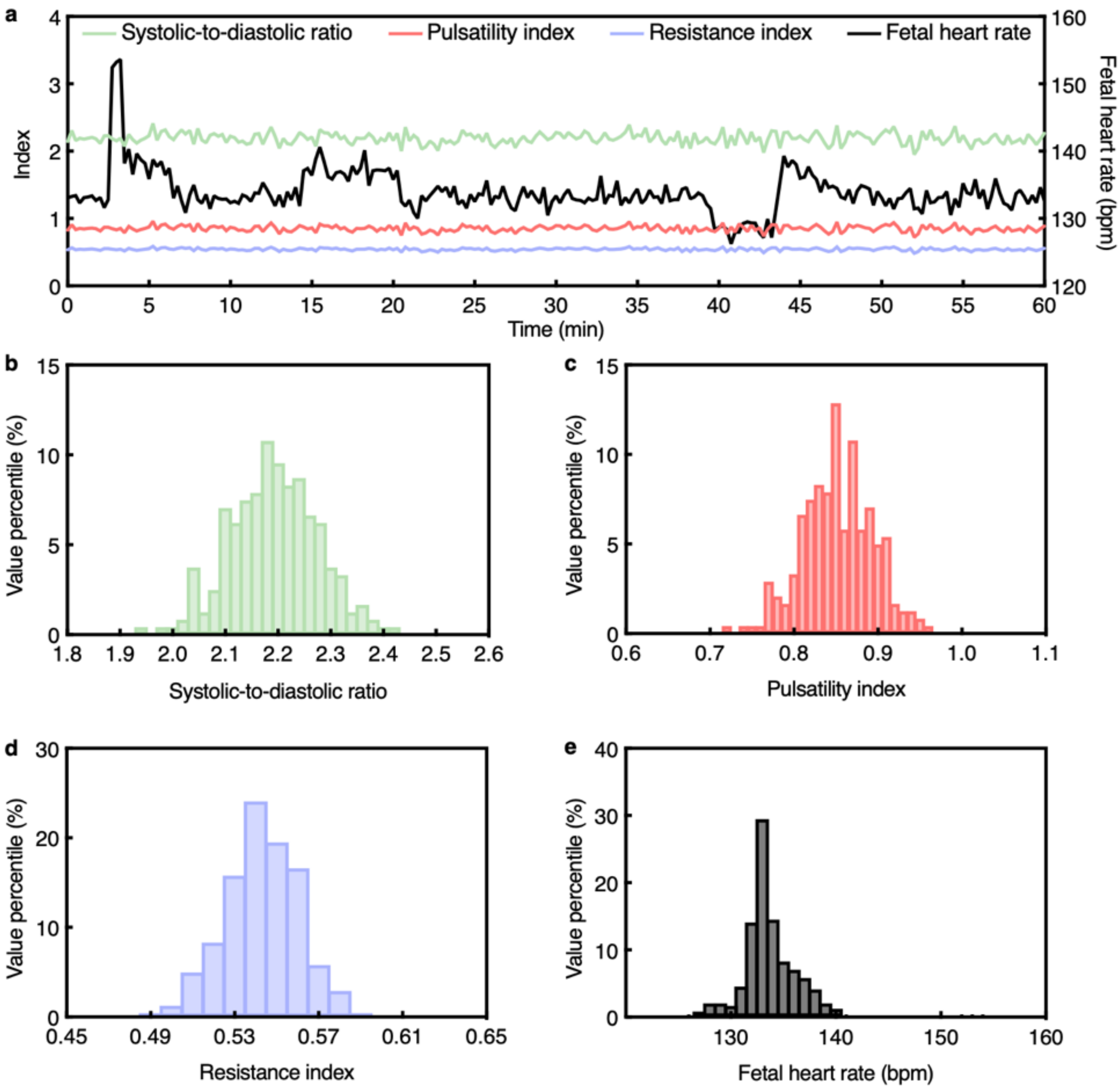

Supplementary Fig. 64 | Continuous fetal monitoring using the UPatch in Participant #25. a, Time series data from the 1-h continuous monitoring session. Systolic-to-diastolic ratio, pulsatility index, and resistance index are plotted on the left y-axis, and fetal heart rate is plotted on the right y-axis. Histograms of **b**, systolic-to-diastolic ratio, **c**, pulsatility index, **d**, resistance index, and **e**, fetal heart rate over the recording period.

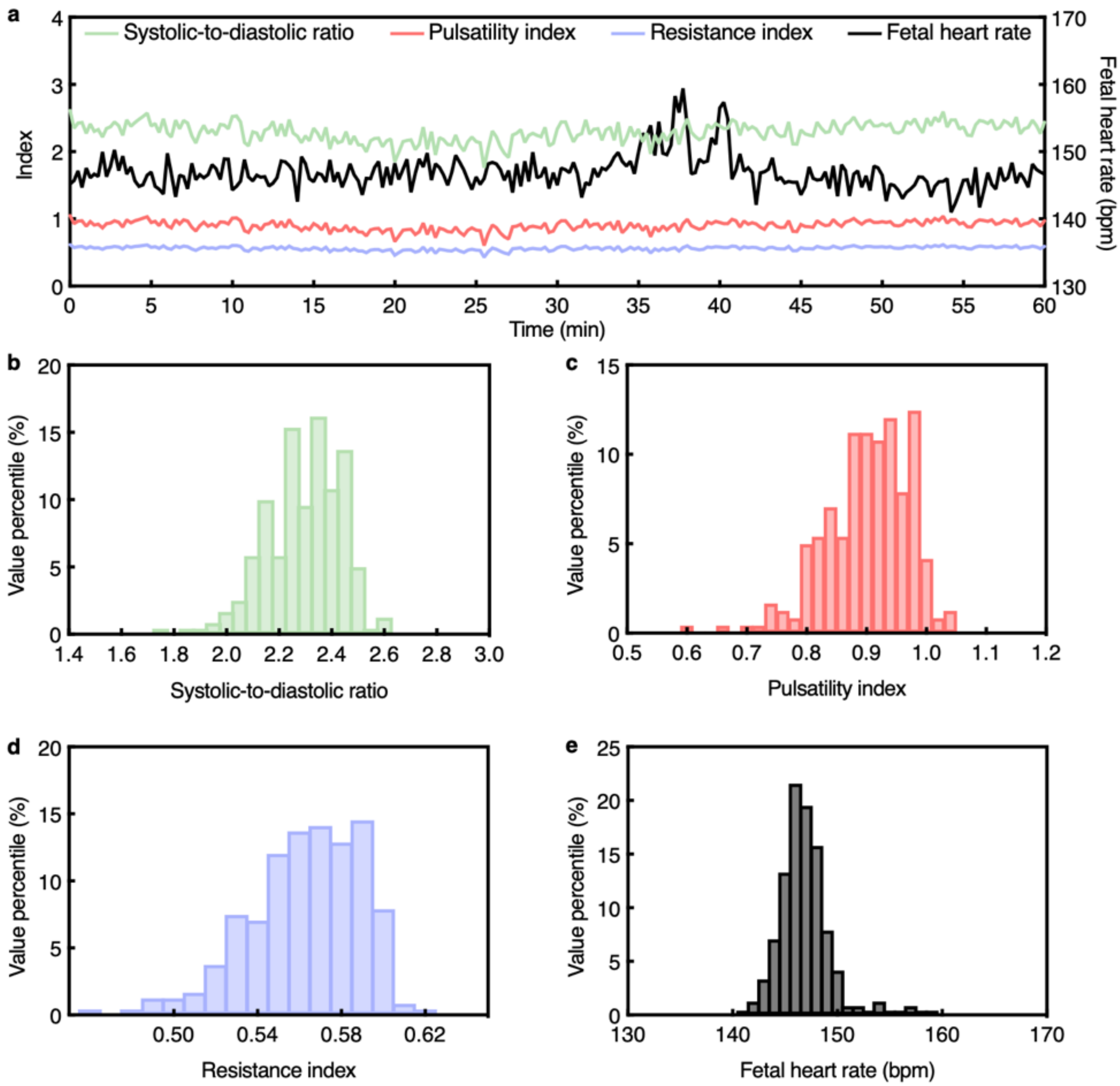

Supplementary Fig. 65 | Continuous fetal monitoring using the UPatch in Participant #26. a, Time series data from the 1-h continuous monitoring session. Systolic-to-diastolic ratio, pulsatility index, and resistance index are plotted on the left y-axis, and fetal heart rate is plotted on the right y-axis. Histograms of **b**, systolic-to-diastolic ratio, **c**, pulsatility index, **d**, resistance index, and **e**, fetal heart rate over the recording period.

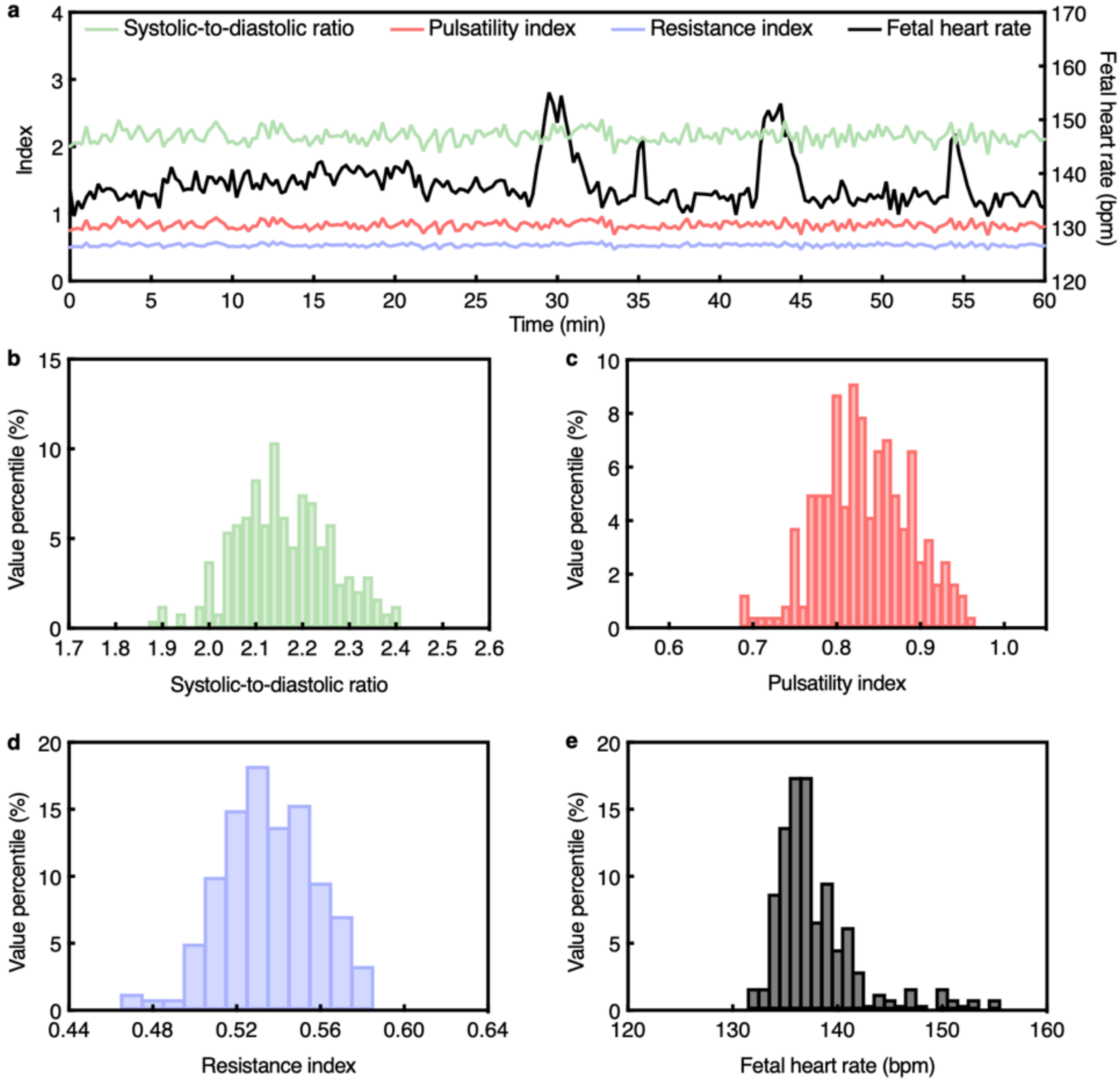

Supplementary Fig. 66 | Continuous fetal monitoring using the UPatch in Participant #27. a, Time series data from the 1-h continuous monitoring session. Systolic-to-diastolic ratio, pulsatility index, and resistance index are plotted on the left y-axis, and fetal heart rate is plotted on the right y-axis. Histograms of **b**, systolic-to-diastolic ratio, **c**, pulsatility index, **d**, resistance index, and **e**, fetal heart rate over the recording period.

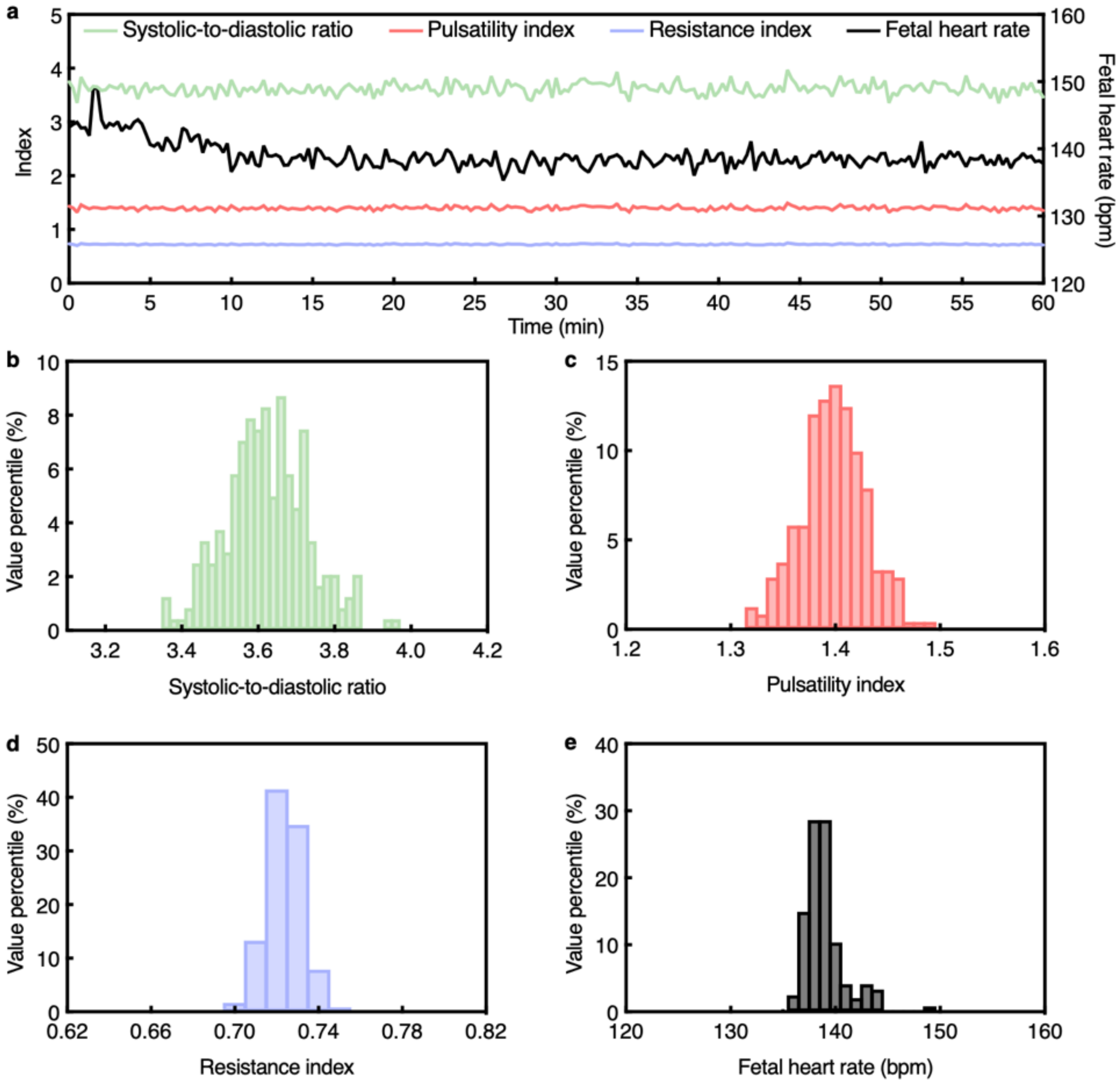

Supplementary Fig. 67 | Continuous fetal monitoring using the UPatch in Participant #28. a, Time series data from the 1-h continuous monitoring session. Systolic-to-diastolic ratio, pulsatility index, and resistance index are plotted on the left y-axis, and fetal heart rate is plotted on the right y-axis. Histograms of **b**, systolic-to-diastolic ratio, **c**, pulsatility index, **d**, resistance index, and **e**, fetal heart rate over the recording period.

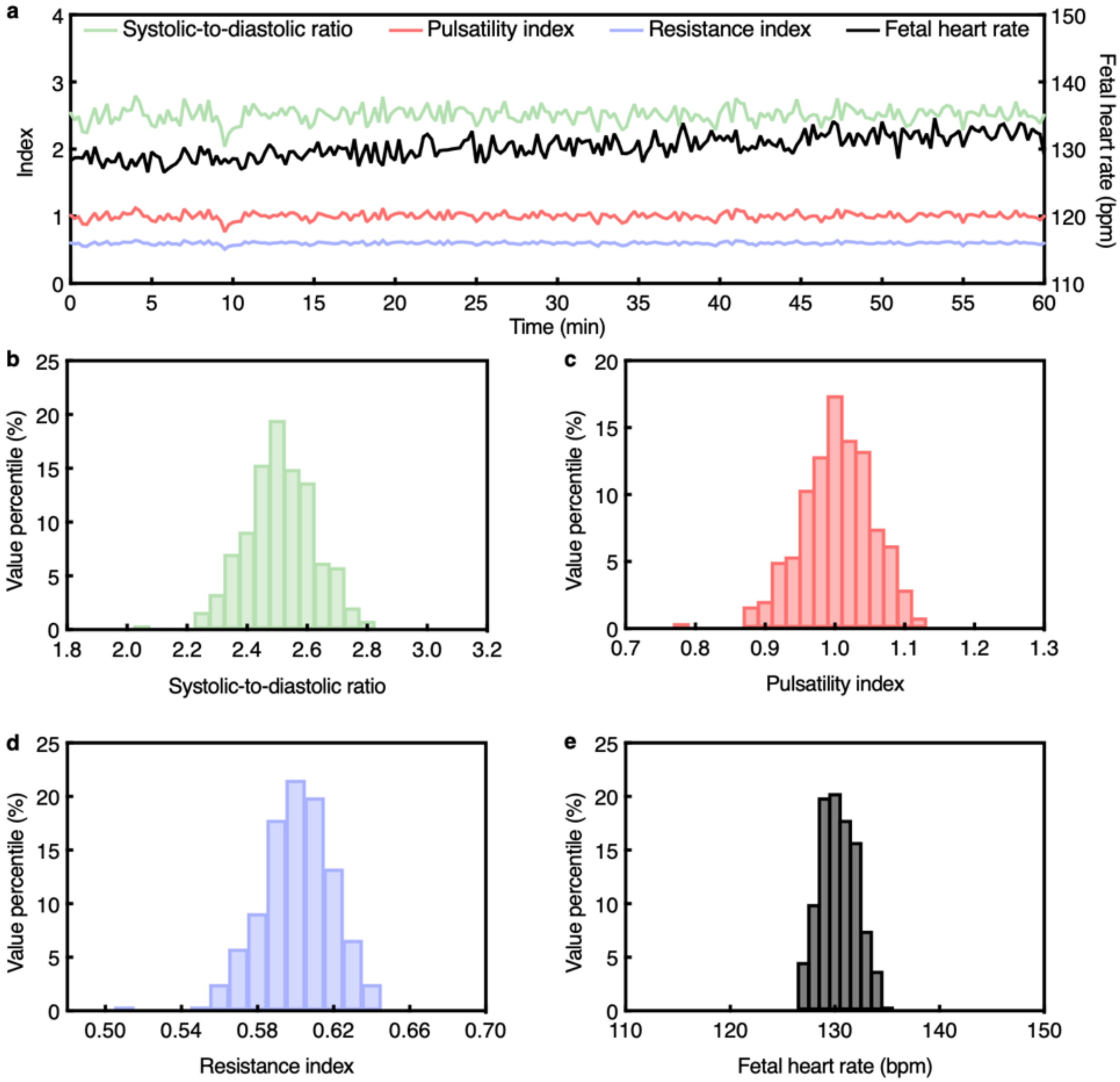

Supplementary Fig. 68 | Continuous fetal monitoring using the UPatch in Participant #29. a, Time series data from the 1-h continuous monitoring session. Systolic-to-diastolic ratio, pulsatility index, and resistance index are plotted on the left y-axis, and fetal heart rate is plotted on the right y-axis. Histograms of **b**, systolic-to-diastolic ratio, **c**, pulsatility index, **d**, resistance index, and **e**, fetal heart rate over the recording period.

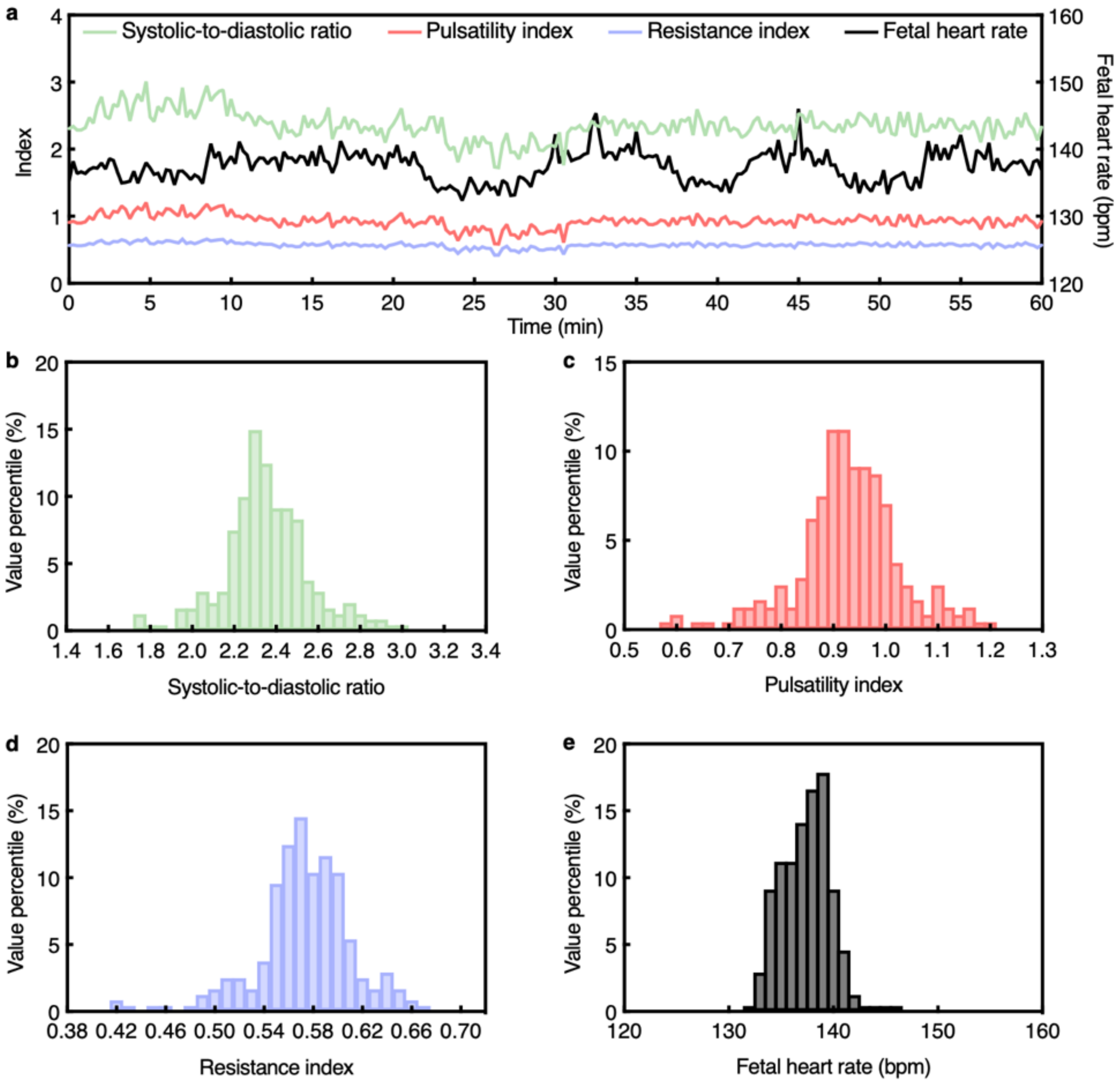

Supplementary Fig. 69 | Continuous fetal monitoring using the UPatch in Participant #30. a, Time series data from the 1-h continuous monitoring session. Systolic-to-diastolic ratio, pulsatility index, and resistance index are plotted on the left y-axis, and fetal heart rate is plotted on the right y-axis. Histograms of **b**, systolic-to-diastolic ratio, **c**, pulsatility index, **d**, resistance index, and **e**, fetal heart rate over the recording period.

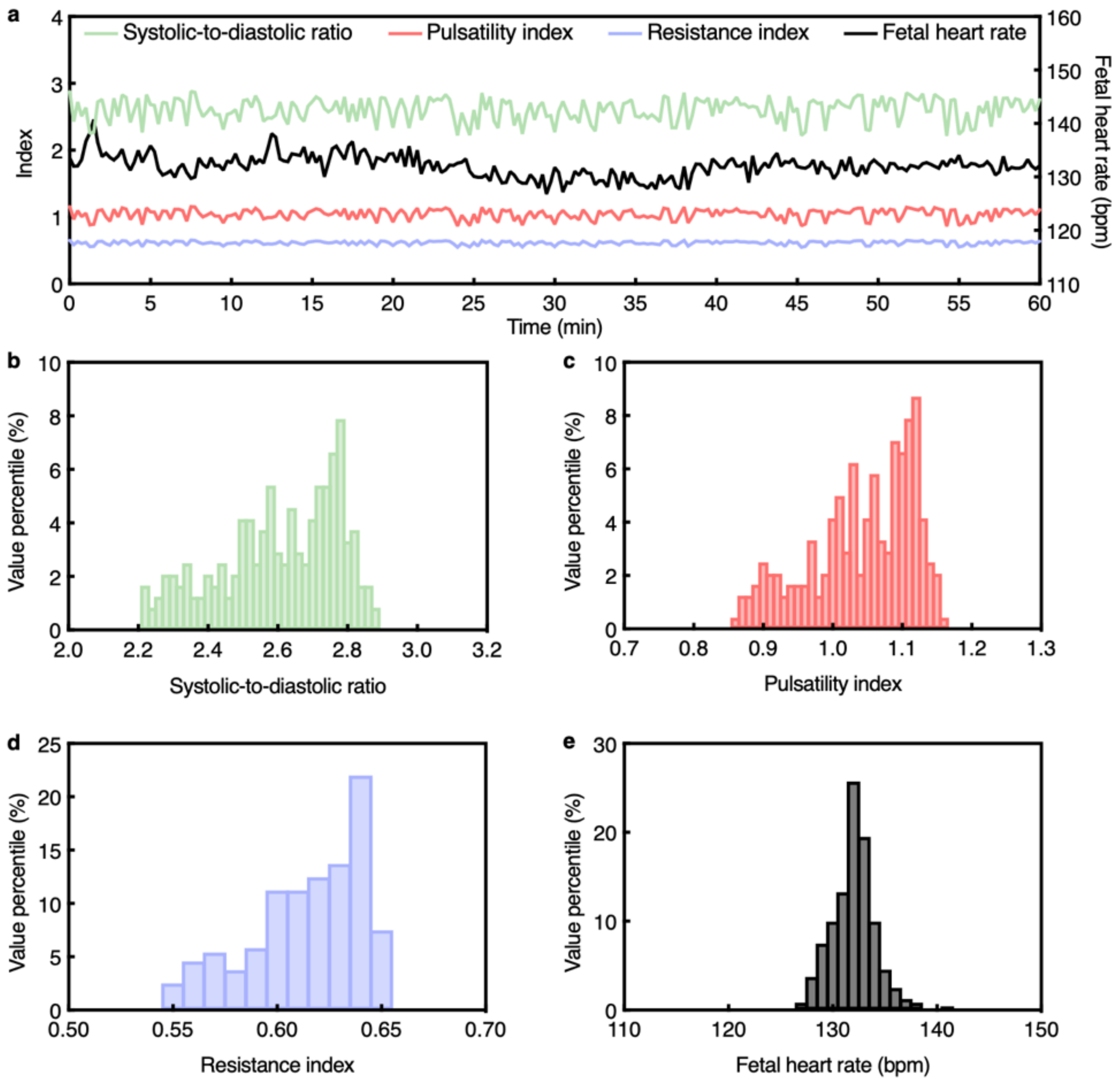

Supplementary Fig. 70 | Continuous fetal monitoring using the UPatch in Participant #31. a, Time series data from the 1-h continuous monitoring session. Systolic-to-diastolic ratio, pulsatility index, and resistance index are plotted on the left y-axis, and fetal heart rate is plotted on the right y-axis. Histograms of **b**, systolic-to-diastolic ratio, **c**, pulsatility index, **d**, resistance index, and **e**, fetal heart rate over the recording period.

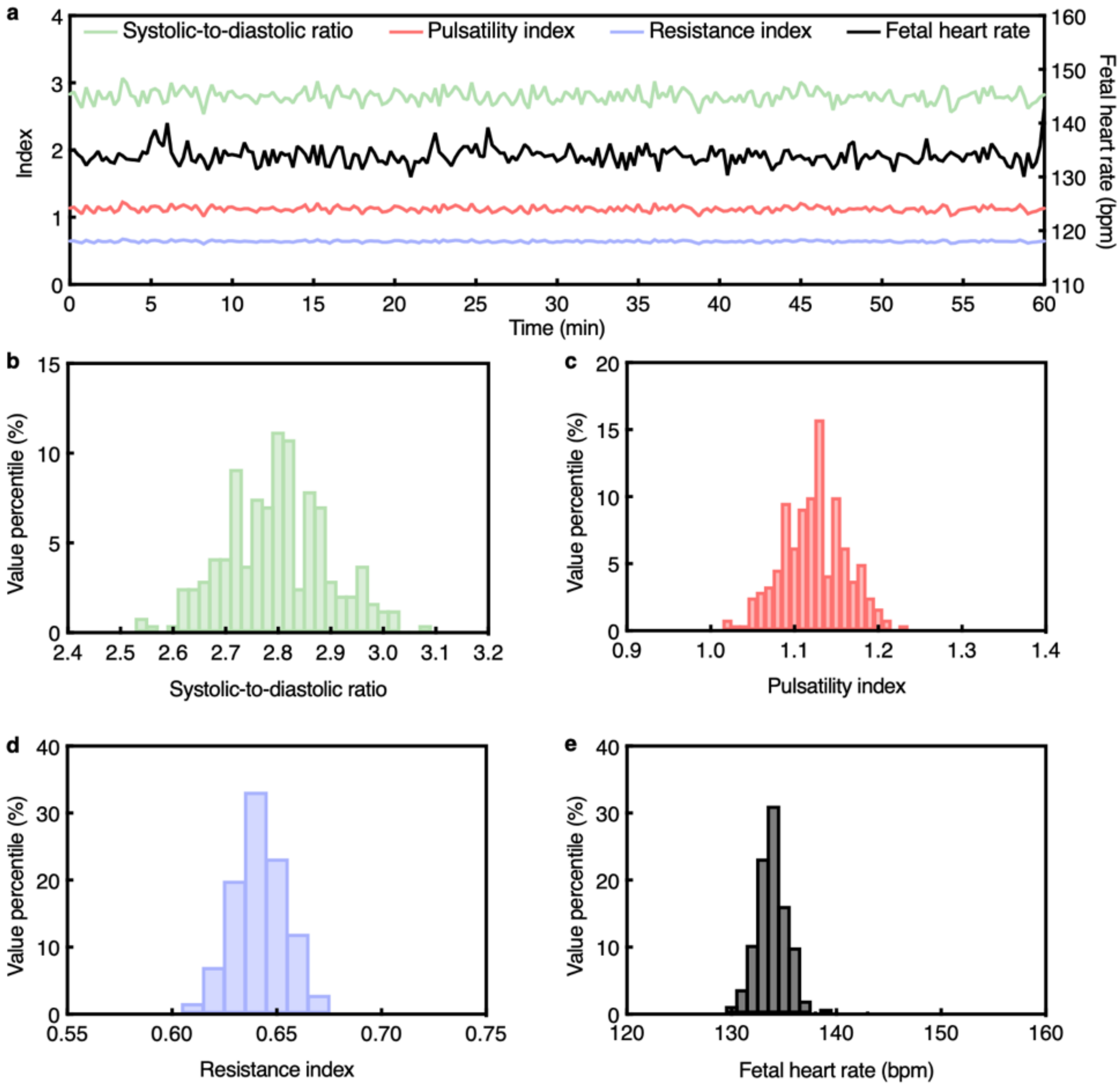

Supplementary Fig. 71 | Continuous fetal monitoring using the UPatch in Participant #32. a, Time series data from the 1-h continuous monitoring session. Systolic-to-diastolic ratio, pulsatility index, and resistance index are plotted on the left y-axis, and fetal heart rate is plotted on the right y-axis. Histograms of **b**, systolic-to-diastolic ratio, **c**, pulsatility index, **d**, resistance index, and **e**, fetal heart rate over the recording period.

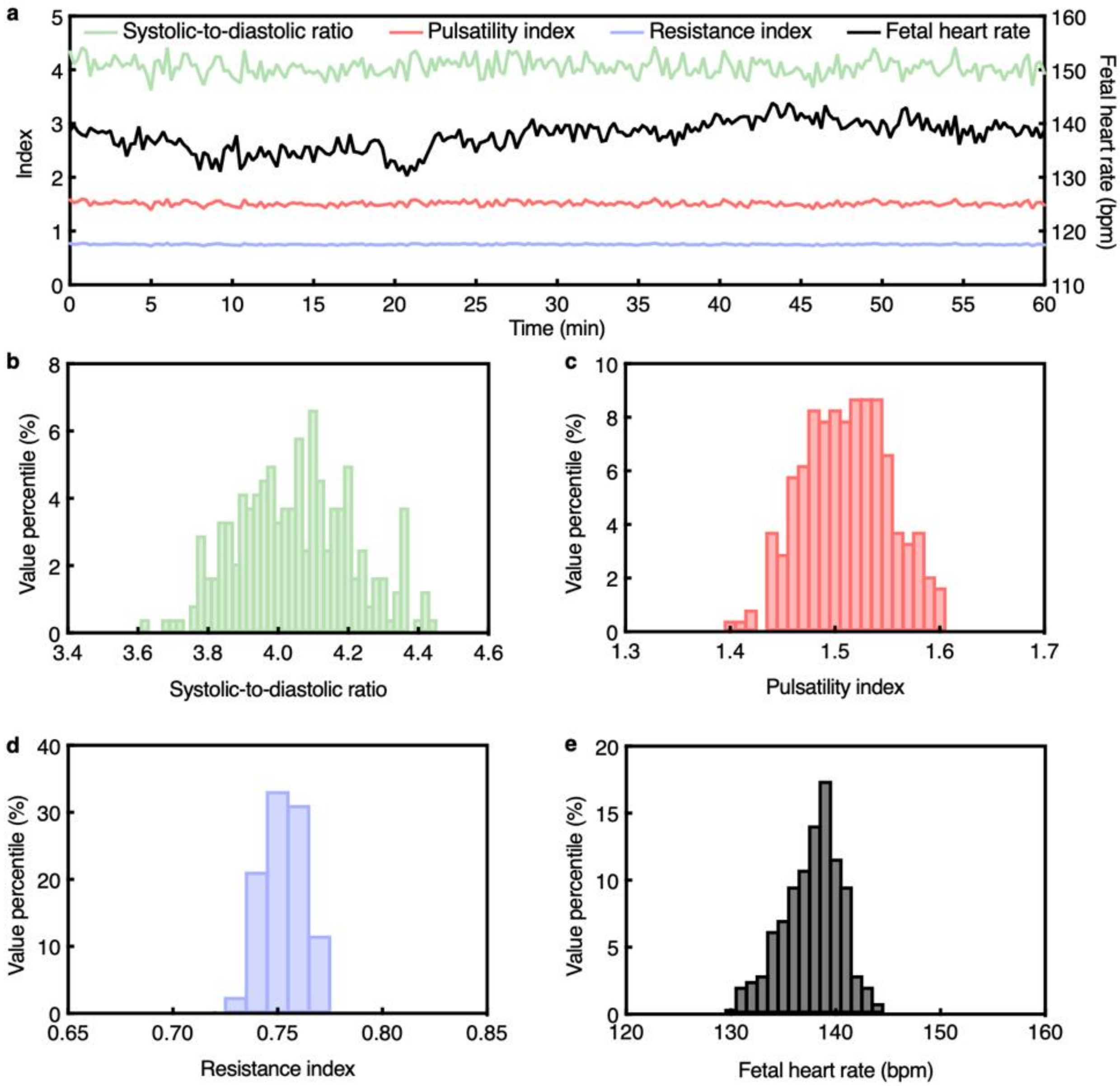

Supplementary Fig. 72 | Continuous fetal monitoring using the UPatch in Participant #33. a, Time series data from the 1-h continuous monitoring session. Systolic-to-diastolic ratio, pulsatility index, and resistance index are plotted on the left y-axis, and fetal heart rate is plotted on the right y-axis. Histograms of **b**, systolic-to-diastolic ratio, **c**, pulsatility index, **d**, resistance index, and **e**, fetal heart rate over the recording period.

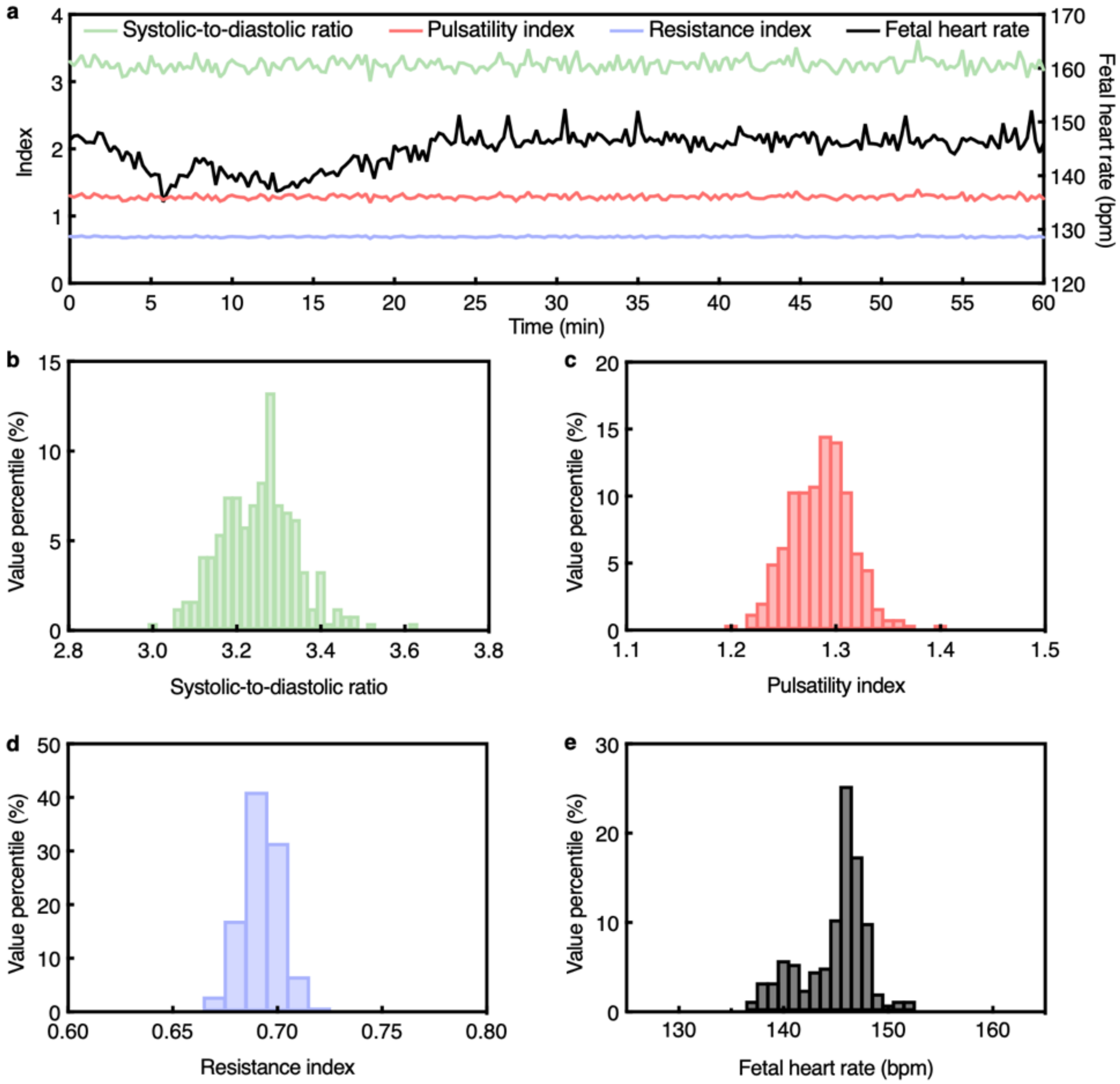

Supplementary Fig. 73 | Continuous fetal monitoring using the UPatch in Participant #34. a, Time series data from the 1-h continuous monitoring session. Systolic-to-diastolic ratio, pulsatility index, and resistance index are plotted on the left y-axis, and fetal heart rate is plotted on the right y-axis. Histograms of **b**, systolic-to-diastolic ratio, **c**, pulsatility index, **d**, resistance index, and **e**, fetal heart rate over the recording period.

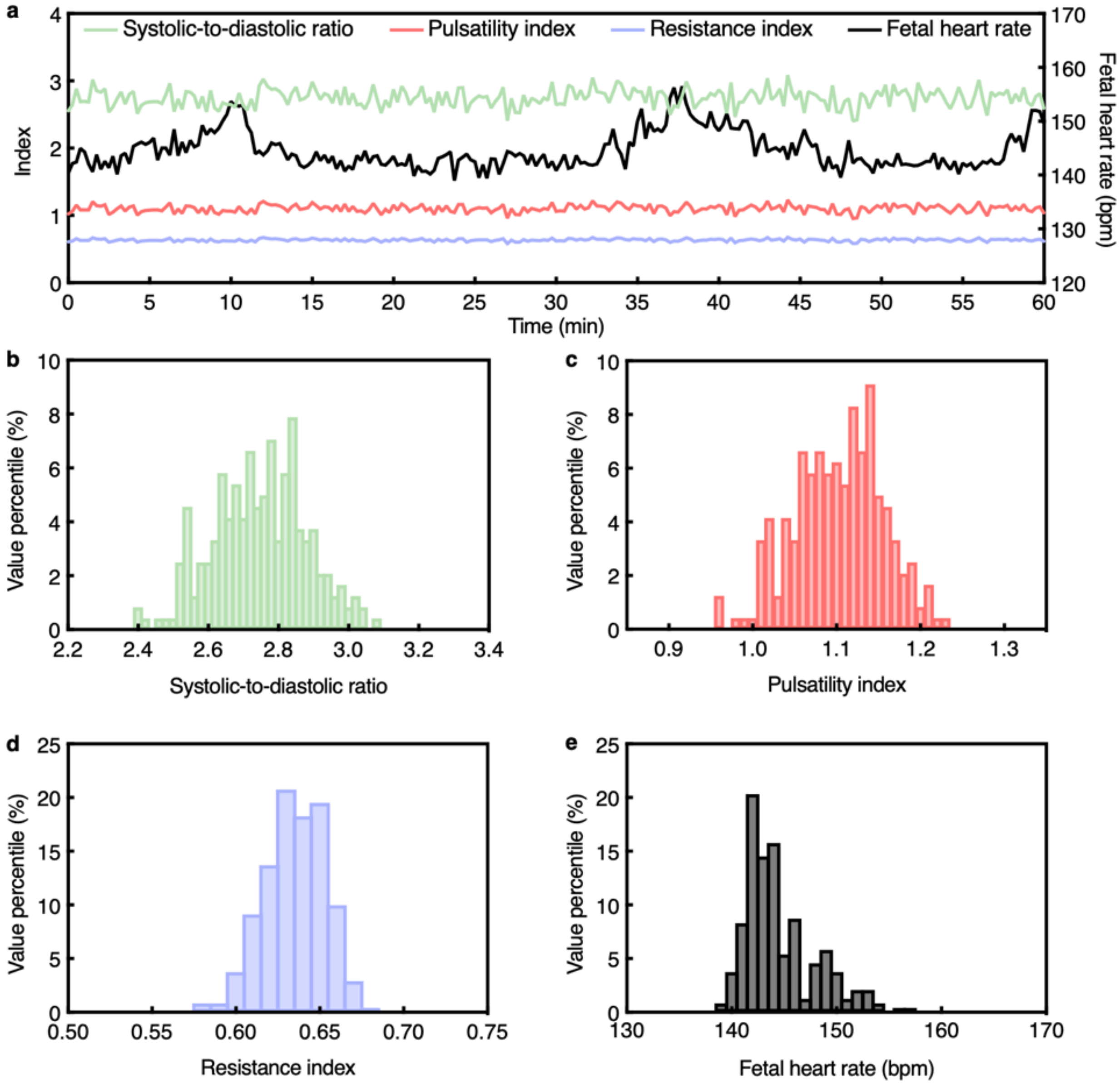

Supplementary Fig. 74 | Continuous fetal monitoring using the UPatch in Participant #35. a, Time series data from the 1-h continuous monitoring session. Systolic-to-diastolic ratio, pulsatility index, and resistance index are plotted on the left y-axis, and fetal heart rate is plotted on the right y-axis. Histograms of **b**, systolic-to-diastolic ratio, **c**, pulsatility index, **d**, resistance index, and **e**, fetal heart rate over the recording period.

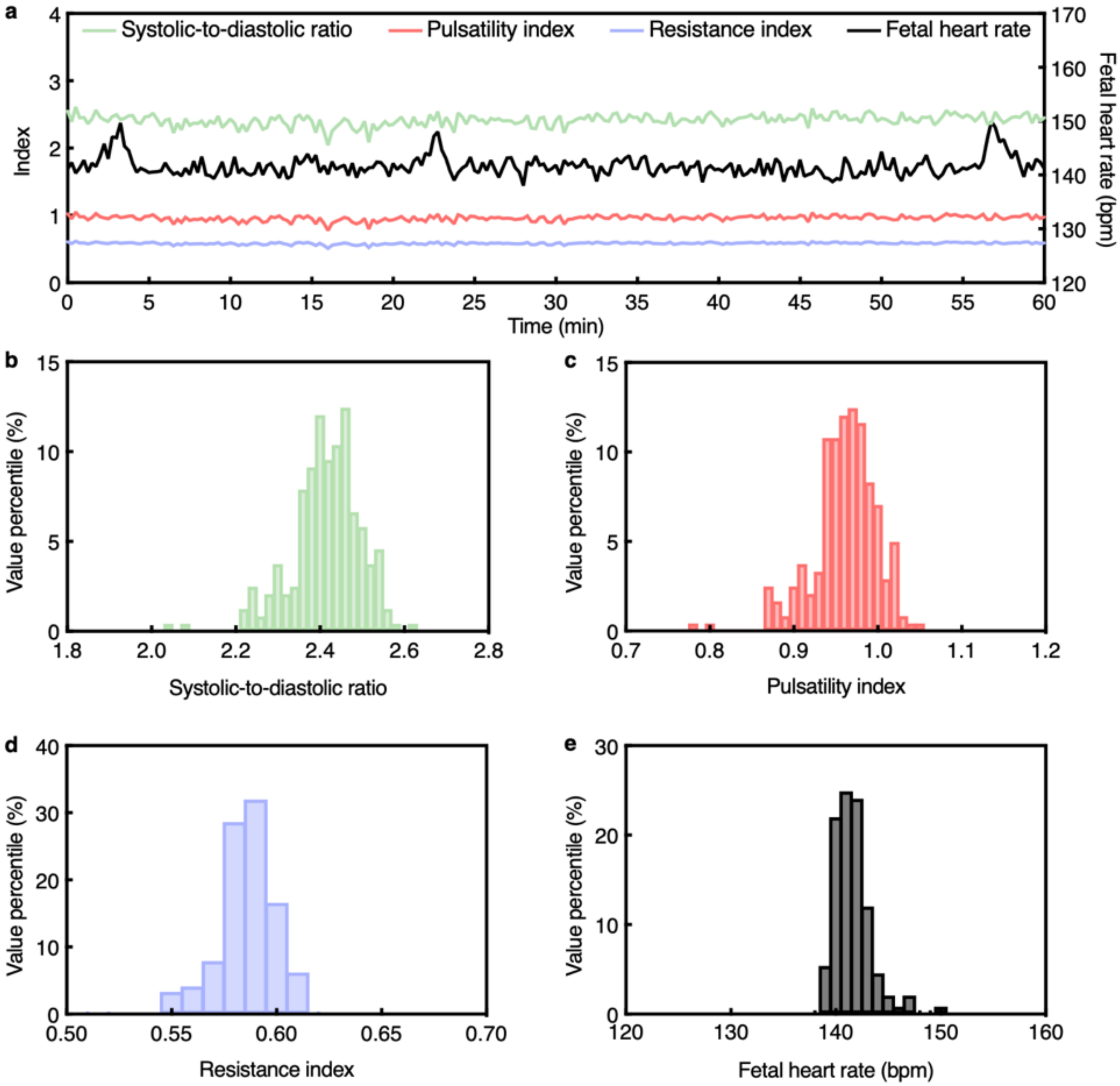

Supplementary Fig. 75 | Continuous fetal monitoring using the UPatch in Participant #36. a, Time series data from the 1-h continuous monitoring session. Systolic-to-diastolic ratio, pulsatility index, and resistance index are plotted on the left y-axis, and fetal heart rate is plotted on the right y-axis. Histograms of **b**, systolic-to-diastolic ratio, **c**, pulsatility index, **d**, resistance index, and **e**, fetal heart rate over the recording period.

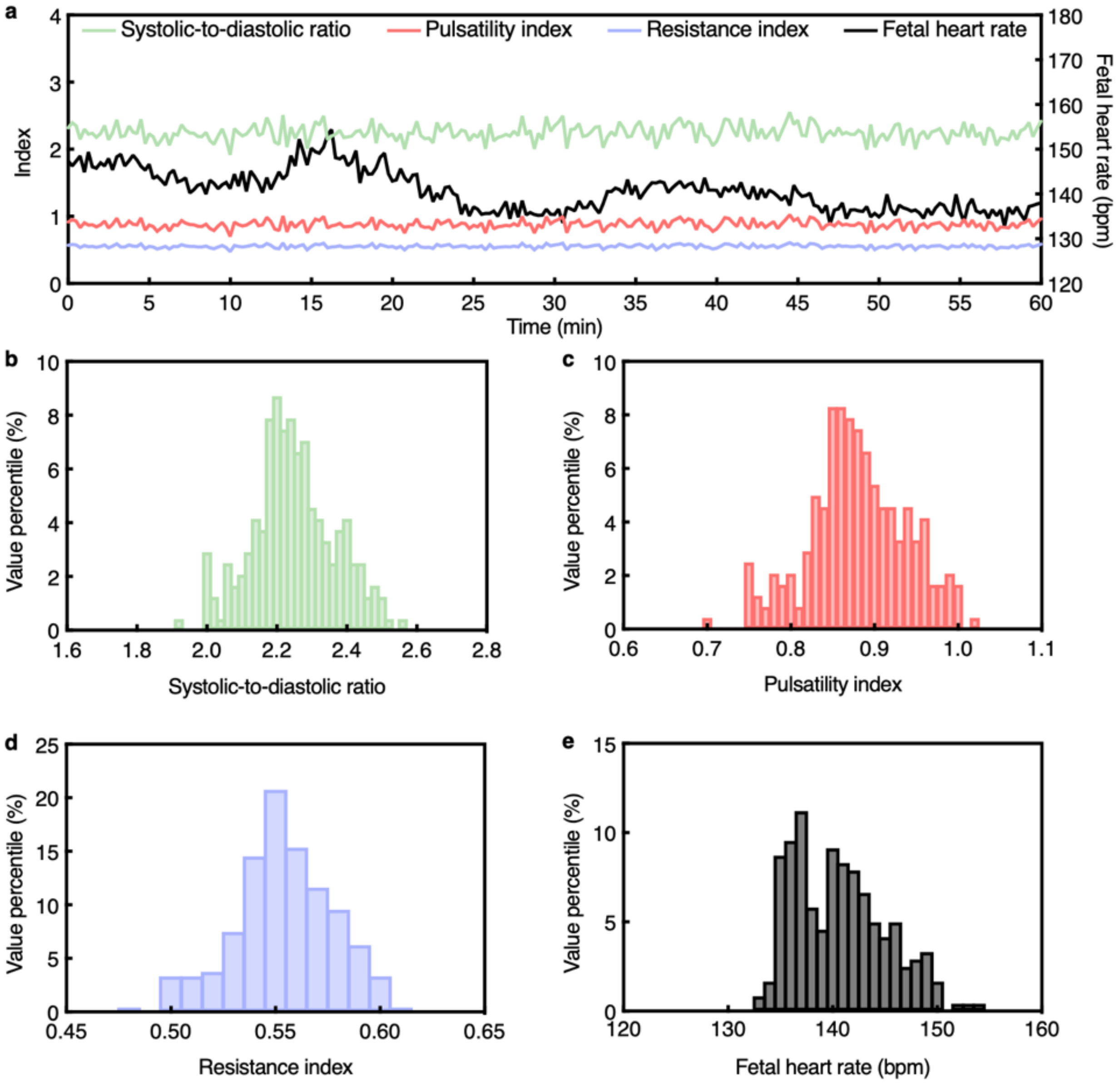

Supplementary Fig. 76 | Continuous fetal monitoring using the UPatch in Participant #37. a, Time series data from the 1-h continuous monitoring session. Systolic-to-diastolic ratio, pulsatility index, and resistance index are plotted on the left y-axis, and fetal heart rate is plotted on the right y-axis. Histograms of **b**, systolic-to-diastolic ratio, **c**, pulsatility index, **d**, resistance index, and **e**, fetal heart rate over the recording period.

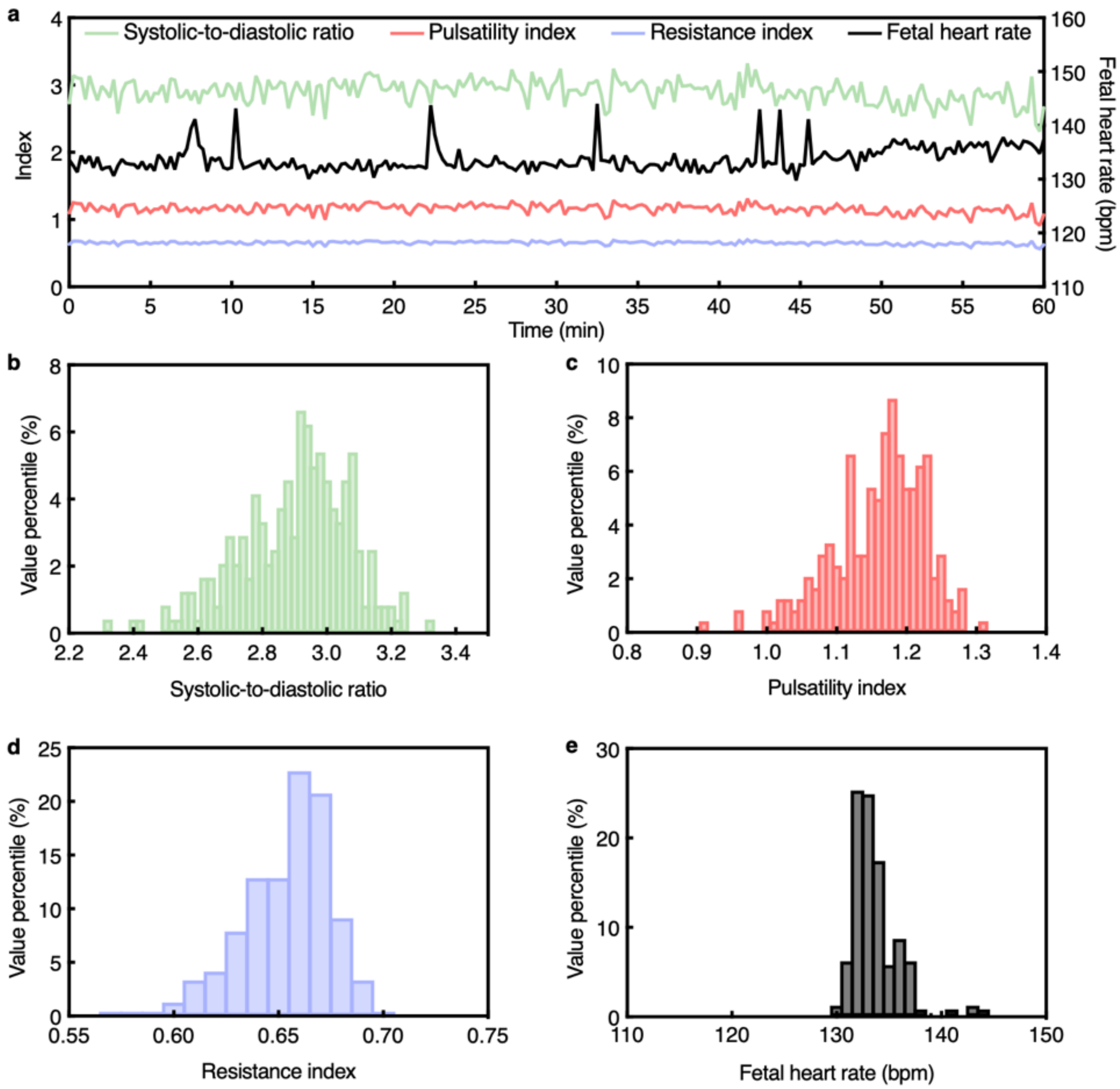

Supplementary Fig. 77 | Continuous fetal monitoring using the UPatch in Participant #38. a, Time series data from the 1-h continuous monitoring session. Systolic-to-diastolic ratio, pulsatility index, and resistance index are plotted on the left y-axis, and fetal heart rate is plotted on the right y-axis. Histograms of **b**, systolic-to-diastolic ratio, **c**, pulsatility index, **d**, resistance index, and **e**, fetal heart rate over the recording period.

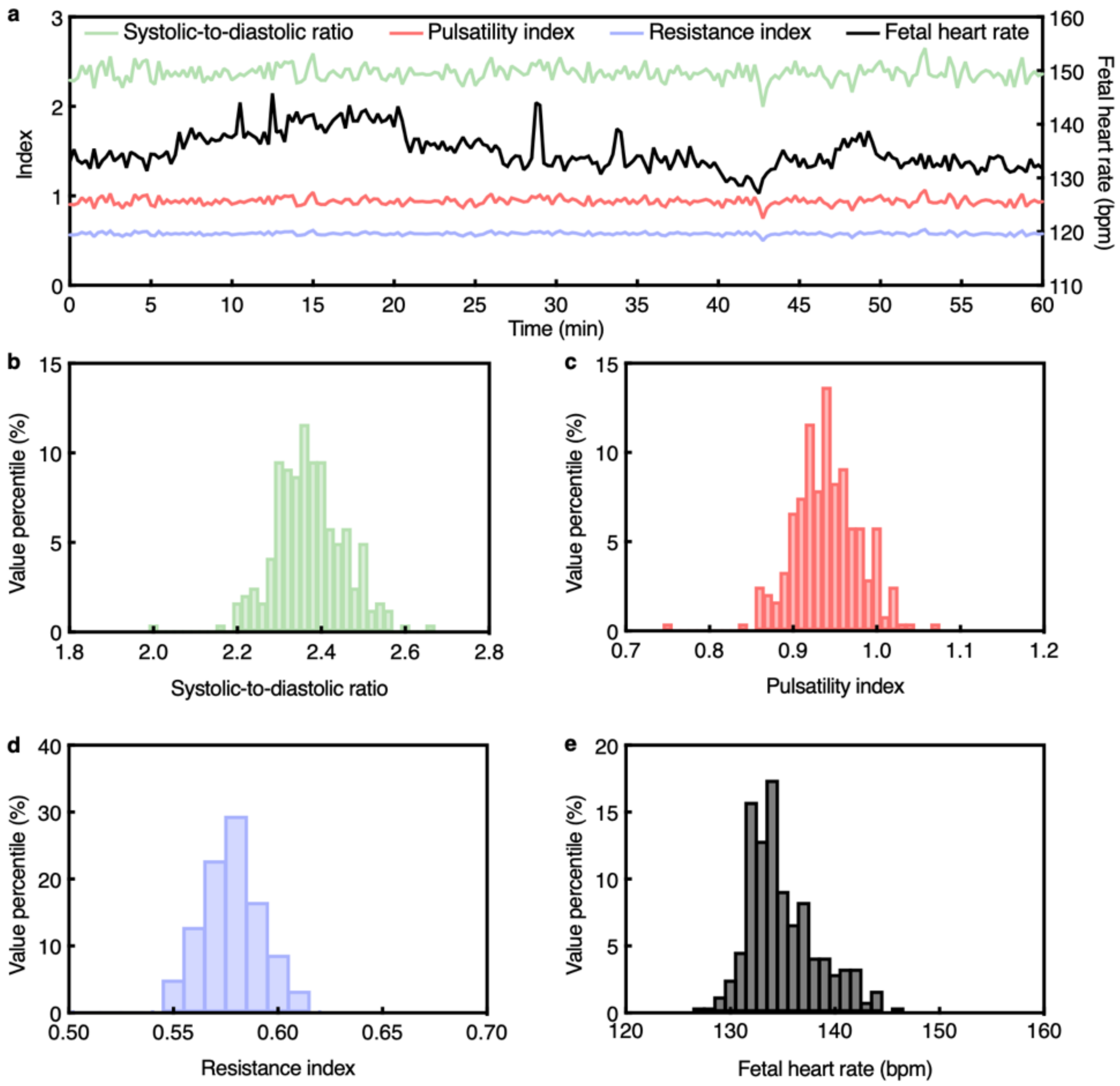

Supplementary Fig. 78 | Continuous fetal monitoring using the UPatch in Participant #39. a, Time series data from the 1-h continuous monitoring session. Systolic-to-diastolic ratio, pulsatility index, and resistance index are plotted on the left y-axis, and fetal heart rate is plotted on the right y-axis. Histograms of **b**, systolic-to-diastolic ratio, **c**, pulsatility index, **d**, resistance index, and **e**, fetal heart rate over the recording period.

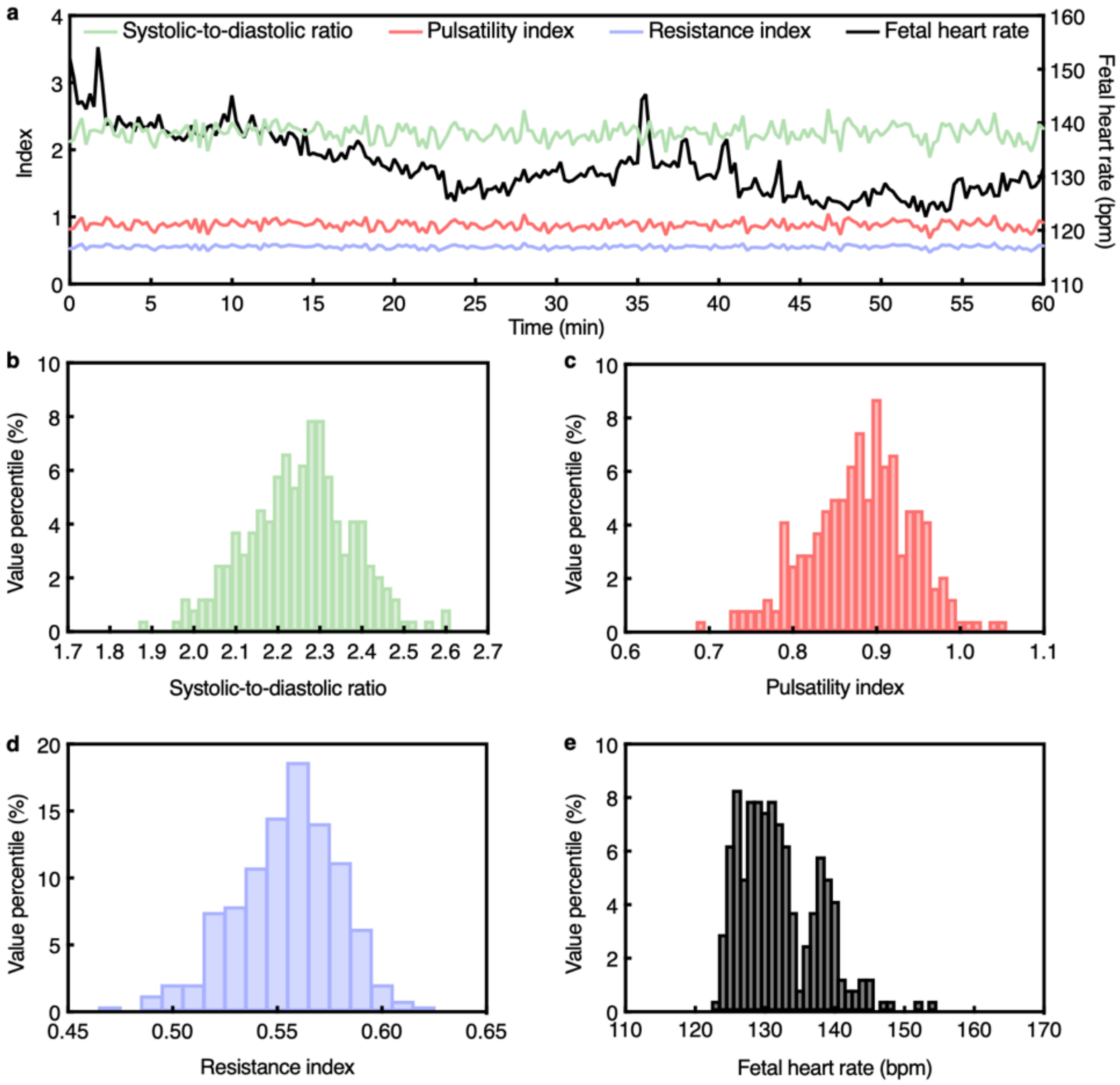

Supplementary Fig. 79 | Continuous fetal monitoring using the UPatch in Participant #40. a, Time series data from the 1-h continuous monitoring session. Systolic-to-diastolic ratio, pulsatility index, and resistance index are plotted on the left y-axis, and fetal heart rate is plotted on the right y-axis. Histograms of **b**, systolic-to-diastolic ratio, **c**, pulsatility index, **d**, resistance index, and **e**, fetal heart rate over the recording period.

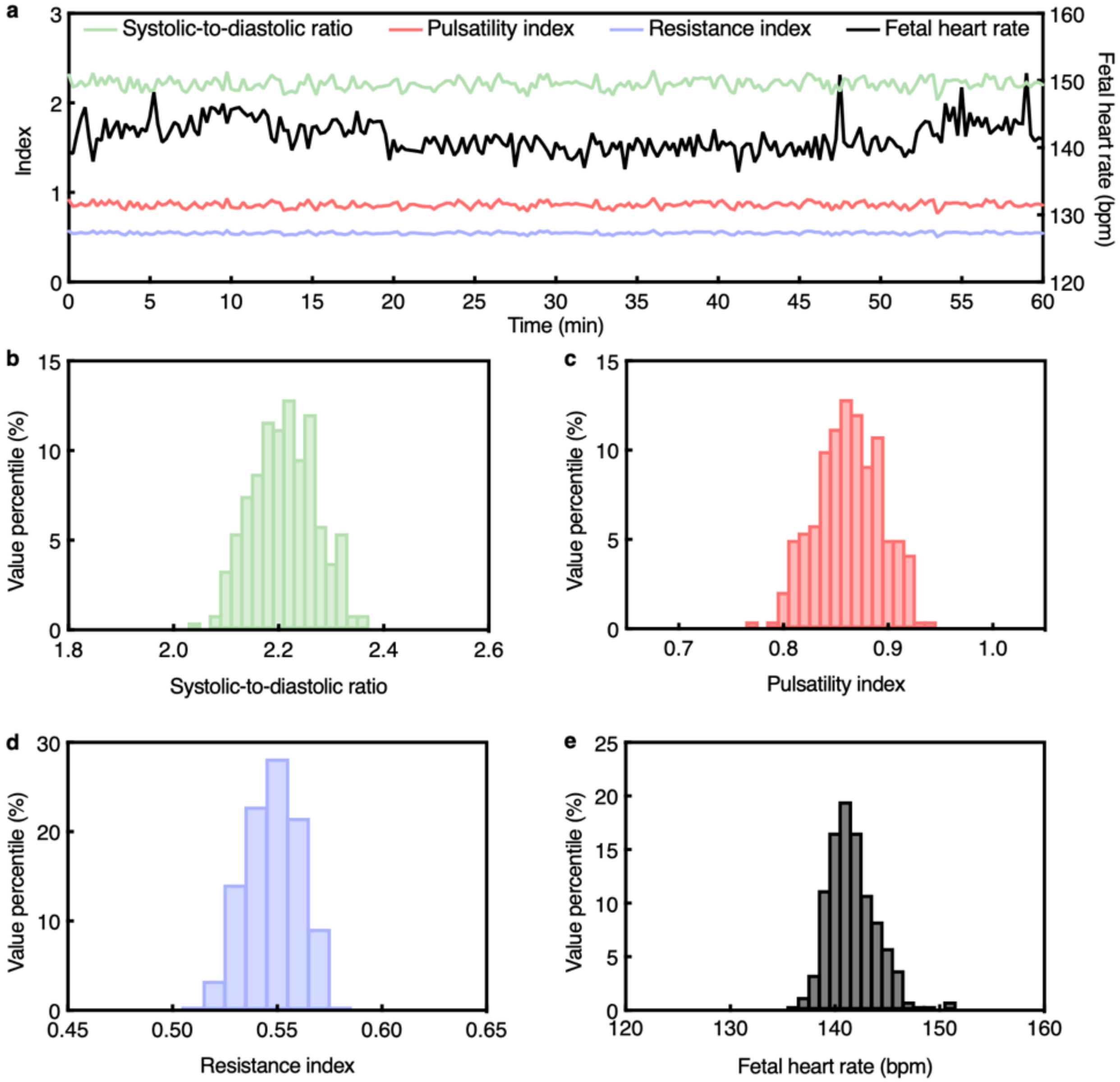

Supplementary Fig. 80 | Continuous fetal monitoring using the UPatch in Participant #41. a, Time series data from the 1-h continuous monitoring session. Systolic-to-diastolic ratio, pulsatility index, and resistance index are plotted on the left y-axis, and fetal heart rate is plotted on the right y-axis. Histograms of **b**, systolic-to-diastolic ratio, **c**, pulsatility index, **d**, resistance index, and **e**, fetal heart rate over the recording period.

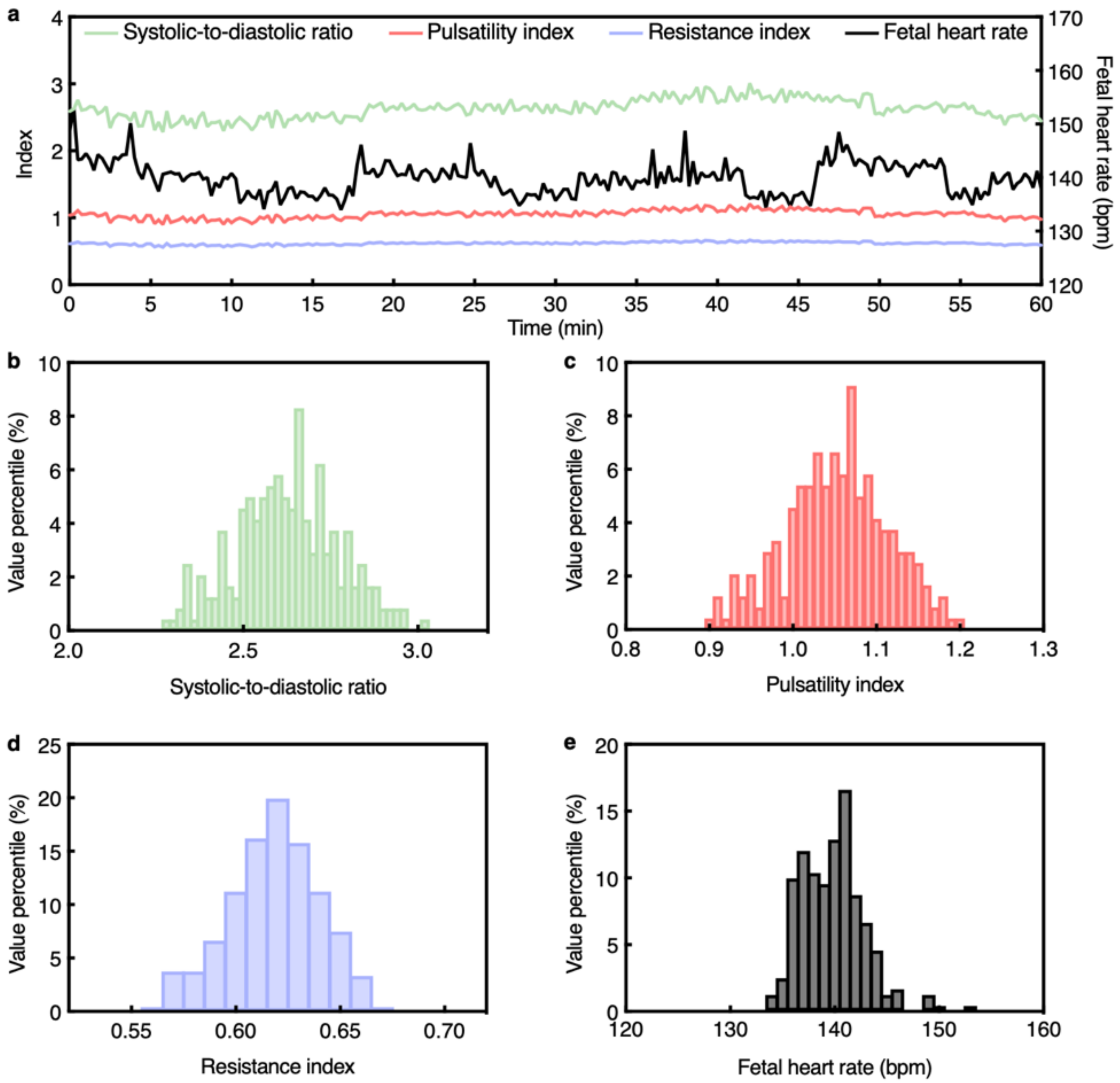

Supplementary Fig. 81 | Continuous fetal monitoring using the UPatch in Participant #42. a, Time series data from the 1-h continuous monitoring session. Systolic-to-diastolic ratio, pulsatility index, and resistance index are plotted on the left y-axis, and fetal heart rate is plotted on the right y-axis. Histograms of **b**, systolic-to-diastolic ratio, **c**, pulsatility index, **d**, resistance index, and **e**, fetal heart rate over the recording period.

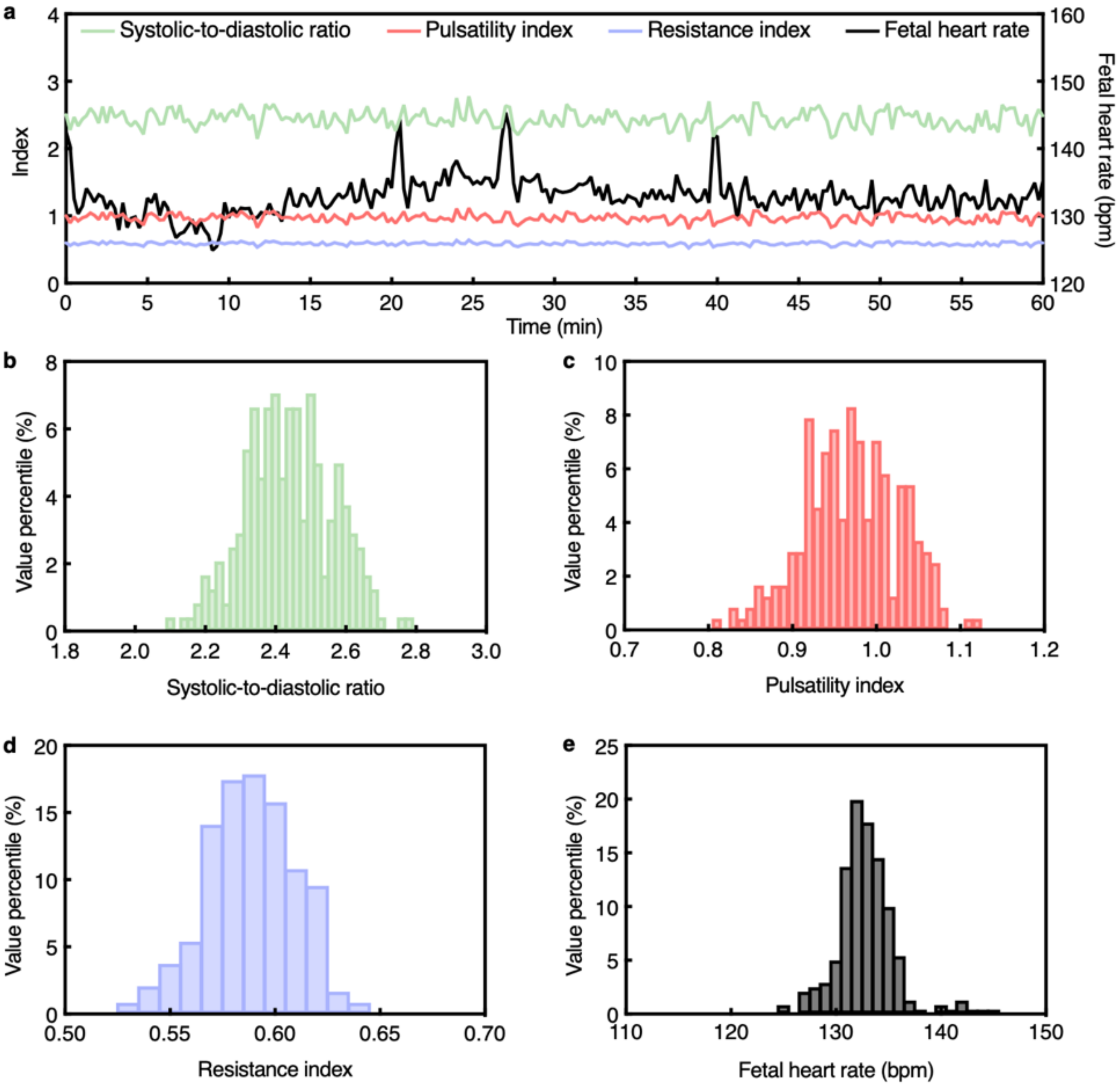

Supplementary Fig. 82 | Continuous fetal monitoring using the UPatch in Participant #43. a, Time series data from the 1-h continuous monitoring session. Systolic-to-diastolic ratio, pulsatility index, and resistance index are plotted on the left y-axis, and fetal heart rate is plotted on the right y-axis. Histograms of **b**, systolic-to-diastolic ratio, **c**, pulsatility index, **d**, resistance index, and **e**, fetal heart rate over the recording period.

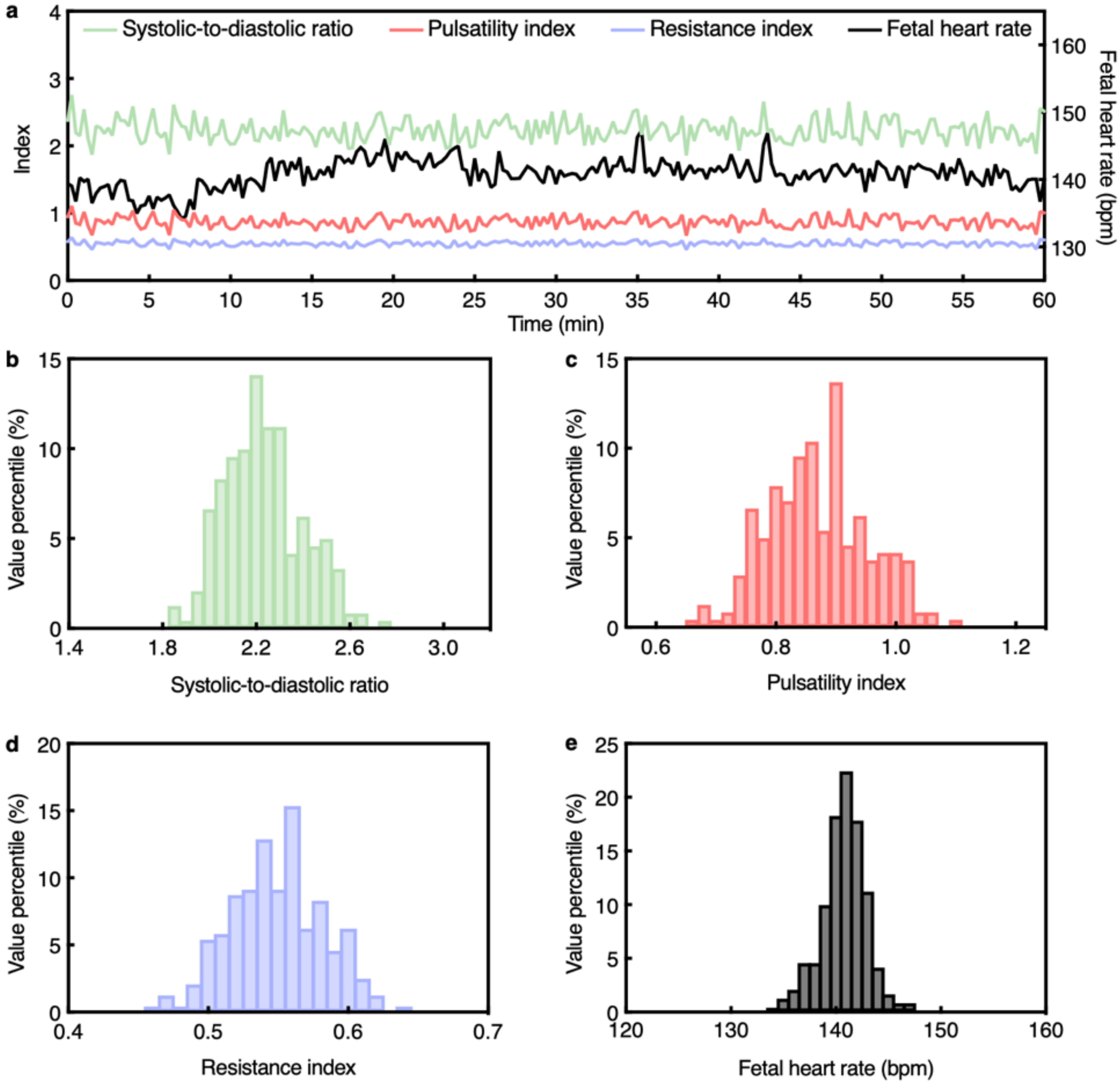

Supplementary Fig. 83 | Continuous fetal monitoring using the UPatch in Participant #44. a, Time series data from the 1-h continuous monitoring session. Systolic-to-diastolic ratio, pulsatility index, and resistance index are plotted on the left y-axis, and fetal heart rate is plotted on the right y-axis. Histograms of **b**, systolic-to-diastolic ratio, **c**, pulsatility index, **d**, resistance index, and **e**, fetal heart rate over the recording period.

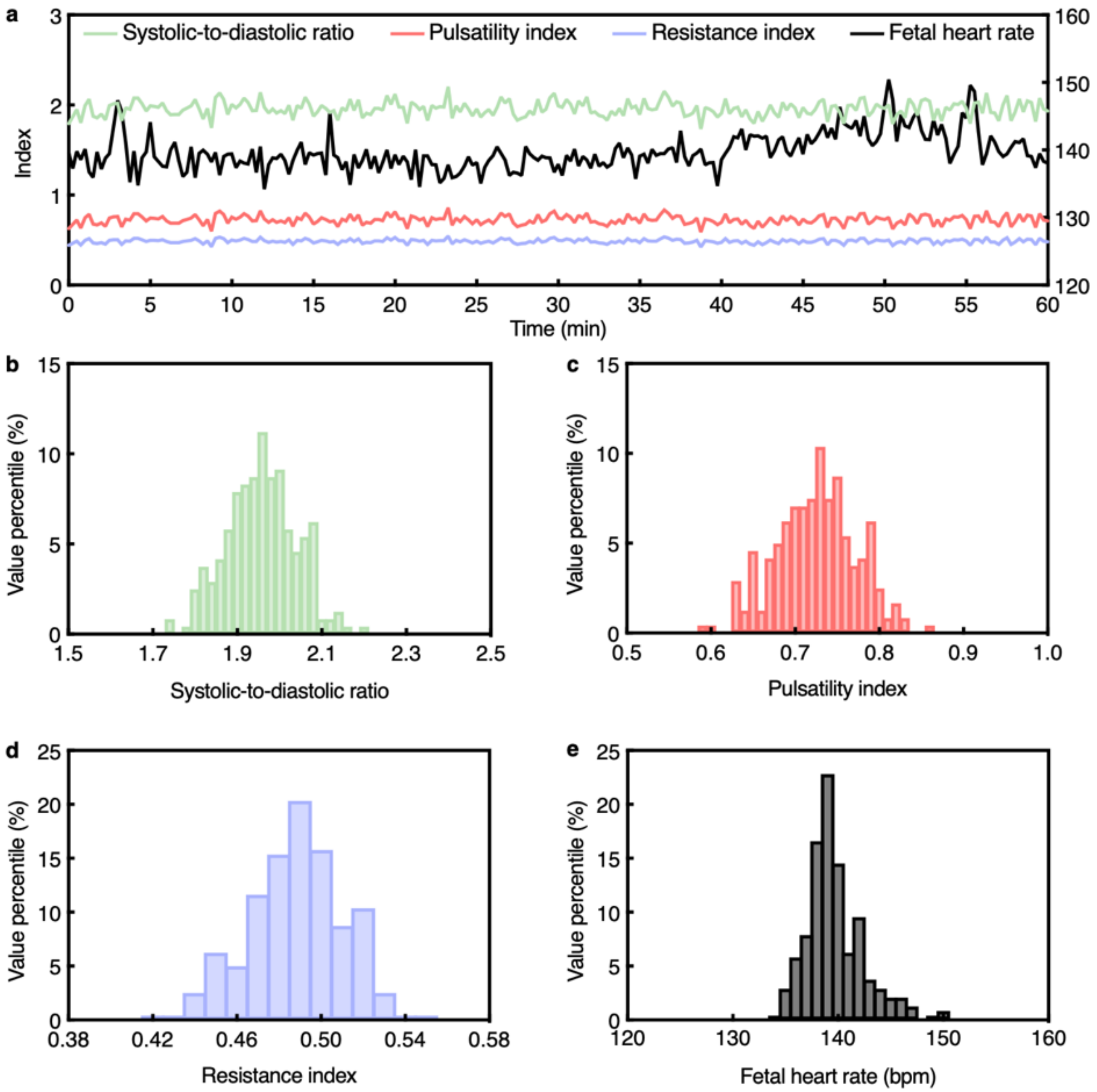

Supplementary Fig. 84 | Continuous fetal monitoring using the UPatch in Participant #45. a, Time series data from the 1-h continuous monitoring session. Systolic-to-diastolic ratio, pulsatility index, and resistance index are plotted on the left y-axis, and fetal heart rate is plotted on the right y-axis. Histograms of **b**, systolic-to-diastolic ratio, **c**, pulsatility index, **d**, resistance index, and **e**, fetal heart rate over the recording period.

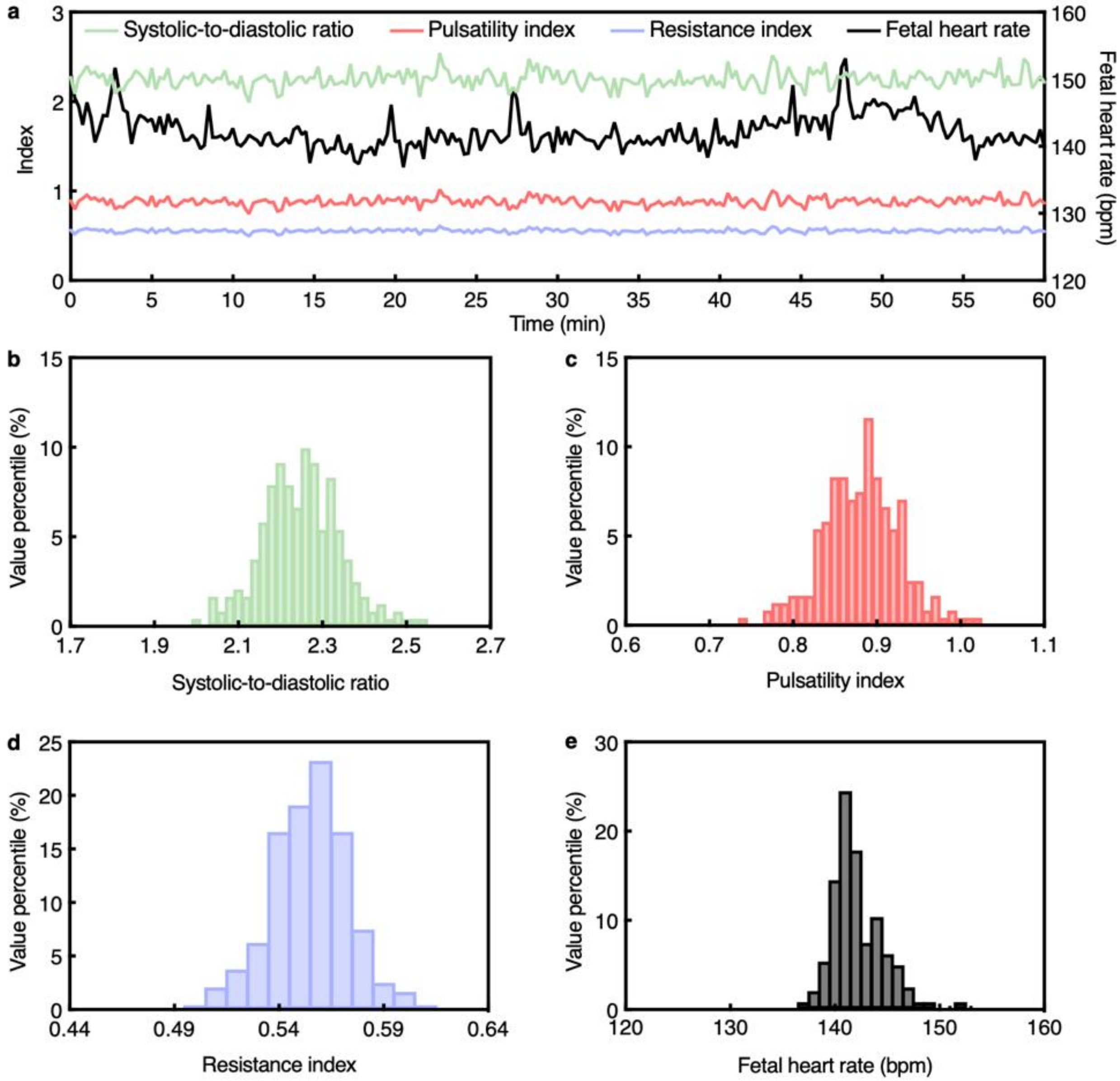

Supplementary Fig. 85 | Continuous fetal monitoring using the UPatch in Participant #46. a, Time series data from the 1-h continuous monitoring session. Systolic-to-diastolic ratio, pulsatility index, and resistance index are plotted on the left y-axis, and fetal heart rate is plotted on the right y-axis. Histograms of **b**, systolic-to-diastolic ratio, **c**, pulsatility index, **d**, resistance index, and **e**, fetal heart rate over the recording period.

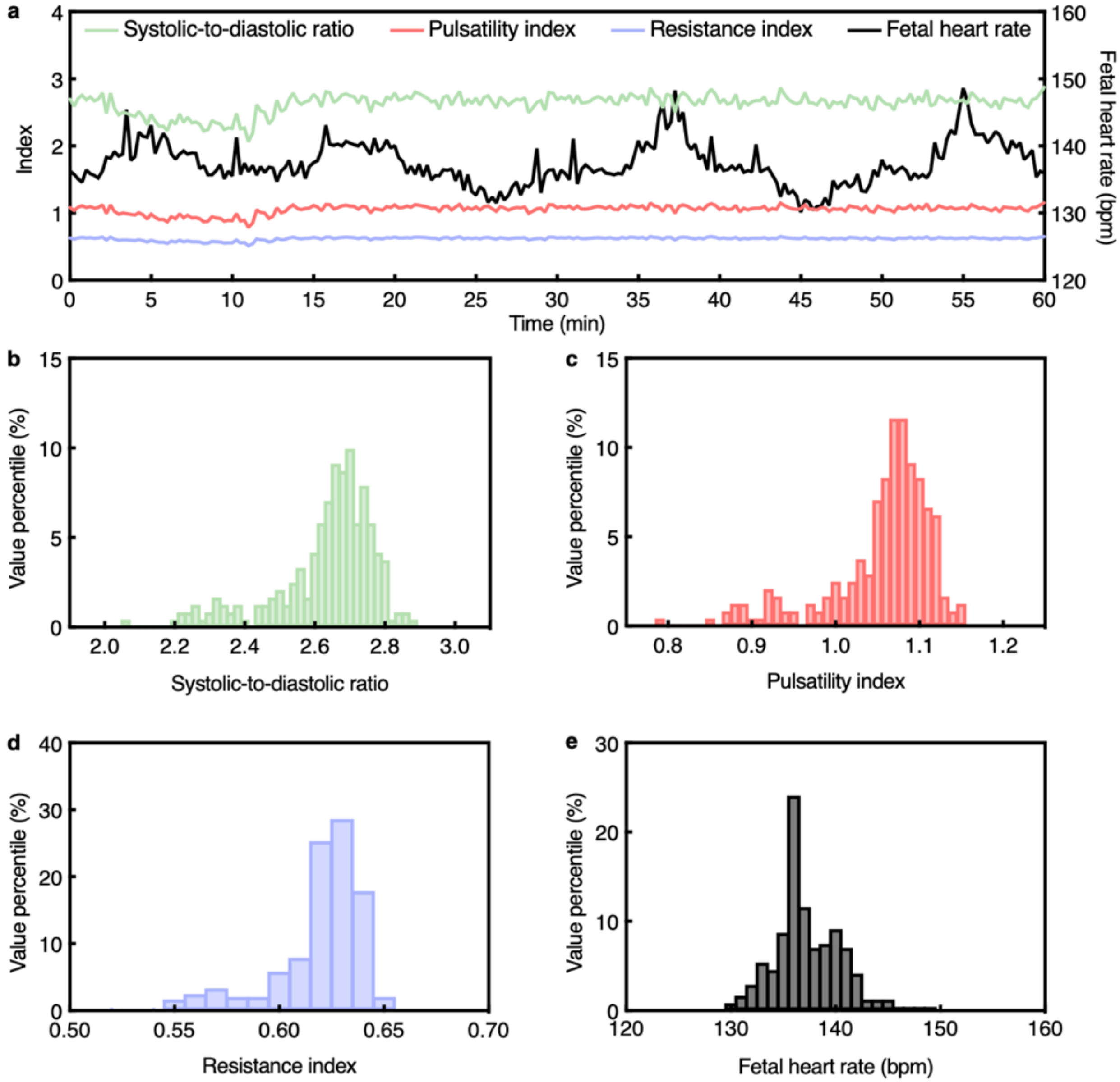

Supplementary Fig. 86 | Continuous fetal monitoring using the UPatch in Participant #47. a, Time series data from the 1-h continuous monitoring session. Systolic-to-diastolic ratio, pulsatility index, and resistance index are plotted on the left y-axis, and fetal heart rate is plotted on the right y-axis. Histograms of **b**, systolic-to-diastolic ratio, **c**, pulsatility index, **d**, resistance index, and **e**, fetal heart rate over the recording period.

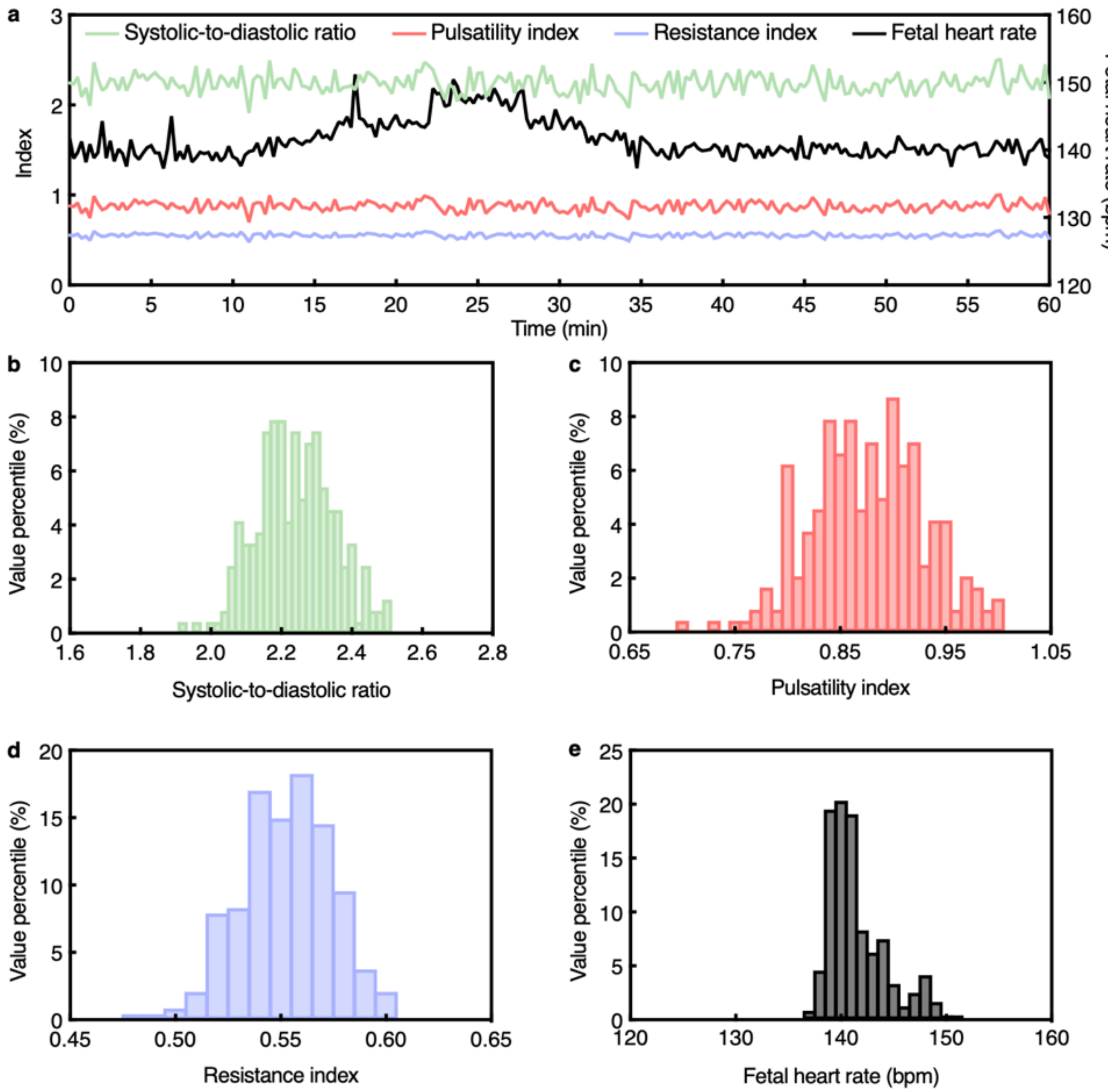

Supplementary Fig. 87 | Continuous fetal monitoring using the UPatch in Participant #48. a, Time series data from the 1-h continuous monitoring session. Systolic-to-diastolic ratio, pulsatility index, and resistance index are plotted on the left y-axis, and fetal heart rate is plotted on the right y-axis. Histograms of **b**, systolic-to-diastolic ratio, **c**, pulsatility index, **d**, resistance index, and **e**, fetal heart rate over the recording period.

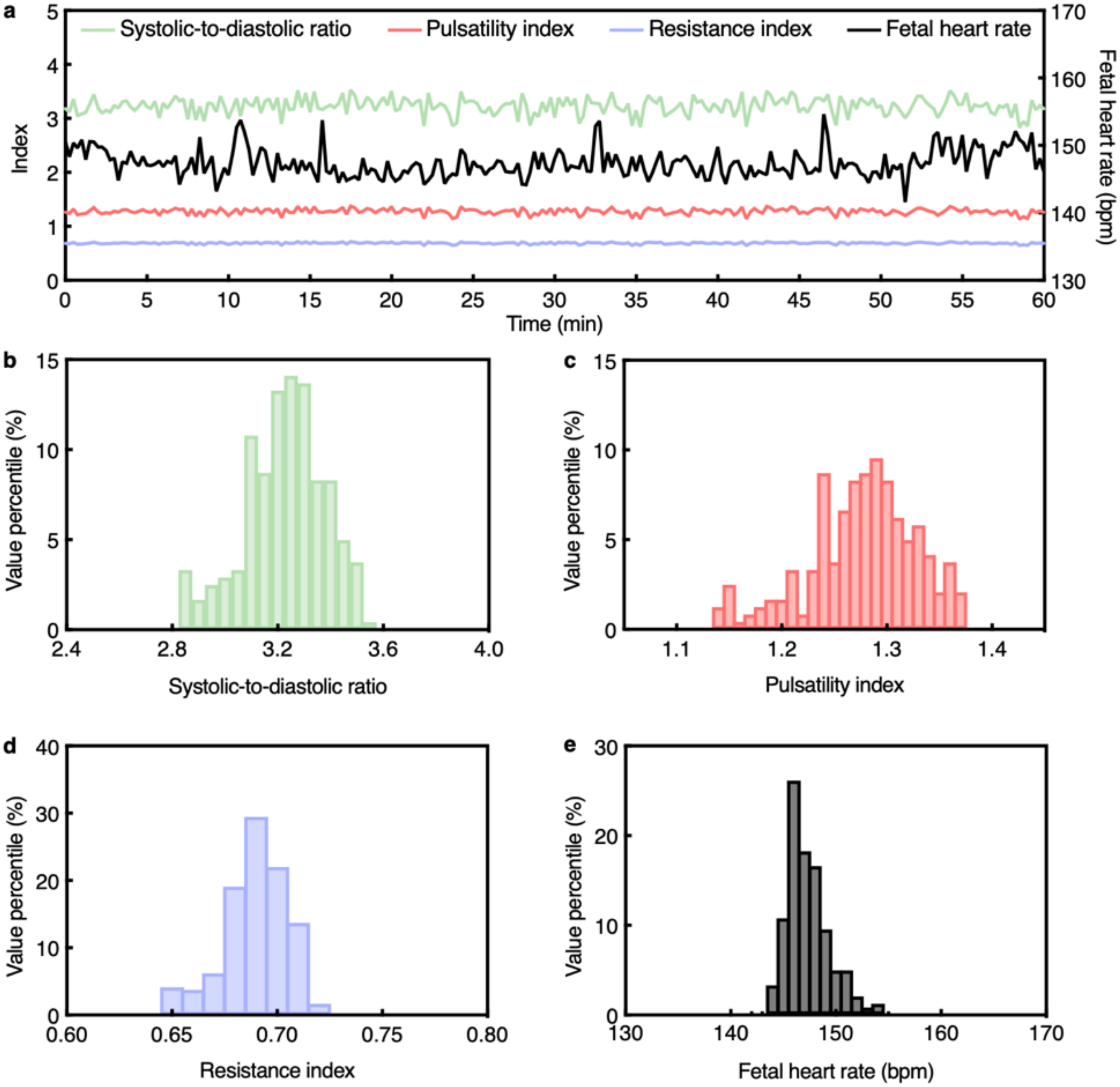

Supplementary Fig. 88 | Continuous fetal monitoring using the UPatch in Participant #49. a, Time series data from the 1-h continuous monitoring session. Systolic-to-diastolic ratio, pulsatility index, and resistance index are plotted on the left y-axis, and fetal heart rate is plotted on the right y-axis. Histograms of **b**, systolic-to-diastolic ratio, **c**, pulsatility index, **d**, resistance index, and **e**, fetal heart rate over the recording period.

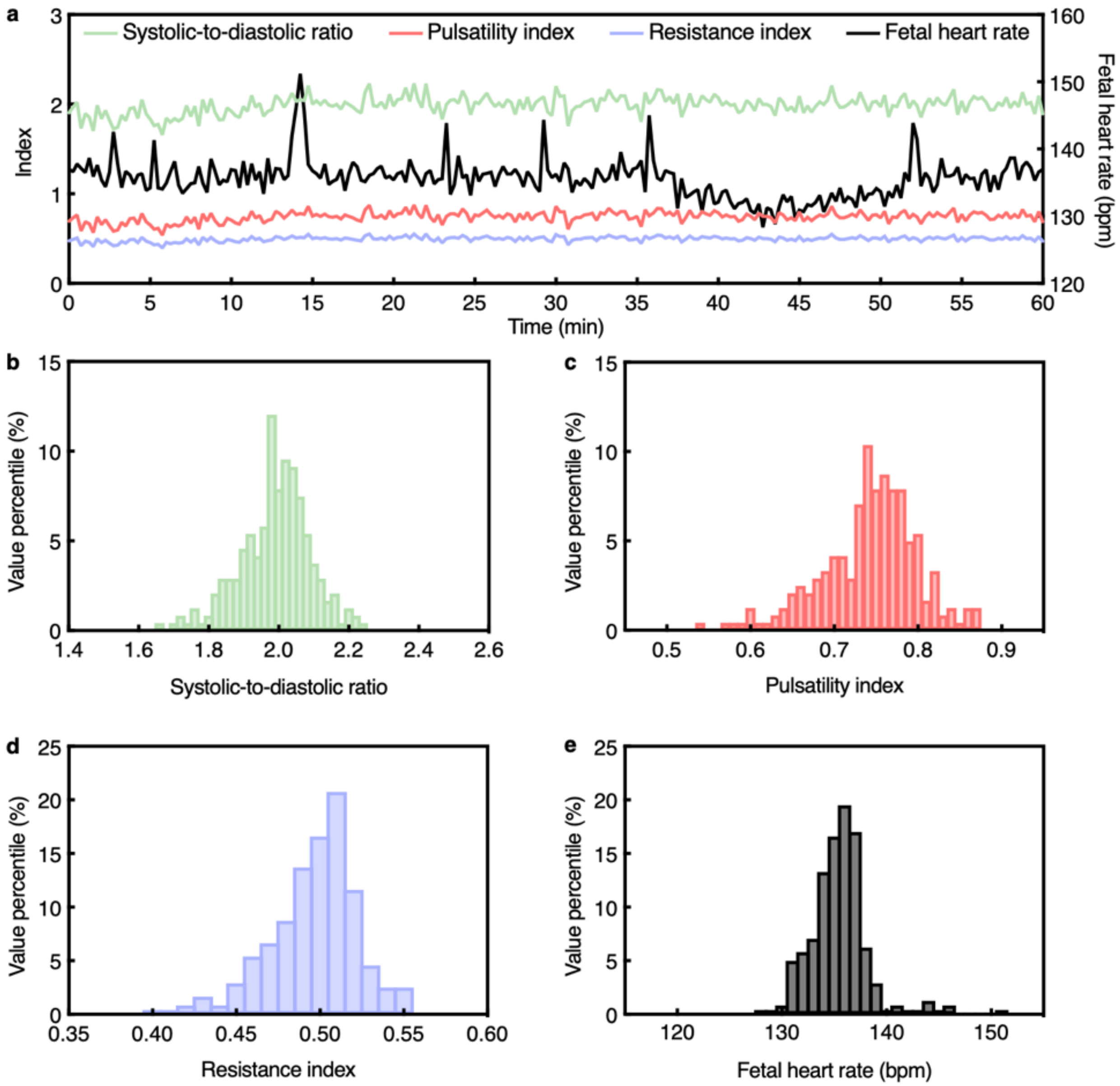

Supplementary Fig. 89 | Continuous fetal monitoring using the UPatch in Participant #50. a, Time series data from the 1-h continuous monitoring session. Systolic-to-diastolic ratio, pulsatility index, and resistance index are plotted on the left y-axis, and fetal heart rate is plotted on the right y-axis. Histograms of **b**, systolic-to-diastolic ratio, **c**, pulsatility index, **d**, resistance index, and **e**, fetal heart rate over the recording period.

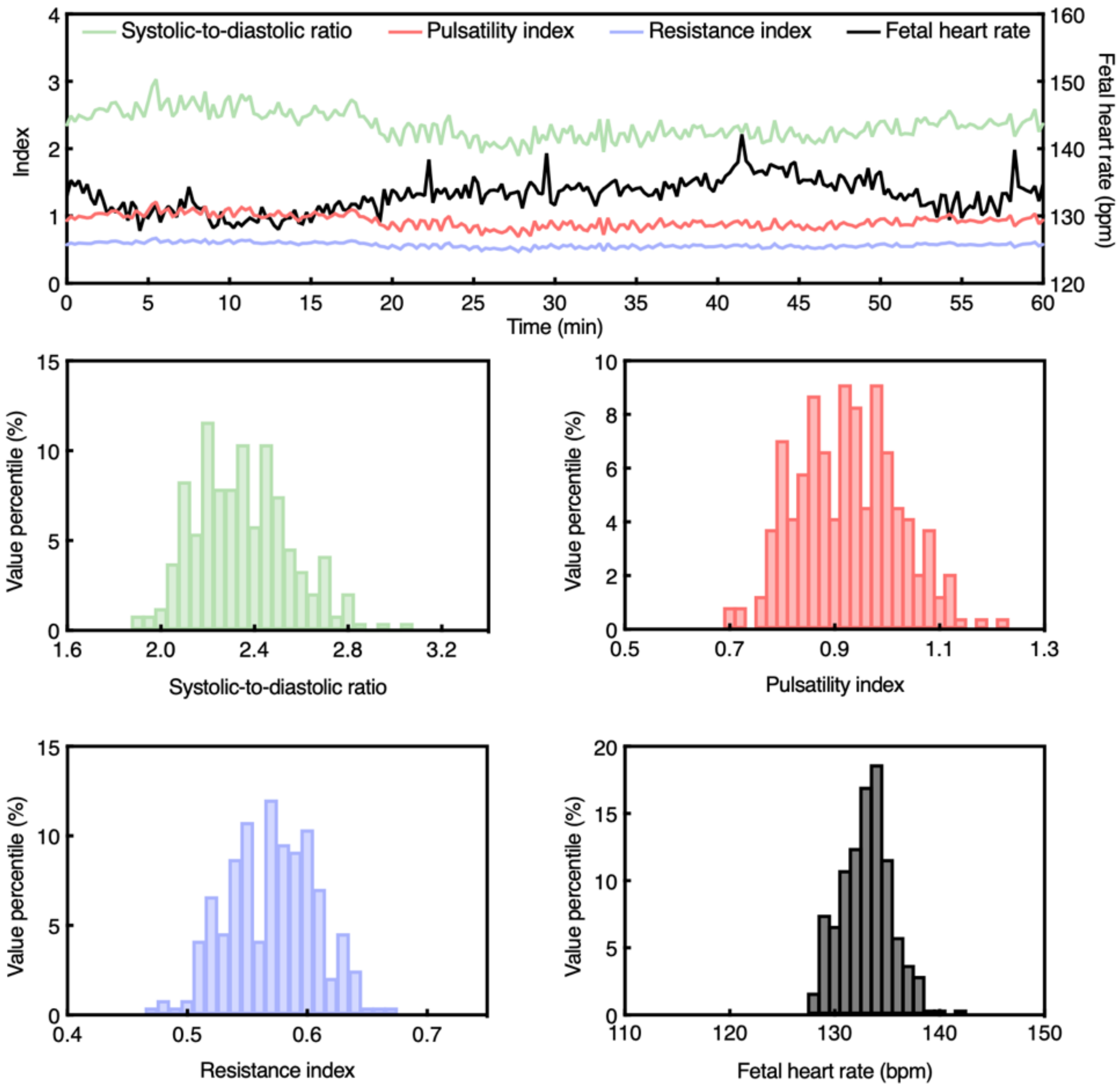

Supplementary Fig. 90 | Continuous fetal monitoring using the UPatch in Participant #51. a, Time series data from the 1-h continuous monitoring session. Systolic-to-diastolic ratio, pulsatility index, and resistance index are plotted on the left y-axis, and fetal heart rate is plotted on the right y-axis. Histograms of **b**, systolic-to-diastolic ratio, **c**, pulsatility index, **d**, resistance index, and **e**, fetal heart rate over the recording period.

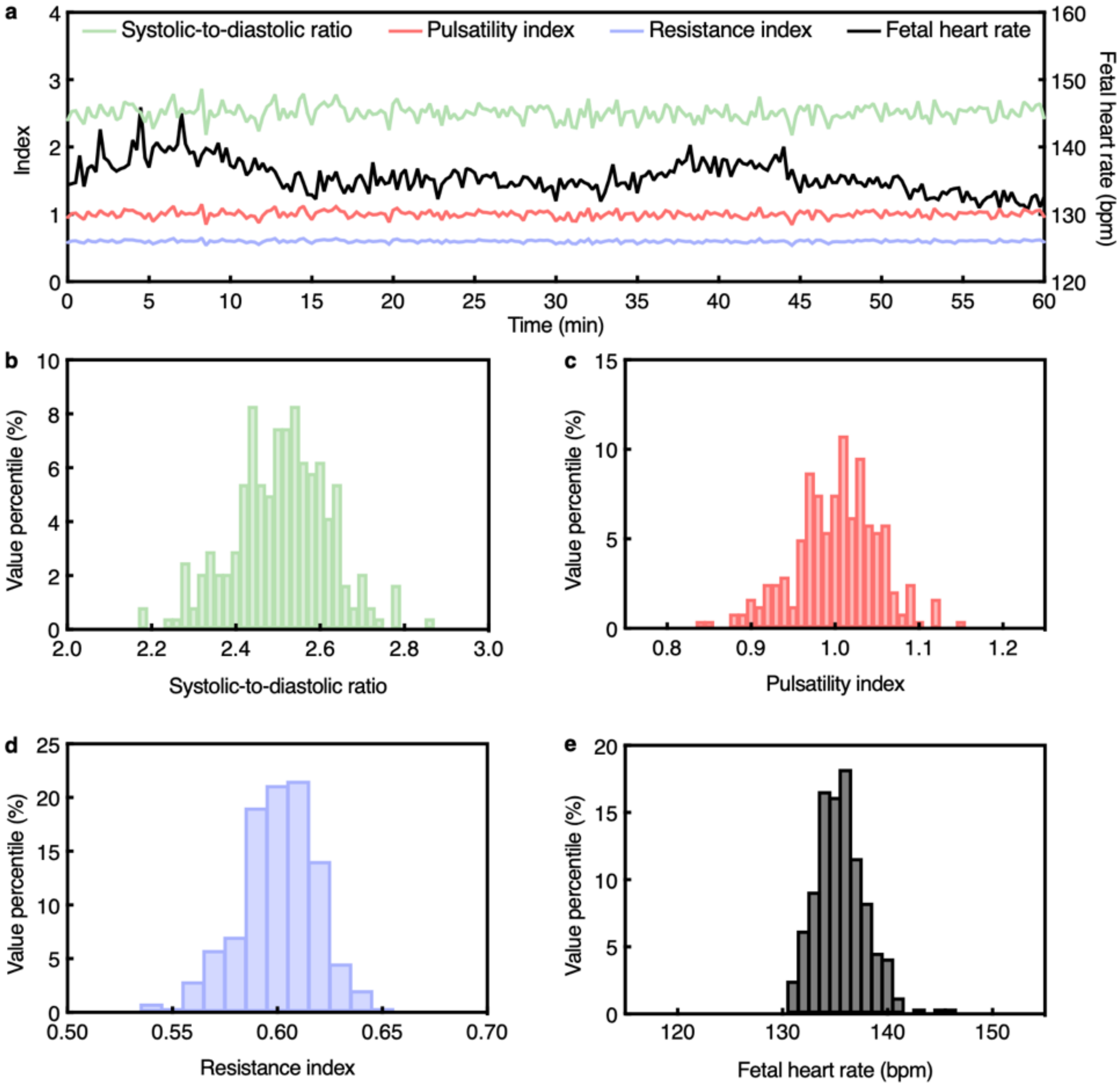

Supplementary Fig. 91 | Continuous fetal monitoring using the UPatch in Participant #52. a, Time series data from the 1-h continuous monitoring session. Systolic-to-diastolic ratio, pulsatility index, and resistance index are plotted on the left y-axis, and fetal heart rate is plotted on the right y-axis. Histograms of **b**, systolic-to-diastolic ratio, **c**, pulsatility index, **d**, resistance index, and **e**, fetal heart rate over the recording period.

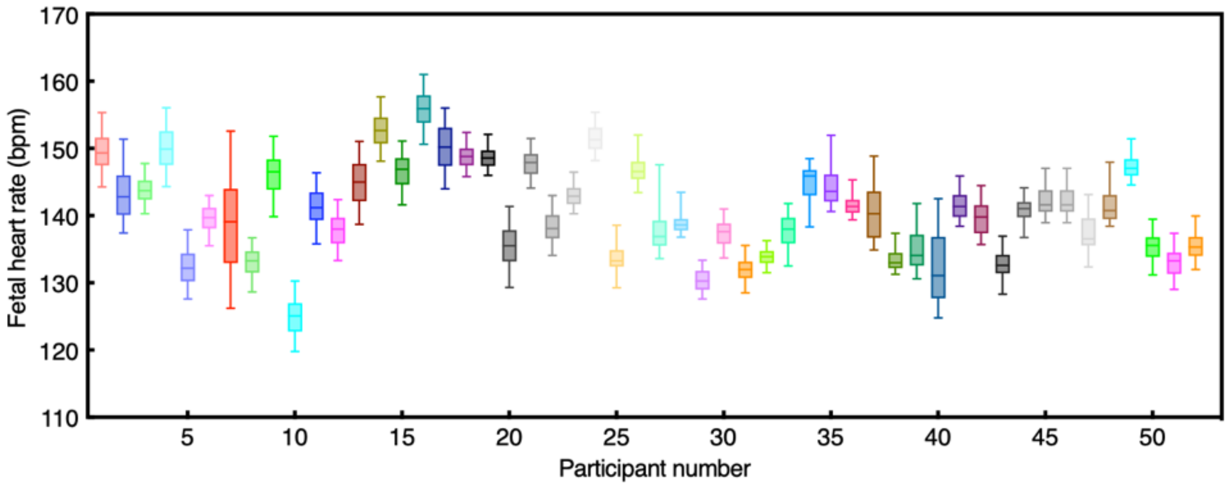

Supplementary Fig. 92 | Box plots of fetal heart rate during continuous monitoring. Distribution of fetal heart rate values across the full monitoring session for all participants. Each box represents the interquartile range (25th to 75th percentiles), the whiskers denote the 5th to 95th percentile range, and the midline indicates the median. The observed variability reflects dynamic physiological changes during the monitoring period.

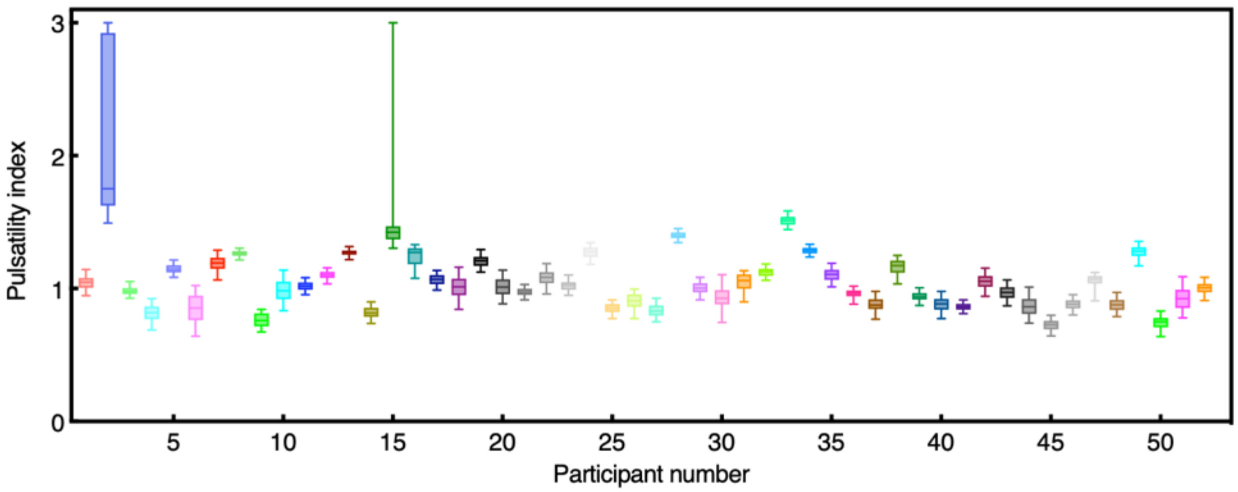

Supplementary Fig. 93 | Box plots of pulsatility index during continuous monitoring. Distribution of pulsatility index values across the full monitoring session for all participants. Each box represents the interquartile range (25th to 75th percentiles), the whiskers denote the 5th to 95th percentile range, and the midline indicates the median. The observed variability reflects dynamic physiological changes during the monitoring period.

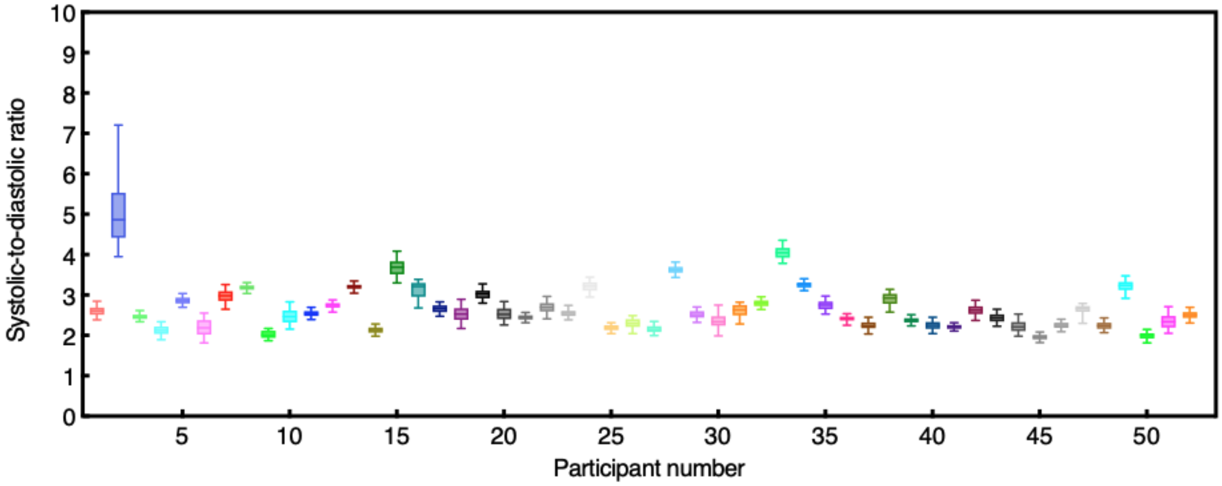

Supplementary Fig. 94 | Box plots of systolic-to-diastolic ratio during continuous monitoring. Distribution of systolic-to-diastolic ratio values across the full monitoring session for all participants. Each box represents the interquartile range (25th to 75th percentiles), the whiskers denote the 5th to 95th percentile range, and the midline indicates the median. The observed variability reflects dynamic physiological changes during the monitoring period. In Participants #2 and #15, systolic-to-diastolic ratios that could not be computed due to absent end diastolic flow were excluded from the analysis; only computable values were included.

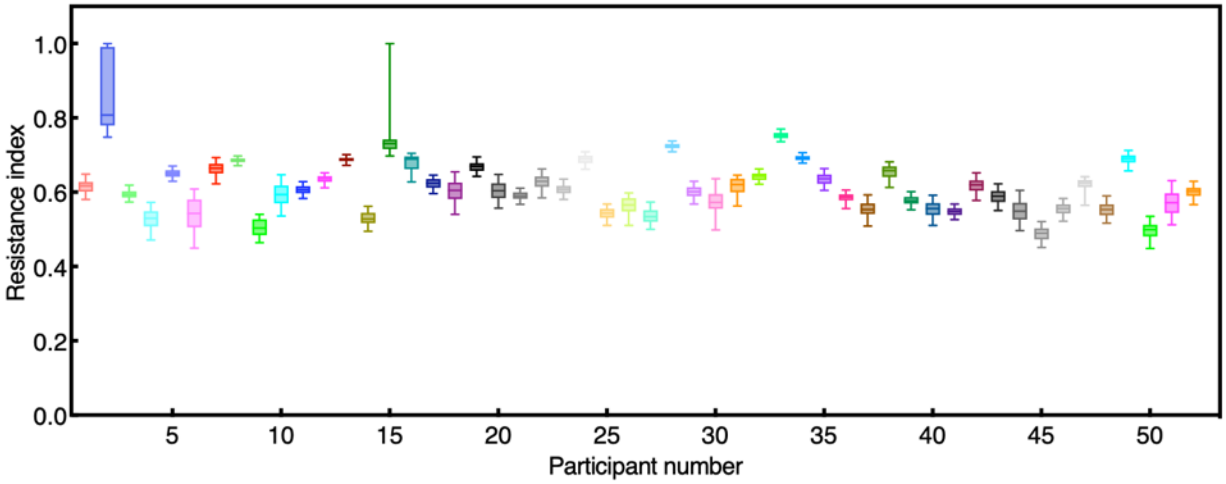

Supplementary Fig. 95 | Box plots of resistance index during continuous monitoring. Distribution of resistance index values across the full monitoring session for all participants. Each box represents the interquartile range (25th to 75th percentiles), the whiskers denote the 5th to 95th percentile range, and the midline indicates the median. The observed variability reflects dynamic physiological changes during the monitoring period.

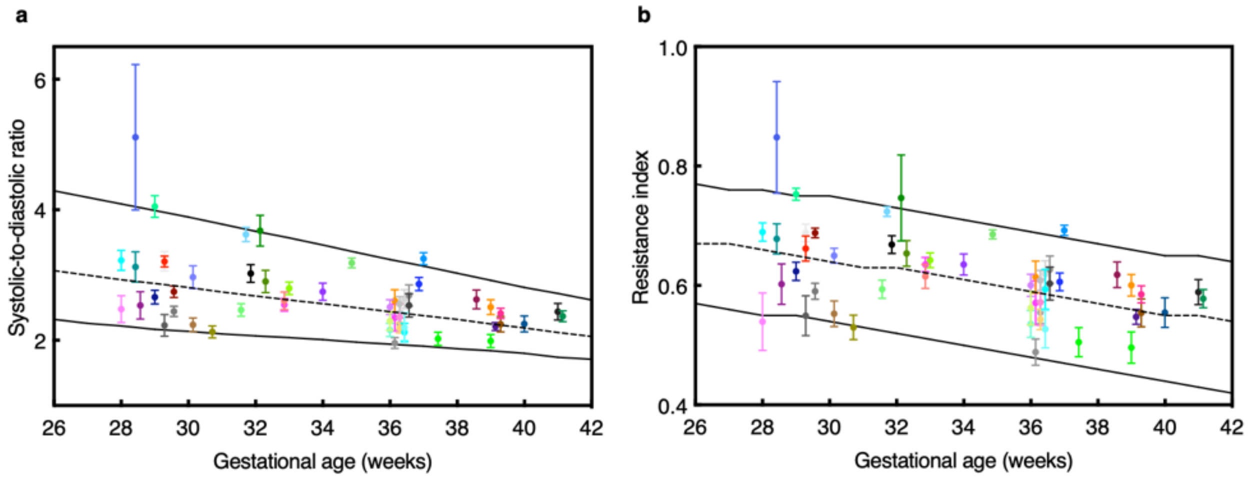

Supplementary Fig. 96 | Gestational trends in systolic-to-diastolic ratio and resistance index measured using the UPatch. a, Umbilical artery systolic-to-diastolic ratio plotted against gestational age. **b**, Umbilical artery resistance index plotted against gestational age. The black dashed line in each plot is the 50th percentile, and the solid black lines are the 5th and 95th percentiles of a widely used reference population[68]. Error bars denote ± standard deviation.

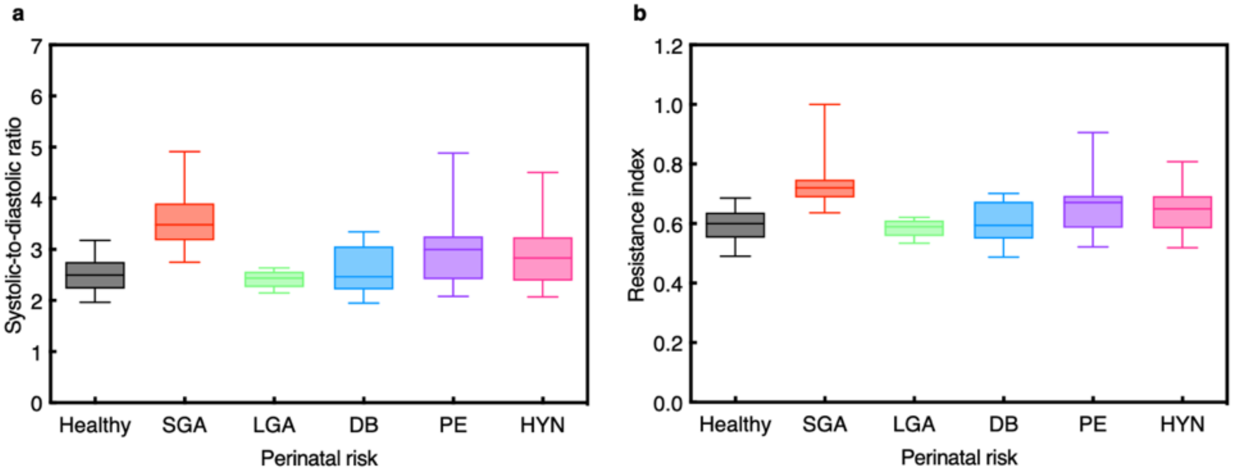

Supplementary Fig. 97 | Risk stratification in systolic-to-diastolic ratio and resistance index measured using the UPatch. Box plots of **a**, systolic-to-diastolic ratio and **b**, resistance index stratified by perinatal condition: healthy (31 participants, 217 data points), small for gestational age (SGA; 7 participants, 46 data points), large for gestational age (LGA; 3 participants, 21 data points), diabetes (DB; 6 participants, 42 data points), preeclampsia (PE; 7 participants, 47 data points), and maternal hypertension (HYN; 10 participants, 68 data points). Each box represents the interquartile range (25th to 75th percentiles), the whiskers denote the 5th to 95th percentile range, and the midline indicates the median. Each participant's data was segmented into 10-min intervals (n = 7 per participant). In Participants #2 and #15, systolic-to-diastolic ratios that could not be computed due to absent end diastolic flow were excluded from the analysis; only computable values were included.

Supplementary Video 1 | Real-time tracking. The UPatch can monitor the umbilical cord in the duplex image. The tracking algorithm can register a sample gate on the moving umbilical artery in real time. Then, blood flow spectra can be recorded from the umbilical arteries.

References

1 Rouse, D. J. Antepartum fetal surveillance ACOG practice bulletin, number 229. *Obstet Gynecol* **137**, E116-E127 (2021).

2 Grivell, R. M., Alfirevic, Z., Gyte, G. M. & Devane, D. Antenatal cardiotocography for fetal assessment. *Cochrane Database of Systematic Reviews* **9**, CD007863 (2015).

3 Warland, J. & Glover, P. Fetal movements: What are we telling women? *Women and Birth* **30**, 23-28 (2017).

4 Khalil, A. *et al.* ISUOG Practice Guidelines: performance of third‐trimester obstetric ultrasound scan. *Ultrasound in Obstetrics & Gynecology* **63**, 131-147 (2024).

5 Maslovich, M. & Burke, L. *Intrauterine Fetal Demise*. (StatPearls Publishing, 2022).

6 Collins, J. H. Umbilical cord accidents: Human studies. *Seminars in Perinatology* **26**, 79-82 (2002).

7 Oyelese, Y. & Ananth, C. V. Placental Abruption. *Obstetrics & Gynecology* **108**, 1005-1016 (2006).

8 Parry, S. & Strauss, J. F. Premature Rupture of the Fetal Membranes. *New England Journal of Medicine* **338**, 663-670 (1998).

9 Marzbanrad, F., Stroux, L. & Clifford, G. D. Cardiotocography and beyond: a review of one-dimensional Doppler ultrasound application in fetal monitoring. *Physiological Measurement* **39**, 08TR01 (2018).

10 Alim, A. & Imtiaz, M. H. Wearable Sensors for the Monitoring of Maternal Health—A Systematic Review. *Sensors* **23**, 2411 (2023).

11 Kim, J. *et al.* Skin-interfaced wireless biosensors for perinatal and paediatric health. *Nature Reviews Bioengineering* **1**, 631-647 (2023).

12 Porter, P. *et al.* Accuracy, interpretability and usability study of a wireless self-guided fetal heartbeat monitor compared to cardiotocography. *npj Digital Medicine* **5**, 167 (2022).

13 Kamala, B. A. *et al.* Implementation of a novel continuous fetal Doppler (Moyo) improves quality of intrapartum fetal heart rate monitoring in a resource-limited tertiary hospital in Tanzania: An observational study. *PLOS ONE* **13**, e0205698 (2018).

14 https://www.sonoline.com/sonoline-b-fetal-doppler.html.

15 https://edanusa.com/wp-content/uploads/sites/12/2020/06/SD1-Series-Specification-V1.0-20180524-1.pdf.

16 https://lib.store.turbify.net/lib/babybeat/BabyBeatManual.pdf.

17 Freeman, R. K., Garite, T. J., Nageotte, M. P. & Miller, L. A. *Fetal Heart Rate Monitoring*. (Lippincott Williams & Wilkins, 2012).

18 https://my.getzhealthcare.com/getzhealthcare/products/ge-healthcare/corometrics-250cx/corometrics250cx_datasheet.pdf.

19 https://www.usa.philips.com/healthcare/product/HC865071/avalon-fm50-fetal-monitor.

20 Harkey, K. T., Casale, M. B., Pantelopoulos, A. A. & Zurcher, M. A. Assessing the Clinical Use of a Novel, Mobile Fetal Monitoring Device. *Obstetrics & Gynecology* **123**, 55S (2014).

21 Kawakita, T. *et al.* Neonatal complications associated with use of fetal scalp electrode: a retrospective study. *BJOG: An International Journal of Obstetrics & Gynaecology* **123**, 1797-1803 (2016).

22 Wilmink, F. A., Wilms, F. F., Heydanus, R., Mol, B. W. J. & Papatsonis, D. N. M. Fetal complications after placement of an intrauterine pressure catheter: A report of two cases

and review of the literature. *The Journal of Maternal-Fetal & Neonatal Medicine* **21**, 880-883 (2008).

23 Ryu, D. *et al.* Comprehensive pregnancy monitoring with a network of wireless, soft, and flexible sensors in high- and low-resource health settings. *Proceedings of the National Academy of Sciences* **118**, e2100466118 (2021).

24 Nguyen, K. *et al.* Wearable Fetal Monitoring Solution for Improved Mobility During Labor & Delivery. *Annu Int Conf IEEE Eng Med Biol Soc* **2018**, 4397-4400 (2018).

25 Hayes‐Gill, B. R. Monica Healthcare: From the research laboratory to commercial reality—A real‐life case study. *Healthcare Technology Letters* **8**, 1-10 (2021).

26 Cohen, W. R. *et al.* Accuracy and reliability of fetal heart rate monitoring using maternal abdominal surface electrodes. *Acta Obstetricia et Gynecologica Scandinavica* **91**, 1306-1313 (2012).

27 https://www.usa.philips.com/healthcare/product/HC866488/avalon-beltless-fetal-monitoring-solution.

28 Mhajna, M. *et al.* Wireless, remote solution for home fetal and maternal heart rate monitoring. *American Journal of Obstetrics & Gynecology MFM* **2**, 100101 (2020).

29 https://www.mindchild.com/assets/22dsp021908-mindchild-patches-data-sheet.pdf.

30 Noirhomme, Q. *et al.* Validation of a new electrophysiological fetal heart rate monitor: comparison with cardiotocography. *American Journal of Obstetrics and Gynecology* **226**, S656-S657 (2022).

31 Lempersz, C. *et al.* Intrapartum non‐invasive electrophysiological monitoring: A prospective observational study. *Acta Obstetricia et Gynecologica Scandinavica* **99**, 1387-1395 (2020).

32 Liu, B., Marler, E., Thilaganathan, B. & Bhide, A. Ambulatory antenatal fetal electrocardiography in high-risk pregnancies (AMBER): protocol for a pilot prospective cohort study. *BMJ Open* **13**, e062448 (2023).

33 Clifford, G., Sameni, R., Ward, J., Robinson, J. & Wolfberg, A. J. Clinically accurate fetal ECG parameters acquired from maternal abdominal sensors. *American Journal of Obstetrics and Gynecology* **205**, 47.e41-47.e45 (2011).

34 https://clinicaltrials.gov/study/NCT04876846.

35 Kasap, B. *et al.* Use of A Novel Transabdominal Fetal Pulse Oximeter (TFO) In Human Pregnancy: A Proof-of-Concept. *American Journal of Obstetrics and Gynecology* **228**, S100 (2023).

36 Gunther, J. E., Jayet, B., Sekar, S. K. V., Kainerstorfer, J. M. & Andersson‐Engels, S. Review of optical methods for fetal monitoring in utero. *Journal of Biophotonics* **15**, e202100343 (2022).

37 Delay, U. *et al.* Novel non-invasive in-house fabricated wearable system with a hybrid algorithm for fetal movement recognition. *PLOS ONE* **16**, e0254560 (2021).

38 Du, Y.-C., Yen, L. B., Kuo, P.-L. & Tsai, P.-Y. A Wearable Device for Evaluation of Relative Position, Force, and Duration of Fetal Movement for Pregnant Woman Care. *IEEE Sensors Journal* **21**, 19341-19350 (2021).

39 Qin, M., Xu, Y., Liang, Y. & Sun, T. A wearable fetal movement detection system for pregnant women. *Frontiers in Medicine* **10**, 1160373 (2023).

40 Xu, J. *et al.* Fetal Movement Detection by Wearable Accelerometer Duo Based on Machine Learning. *IEEE Sensors Journal* **22**, 11526-11534 (2022).

41 Lai, J. *et al.* Performance of a wearable acoustic system for fetal movement discrimination. *PLOS ONE* **13**, e0195728 (2018).

42 Ghosh, A. K., Catelli, D. S., Wilson, S., Nowlan, N. C. & Vaidyanathan, R. Multi-modal detection of fetal movements using a wearable monitor. *Information Fusion* **103**, 102124 (2024).

43 Kauffmann, T. & Silberman, M. *Fetal Monitoring*. (StatPearls Publishing, 2023).

44 Goldenberg, R. L., Harrison, M. S. & McClure, E. M. Stillbirths: The Hidden Birth Asphyxia — US and Global Perspectives. *Clinics in Perinatology* **43**, 439-453 (2016).

45 Freeman, R. K. Problems with intrapartum fetal heart rate monitoring interpretation and patient management. *Obstet Gynecol* **100**, 813-826 (2002).

46 Baschat, A. A. & Gembruch, U. The cerebroplacental Doppler ratio revisited. *Ultrasound in Obstetrics & Gynecology* **21**, 124-127 (2003).

47 Alfirevic, Z., Devane, D., Gyte, G. M. & Cuthbert, A. Continuous cardiotocography (CTG) as a form of electronic fetal monitoring (EFM) for fetal assessment during labour. *Cochrane Database Syst Rev* **2**, CD006066-CD006066 (2017).

48 Kypros Nicolaides, G. R., Kurt Hecher, Renato Ximenes. *Doppler in Obstetrics*. (2002).

49 Berkley, E., Chauhan, S. P. & Abuhamad, A. Doppler assessment of the fetus with intrauterine growth restriction. *American Journal of Obstetrics and Gynecology* **206**, 300-308 (2012).

50 Kennedy, A. M. & Woodward, P. J. A Radiologist's Guide to the Performance and Interpretation of Obstetric Doppler US. *RadioGraphics* **39**, 893-910 (2019).

51 Maulik, D. & Lees, C. C. *Doppler Ultrasound in Obstetrics and Gynecology*. (Springer, 2023).

52 Dall'asta, A. *et al.* Intrapartum Doppler ultrasound: where are we now? *Minerva Obstet Gynecol* **73**, 94-102 (2021).

53 Woodward, P. J., Kennedy, A. & Sohaey, R. *Diagnostic imaging: obstetrics*. (Elsevier, 2021).

54 Nabeshima, Y., Sasaki, J., Mesaki, N., Sohda, S. & Kubo, T. Effect of Maternal Exercise on Fetal Umbilical Artery Waveforms: The Comparison of IUGR and AFD Fetuses. *Journal of Obstetrics and Gynaecology Research* **23**, 255-259 (1997).

55 Skow, R. J. *et al.* Effects of prenatal exercise on fetal heart rate, umbilical and uterine blood flow: a systematic review and meta-analysis. *British Journal of Sports Medicine* **53**, 124-133 (2019).

56 Smith, G. C. S. & Fretts, R. C. Stillbirth. *The Lancet* **370**, 1715-1725 (2007).

57 Douglas-Escobar, M. & Weiss, M. D. Hypoxic-Ischemic Encephalopathy. *JAMA Pediatrics* **169**, 397 (2015).

58 Nelson, K. B. & Grether, J. K. Causes of cerebral palsy. *Current Opinion in Pediatrics* **11**, 487-491 (1999).

59 Alfirevic, Z., Stampalija, T. & Dowswell, T. Fetal and umbilical Doppler ultrasound in high-risk pregnancies. *Cochrane Database of Systematic Reviews* **6**, CD007529 (2017).

60 Bhide, A. *et al.* ISUOG Practice Guidelines (updated): use of Doppler velocimetry in obstetrics. *Ultrasound in Obstetrics & Gynecology* **58**, 331-339 (2021).

61 Lees, C. C. *et al.* ISUOG Practice Guidelines: diagnosis and management of small-for-gestational-age fetus and fetal growth restriction. *Ultrasound in Obstetrics & Gynecology* **56**, 298-312 (2020).

62 Sotiriadis, A. *et al.* ISUOG Practice Guidelines: role of ultrasound in screening for and follow-up of pre-eclampsia. *Ultrasound in Obstetrics & Gynecology* **53**, 7-22 (2019).

63 Rouse, D. J., Owen, J., Goldenberg, R. L. & Cliver, S. P. Determinants of the optimal time in gestation to initiate antenatal fetal testing: a decision-analytic approach. *Am J Obstet Gynecol* **173**, 1357-1363 (1995).

64 McClure, E. *et al.* Global Network for Women's and Children's Health Research: probable causes of stillbirth in low- and middle- income countries using a prospectively defined classification system. *BJOG: An International Journal of Obstetrics & Gynaecology* **125**, 131-138 (2018).

65 Leon, R. L. *et al.* Cerebral Blood Flow Monitoring in High-Risk Fetal and Neonatal Populations. *Frontiers in Pediatrics* **9**, 748345 (2022).

66 Acharya, G., Wilsgaard, T., Berntsen, G. K. R., Maltau, J. M. & Kiserud, T. Reference ranges for serial measurements of blood velocity and pulsatility index at the intra-abdominal portion, and fetal and placental ends of the umbilical artery. *Ultrasound in Obstetrics & Gynecology* **26**, 162-169 (2005).

67 Acharya, G., Wilsgaard, T., Berntsen, G. K. R., Maltau, J. M. & Kiserud, T. Reference ranges for serial measurements of umbilical artery Doppler indices in the second half of pregnancy. *American journal of obstetrics and gynecology* **192**, 937-944 (2005).

68 Drukker, L. *et al.* International gestational age-specific centiles for umbilical artery Doppler indices: a longitudinal prospective cohort study of the INTERGROWTH-21st Project. *American Journal of Obstetrics and Gynecology* **222**, 602.e601-602.e615 (2020).

69 Mari, G. *et al.* Noninvasive Diagnosis by Doppler Ultrasonography of Fetal Anemia Due to Maternal Red-Cell Alloimmunization. *New England Journal of Medicine* **342**, 9-14 (2000).

70 Chudleigh, T., Smith, A. & Cumming, S. *Obstetric & Gynaecological Ultrasound: How, Why and When*. (Elsevier, 2016).

71 Ali, S. *et al.* Standardization and quality control of Doppler and fetal biometric ultrasound measurements in low-income setting. *Ultrasound in Obstetrics & Gynecology* **61**, 481-487 (2023).

72 Li, K., Zeng, D. W., Yung, K. C., Chan, H. L. W. & Choy, C. L. Study on ceramic/polymer composite fabricated by laser cutting. *Materials Chemistry and Physics* **75**, 147-150 (2002).

73 Lukacs, M. *et al.* Performance and Characterization of New Micromachined High-Frequency Linear Arrays. *IEEE Transactions on Ultrasonics, Ferroelectrics and Frequency Control* **53**, 1719-1729 (2006).

74 Foster, F. S. *et al.* A new 15-50 MHz array-based micro-ultrasound scanner for preclinical imaging. *Ultrasound Med Biol* **35**, 1700-1708 (2009).

75 Zeng, D. W. *et al.* UV laser micromachining of piezoelectric ceramic using a pulsed Nd:YAG laser. *Applied Physics A* **78**, 415-421 (2004).

76 Yuan, Z., Riaz, A. & Chohan, B. S. Precision Machining by Dicing Blades: A Systematic Review. *Machines* **11**, 259 (2023).

77 Lu, G. *et al.* Noninvasive imaging-guided ultrasonic neurostimulation with arbitrary 2D patterns and its application for high-quality vision restoration. *Nature Communications* **15**, 4481 (2024).

78 Kang, H. *et al.* 2-D Array Design and Fabrication With Pitch-Shifting Interposer at Frequencies From 4 MHz up to 10 MHz. *IEEE Transactions on Ultrasonics, Ferroelectrics, and Frequency Control* **69**, 3382-3391 (2022).

79 Wodnicki, R. *et al.* Co-Integrated PIN-PMN-PT 2-D Array and Transceiver Electronics by Direct Assembly Using a 3-D Printed Interposer Grid Frame. *IEEE Transactions on Ultrasonics, Ferroelectrics, and Frequency Control* **67**, 387-401 (2020).

80 https://www.disco.co.jp/eg/solution/library/dicing/basic.html.

81 Hoskins, P. R., Martin, K. & Thrush, A. *Diagnostic Ultrasound Physics and Equipment*. (CRC Press, 2019).

82 Evans, D. H., Jensen, J. A. & Nielsen, M. B. Ultrasonic colour Doppler imaging. *Interface Focus* **1**, 490-502 (2011).

83 Zhang, L., Du, W., Kim, J.-H., Yu, C.-C. & Dagdeviren, C. An Emerging Era: Conformable Ultrasound Electronics. *Advanced Materials* **36**, 2307664 (2024).

84 Li, Y., Liang, B., Gu, Z.-M., Zou, X.-Y. & Cheng, J.-C. Reflected wavefront manipulation based on ultrathin planar acoustic metasurfaces. *Scientific Reports* **3** (2013).

85 Kuhn, C. Impact of extracorporeal shock waves on the human skin with cellulite: A case study of an unique instance. *Clinical Interventions in Aging* **3**, 201-210 (2008).

86 Gajasinghe, R. W. R. L. *et al.* Experimental study of PDMS bonding to various substrates for monolithic microfluidic applications. *Journal of Micromechanics and Microengineering* **24**, 075010 (2014).

87 Chang, C. *et al.* Acoustic lens for capacitive micromachined ultrasonic transducers. *Journal of Micromechanics and Microengineering* **24**, 085007 (2014).

88 Hao, B. *et al.* Focused ultrasound enables selective actuation and Newton-level force output of untethered soft robots. *Nature Communications* **15**, 5197 (2024).

89 Grand-Perret, V. *et al.* A Novel Microflow Phantom Dedicated to Ultrasound Microvascular Measurements. *Ultrasonic Imaging* **40**, 325-338 (2018).

90 Di Sieno, L. *et al.* in *Novel Biophotonics Techniques and Applications V.* 11075 (Optica Publishing Group).

91 Tsou, J. K., Liu, J., Barakat, A. I. & Insana, M. F. Role of Ultrasonic Shear Rate Estimation Errors in Assessing Inflammatory Response and Vascular Risk. *Ultrasound in Medicine & Biology* **34**, 963-972 (2008).

92 Aksoy, B. *et al.* Shielded soft force sensors. *Nature Communications* **13**, 4649 (2022).

93 https://www.analog.com/media/en/training-seminars/tutorials/mt-012.pdf.

94 Ballou, G. *Handbook for Sound Engineers*. (Routledge, 2008).

95 https://download.tek.com/document/3AW_19134_2_MR_Letter.pdf.

96 Nath, M., Maity, S., Avlani, S., Weigand, S. & Sen, S. Inter-body coupling in electro-quasistatic human body communication: theory and analysis of security and interference properties. *Scientific Reports* **11**, 4378 (2021).

97 Kibret, B., Teshome, A. & Lai, D. Human Body as Antenna and Its Effect on Human Body Communications. *Progress In Electromagnetics Research* **148**, 193-207 (2014).

98 Li, J., Nie, Z., Liu, Y., Wang, L. & Hao, Y. Evaluation of Propagation Characteristics Using the Human Body as an Antenna. *Sensors* **17**, 2878 (2017).

99 Razavi, B. *RF Microelectronics*. (Pearson, 2011).

100 Kledrowetz, V., Fujcik, L., Prokop, R. & Háze, J. A 1 V 92 dB SNDR 10 kHz Bandwidth Second-Order Asynchronous Delta-Sigma Modulator for Biomedical Signal Processing. *Sensors* **20**, 4137 (2020).

101 https://resources.altium.com/p/everything-you-need-know-about-stitching-vias.

102 Zhou, S. *et al.* Transcranial volumetric imaging using a conformal ultrasound patch. *Nature* **629**, 810-818 (2024).

103 Basyigit, I. B., Dogan, H. & Helhel, S. The effect of aperture shape, angle of incidence and polarization on shielding effectiveness of metallic enclosures. *Journal of Microwave Power and Electromagnetic Energy* **53**, 115-127 (2019).

104 Razavi, B. *Design of Analog CMOS Integrated Circuits*. (McGraw-Hill Education, 2017).

105 Ding, N. *et al.* in *Proceedings of the ACM SIGMETRICS/international conference on Measurement and modeling of computer systems* 29–40 (Association for Computing Machinery, Pittsburgh, PA, USA, 2013).

106 Wu, J. *et al.* in *2023 IEEE International Symposium on Circuits and Systems (ISCAS).* 1-5.

107 Horowitz, P. & Hill, W. *The Art of Electronics*. (Cambridge University Press, 2015).

108 Haykin, S. & Moher, M. *Communication Systems*. (John Wiley & Sons, 2009).

109 https://www.sunnuclear.com/uploads/documents/datasheets/068-DS-072120.pdf.

110 Köşüş, A., Köşüş, N. & Turhan, N. Ö. Is there any relation between umbilical artery and vein diameter and estimated fetal weight in healthy pregnant women? *Journal of Medical Ultrasonics* **39**, 227-234 (2012).

111 Fitzsimmons, E. D. & Bajaj, T. *Embryology, Amniotic Fluid*. (StatPearls Publishing, 2023).

112 Mark, J. E. *Physical Properties of Polymers Handbook*. (Springer New York, 2007).

113 Formlabs. Elastic 50A.

114 Mencarelli, M., Puggelli, L., Virga, A., Furferi, R. & Volpe, Y. Acoustic velocity and stability of tissue-mimicking echogenic materials for ultrasound training phantoms. *Journal of Materials Science* **59**, 6509-6524 (2024).

115 Food and Drug Administration. Marketing clearance of diagnostic ultrasound systems and transducers: Guidance for industry and food and drug administration staff. *U.S. Food and Drug Administration, Silver Spring, MD, USA*, Tech. Rep. FDA-2017-D-5372 (2023).

116 International Electrotechnical Commission. IEC 62359:2010/AMD1:2017 "Ultrasonics: Field Characterization—Test Methods for the Determination of Thermal and Mechanical Indices Related to Medical Diagnostic Ultrasonic Fields". *International Electrotechnical Commission, Geneva, Switzerland*, Ed. 2.1 (2017).

117 International Electrotechnical Commission. IEC 62127-1:2022 "Ultrasonics – Hydrophones – Part 1: Measurement and characterization of medical ultrasonic fields". *International Electrotechnical Commission, Geneva, Switzerland*, Ed. 2.0 (2022).

118 Commission, I. E. IEC 62127-1:2022 "Ultrasonics – Hydrophones – Part 1: Measurement and characterization of medical ultrasonic fields". *International Electrotechnical Commission, Geneva, Switzerland*, Ed. 2.0 (2022).

119 Duck, F. A. Medical and non-medical protection standards for ultrasound and infrasound. *Progress in Biophysics and Molecular Biology* **93**, 176-191 (2007).

120 Bigelow, T. A. *et al.* The Thermal Index. *Journal of Ultrasound in Medicine* **30**, 714-734 (2011).

121 AIUM Official Statement for Recommended Maximum Scanning Times for Displayed Thermal Index Values. *Journal of Ultrasound in Medicine* **42**, E74-E75 (2023).

122 Safety Group of the British Medical Ultrasound Society. Guidelines for the safe use of diagnostic ultrasound equipment. *Ultrasound* **18**, 52-59 (2010).

123 International Electrotechnical Commission. IEC 60601-2-37:2024 "Medical electrical equipment - Part 2-37: Particular requirements for the basic safety and essential performance of ultrasonic medical diagnostic and monitoring equipment". *International Electrotechnical Commission, Geneva, Switzerland*, Ed. 3.0 (2024).

124 Drukker, L., Droste, R., Chatelain, P., Noble, J. A. & Papageorghiou, A. T. Safety Indices of Ultrasound: Adherence to Recommendations and Awareness During Routine Obstetric Ultrasound Scanning. *Ultraschall in der Medizin - European Journal of Ultrasound* **41**, 138-145 (2020).

125 SATTAR, N. *et al.* Antenatal Waist Circumference and Hypertension Risk. *Obstetrics & Gynecology* **97**, 268-271 (2001).

126 Sohn, M. & Bye, E. Visual analysis of body shape changes during pregnancy. *International Journal of Fashion Design, Technology and Education* **5**, 117-128 (2012).

127 Ahmadibeni, A., Kashani, P., Hallaj, M. S., Ghanbari, S. & Javadifar, N. The relationship of pre-pregnancy body mass index with maternal anthropometric indices, weight retention and the baby's weight and nutrition in the first 6 months post-partum. *BMC Pregnancy and Childbirth* **23**, 802 (2023).

128 Karlsson, B., Berson, M., Helgason, T., Geirsson, R. T. & Pourcelot, L. Effects of fetal and maternal breathing on the ultrasonic Doppler signal due to fetal heart movement. *Eur J Ultrasound* **11**, 47-52 (2000).

129 Cahill, L. S. *et al.* Determination of fetal heart rate short-term variation from umbilical artery Doppler waveforms. *Ultrasound in Obstetrics & Gynecology* **57**, 70-74 (2021).

130 Wilson, L. S., Dadd, M. J. & Gill, R. W. Automatic vessel tracking and measurement for Doppler studies. *Ultrasound Med Biol* **16**, 645-652 (1990).

131 Saad, A. A., Loupas, T. & Shapiro, L. G. Computer Vision Approach for Ultrasound Doppler Angle Estimation. *Journal of Digital Imaging* **22**, 681-688 (2009).

132 Lin, M. *et al.* A fully integrated wearable ultrasound system to monitor deep tissues in moving subjects. *Nature Biotechnology* **42**, 448-457 (2024).

133 https://www.fujifilm.com/de/en/healthcare/ultrasound/arietta/arietta-65/applications.

134 https://www.accessdata.fda.gov/cdrh_docs/pdf20/K202422.pdf.

135 https://www.accessdata.fda.gov/cdrh_docs/pdf23/K232145.pdf.

136 https://marketing.webassets.siemens-healthineers.com/b2b416820d9a212a/a8185f7fda1a/ACUSON-Origin-Brochure.PDF.

137 https://www.youtube.com/watch?v=-xQGIj5DaPE.

138 https://echonous.com/kosmos-ai-ultrasound/.

139 https://www.youtube.com/watch?v=JxDFp59R670.

140 https://www.accessdata.fda.gov/cdrh_docs/pdf23/K233826.pdf.

141 Vincent, L. 197-208 (Springer Berlin Heidelberg).

142 Serra, J. & Vincent, L. An overview of morphological filtering. *Circuits, Systems and Signal Processing* **11**, 47-108 (1992).

143 Ferrazzi, E. *et al.* Umbilical vein blood flow in growth-restricted fetuses. *Ultrasound in Obstetrics & Gynecology* **16**, 432-438 (2000).

144 Ma, J. *et al.* Segment anything in medical images. *Nature Communications* **15**, 654 (2024).

145 So, H., Chen, J., Yiu, B. & Yu, A. Medical Ultrasound Imaging: To GPU or Not to GPU? *IEEE Micro* **31**, 54-65 (2011).

146 Chang, L. W., Hsu, K. H. & Li, P. C. Graphics Processing Unit-Based High-Frame-Rate Color Doppler Ultrasound Processing. *IEEE Transactions on Ultrasonics, Ferroelectrics, and Frequency Control* **56**, 1856-1860 (2009).

147 AIUM Practice Parameter for the Performance of Standard Diagnostic Obstetric Ultrasound. *Journal of Ultrasound in Medicine* **43**, E20-E32 (2024).

148 Wang, X., Yang, Y.-Q., Cai, S., Li, J.-C. & Wang, H.-Y. Deep-learning-based sampling position selection on color Doppler sonography images during renal artery ultrasound scanning. *Scientific Reports* **14**, 11768 (2024).

149 Oates, C. *Ultrasound Technology for Clinical Practitioners*. (Wiley, 2023).

150 Balkawade, N. U. & Shinde, M. A. Study of Length of Umbilical Cord and Fetal Outcome: A Study of 1,000 Deliveries. *The Journal of Obstetrics and Gynecology of India* **62**, 520-525 (2012).

151 Spencer, J. A., Price, J. & Lee, A. Influence of fetal breathing and movements on variability of umbilical Doppler indices using different numbers of waveforms. *Journal of Ultrasound in Medicine* **10**, 37-41 (1991).

152 Stroux, L., Redman, C. W., Georgieva, A., Payne, S. J. & Clifford, G. D. Doppler-based fetal heart rate analysis markers for the detection of early intrauterine growth restriction. *Acta Obstet Gynecol Scand* **96**, 1322-1329 (2017).

153 Pildner Von Steinburg, S. *et al.* What is the “normal” fetal heart rate? *PeerJ* **1**, e82 (2013).

154 Oros, D. *et al.* Reference ranges for Doppler indices of umbilical and fetal middle cerebral arteries and cerebroplacental ratio: systematic review. *Ultrasound in Obstetrics & Gynecology* **53**, 454-464 (2019).

155 Zohav, E. *et al.* Third-trimester Reference Ranges for Cerebroplacental Ratio, Middle Cerebral Artery, and Umbilical Artery Pulsatility Index in Normal-growth Singleton Fetuses in the Israeli Population. *Rambam Maimonides Medical Journal* **10**, e0025 (2019).

156 Khandre, V., Potdar, J. & Keerti, A. Preterm Birth: An Overview. *Cureus* **14**, e33006 (2022).

157 Deng, Y., Rouze, N. C., Palmeri, M. L. & Nightingale, K. R. Ultrasonic Shear Wave Elasticity Imaging Sequencing and Data Processing Using a Verasonics Research Scanner. *IEEE Transactions on Ultrasonics, Ferroelectrics, and Frequency Control* **64**, 164-176 (2017).

158 Yu, J., Yoon, H., Khalifa, Y. M. & Emelianov, S. Y. Design of a Volumetric Imaging Sequence Using a Vantage-256 Ultrasound Research Platform Multiplexed With a 1024-Element Fully Sampled Matrix Array. *IEEE Transactions on Ultrasonics, Ferroelectrics, and Frequency Control* **67**, 248-257 (2020).

159 Georgieva, A., Abry, P., Nunes, I. & Frasch, M. G. Editorial: Fetal-maternal monitoring in the age of artificial intelligence and computer-aided decision support: A multidisciplinary perspective. *Frontiers in Pediatrics* **10**, 2296-2360 (2022).

160 Xu, S., Kim, J., Walter, J. R., Ghaffari, R. & Rogers, J. A. Translational gaps and opportunities for medical wearables in digital health. *Science Translational Medicine* **14**, eabn6036 (2022).

161 Demi, L. Practical Guide to Ultrasound Beam Forming: Beam Pattern and Image Reconstruction Analysis. *Applied Sciences* **8**, 1544 (2018).

162 Chen, C. & Pertijs, M. A. P. Integrated Transceivers for Emerging Medical Ultrasound Imaging Devices: A Review. *IEEE Open Journal of the Solid-State Circuits Society* **1**, 104-114 (2021).

163 Zhang, Y. & Demosthenous, A. Integrated Circuits for Medical Ultrasound Applications: Imaging and Beyond. *IEEE Transactions on Biomedical Circuits and Systems* **15**, 838-858 (2021).

164 Browne, J. E. A review of Doppler ultrasound quality assurance protocols and test devices. *Physica Medica* **30**, 742-751 (2014).

165 https://www.cirsinc.com/wp-content/uploads/2020/07/769DF-DS-072220.pdf.

166 Calvert, J. & Duck, F. Self-heating of Diagnostic Ultrasound Transducers in Air and in Contact with Tissue Mimics. *Ultrasound* **14**, 100-108 (2006).

167 Hadlock, F. P., Harrist, R. B., Sharman, R. S., Deter, R. L. & Park, S. K. Estimation of fetal weight with the use of head, body, and femur measurements--a prospective study. *Am J Obstet Gynecol* **151**, 333-337 (1985).